Volatiles in the Earth and Moon: Constraints on planetary formation and evolution

Volatiles in the Earth and Moon: Constraints on planetary formation and evolution

A dissertation presented

by

Rita Parai

to

The Department of Earth and Planetary Sciences

in partial fulfillment of the requirements

for the degree of

Doctor of Philosophy

in the subject of

Earth and Planetary Sciences

Harvard University

Cambridge, Massachusetts

May 2014

Dissertation Advisors: Professors Sujoy Mukhopadhyay and Stein Jacobsen Rita Parai

Volatiles in the Earth and Moon: Constraints on planetary formation and evolution

Abstract

The volatile inventories of the Earth and Moon reflect unique histories of volatile acquisition and loss in the early Solar System. The terrestrial volatile inventory was established after the giant impact phase of accretion, and the planet subsequently settled into a regime of long-term volatile exchange between the mantle and surface reservoirs in association with plate tectonics. Therefore, volatiles in the Earth and Moon shed light on a diverse array of processes that shaped planetary bodies in the Solar System as they evolved to their present-day states.

Here we investigate new constraints on volatile depletion in the early Solar System, early outgassing of the terrestrial mantle, and the long-term evolution of the deep Earth volatile budget. We develop a Monte Carlo model of long-term water exchange between the mantle and surface reservoirs. Previous estimates of the deep Earth return flux of water are up to an order of magnitude too large, and incorporation of recycled slabs on average rehydrates the upper mantle but dehydrates the plume source.

We find evidence for heterogeneous recycling of atmospheric argon and xenon into the upper mantle from noble gases in Southwest Indian Ridge basalts. Xenon isotope systematics indicate that xenon budgets of mid-ocean ridge and plume-related mantle sources are dominated by recycled atmospheric xenon, though the two sources have experienced different degrees of degassing. Differences between the mid-ocean ridge and

plume sources were initiated within the first 100 million years of Earth history, and the two sources have never subsequently been homogenized. New high-precision xenon isotopic data contribute to an emerging portrait of two mantle reservoirs with distinct histories of outgassing and incorporation of recycled material in association with plate tectonics.

Xenon isotopes indicate that the Moon likely formed within ~70 million years of the start of the Solar System. To further investigate early Solar System chronology, we determined strontium isotopic compositions in a suite of planetary materials. If the Moon is derived from proto-Earth material, then rubidium-strontium systematics in the lunar anorthosite 60025 and Moore County plagioclase indicate that Moon formation occurred within ~62 million years of the start of the Solar System.

Table of Contents

Abstract…… iii

Table of contents……. v

List of figures…….. xi

List of tables……... xvii

Acknowledgments…….. xix

Chapter 1: Volatiles in the Earth and Moon……. 1

1.1 Introduction……. 1

1.2 How large is the subducted water flux? New constraints on mantle regassing rates……. 3

1.3 Heterogeneous upper mantle Ne, Ar and Xe isotopic compositions and a possible Dupal noble gas signature recorded in basalts from the Southwest Indian Ridge…….. 4

1.4 Constraints from I-Pu-U-Xe systematics on the nature of mantle reservoirs, planetary volatile evolution and the timing of the Moon-forming giant impact……. 5

1.5 Strontium isotopic constraints on early Solar System chronology and the history of planetary volatile depletion……. 7

1.6 Conclusions…… 8

1.7 References…….. 8

Chapter 2: How large is the subducted water flux? New constraints on mantle regassing rates……. 10

2.1 Introduction……. 12

2.2 Model…….. 15

2.2.1 Defining the model parameter space……... 16

2.2.2 Model setup……. 17

2.2.3 Model constraints…… 19

2.2.3.1 Model success criterion 1: The global slab-derived arc and back-arc water output must not exceed the global water input at trenches……. 19

2.2.3.2 Model success criterion 2: Net flux must satisfy constraints on Phanerozoic sea level change…….. 23

2.3 Results…… 28

2.4 Discussion……. 33

2.4.1 The hydration state of subducting slab……... 33

2.4.2 Previous estimates of the return flux of water to the mantle 34

2.4.3 Mantle regassing rates……. 36

2.4.4 Implications for the evolution of mantle volatile budgets 38

2.5 Conclusions…… 40

2.6 References……. 41

Chapter 3: Heterogeneous upper mantle Ne, Ar and Xe isotopic compositions and a possible Dupal noble gas signature recorded in basalts from the Southwest Indian Ridge…….. 49

3.1 Introduction……. 51

3.2 Background and methods…… 55

3.2.1 Sample background…….. 55

3.2.2 Analytical methods…….. 56

3.3 Results……. 58

3.3.1 CO_2– Helium systematics…… 58

3.3.2 Measured Ne, Ar, Xe compositions…… 59

3.4. Source Ne, Ar and Xe isotopic compositions corrected for syn- to post-eruptive atmospheric contamination……. 59

3.4.1 Mantle source neon isotopic compositions……. 60

3.4.2 Mantle source argon isotopic compositions……... 62

3.4.3 Mantle source xenon isotopic compositions…….. 64

3.5 Discussion……. 67

3.5.1 Variations in MORB source composition along the SWIR from 7 to 25°E…… 67

3.5.2 A heterogeneous MORB source mantle in heavy noble gas isotopes…….. 72

3.5.3 The nature of the heterogeneities observed at SWIR 7-25°E…… 73

3.5.3.1 The 7°E ridge segment…….. 73

3.5.3.2 The Oblique Supersegment…….. 74

3.5.3.3 The Orthogonal Supersegment……..... 76

3.5.3.4. Constraints on the origin of the Dupal mantle domain……. 78

3.5.4. SWIR Xe evidence for upper mantle heterogeneity, early differentiation and preservation of ancient mantle reservoirs……. 79

3.6 Conclusions…….. 84

3.7 References……..... 85

Chapter 4: Constraints from I-Pu-U-Xe systematics in Southwest Indian Ridge basalts on mantle volatile evolution and the timing of the Moon-forming giant impact……. 92

4.1 Introduction……... 94

4.2 Samples and methods…… 98

4.2.1 Sample preparation, gas extraction and mass spectrometry 99

4.2.2 Corrections for syn- to post-eruptive atmospheric contamination……... 101

4.2.3 Linear least squares determination of initial, recycled atmospheric, Pu- and U-fissiogenic Xe components in the SWIR mantle source……... 102

4.3 Results……..... 106

4.4. A two-stage model of MORB source degassing…… 116

4.4.1 Model details…… 118

4.4.1.1 Early degassing stage…… 118

4.4.1.2 Long-term degassing stage……... 123

4.4.1.2.1 Mantle processing……..... 124

4.4.1.2.2 Continental crust growth models…… 125

4.4.2 Comparison with previous early Earth degassing models 128

4.4.3 Model results……. 134

4.4.3.1 Effect of varying accretion timescales…….. 138

4.4.3.2 Effect of long-term mantle processing…….. 141

4.4.3.3 Effect of varying Xe retention in early degassing stage…… 142

4.5 Discussion……. 150

4.5.1 Recycling of atmospheric Xe into MORB and plume sources: Evidence for incorporation of recycled material into mantle reservoirs…… 150

4.5.2 MORB and plume sources have experienced different degassing histories……. 152

4.5.3 Constraints on the age of the Moon-forming giant impact from I-Pu-U-Xe systematics…….. 153

4.5.4 The emerging portrait of distinct ancient, heterogeneous and continuously-evolving mantle sources…… 157

4.6 Conclusions……. 159

4.7 References…….. 160

Chapter 5: Strontium isotopic constraints on early Solar System chronology and the history of planetary volatile depletion…….. 166

5.1 Introduction…….. 167

5.2 Samples and methods…….. 170

5.2.1 Dissolution and chemical separation of Sr…….. 170

5.2.2 Thermal ionization mass spectrometry……. 171

5.3 Results……. 173

5.3.1 Measurements of $^{87}Sr/^{86}Sr$ in planetary materials…… 174

5.3.2 A new normalized compilation of initial $^{87}Sr/^{86}Sr$ in planetary materials……... 181

5.4 Discussion…….. 182

5.4.1 Issues resolved by our new normalization……..... 182

5.4.2 Early Solar System Rb-Sr chronology…… 186

5.5 Conclusions…… 196

5.6 References…….. 197

Appendices…… …… 201

Appendix 1 Hyperbolic fitting ……..... 202

Appendix 2 Supplement to Chapter 2…… 207

Appendix 3 Supplement to Chapter 3…… 210

Appendix 4 Supplement to Chapter 4…… 227

List of Figures

Chapter 2: How large is the subducted water flux? New constraints on mantle regassing rates

Figure 2.1 Schematic of global water fluxes considered between the mantle and exosphere…… 13

Figure 2.2 Arc and back-arc H_2O-Ti systematics…….. 21

Figure 2.3 Reconstructions of Phanerozoic sea level…… 25

Figure 2.4 Model success rate contoured for arc water content and trench input……. 31

Figure 2.5 Model success rate for three different arc magmatic production rate intervals…… 32

Figure 2.6 Sea level decrease over 542 Myr as a function of return flux to the mantle……... 35

Chapter 3: Heterogeneous upper mantle Ne, Ar and Xe isotopic compositions and a possible Dupal noble gas signature recorded in basalts from the Southwest Indian Ridge

Figure 3.1 Map of the Southwest Indian Ridge study area…… 56

Figure 3.2 Correction for syn- to post-eruptive atmospheric contamination to determine mantle source $^{21}Ne/^{22}Ne$…… 61

Figure 3.3 Correction for syn- to post-eruptive atmospheric contamination to determine mantle source $^{40}Ar/^{36}Ar$……. 65

Figure 3.4 Correction for syn- to post-eruptive atmospheric contamination to determine mantle source $^{129}Xe/^{130}Xe$……. 66

Figure 3.5 Mantle source $CO_2/^3He$, Ne, Ar and Xe isotopic variations with longitude along the SWIR from 7°E to 25°E……. 68

Figure 3.6 He-Ne, He-Ar and Ne-Ar systematics in SWIR mantle sources 70

Figure 3.7 He-Xe, Ne-Xe and Ar-Xe systematics in SWIR mantle sources…… 71

Figure 3.8 SWIR Xe isotope systematics in $^{136}Xe/^{130}Xe$ vs. $^{129}Xe/^{130}Xe$ space for Orthogonal Supersegment samples…… 80

Figure 3.9 Error-weighted averages of measured $^{129}Xe/^{136}Xe$ plotted against error-weighted average of measured $^{130}Xe/^{136}Xe$ for the SWIR Orthogonal Supersegment…….. 81

Chapter 4: Constraints from I-Pu-U-Xe systematics in Southwest Indian Ridge basalts on mantle volatile evolution and the timing of the Moon-forming giant impact

Figure 4.1 Map of the Southwest Indian Ridge study area…… 98

Figure 4.2 Correction for syn- to post-eruptive atmospheric contamination to determine mantle source $^{129}Xe/^{132}Xe$…… 102

Figure 4.3 Proportions of present-day mantle ^{132}Xe derived from solar wind, recycled atmosphere, U-fission and Pu-fission in MORB and plume mantle sources…… 108

Figure 4.4 $^{129}Xe^*/^{136}Xe_{Pu}$ in individual MORB and plume-influenced mantle sources…… 110

Figure 4.5 $^{136}Xe_{Pu}/(^{136}Xe_{Pu}+^{136}Xe_U)$ in individual MORB and plume-influenced mantle sources…….. 111

Figure 4.6 Fraction of recycled atmospheric Xe in individual MORB and plume-influenced mantle sources……... 112

Figure 4.7 Error-weighted group average MORB and plume-influenced mantle source $^{129}Xe^*/^{136}Xe_{Pu}$……..... 113

Figure 4.8 Error-weighted group average MORB and plume-influenced mantle source $^{136}Xe_{Pu}/(^{136}Xe_{Pu}+^{136}Xe_{U})$……. 114

Figure 4.9 Early degassing stage illustration…… 119

Figure 4.10 Continental crust growth models used for the long-term degassing stage…….. 126

Figure 4.11 Forward modeled $^{129}Xe^*/^{136}Xe_{Pu}$ as a function of time of closure using classical early degassing parameters…… 130

Figure 4.12 Forward modeled $^{129}Xe^*/^{136}Xe_{Pu}$ contoured as a function of t_{LGI} and fraction of Xe retained for discrete loss events…… 133

Figure 4.13 Example time evolution curves for ^{129}I, ^{244}Pu and ^{238}U….. 135

Figure 4.14 Example time evolution curves for ^{129}Xe, $^{136}Xe_{Pu}$ and $^{136}Xe_{U}$ 137

Figure 4.15 Forward modeled $^{129}Xe^*/^{136}Xe_{Pu}$ as a function of accretion time constant α…….. 139

Figure 4.16 Forward modeled $^{136}Xe_{Pu}/(^{136}Xe_{Pu}+^{136}Xe_{U})$as a function of accretion time constant α 140

Figure 4.17 Forward modeled $^{129}Xe^*/^{136}Xe_{Pu}$ as a function of t_{LGI} for a range of N_{res}……. 141

Figure 4.18 Forward modeled $^{136}Xe_{Pu}/(^{136}Xe_{Pu}+^{136}Xe_{U})$ as a function of N_{res}…… 143

Figure 4.19 Forward modeled $^{129}Xe^*/^{136}Xe_{Pu}$ as a function of *retXe_preLGI*…….. 145

Figure 4.20 Forward modeled $^{129}Xe^*/^{136}Xe_{Pu}$ as a function of t_{LGI} for an example discrete loss event…… 147

Figure 4.21 Example time evolution curves for ^{129}Xe, $^{136}Xe_{Pu}$ for discrete loss events……. 148

Figure 4.22 Forward modeled $^{129}Xe^*/^{136}Xe_{Pu}$ and $^{136}Xe_{Pu}/(^{136}Xe_{Pu}+^{136}Xe_{U})$ as a function of *retXe_postLGI*…… 149

Chapter 5: Strontium isotopic constraints on early Solar System chronology and the history of planetary volatile depletion

Figure 5.1 Analyses of standard reference materials in Spring 2014…… 172

Figure 5.2 Reproducibility of offset between standard reference materials in Summer 2013 and Spring 2014……... 173

Figure 5.3 Measured $^{87}Sr/^{86}Sr$ in planetary materials……... 180

Figure 5.4 Normalized compilation of literature initial $^{87}Sr/^{86}Sr$ in planetary materials……. 183

Figure 5.5 Normalized compilation of literature initial $^{87}Sr/^{86}Sr$ grouped by type of planetary material……. 184

Figure 5.6 Three stage evolution models of Sr isotopic evolution…….. 188

Figure 5.7 Effective $^{87}Rb/^{86}Sr$ in the lunar precursor as a function of the crystallization age of 60025…….. 190

Figure 5.8 Two-stage Sr isotopic evolution models……... 192

Figure 5.9 Three-stage models illustrating Sr isotopic evolution if the Moon is derived from the proto-Earth…… 194

Appendices

Figure A3.1 CO_2–^{3}He linear regressions…… 211

Figure A3.2 $^{20}Ne/^{22}Ne$–$^{40}Ar/^{36}Ar$ hyperbolic fitting chi square evaluation 213

Figure A3.3 $^{40}Ar/^{36}Ar$–$^{129}Xe/^{130}Xe$ hyperbolic fitting chi square evaluation 214

Figure A4.1 $^{40}Ar/^{36}Ar$–$^{129}Xe/^{132}Xe$ hyperbolic fitting chi square evaluation 228

Figure A4.2 Linear least squares determination of mantle source $^{131,134,136}Xe/^{132}Xe$ for SWIR Western Orthogonal Supersegment…….. 229

Figure A4.3 Linear least squares determination of mantle source $^{131,134,136}Xe/^{132}Xe$ for SWIR Eastern Orthogonal Supersegment 230

Figure A4.4 Linear least squares determination of mantle source $^{131,134,136}Xe/^{132}Xe$ for AG22 1-1 & 1-4…… 231

Figure A4.5 Linear least squares determination of mantle source $^{131,134,136}Xe/^{132}Xe$ for KN162-7 11-25…… 232

Figure A4.6 Linear least squares determination of mantle source $^{131,134,136}Xe/^{132}Xe$ for KN162-7 22-14…… 233

Figure A4.7 Linear least squares determination of mantle source $^{131,134,136}Xe/^{132}Xe$ for AG22 9-2……. 234

Figure A4.8 Linear least squares determination of mantle source $^{131,134,136}Xe/^{132}Xe$ for AG22 13-1…….. 235

Figure A4.9 Pie chart illustrating mantle ^{132}Xe mixing proportions from recycled atmosphere, AVCC initial Xe, Pu-fission and U-fission…….. 236

Figure A4.10 Pie chart illustrating mantle ^{132}Xe mixing proportions from recycled atmosphere, U-Xe initial Xe, Pu-fission and U-fission 237

List of Tables

Chapter 2: How large is the subducted water flux? New constraints on mantle regassing rates

Table 2.1 Water cycle model parameter space……. 16

Table 2.2 Trench input fluxes……... 18

Table 2.3 Results of Monte Carlo simulation of global water cycle… 29

Chapter 3: Heterogeneous upper mantle Ne, Ar and Xe isotopic compositions and a possible Dupal noble gas signature recorded in basalts from the Southwest Indian Ridge

Table 3.1 SWIR mantle source He, CO_2, Ne, Ar, Xe compositions…. 63

Chapter 4: Constraints from I-Pu-U-Xe systematics in Southwest Indian Ridge basalts on mantle volatile evolution and the timing of the Moon-forming giant impact

Table 4.1 SWIR mantle source Xe isotopic compositions……... 103

Table 4.2 Xe endmember component compositions…… 105

Table 4.3 Linear least squares solutions for mixing proportions of ^{132}Xe…… 107

Table 4.4 Two-stage degassing model parameters……. 117

Table 4.5 Radioactive decay constants and fission yields……. 121

Chapter 5: Strontium isotopic constraints on early Solar System chronology and the history of planetary volatile depletion

Table 5.1 Sr isotopic measurements in standard reference materials… 175

Table 5.2 Sr isotopic measurements in planetary materials……. 176

Table 5.3 Normalized literature Sr isotopic data……. 177

Table 5.4 Normalized literature initial $^{87}Sr/^{86}Sr$ by planetary material 179

Table 5.5 Bulk Rb and Sr abundances in planetary bodies……. 187

Appendices

Table A2.1 Compilation of measured magmatic H_2O contents by tectonic setting……. 208

Table A3.1 Southwest Indian Ridge 7-25°E He, CO_2, Ne, Ar and Xe abundances and He, Ne, Ar and Xe isotopic compositions…….. 215

Table A4.1 Southwest Indian Ridge 16-25°E fission Xe isotopic compositions…….. 238

Acknowledgments

I am extremely grateful for the opportunity to pursue research with my advisors, Professors Sujoy Mukhopadhyay and Stein Jacobsen. I thank Sujoy for first sparking my interest in new tools to study the chemical signatures of plate tectonics and mantle convection when I was starting out as an undergraduate, and for sharpening my thought process, writing style and analytical skills ever since. I also thank Sujoy for the opportunity to work in such an interesting, innovative and creative laboratory environment. Sujoy's talent, enthusiasm, clarity of thought and dedication to teaching have continually impressed and inspired me. I am so grateful for the years Sujoy has spent contributing to my development as a scientist; I have truly enjoyed being his graduate student.

I thank Professor Stein Jacobsen for his enthusiasm and kindness and for training me to be a rigorous isotope geochemist over the years. Stein taught one of the first Earth and Planetary Science classes I took at Harvard, and I have greatly benefited from Stein's expertise and breadth of knowledge in the classroom, in the laboratory and beyond. It has been truly exciting and enjoyable to gather high-precision data and to try to better understand the big questions that persist about the Moon and planet formation with Stein. I am very grateful for his support and guidance.

I am truly fortunate to have pursued my doctorate in the Department of Earth and Planetary Sciences. I thank my committee members, Professors Charles Langmuir and Richard O'Connell, for many stimulating discussions over the years and for their interest and support throughout my graduate career. I have benefited greatly from spirited and enjoyable conversations with Professors Sarah Stewart, Jerry Mitrovica, Miaki Ishii,

Brendan Meade and Jason Morgan. I thank all of the professors who have taught and challenged me over the years.

I thank my labmates and officemates for their guidance, support, encouragement and for the joy of shared experiences in the laboratory and afield: Jennifer Middleton, Jonathan Tucker, Maria Pető and Robert Ackert in the Noble Gas Laboratory; and Shichun Huang, Eugenia Hyung, Ramananda Chakrabarti, Kun Wang, Fatemeh Sedaghatpour and Michail Petaev in the Isotope Geochemistry and Cosmochemistry Laboratory. I especially thank Jennifer Middleton for her enthusiasm and encouragement throughout my dissertation process. I also thank the greater planetary science group, including Simon Lock, Gal Sarid and Dylan Spaulding, and my friends Elizabeth Day, Vedran Lekic and Sanne Cottaar. These remarkable scientists have created collaborative environments that have made early Earth and deep Earth research high enjoyable for me. I thank my friends and collaborators for their comments and suggestions to improve the work detailed in this dissertation. Thanks also to the National Science Foundation Graduate Research Fellowship Program for funding my research.

I have been very fortunate in my friends over the years. I thank my roommates: Kevin Wecht, Phoebe Robinson-DeVries, David Toniatti, Richard Kraus and my great friend Daniel Dobies, for their support and for the cheerful home environment we were able to create together at 81 Huron Avenue and 18 Whittier Street. My friends and fellow students have been a great source of joy, especially Eileen Evans, Allison Gale, Stephen Turner, Michael Ranen, Karin Louzada, Hilary Close, Victor Tsai, Jessica Creveling, Kristian Bergen, Roderick Bovee, Natalya Gomez, Katherine Dagon, Hannah Horowitz, Shannon Koplitz, Jacqueline Austermann, Harriet Lau, William Steinhardt and Julianna

Brunini. I also thank Evie Spanos for her insights, laughter, support and presence in my life despite a rather great distance. I've been enriched by each one of you.

I am greatly indebted to the Harvard Department of Earth and Planetary Sciences for fostering such a welcoming, collegial and vibrant community of students and scientists. I thank Christine Benoit, Trina Hirsig, Ganna Savostyanova and Elizabeth Busky for administrative support and friendship throughout the years. I thank Sarah Colgan for her support and guidance, and Maryorie Grande for everything she has done to make this department a second home. I especially thank Chenoweth Moffatt for first alerting me (with unforgettable verve) to the fact that I could study planets as a career; and for her insight, advice and wonderful presence over the years.

I thank my parents, Rama and Amar Parai, and my brother, Rajarshi Parai, for their support. My parents have always known what to say and what to send to make things go better for me; you have been there for me always, and I am extraordinarily grateful.

Chapter 1: Volatiles in the Earth and Moon

1.1 INTRODUCTION

The volatile inventories of the Earth and Moon reflect unique histories of volatile acquisition and loss during accretion and early processing. Early elemental fractionation based on volatility reflects some combination of incomplete condensation in the cooling solar nebula (Humayun and Clayton, 1995) and partial mass ejection due to energetic collisions in the proto-planetary disk. In the late stages of accretion, giant impacts may drive partial or total loss of early planetary atmospheres (Genda and Abe, 2005; Stewart et al., 2014; Tucker and Mukhopadhyay, 2014). Thus, further volatility-based fractionation occurs as elements partition between planetary interiors and transient surface reservoirs. The Moon-forming giant impact initiated the last catastrophic outgassing and mass ejection event on the early Earth. The terrestrial volatile inventory was established soon after the last giant impact, as late accretion of volatiles was limited (Halliday, 2013; Tucker and Mukhopadhyay, 2014). The planet subsequently settled into a regime of long-term exchange of volatiles between the mantle and exosphere (atmosphere, oceans and crust) in association with plate tectonics. Therefore, volatile chemistry in the Earth and Moon records information about a diverse array of processes that shaped planetary bodies in the Solar System as they evolved to their present-day states.

Here we explore new noble gas and rubidium-strontium isotopic constraints on volatile depletion in the early Solar System, early outgassing of the terrestrial mantle, and the long-term evolution of the deep Earth volatile budget. We begin by investigating

constraints on long-term volatile exchange between the mantle and surface reservoirs. We then work backwards in time and outwards in scope to examine the nature of terrestrial mantle reservoirs, constraints on early mantle outgassing, and ultimately volatile accretion and loss during planet formation.

Volatility describes the partitioning of an element between gas and condensed phases as a function of temperature. In the context of the early solar nebula, volatility is discussed in terms of equilibrium condensation temperatures at solar nebular pressures (e.g., Wasson, 1985). It should be noted that the volatility of a given element depends strongly on physical context: for example, pressure and speciation both affect the volatility of different elements. Elements with nebular equilibrium condensation temperatures below ~640 K are referred to as highly volatile; these include the noble gases (He, Ne, Ar, Kr and Xe), halogens (F, Cl, Br, I) and the chief elemental constituents of life on Earth (H, C, N, O). Moderately volatile elements condense from the solar nebula between ~640-1230 K and include the alkali metals Na, K and Rb. Elements that condense above ~1230 K are relatively refractory; these include Sr, Th, U and Pu. In the noble gas chapters of this work (Chapters 3 and 4), we examine a variety of processes that fractionate radioactive parent nuclides from their volatile, atmophile daughter decay products: refractory-volatile systems (^{235,238}U-^{232}Th-^{4}He; ^{238}U-Xe, ^{244}Pu-Xe), a moderately volatile-volatile system (^{40}K-^{40}Ar) and a volatile-volatile system (^{129}I-^{129}Xe). In the fifth chapter, we explore a system with a moderately volatile parent and refractory daughter (^{87}Rb-^{87}Sr). Below we give a brief synopsis of the next four chapters.

1.2 How large is the subducted water flux? New constraints on mantle regassing rates

Water is outgassed from the Earth's mantle in association with volcanic activity, and input to the mantle via hydrous minerals carried within subducting slabs. Any sustained imbalances between water input and output will generate variations in how Earth's water is distributed between the exosphere and the mantle. Long-term variations in mantle water contents have dramatic effects on mantle rheology and melting, and a return flux of exospheric water to the deep interior may control cycling of other volatiles, such as the noble gases. Therefore, a quantitative assessment of the deep Earth water cycle is critical to our understanding of mantle structure, dynamics and the broader evolution of the deep Earth volatile budget. However, estimates of the magnitude of water input to mantle via hydrous minerals in subducting slabs are very poorly constrained, leading to significant uncertainties in the exchange of water between the deep Earth and exosphere.

To address this issue, we developed a Monte Carlo simulation of the mantle-exosphere water cycle. Based on estimates of magmatic production rates, mantle source water contents and constraints on long-term sea level change, we were able to set constraints on the long-term (~500 million year) average input flux of water carried in subducting slabs, as well as the average return flux of water beyond depths of magma generation at arc settings. We found that previous estimates of the deep Earth return flux were up to an order of magnitude too large, and that incorporation of recycled slabs would on average rehydrate the upper mantle, but dehydrate the plume source (Parai and Mukhopadhyay, 2012).

1.3 Heterogeneous upper mantle Ne, Ar and Xe isotopic compositions and a possible Dupal noble gas signature recorded in basalts from the Southwest Indian Ridge

Noble gases are unique tracers in that they are inert and thus unaffected by chemical reactions. Particular noble gas isotopes are produced by radioactive decay and fission of species with a diverse range of half-lives (Table 1.1; for example, ^{129}I decays with a half-life of 15.7 Myr to produce ^{129}Xe; on the other extreme, ^{232}Th undergoes alpha decay to produce ^{4}He with a half-life of 14 Gyr). As a result, the abundances and isotopic compositions of noble gases in mantle-derived samples provide information about planetary ingassing and outgassing on a variety of timescales of cosmochemical and geochemical interest.

We measured CO_2, He, Ne, Ar and Xe abundances and Ne, Ar and Xe isotopic compositions with high precision in a suite of basalt glasses from the Southwest Indian Ridge between 7-25°E. Measured values were corrected for syn- to post-eruptive atmospheric contamination to give mantle source noble gas isotopic compositions. In the region of the study area removed from the influence of hotspots, we found large variations in mantle source Ar and Xe isotopic composition, representing ~70-80% of the total observed mantle variations in Ar and Xe, associated with very limited variation in He and Ne isotopic composition. Our results are most consistent with the heterogeneous incorporation of material carrying atmospheric Ar and Xe into the mantle source supplying the Southwest Indian Ridge, and provide direct evidence that subduction is not an efficient barrier to the recycling of atmospheric Ar and Xe (Parai et al., 2012).

1.4 Constraints from I-Pu-U-Xe systematics on the nature of mantle reservoirs, planetary volatile evolution and the timing of the Moon-forming giant impact

We continue our study of planetary outgassing and regassing with high-precision measurements of the fission isotopes of Xe in basalts from the Southwest Indian Ridge between 16 and 25°E. The present-day Xe inventory of the SWIR mantle source represents a mixture of primordial mantle Xe, recycled atmospheric Xe, ^{129}Xe produced by decay of short-lived ^{129}I, and Xe produced by the fission of extinct ^{244}Pu and of extant ^{238}U. Fission Xe isotope systematics evident in SWIR basalts and other mantle-derived samples (Mukhopadhyay, 2012; Pető et al., 2013; Tucker et al., 2012) provide new insights into the integrated history of mantle source degassing and regassing. We find further evidence for the recycling of atmospheric Xe into the mantle, in that recycled atmospheric Xe dominates the Xe inventories of the SWIR Western and Eastern Orthogonal Supersegment mantle sources (~80-90% of ^{132}Xe is recycled in origin). Our results are consistent with recent studies of fission Xe in Equatorial Atlantic MORBs (Tucker et al., 2012) plume-influenced basalts from Iceland (Mukhopadhyay, 2012) and the Rochambeau Rift (Pető et al., 2013). We note that depleted lithophile isotopic compositions in mantle sources with primitive He and Ne do not indicate a non-chondritic bulk silicate Earth; rather, the prevalence of recycled atmospheric Xe in mantle sources likely reflects incorporation of depleted recycled material into even mantle sources.

Although significant recycling of atmospheric heavy noble gases has occurred over Earth history, the Xe isotopic compositions of mantle sources have not been entirely overprinted by recycling, and preserve a record of very early differentiation of the plume

source and the upper mantle. We find that preferential regassing of atmospheric Xe cannot explain the systematics observed in MORB and plume source Xe isotopes and that instead, differences in the delivery and retention of volatiles in the two mantle sources must have been established early in Earth history (before 4.45 Ga based on ^{129}Xe systematics; Chapter 3; Chapter 4; Mukhopadhyay, 2012; Tucker et al., 2012; Parai et al., 2012; Pető et al., 2013). Accordingly, the two reservoirs cannot have been completely homogenized by 4.45 Gyr of mantle convection.

We also find differences in the extent of degassing of the MORB and plume sources. MORB sources are consistently characterized by a lower fraction of fission Xe derived from Pu-fission, indicating a greater extent of degassing relative to the plume source. To further investigate constraints from fission Xe systematics on both early and long-term degassing of the upper mantle, we develop a parameterized two-stage model of MORB source degassing. Based on our determinations of the ratio of radiogenic ^{129}Xe* to Pu-fission $^{136}Xe_{Pu}$ in MORB sources, we compute a classical closure age range of 44-70 Myr for the last giant impact. Our model results indicate that for late t_{LGI} (>80 Myr), our model cannot simultaneously satisfy 68% confidence limits for $^{129}Xe^*/^{136}Xe_{Pu}$ and $^{136}Xe_{Pu}/(^{136}Xe_{Pu}+^{136}Xe_{U})$ in the MORB mantle without invoking partial retention of Xe prior to the last giant impact. Further investigation of early retention of Xe during planet formation is needed to better constrain the timing of the Moon-forming giant impact.

1.5 Strontium isotopic constraints on early Solar System chronology and the history of planetary volatile depletion

The long-lived radioactive ^{87}Rb-^{87}Sr system provides a powerful chronometer for volatile depletion in the early Solar System. We present a new suite of high-precision $^{87}Sr/^{86}Sr$ determinations for lunar anorthosite 60025, Moore County plagioclase, the eucrite Juvinas and the angrite D'Orbigny. We compute initial $^{87}Sr/^{86}Sr$ ratios for lunar anorthosite 60025, Juvinas and Moore County plagioclase and place these in context of a normalized compilation of initial $^{87}Sr/^{86}Sr$ data from the literature. Careful normalization of literature data resolves some discrepancies among different studies; however, in many cases, we find that inter-laboratory differences persist. We are able to reproduce previous determinations of the initial $^{87}Sr/^{86}Sr$ in the eucrite Juvinas (Allegre et al., 1975; Papanastassiou and Wasserburg, 1969) with an order of magnitude improvement in precision. However, our results are not in agreement with a recent determination of initial $^{87}Sr/^{86}Sr$ in eucrites (Hans et al., 2013). These discrepancies may reflect artifacts related to fractionation that occurs during thermal ionization mass spectrometric analysis, or may be related to heterogeneous resetting of the Rb-Sr system in brecciated eucrites.

Constraints on the timing of Moon formation inform our understanding of Earth's accretion, segregation of the metallic core, silicate differentiation, early mantle outgassing and formation of the atmosphere. We explore models of volatile depletion in the early Solar System that may explain the observed Sr isotopic systematics in the lunar anorthosite 60025 and Moore County plagioclase. If the Moon is derived from proto-Earth material, then lunar precursor material evolved with Earth-like Rb/Sr until the time of Moon formation. If the bulk lunar Rb/Sr determined today is the result of fractionation

that occurred in the aftermath of the Moon-forming giant impact, then the Moon formed prior to ~62 Myr.

1.6 CONCLUSIONS

In this thesis, we examine long-term volatile exchange between the deep Earth and the atmosphere based on mass balance constraints on the deep Earth water cycle. Based on high-precision measurements of noble gas (He, Ne, Ar and Xe) abundances and isotopic compositions in mantle-derived rocks, we explore constraints on regassing and degassing of the Earth's interior, Earth's accretion and the nature of MORB and plume mantle sources. Lastly, we use Rb-Sr systematics determined in a suite of planetary materials to investigate volatile depletion in the early Solar System and the time of Moon formation.

1.7 REFERENCES

Allegre, C.J., Birck, J.L., Fourcade, S., Semet, M.P., 1975. Rubidium-87/Strontium-87 Age of Juvinas Basaltic Achondrite and Early Igneous Activity in Solar-System. Science, 187(4175): 436-438.

Genda, H., Abe, Y., 2005. Enhanced atmospheric loss on protoplanets at the giant impact phase in the presence of oceans. Nature, 433(7028): 842-844.

Halliday, A.N., 2013. The origins of volatiles in the terrestrial planets. Geochimica et Cosmochimica Acta, 105: 146-171.

Hans, U., Kleine, T., Bourdon, B., 2013. Rb-Sr chronology of volatile depletion in differentiated protoplanets: BABI, ADOR and ALL revisited. Earth and Planetary Science Letters, 374: 204-214.

Humayun, M., Clayton, R.N., 1995. Potassium isotope cosmochemistry: Genetic implications of volatile element depletion. Geochimica et Cosmochimica Acta, 59(10): 2131-2148.

Mukhopadhyay, S., 2012. Early differentiation and volatile accretion recorded in deep-mantle neon and xenon. Nature, 486(7401): 101-U124.

Papanastassiou, D.A., Wasserburg, G.J., 1969. Initial Strontium Isotopic Abundances and Resolution of Small Time Differences in Formation of Planetary Objects. Earth and Planetary Science Letters, 5(6): 361-376.

Parai, R., Mukhopadhyay, S., 2012. How large is the subducted water flux? New constraints on mantle regassing rates. Earth and Planetary Science Letters, 317: 396-406.

Parai, R., Mukhopadhyay, S., Standish, J.J., 2012. Heterogeneous upper mantle Ne, Ar and Xe isotopic compositions and a possible Dupal noble gas signature recorded in basalts from the Southwest Indian Ridge. Earth and Planetary Science Letters, 359: 227-239.

Pető, M.K., Mukhopadhyay, S., Kelley, K.A., 2013. Heterogeneities from the first 100 million years recorded in deep mantle noble gases from the Northern Lau Back-arc Basin. Earth and Planetary Science Letters, 369: 13-23.

Stewart, S.T., Lock, S.J., Mukhopadhyay, S., 2014. Atmospheric loss and volatile fractionation during giant impacts. Abstracts of the Lunar and Planetary Science Conference, 45: 2869.

Tucker, J.M., Mukhopadhyay, S., 2014. Evidence for multiple magma ocean outgassing and atmospheric loss episodes from mantle noble gases. Earth and Planetary Science Letters, 393(0): 254-265.

Tucker, J.M., Mukhopadhyay, S., Schilling, J.G., 2012. The heavy noble gas composition of the depleted MORB mantle (DMM) and its implications for the preservation of heterogeneities in the mantle. Earth and Planetary Science Letters, 355: 244-254.

Wasson, J.T., 1985. Meteorites: Their record of early Solar System history. W. H. Freeman, New York, 267 pp.

Chapter 2: How large is the subducted water flux? New constraints on mantle regassing rates

[Parai, R., Mukhopadhyay, S., 2012. How large is the subducted water flux? New constraints on mantle regassing rates. *Earth and Planetary Science Letters* **317**, 396-406, doi: 10.1016/j.epsl.2011.11.024.]

ABSTRACT

Estimates of the subducted water (H_2O) flux have been used to discuss the regassing of the mantle over Earth history. However, these estimates vary widely, and some are large enough to have reduced the volume of water in the global ocean by a factor of two over the Phanerozoic. In light of uncertainties in the hydration state of subducting slabs, magma production rates and mantle source water contents, we use a Monte Carlo simulation to set limits on long-term global water cycling and the return flux of water to the deep Earth. Estimates of magma production rates and water contents in primary magmas generated at ocean islands, mid-ocean ridges, arcs and back-arcs are paired with estimates of water entering trenches via subducting oceanic slab in order to construct a model of the deep Earth water cycle. The simulation is constrained by reconstructions of Phanerozoic sea level change, which suggest that ocean volume is near steady-state, though a sea level decrease of up to 360 meters may be supported. We provide limits on the return flux of water to the deep Earth over the Phanerozoic corresponding to a near steady-state exosphere (0–100 meters sea level decrease) and a maximum sea level decrease of 360 meters. For the near steady-state exosphere, the return flux is $1.4 - 2.0^{+0.4}_{-0.3} \times 10^{13}$ moles/yr, corresponding to 2–3% serpentinization in 10

km of lithospheric mantle. The return flux that generates the maximum sea level decrease over the Phanerozoic is $3.5^{+0.4}_{-0.3} \times 10^{13}$ moles/yr, corresponding to 5% serpentinization in 10 km of lithospheric mantle. Our estimates of the return flux of water to the mantle are up to 7 times lower than previously suggested. The imbalance between our estimates of the return flux and mantle output flux leads to a rate of increase in bulk mantle water content of up to 24 ppm/Gyr.

2.1. INTRODUCTION

Exchange of water between the Earth's interior and the exosphere (defined here as the atmosphere, ocean and crust) is critically dependent on water systematics at subduction zones. Water is outgassed from the mantle in association with volcanism at mid-ocean ridges, ocean islands, arcs and back-arc basins. Water is removed from the exosphere at subduction zones, carried as pore water and chemically-bound water in sediments, altered oceanic crust and serpentinized lithospheric mantle within the downgoing slab. At a given subduction zone, some amount of subducted water is released from the slab due to breakdown of hydrous minerals at high pressure and temperature; this slab-derived water flux drives melting in the mantle wedge and is ultimately outgassed to the exosphere via arc and back-arc volcanism. Any water retained within the subducting slab beyond depths of magma generation constitutes a return flux of water to the interior, often referred to as the post-arc subducted water flux (Figure 1.1). A quantitative assessment of the long-term water cycle is critical to our understanding of wide variety of solid Earth phenomena: the abundance and distribution of water in the Earth's interior has dramatic effects on mantle melting (e.g. Inoue, 1994; Hirschmann, 2006), rheology (e.g. Hirth and Kohlstedt, 1996; Mei and Kohlstedt, 2000; Karato and Jung, 2003), structure and style of convection (Crowley et al., 2011), and a return flux of exospheric water to the deep interior may affect cycling of other volatiles, such as the noble gases (Holland and Ballentine, 2006). Here we present new constraints on water exchange between the mantle and exosphere over the past 542 Myr.

Previous estimates of the deep Earth water return flux are based on calculations of the equilibrium stability of hydrous phases at subduction zone pressures and temperatures

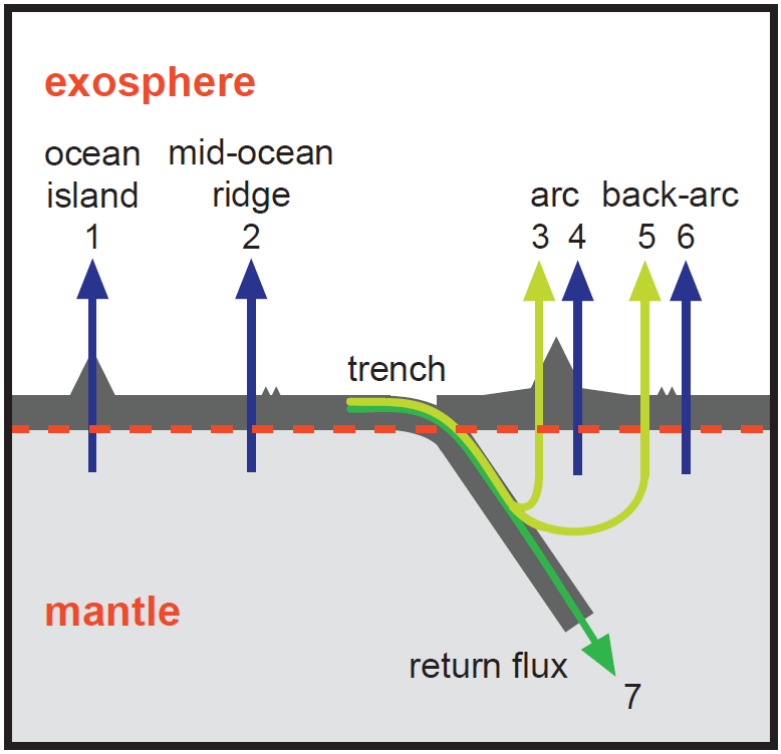

Figure 2.1 Schematic of global water fluxes considered between the mantle and exosphere. Water is outgassed from the mantle due to magmatism at ocean islands, mid-ocean ridges, arcs and back-arcs (arrows 1-6). Water is removed from the exosphere at trenches. Some fraction of the trench input flux is directly outgassed via the arc and back-arc system (arrows 3 and 5). The majority of arc and back-arc water output is thought to be slab-derived, but some portion is derived from water present in the ambient mantle wedge (arrows 4 and 6). Water retained past depths of magma generation constitutes a return flux of water to the deep Earth (arrow 7). The net flux between mantle and exosphere is determined by the difference between the return flux and mantle-derived output fluxes.

(*e.g.*, Schmidt and Poli, 1998, 2003; Rüpke et al., 2004; Hacker, 2008; van Keken et al., 2011). Assuming an initial slab lithology and estimated pressure-temperature (P-T) conditions for a particular subduction zone, the water content of the equilibrium phase assemblage is determined as a function of depth. Thus, the amount of water retained in

the slab past depths of magma generation is estimated by tracking the breakdown of hydrous phases along a given P-T path of subduction. However, in order to obtain an estimate of the global return flux of water to the deep Earth, initial slab lithologies and P-T profiles at individual subduction zones around the world must be established (Hacker, 2008; van Keken et al., 2011). Thus, such estimates of the deep Earth water return flux are subject to significant uncertainty, particularly with respect to the serpentine content of the lithospheric mantle. While serpentinized lithospheric mantle could be generated by seawater infiltration along transform faults or deep faults (15-20 km) into the oceanic plate at the outer rise (Ranero et al., 2003; Ranero et al., 2005; Nedimović et al., 2009), the degree and spatial extent of serpentinization around the faults remain poorly constrained.

Reasonable physical considerations can be used to establish upper limit or order-of-magnitude constraints on the amount of water carried by serpentinized lithosphere in the subducting slab. Schmidt and Poli (1998) use buoyancy considerations to set an upper limit on the extent of lithospheric serpentinization: since serpentinite is less dense than unaltered peridotite, serpentinization lessens the negative buoyancy of the subducting slab. A 10 km thick section of lithosphere with average 10% serpentinization has a density of 3.15 g/cm^3 (Schmidt and Poli, 1998); beyond this degree of serpentinization, slab descent becomes problematic. Alternately, Li and Lee (2006) use an approximation of the spatial distribution of faults and fractures in oceanic lithosphere and an estimated lateral extent of serpentinization around faults or fractures (based on the diffusivity of water in serpentinite) to compute an order-of-magnitude estimate of initial slab hydration

condition. However, order-of-magnitude estimates may represent the difference between removing an ocean's worth of water from the exosphere in 5 Gyr vs. 500 Myr.

We take an alternative approach to assess long-term cycling of water between the exosphere and the mantle. We use independent constraints on (a) mantle water output fluxes and (b) global sea level change over time to provide limits on the initial slab water input flux, as well as the return flux of water to the deep mantle. A statistical (Monte Carlo) approach is used to efficiently search the parameter space (which is based on literature estimates of water input at subduction zones and output at ocean islands, mid-ocean ridges, arcs and back-arcs) for water cycling scenarios that best satisfy constraints on Phanerozoic sea level change. We do not track the breakdown of hydrous phases or make assumptions regarding whether the water return flux circulates within the upper mantle or is injected into the lower mantle. Rather, we focus on establishing limits on the magnitudes of global fluxes across the mantle-exosphere boundary to provide key constraints on the following questions:

(1) How much water is subducted into the mantle at trenches?

(2) What fraction of the water subducted into the mantle is recycled past the arcs into the deep Earth?

2.2. MODEL

Figure 2.1 shows the fluxes considered in our model of the global water cycle. Based on literature estimates, we define upper and lower limits for ten model parameters (Table 2.1). Total magmatic water output fluxes are computed by coupling literature estimates of magma production rate to primary magmatic water contents at each tectonic

Table 2.1: Water cycle model parameter space

Parameter	min	max	References
Magma production rate at:	(km^3/yr)	(km^3/yr)	
ocean islands	1.8	4.8	Crisp (1984)
mid-ocean ridges	17	25	Reymer and Schubert (1984)
arcs	1.1	8.6	Reymer and Schubert (1984); Crisp (1984)
Fraction N-MORB:	0.8	0.9	
Primary magmatic H_2O content in:*	(wt %)	(wt %)	
ocean island basalt	0.3	1.6	Simons et al. (2002)
N-MORB	0.04	0.26	Almeev et al. (2008); Pineau et al. (2004)
E-MORB	0.26	0.92	Michael et al. (1995); Standish et al. (2008)
arc basalt	1.0	6.0	Benjamin et al. (2007); Roggensack (2001)
back-arc basin basalt	0.1	2.8	Fretzdorff et al. (2002); Newman et al. (2000)
	(x10^{13} moles/yr)		
Trench input flux:	4.1	16	Jarrard (2003); Schmidt and Poli (1998)

* Full compilation of measured magmatic water contents by tectonic setting in supplement: Table A2.1. The compilation shows that measured values fill in the ranges listed above.

setting. Input fluxes at trenches are drawn from literature estimates of the amount of chemically-bound water carried in subducting slabs, and a Monte Carlo technique is used to explore the entire parameter space. A successful run meets two criteria: (1) the global slab-derived arc and back-arc water output does not exceed the global water input at trenches; and (2) the imbalance between mantle input and output fluxes is consistent with reconstructions of Phanerozoic sea level change.

2.2.1 Defining the model parameter space

Mantle output fluxes are quantified based on magma production rates (Table 2.1) and the range of measured magmatic water contents at individual tectonic settings (Table 2.1; see the full compilation in supplementary Table A2.1). We assume that over the Phanerozoic, secular variation in mid-ocean ridge magma production rates has not

exceeded 20% of present day rates (Table 2.1). There is no evidence for secular change in seafloor spreading rates over the past 180 Myr (Parsons, 1982; Rowley, 2002), and our assumption is further supported by studies indicating limited change in mantle potential temperature of ~50-100 K per Gyr (Abbott et al., 1994; Vlaar et al., 1994; Labrosse and Jaupart, 2007), as well as geodynamic models indicating a change in heat flow of only ~10% in the past Gyr (van Keken et al., 2001). We double the upper limit OIB magma production rate of Crisp (1984) in order to capture possible elevated long-term mean production rates associated with flood basalt volcanism.

The trench water input flux is carried as pore water and chemically-bound water in sediments, altered oceanic crust and, potentially, serpentinized lithospheric mantle. Pore water is thought to be entirely expelled from the slab at shallow levels and returned to the exosphere (Jarrard, 2003) and so we do not discuss it further. A summary of literature estimates of the chemically-bound water flux into trenches is given in Table 2.2. We note that most of the flux magnitudes are in broad agreement, with the exception of Schmidt and Poli (1998), who estimate an altered igneous crust lower limit flux that by itself exceeds some of the other total bound water flux estimates. The bulk of the Schmidt and Poli (1998) altered igneous flux is carried by 3.5 km of water-saturated basalt, which may be considered as a carrying capacity. Total estimates of the chemically-bound water flux into trenches vary from 4.1 to 16×10^{13} moles/yr.

2.2.2 Model setup

A single Monte Carlo realization of the global water cycle draws a random value from the allowed range to represent the global mean for each of the ten model

Table 2.2: Trench input fluxes

Reference	Water flux (x10^{13} moles/yr) carried in:			
	Sediment	*Altered igneous crust*	*Serpentinized mantle*	*Total entering trench*
Schmidt and Poli (1998)	0.15-0.30	9.2-12	1.6-6.3	**11-16***
Jarrard (2003)	0.71	3.4	---	**4.1**
Rupke et al. (2004)	0.90	2.6	1.4-6.8	**4.8-10**
Hacker (2008)	0.83	3.4	3.2	**7.4**
van Keken et al. (2011)	0.39	3.5	1.7	**5.6**

*Schmidt and Poli (1998) model the slab as 200-400 m sediment, 3.5 km of H_2O-saturated basalt, 3.5 km of hydrated gabbro (20-30% hydration by volume) and 5 km of 5-20% serpentinized mantle. Assuming 2.7 km^2 of convergence per year (Rüpke et al., 2004; Hacker, 2008), this corresponds to a total H_2O flux of 12-18 x 10^{13} moles/yr. However, Schmidt and Poli (1998) report a total flux into trenches at 20 km of 11-16 x 10^{13} moles/yr moles per year, ~10% lower than the numbers discussed above, possibly reflecting shallow dehydration reactions. We use their preferred total input at 20 km to constrain our trench input flux parameter, and scale the fluxes of sediment, altered crust and serpentinite down to reflect the smaller flux in Figure 2.4.

parameters: magma production rate at ocean islands, mid-ocean ridges, and arcs; proportion of N-MORB out of total MORB production; primary magmatic water content in ocean island basalt, N-MORB, E-MORB, arc basalt and back-arc basin basalt; and lastly, trench water input flux. Since back-arc spreading occurs at rates comparable to mid-ocean ridge spreading, the back-arc production rate is computed by scaling the selected MORB production rate by the present-day ratio of back-arc to mid-ocean ridge length (~10%, Baker and German, 2004). Mantle water output fluxes are computed by multiplying magmatic water content by magma production rate at each tectonic setting, assuming a density of 2.9 g/cm^3 for OIB, MORB and back-arc production, and 2.8 g/cm^3 for arcs (Plank, 2005). The total water flux into the trench is drawn from literature estimates for initial chemically-bound water content in the subducting slab, and the fraction of trench input flux that is returned to the exosphere is determined from H_2O-Ti

systematics in arc and back-arc basalts (Section 2.2.3.1). Thus, all fluxes across the mantle-exosphere boundary are specified (Figure 2.1). The mantle return flux is the difference between the trench input flux and the slab-derived arc and back-arc water fluxes. Finally, the net flux across the mantle-exosphere boundary is defined as the difference between the mantle output flux and return flux.

2.2.3 Model constraints

For a given Monte Carlo realization to be classified as a success, the two criteria discussed below must be satisfied:

2.2.3.1 Model success criterion 1: The global slab-derived arc and back-arc water output must not exceed the global water input at trenches

The combined arc and back-arc magmatic water output flux is derived from two sources: slab fluids released by dehydration reactions, and ambient water in the mantle wedge (Figure 2.1). For a given realization, the slab-derived fractions of arc and back-arc output fluxes cannot exceed the trench input flux: *i.e.*, water cannot be created at arcs. This first success criterion requires a method to estimate the fraction of arc and back-arc water output that derives from the slab. The fraction of the arc water flux derived from the slab fluid, f_{slab}, is:

$$f_{slab} = \left(1 - f_{mantlewedge}\right) = \frac{\left[\left(H_2O\right)_{arc} - \left(H_2O\right)_{mantlewedge}\right]}{\left(H_2O\right)_{arc}} \qquad \text{Eq. 2.1}$$

where $f_{mantlewedge}$ is the fraction of arc water derived from the mantle wedge, $(H_2O)_{arc}$ is the primary magmatic water content of arc magmas, and $(H_2O)_{mantlewedge}$ is the amount of

water in the arc magma that is derived from the mantle wedge. The expressions for back-arc water are analogous. Given $(H_2O)_{arc}$ or $(H_2O)_{back\text{-}arc}$, if $(H_2O)_{mantlewedge}$ can be determined, then f_{slab} can be calculated.

We use water-titanium (H_2O-Ti) systematics observed in a global compilation of arc and back-arc basalts to calculate $H_2O_{mantlewedge}$ and thereby estimate the slab-derived component of arc and back-arc water output fluxes in the simulations. Ti is a relatively fluid-immobile element and is not expected to migrate with fluids released due to slab dehydration (Ryerson and Watson, 1987; Kelley et al., 2006, 2010). Thus, Ti in arc and back-arc magmas should be derived primarily from the ambient mantle wedge. Previous work has established that magmatic Ti concentrations are controlled by the degree of partial melting (F) and the Ti concentration in the mantle source (Stolper and Newman, 1994; Lee et al., 2005; Kelley et al., 2006, 2010).

Figure 2.2 shows primary magmatic H_2O vs. TiO_2 in a global compilation of arc and back-arc data. A broad negative correlation between H_2O and TiO_2 is evident in the global arc and back-arc data set, though least-squares regression yields distinct slopes for the arc data (slope = -0.079, R = 0.77) and back-arc data (slope = -0.29, R = 0.81). At a given magmatic H_2O content, the observed ~15–25% scatter in magmatic TiO_2 content is likely due to variations in source Ti concentration and the potential temperature of the mantle wedge. However, the broad negative trend in the global data set is consistent with the hypothesis that higher H_2O contents lead to a higher degree of the melting and thus a lower magmatic TiO_2 content, supporting the use of Ti as a proxy for the degree of melting at arc and back-arc environments (Stolper and Newman, 1994; Lee et al., 2005; Kelley et al., 2006, 2010).

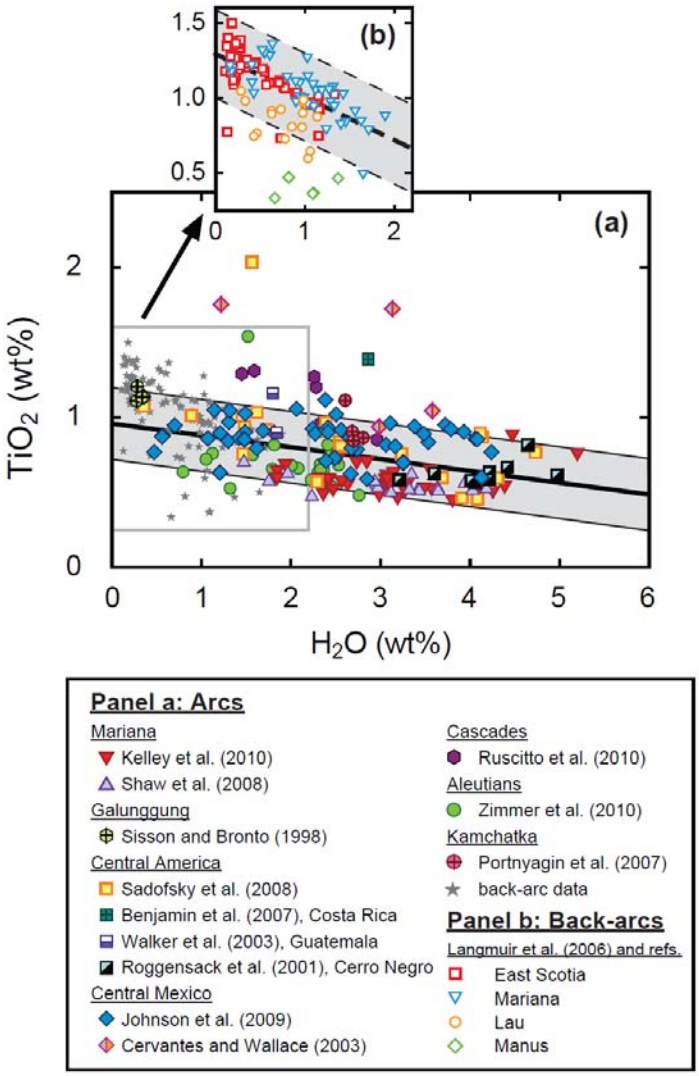

Figure 2.2 H_2O-TiO_2 systematics in (panel a) a global compilation of arc melt inclusion data and back-arc glass data. Panel (b) shows the back-arc data in detail (Langmuir et al., 2006, and references therein). Arc melt inclusion data are corrected for fractional crystallization (corrected for post-entrapment crystallization, screened for MgO>6 wt%, and brought into equilibrium with Fo_{90} mantle through olivine addition). Back-arc data were compiled and corrected for hydrous fractional crystallization to 8 wt% MgO by Langmuir et al., (2006). We selected samples with "plag-in" MgO values ≤ 8 wt% and adjusted the reported $H_{8.0}$ and $Ti_{8.0}$ values of Langmuir et al. (2006) by olivine addition to equilibrium with Fo_{90} mantle (assuming $Fe^{3+}/\Sigma Fe = 0.15$). Least squares regression with bi-square weights to minimize the influence of outliers (robust regression) yields distinct fits for the arc ($y = -0.079x + 0.96$, $R = 0.77$) and back-arc data ($y = -0.29x + 1.29$, $R = 0.81$). There is significant scatter in the global compilation, which probably reflects source Ti heterogeneity as well as variation in subduction zone thermal profiles from arc to arc. We simulate the observed scatter by adding ±25% random variation to the calculated TiO_2 for a given magmatic H_2O content (shaded regions; ±20% for back-arcs).

While in detail, each arc and back-arc environment is likely to have a slightly different relationship between H_2O and TiO_2 contents, we use the broad correlation in the global data set to model the relationship between arc magmatic H_2O content and degree of melting. We note that the mantle wedge beneath arcs may be heterogeneous and/or depleted with respect to average MORB mantle (e.g., Kelley et al., 2010). To model this, the global average mantle wedge source concentrations of H_2O and Ti are allowed to co-vary between 43 and 320 ppm H_2O (such that 10% melting will produce magmatic H_2O contents between the most depleted N-MORB and a slightly-enriched MORB magmatic H_2O content) and 500 and 1200 ppm Ti (Kelley et al., 2006). The fraction of arc (or back-arc) H_2O output derived from the slab is computed for each realization as follows: once the arc primary magmatic H_2O content has been randomly selected, TiO_2 content in the primary magma is calculated using the best fit slopes for arc H_2O vs. TiO_2, and a ±25% random variation is added to the calculated Ti concentration (±20% for the back-arc) to simulate the scatter observed in the global data set (Figure 2.2). Mantle wedge H_2O and Ti concentrations are then drawn from the ranges specified above, and using the batch melting equation and D_{Ti} between 0.04 and 0.10 (Kelley et al., 2006 and references therein), we solve for the degree of melting, F. Since we explore a very large parameter space in D_{Ti} and source Ti concentrations, some realizations yield non-physical values of F and are excluded. Non-physical F values indicate that certain combinations of D_{Ti} and source Ti concentration, such as high D_{Ti} and low source Ti concentrations, cannot characterize a real system (also see Kelley et al., 2006).

Once F for a given realization is determined, we use the mantle wedge source H_2O concentration and D_{H_2O} between 0.007 and 0.012 (Aubaud et al., 2004; Hauri et al.,

2006; Kelley et al., 2006) to calculate the amount of magmatic water derived from the mantle wedge, $(H_2O)_{mantlewedge}$. The fraction of arc water that is derived from the slab is thus determined (Equation 1). The same calculation is carried out for back-arcs. The first criterion for success is now tested: if the combined arc and back-arc water demand on the slab exceeds the trench water input flux, then the model realization constitutes a Failure 1 scenario.

2.2.3.2 Model success criterion 2: Net flux must satisfy constraints on Phanerozoic sea level change

We assume that the net flux between the mantle and exosphere is accommodated by the ocean, since it is the dominant exospheric reservoir and hydration of subducting slabs draws water directly from the ocean. Therefore, a long-term sustained imbalance between water supplied to the exosphere by volcanism and water subducted back into the mantle would generate secular global, or eustatic, change in sea level. However, eustatic sea level change may also arise from variation in the volume of the ocean basin, attributed to ~100 Myr-timescale plate tectonic processes such as changes in mid-ocean ridge spreading rates and super-continent cycles (*tectonoeustasy*; ***e.g.*** Hays and Pitman, 1973; Schubert and Reymer, 1985), as well as from oscillations in the volume of continental ice sheets on timescales of tens of ka to several Myr (*glacioeustasy*; e.g. Miller et al., 1991; Zachos et al., 2001; Miller et al., 2005). Furthermore, variations in dynamic topography in response to mantle convection may both contribute to ocean basin volume changes, as well as affect local measurements of sea level by vertically displacing the continental platforms on which sediments are deposited (e.g. Moucha et al., 2008,

Müller et al., 2008; Conrad and Husson, 2009). Thus, the sedimentary record of long-term sea level reflects a combination of dynamic effects, changes in the volume of the ocean basin, and changes in the volume of water in the oceans.

Continental freeboard studies indicate that sea level has varied by approximately 500 m since the end of the Archean (Wise, 1974, Windley 1977; Galer 1991; Kasting and Holm, 1992). However, detailed eustatic sea level reconstructions are only available for the Phanerozoic Eon (e.g., Vail et al., 1977; Hardenbol et al., 1981; Hallam, 1984; Haq et al., 1987; Hallam, 1992; Haq and Schutter, 2008; Figure 2.3). Therefore, we limit our simulation of the water cycle to the Phanerozoic, although we will discuss some implications of our results for water cycling into deep time. The amount of secular eustatic sea level change that may have occurred over the Phanerozoic is estimated by linear regression on the available reconstructions.

Based on the spatial distribution of marine sedimentary facies on continents, Hallam (1984) generates a sea level curve by assuming that present-day continental hypsometry is representative of the entire Phanerozoic. Hallam's sea level curve yields 360 m of secular decrease over 542 Myr (Figure 2.3a). Rüpke et al. (2004) adopted ~500 m as the net decrease in Phanerozoic sea level based on Hallam (1984). However, 500 m represents the peak-to-trough variation associated with oscillations in sea level, rather than the magnitude of secular decrease. Furthermore, Algeo and Wilkinson (1991) pointed out that continental hypsometry in the Phanerozoic has not been constant over time, as the continents were widely dispersed during the early Paleozoic. Accordingly, Hallam (1992) reduced the magnitude of the Paleozoic high stand from +600 m to +400 m relative to present-day sea level (Figure 2.3b). This modification would reduce the

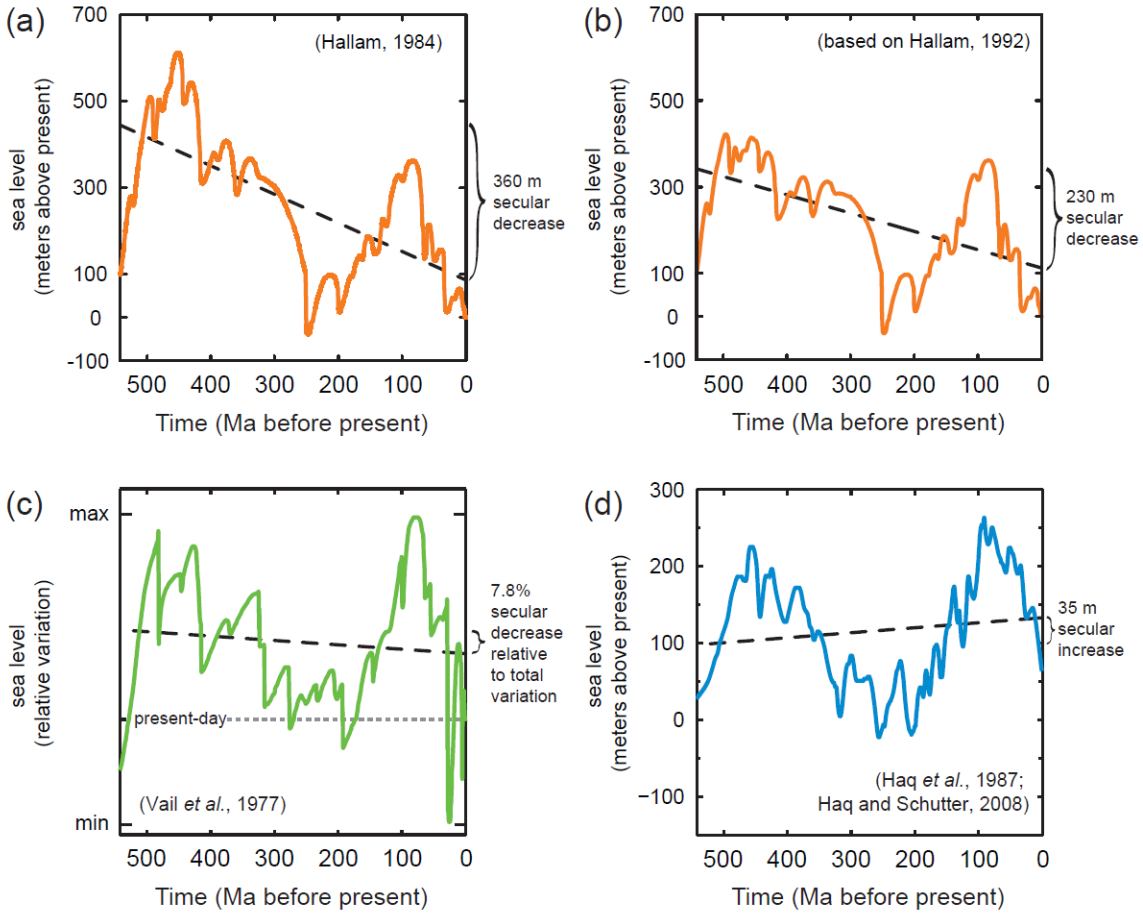

Figure 2.3. Reconstructions of Phanerozoic sea level. The magnitude of secular variation that may have occurred is determined by linear regression. (a) Hallam (1984) gives absolute estimates of sea level based on the spatial distribution of marine sedimentary facies on continents, assuming present-day continental hypsometry represents the entire Phanerozoic. Linear regression yields a secular decrease of 360 m over 542 Myr. (b) Hallam (1992) revised his estimated Paleozoic high stand from 600 m to 400 m above present-day, as continental hypsometry likely changed over time and continents were widely dispersed during the early Paleozoic (Algeo and Wilkinson, 1991). We apply a linear scaling to the Paleozoic portion of Hallam (1984)'s curve to reflect the revision, and find a decrease in sea level of 230 m over 542 Myr. The ~500 m secular decrease in sea level inferred from Hallam's curve by Rüpke et al. (2004) overestimates the secular change that can be supported by the reconstruction. (c) Vail et al. (1977) give relative estimates of eustatic sea level over the Phanerozoic. Linear regression yields a secular decrease equivalent to 7.8% of the total amplitude. (d) Haq et al. (1987) and Haq and Schutter (2008) give absolute estimates of sea level, yielding a secular *increase* in sea level of 35 m over the Phanerozoic. All reconstructions argue for limited long-term secular variation in sea level.

secular trend to yield ~230 m of sea level decrease (Figure 2.3b). Therefore, we suggest that Rüpke et al.'s (2004) 500 m overestimates Phanerozoic sea level decrease. While Hallam's reconstruction can support an upper limit of 360 m of sea level decrease (Hallam, 1984), 230 m of secular decrease appears to be more realistic (Hallam, 1992).

Hallam's reconstructions generate the largest secular eustatic sea level decrease out of all available studies. Reconstructions based on seismic reflection data on maritime depositional sequences by Vail et al. (1977), Haq et al. (1987) and Haq and Schutter (2008) show more limited variations (Figure 2.3). While Vail et al. (1977) provide only relative eustatic variations in sea level over time (Figure 2.3c), Haq et al. (1987) and Haq and Schutter (2008) give absolute variations in sea level with peak-to-trough variations of ~250 m (Figure 2.3d). Linear regression yields a secular decrease in sea level equal to 7.8% of the total amplitude for Vail et al. (1977), and a secular *increase* in sea level of 35 m over the Phanerozoic for Haq et al. (1987) and Haq and Schutter (2008). We note that if the total amplitude of sea level variability is taken as 400 m, then Vail et al. (1977) yields ~30 m of sea level decrease over the Phanerozoic, significantly less than the 230 m estimate based on Hallam (1992).

While the above studies disagree on the precise timing and relative magnitude of specific transgressions and regressions, they share a number of common features. All studies agree in terms of overall shape: sea level rose throughout the Cambrian, broadly fell until ~200 Myr ago, rose and peaked ~100 Myr ago, and then fell to the present day level. The three sea level curves (Figure 2.3b-d) all indicate that secular change in sea level, if present, was limited (-230 m for the corrected Hallam curve, -30 m for the Vail curve, and +35 m for the Haq curve, yielding an average of ~ -100 m). Hence, we suggest

that the sedimentary record is most compatible with a secular decrease of 0–100 m for sea level over the Phanerozoic, which constitutes our preferred scenario ("near steady-state ocean;" Section 2.5). We cannot rule out a secular increase in long-term sea level from the Phanerozoic record (Figure 2.3d); however, since we are interested in setting upper limits on mantle regassing, we will focus on secular sea level decrease. We note that there is no *requirement* for any portion of the observed sea level record to reflect a change in the water budget of the exosphere. For example, previous studies quantitatively ascribe the ~200 m amplitude of sea level change over the past ~60 Myrs to changes in ridge volume (Figure 2.3; Xu et al., 2006; Müller et al., 2008) dynamic topography (Moucha et al., 2008; Conrad and Husson, 2009) and ice volume (Harrison, 1990). However, if we assume for our simulation that the entire Phanerozoic secular trend reflects the water budget of the exosphere, we can set limits on the imbalance between mantle water input and output fluxes. To an extent, ridge volume and dynamic topography effects may obscure the magnitude, and potentially the sign, of a secular eustatic signal from changes in the exospheric water budget. However, in order to mask a large net inward flux of water into the mantle, ridge volume must increase, or dynamic topography must raise sea level over time. Ridge volume is unlikely to have increased over the Phanerozoic as seafloor spreading rates should generally decrease over long timescales. Furthermore, the age distribution of the ocean floor has either been constant since ~200 Ma (Parsons, 1982; Rowley, 2002) or has increased over the past ~60 Myr (Xu et al., 2006). Dynamic topography is expected to produce sea level changes on order ±100 m in association with a full Wilson cycle (Conrad and Husson, 2009). We therefore use the 360 m decrease of the original Hallam (1984) reconstruction in our model to

place an upper limit on the net inward water flux imbalance, despite the fact that it most likely overestimates the magnitude of secular Phanerozoic sea level change. An imbalance between mantle output and input may therefore be tolerated in our model, as long as the net inward flux does not exceed 2.1×10^{13} moles/yr, which is the flux required to reduce sea level by 360 m over 542 Myr (using present-day hypsometry; after Harrison, 1990). We also set a net outward flux limit at 1.9×10^{12} moles/yr, corresponding to a sea level increase of 35 m (Figure 2.3d). The second criterion for success can now be assessed: if the net flux is outside the sea level limits, then the realization is classified as a Failure 2 scenario.

2.3. RESULTS

The Monte Carlo approach allows us to quantify the global water fluxes with associated 68% confidence intervals. A simulation of the global water cycle with 10^7 model realizations was performed based on the input parameters given in Table 2.1. Repeat simulations were performed to ensure that the results had converged. A summary of model results is presented in Table 2.3. A striking aspect of the simulation is that 86% of the realizations resulted in failure, where one or both of the criteria were violated (Sections 2.2.2, 2.2.3). A parameter sensitivity test indicates that arc water output and trench water input exert primary control over the global water cycle, as these two fluxes are significantly larger than the MORB, OIB and back-arc fluxes (Table 2.3). The total mantle-derived water output flux is $1.4^{+0.4}_{-0.3} \times 10^{13}$ moles/yr (Table 2.3). The outgassing flux of water at arcs is $3.2^{+2.3}_{-1.4} \times 10^{13}$ moles/yr. While the mean arc output flux is a factor

of two higher than the estimate of 1.7×10^{13} moles/yr by Wallace (2005), the two estimates are consistent at the 68% confidence limit.

Table 2.3: Results of Monte Carlo simulation of global water cycle

Statistics for all successful realizations:	mean	(x10^{13} moles/yr) mean	conf.	min	max
Ocean island flux		0.52	$^{+0.35}_{-0.23}$	0.09	1.2
Mid-ocean ridge flux		0.75	$^{+0.25}_{-0.24}$	0.18	1.6
Total arc flux		3.2	$^{+2.3}_{-1.4}$	0.17	8.0
Slab-derived arc flux		3.1	$^{+2.3}_{-1.4}$	0.13	7.9
Total back-arc flux		0.44	$^{+0.25}_{-0.28}$	0.02	0.97
Slab-derived back-arc flux		0.38	$^{+0.26}_{-0.31}$	0	0.95
Trench input flux		6.0	$^{+2.6}_{-1.3}$	4.1	13
Total mantle-derived output flux = (OIB + MORB + mantle-derived arc + mantle-derived back-arc)		1.4	$^{+0.4}_{-0.3}$	0.38	3.0

Net flux and return flux to the mantle:*	(x10^{13} moles/yr) net flux	return flux	
<u>Near-steady state scenario:</u>			
0 m over 542 Myr	0	1.4	$^{+0.4}_{-0.3}$
100 m over 542 Myr	0.56	2.0	$^{+0.4}_{-0.3}$
<u>Maximum permissible sea level change:</u>			
360 m over 542 Myr	2.1	3.5	$^{+0.4}_{-0.3}$

Means are given with 68% confidence limits ("conf.").

* Net flux is the difference between mantle return and output fluxes, and is accomodated by a corresponding change in sea level. Statistics for the return flux are calculated based on realizations with a net flux within 10^{11} moles/yr of the net flux for specified sea level change scenarios.

Figure 2.4 shows model success rate contoured across trench water input flux and arc magmatic water content parameter space. Contours indicate the fraction of successful realizations at the specified arc and trench values, given independent random variation in all other parameters, including arc magma production rate. We emphasize that the simulation does not directly provide information about which successful scenarios are most likely to reflect reality—the simulation only determines what regions of parameter space are allowed given the observational constraints. Thus, an area of arc-trench parameter space with low (but non-zero) success rates is not necessarily unrealistic, but it does require very specific tuning of the remaining parameters to satisfy observational constraints. The most striking aspect of Figure 2.4 is that approximately two-thirds of the arc-trench parameter space is devoid of successful realizations. The upper limit trench intake (Schmidt and Poli, 1998) results in zero successful realizations. The highest trench input flux with a success rate > 0.1% is 12 x 10^{13} moles/yr. The trench input flux estimates of Rüpke et al. (2004), Hacker (2008) and van Keken et al. (2011) result in maximum success rates of ~20, 40, and ~55% at global mean arc H_2O contents of ~6.0, 4.5 and 3.0 wt%, respectively. Success rate is maximized at low trench inputs and a global mean arc magmatic H_2O of ~2 wt%: in this region of parameter space, the model is least sensitive to variations in the remaining parameters. Failure rates increase at high magmatic water contents as the simulation becomes sensitive to arc magma production rate.

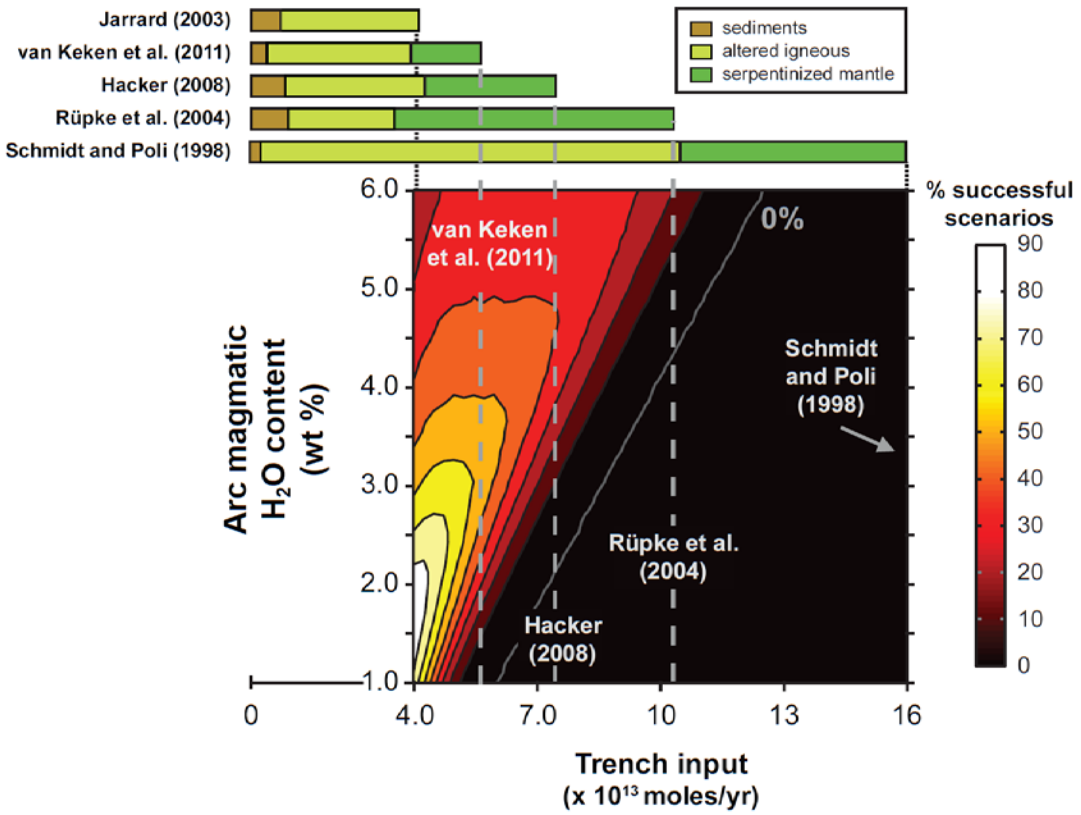

Figure 2.4 Contour of model success rate (% successful realizations out of total realizations) as a function of trench H_2O input flux and arc magmatic H_2O content parameter space. Black parameter space is devoid of successful scenarios (100% Failure 2; sea level decrease > 360 m), and makes up ~60% of the arc-trench parameter space explored. The highest trench input flux for which there is a single successful scenario is 12×10^{13} moles per year. Success rate is maximized at low trench inputs and an arc magmatic H_2O content of ~2 wt%; here, the model is least sensitive to variation in the remaining parameters. Failure 1 occurs only in the upper left corner: here, low trench inputs cannot support the arc fluxes generated given high arc H_2O contents. Failure 2 due to sea level increase > 35m is also confined to the upper left corner.

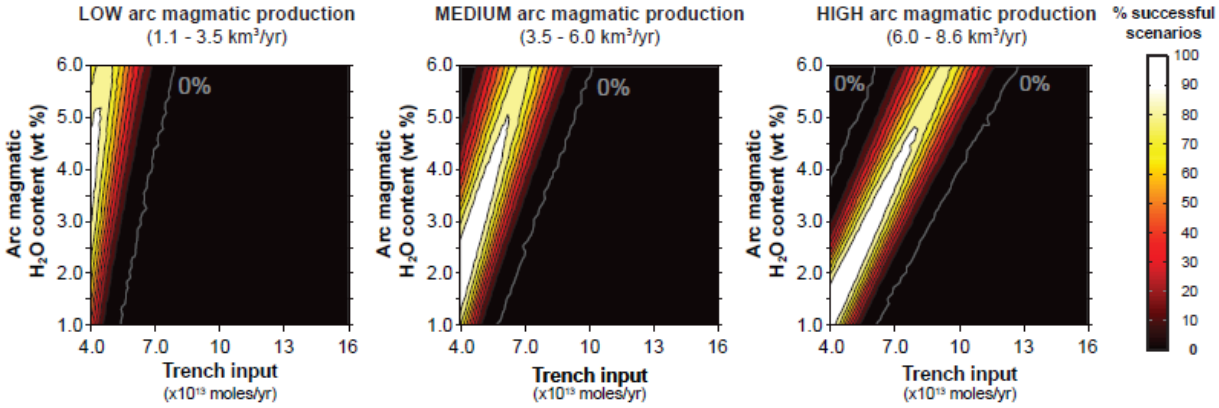

Figure 2.5 Contour of model success rate for three different arc magmatic production intervals: (a) a "low" interval (1.1 to 3.5 km^3 per year), (b) an "intermediate" interval (3.5 to 6.0 km^3 per year), and (c) a "high" interval (6.0 to 8.6 km^3 per year). Axes are the same as in Figure 2.4.

To better understand model sensitivity to arc magma production rates, we ran simulations at three magma production rate intervals (Figure 2.5): low (1.1-3–5 km^3 per year), medium (3.5–6.0 km^3 per year) and high (6.0–8.6 km^3 per year). At low magma production rates (Figure 2.5a), high success rates occur over arc magmatic H_2O contents of 2–5 wt%, but success is limited to the very lowest trench inputs, and Failure 2 dominates most of the space. Higher arc magma production rates (Figure 2.5b,c) enable success at higher trench inputs, but inhibit success at low trench inputs since resulting arc output fluxes are too high to be supported by the trench intake (Failure 1 in the upper left corners of Figure 2.5b,c). Figure 2.5 also illustrates why maximum model success rate in Figure 2.4 occurs near 2 wt% arc magmatic H_2O and low trench input: this region of parameter space maintains moderate-to-high success rates over all three arc magma production intervals.

2.4. DISCUSSION

We now explore the implications of our Monte Carlo simulation for water exchange between the mantle and exosphere. We discuss two water cycling scenarios over the past 542 Myr. The first, our preferred scenario based on the available data, is a near steady-state ocean where the return flux of water to the mantle generates between 0 and 100 m of sea level decrease (Section 2.3.2 discusses the evidence supporting this scenario). In the second scenario, the mantle return flux generates the maximum-supported sea level decrease of 360 m over 542 Myr.

2.4.1 The hydration state of subducting slab

Total trench input fluxes are poorly estimated, as illustrated by the large number of failures for most of trench parameter space (Figure 2.4). However, estimates of the global trench input flux differ primarily due to varying estimates of the poorly-constrained serpentinized lithospheric mantle water flux; that is, studies agree on the flux of water carried in sediments and altered igneous crust (~4×10^{13} moles/yr, Figure 2.4; Jarrard 2003; Rüpke et al. 2004; Hacker 2008; van Keken et al. 2011). The trench inputs in realizations that generate our preferred near steady-state ocean (0–100m sea level decrease) scenario and the maximum sea level scenario are $5.7_{-1.2}-5.9^{+2.2} \times 10^{13}$ moles/yr and $6.5^{+2.8}_{-1.4} \times 10^{13}$ moles/yr, respectively (means and 68% confidence limits). Assuming that 4.0×10^{13} moles/yr are carried in sediments and altered igneous crust (see above), the trench input flux carried in serpentinized lithospheric mantle ranges from $1.7_{-1.2}-1.9^{+2.2} \times 10^{13}$ and $2.5^{+2.8}_{-1.4} \times 10^{13}$ moles/yr, corresponding to $2.7_{-1.8}-2.9^{+3.4}$ %

and $3.8^{+4.3}_{-2.1}$% serpentinization of 10 km of lithospheric mantle, respectively. The preferred near steady-state serpentinite fluxes fall at the low end of estimates given by Schmidt and Poli (1998) and Rüpke et al. (2004), are ~50% lower than estimates by Hacker (2008) and more than 20 times lower than the estimate given by Li and Lee (2006).

We now use the above limits on trench input flux to explore the spatial extent of serpentinization in slabs. Hydration of lithospheric mantle is thought to occur along deep faults formed at the outer rise. We assume a fault spacing of 3 km (Ranero et al., 2003), fault depth of 10 km, and 45 000 km length of trench (Jarrard, 2003). If serpentinization reactions begin at fault surfaces and propagate laterally, we calculate a lateral extent of serpentinization of 51-55 m and 73 m from each fault surface (for the near steady-state and 360 m sea level decrease scenarios, respectively; based on pure 13 wt% H_2O serpentine, 2.6 g/cm^3 density). We note that a laterally continuous serpentinite layer would not form unless the depths of serpentinization were limited to 340-360 m and 480 m, respectively.

2.4.2 Previous estimates of the return flux of water to the mantle

Previously-estimated return fluxes range from 3.5-9.4 × 10^{13} (Rüpke et al., 2004), 4.7 × 10^{13} (Hacker, 2008), and 3.8 × 10^{13} (van Keken et al., 2011) moles/yr (Figure 2.6). Return fluxes are taken as the authors' estimates of bound water flux beyond depths of arc magma generation (~4–5 GPa or 120–150 km; Syracuse and Abers, 2006; Hacker, 2008). Rüpke et al. (2004) provide water release curves with depth; we use these to calculate the range of bound water at 120 km depth (after Hacker, 2008). van Keken et al.

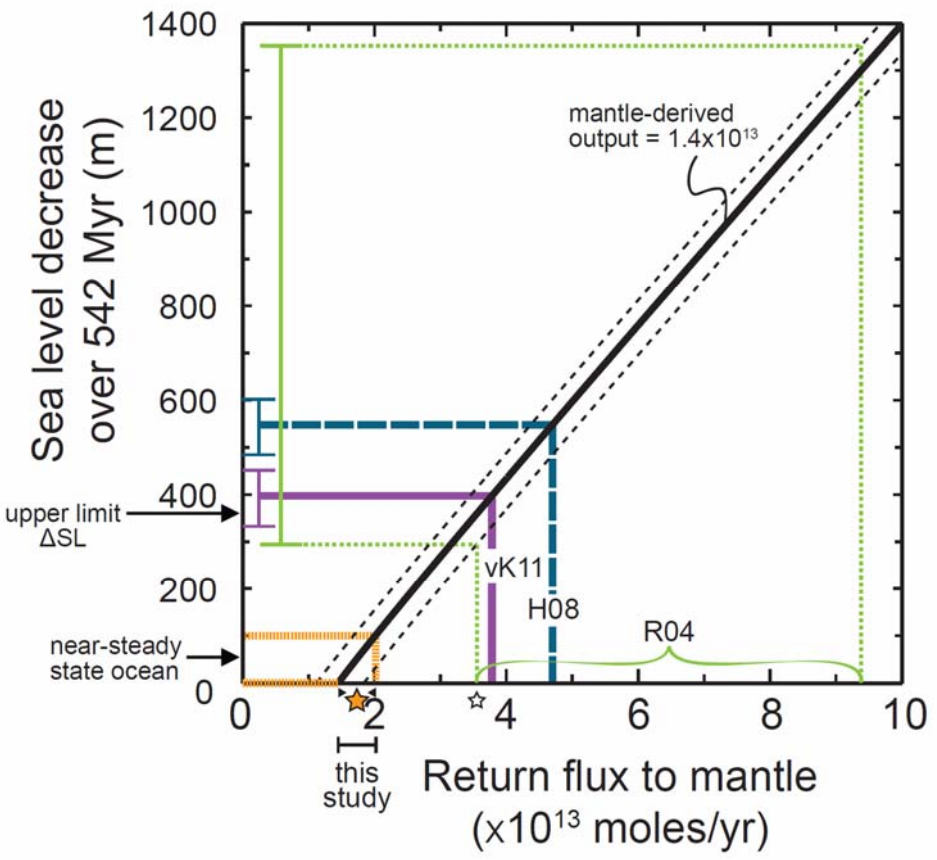

Figure 2.6 Sea level decrease over 542 Myr as a function of return flux to the mantle. R04 = Rüpke et al. (2004), H08 = Hacker (2008) and vK11 = van Keken et al. (2011). The solid black line represents sea level change given the mean total mantle-derived output flux of 1.4×10^{13} moles/yr (accompanying dashed black lines represent the 68% confidence limits of total mantle-derived output; $1.1\text{-}1.8 \times 10^{13}$ moles/yr). The range in sea level change for each study is based on the 68% confidence limits of total mantle-derived water output. All literature return flux estimates exceed the near-steady state ocean return flux range. Only at the 68% confidence limit are the estimate of van Keken et al. (2011) and the lower limit of Rüpke et al. (2004) consistent with the upper limit sea level decrease of 360 m. Our preferred return flux based on the near-steady state ocean scenario (0–100 m sea level decrease), is $1.4 - 2.0^{+0.4}_{-0.3} \times 10^{13}$ moles/yr, indicated by the solid star. Open star indicates our upper limit return flux to the mantle.

(2011) estimate that ~1/3 of their initial slab water input is released above 100 km depth and constitutes the flux supplying global arc volcanism. Another 1/3 of the initial flux is retained beyond 230 km depth and is discussed as the deep mantle return flux. The fate of the remaining 1/3 (released between 100 and 230 km) is unspecified, but since it is

largely released below depths of magma generation and the authors do not include it in their arc magmatic flux (van Keken et al., 2011), it is considered here as part of the return flux.

All literature return fluxes exceed the total mantle-derived output flux given by our model (Table 2.3; Figure 2.6), indicating net mantle regassing. Figure 2.6 shows the decrease in sea level if the imbalance between the return fluxes and mantle output fluxes are sustained over the entire Phanerozoic. All literature estimates generate sea level change in excess of our preferred limit (0–100 m). Furthermore, most of the estimates also violate the upper limit (360 m) sea level decrease: the estimates of van Keken et al. (2011) and the lower limit of Rüpke et al. (2004) are only compatible with a sea level decrease of 360 m if mantle output is high (Figure 2.6). Thus, the vast majority of literature return fluxes are too large to reflect long-term water cycling between the mantle and exosphere. If sustained, they would reduce the amount of exospheric water by an amount inconsistent with reconstructions of Phanerozoic sea level. In particular, the highest estimated return flux (Rüpke et al., 2004) would remove a volume of water equal to half the present-day ocean in 500 Myr.

2.4.3 Mantle regassing rates

The sea level reconstructions discussed in Section 2.3.2 indicate that long-term secular decrease in sea level over the Phanerozoic was limited to ~0–100 m. Accordingly, the near steady-state ocean scenario described above yields our preferred return flux range of $1.4 - 2.0^{+0.4}_{-0.3} \times 10^{13}$ moles/yr to the mantle (Table 2.3). The upper limit of 360 m of sea level decrease over the Phanerozoic yields a return flux of $3.5^{+0.4}_{-0.3} \times 10^{13}$ moles/yr

into the mantle (Table 2.3). All of these fluxes are low compared to previous estimates (Figure 2.6). If the entire return flux is distributed uniformly throughout 10 km of lithospheric mantle as serpentine, the above fluxes correspond to $2.2-3.1^{+0.6}_{-0.5}$ % serpentinization and $5.4^{+0.6}_{-0.5}$ % serpentinization, respectively, assuming 2.7 km^2 of convergence per year and 3.3 g/cm^3 density for lithospheric mantle. These numbers are in some cases higher than the initial serpentinized mantle input fluxes to trenches estimated in Section 2.4.1, suggesting that up to 70% of the return flux is carried in the igneous crust, in minerals such as lawsonite and phengite (e.g., Schmidt and Poli, 1998; Hacker et al., 2008; van Keken et al., 2011). It is also possible that all of the previous studies have overestimated the flux of water carried in sediments and altered igneous crust (Figure 2.4; Section 2.4.1), which would allow the initial serpentinized mantle input flux to the trench to be larger.

Our preferred and upper limit return fluxes over the Phanerozoic correspond to preferred and upper limit net mantle regassing rates of 0–5.6 × 10^{13} moles/yr and of 2.1 × 10^{13} moles/yr, respectively (Table 2.3). While we have discussed water cycling only over the Phanerozoic, as observational constraints are strongest for this period of time, we note that the Phanerozoic upper limit of 2.1 × 10^{13} moles/yr for the net mantle regassing rate cannot reflect conditions into deep time. Continental freeboard arguments suggest that sea surface height with respect to continents has remained within 500 m of the present value since the end-Archean (Wise, 1974, Windley 1977; Galer 1991; Kasting and Holm, 1992), suggesting that the upper limit net flux might only be sustained for up to ~750 Myr; if sustained since the end-Archean, the upper limit would generate ~1600m of sea level decrease. In contrast, our preferred net regassing flux for the Phanerozoic (0–5.6 ×

10^{12} moles/yr) would be consistent into deep time as it would generate a sea level decrease of up to ~0–500 m since 2.5 Gyr. The preferred net mantle regassing rate would lead to at most a 60 ppm increase in bulk mantle water content since 2.5 Gyr, which is a factor of 3.5 less than van Keken et al.'s (2011) estimate of 200 ppm (370 ppm over 4.5 Gyr). However, the factor of 3.5 difference is readily explained by the fact that van Keken et al. (2011) neglected any mantle-derived water output flux in computing the net mantle regassing rate, resulting in an unrealistically high increase in mantle water content.

2.4.4 Implications for the evolution of mantle volatile budgets

Our preferred and upper limit return fluxes of water to the mantle correspond to bulk water contents in a 100 km-thick slab of 280–400 ppm and 700 ppm H_2O, respectively. Since some part of the return flux may be stored in nominally anhydrous minerals in the mantle wedge without being returned to the exosphere, the bulk slab water contents are upper limits. Convective stirring and assimilation of recycled slabs with our preferred slab water contents of 280–400 ppm into the MORB source could account for the MORB source water, as source concentrations are between 50–230 ppm (Saal et al., 2002; Simons et al., 2002). Furthermore, the MORB source may be getting wetter: since water concentrations in the slab are higher than the MORB source, mixing and assimilation should enrich the mantle source. In contrast, convective stirring of recycled slabs is not likely to account for all of the OIB source water (Table 2.1), particularly for the high $^3He/^4He$ FOZO plumes that have ~750 ppm water in their source (e.g. Dixon et al., 2002). Thus, we suggest that a source of juvenile water is required for

OIB magmatism, consistent with the inference of Dixon et al. (2002) based on H_2O/Ce ratios. Furthermore, mixing and assimilation of slabs with 280-400 ppm water may be diluting the OIB source water over time; i.e., the OIB source may be getting drier. It is conceivable that if subducted slabs have the upper limit 700 ppm H_2O, then all of the water in the OIB source could be associated with recycling of subducted water. However, the residence time of material in the OIB source region is on order ~1-2 Gyr (Allegre 2002; Gonnermann and Mukhopadhyay, 2009; Kawabata et al., 2011) and the upper limit slab water content cannot be sustained much further back than 750 Myr.

The relatively low magnitude of our preferred total trench input flux and return flux estimates is significant in light of suggestions that the return flux of water to the mantle affects cycling of other volatiles, such as the noble gases. Since heavy noble gases (e.g., Ar and Xe) have been used to place constraints on mantle structure and dynamics, it is especially important to understand the origin of noble gas signatures. For example, based on apparent similarities in the noble gas abundance patterns of the mantle and seawater, Holland and Ballentine (2006) argue that differences in OIB and MORB source noble gases reflect preferential recycling of seawater-derived atmospheric noble gases into the OIB source. Such a conclusion has important ramifications for mantle geodynamics, as it implies that differences between MORB and OIB noble gases are related to recycling of atmospheric gases, rather than the preservation of a less-degassed mantle source. However, the Holland and Ballentine (2006) hypothesis specifically requires unfractionated atmospheric noble gases dissolved in seawater to be carried as pore water trapped within subducting slabs. Given the difficulty in retaining significant amounts of pore water beyond depths of magma generation, Sumino et al. (2010) propose

that the noble gases may be carried by unfractionated seawater trapped in fluid inclusions. To account for the mantle Ar budget, 0.37×10^{13} moles/yr of unfractionated seawater trapped within pores or in fluid inclusions must return to the mantle (Holland and Ballentine, 2006). Unless a surprisingly large percentage of the preferred mantle return flux (~20–30%) is carried as pore water or within fluid inclusions, preferential transport of unfractionated noble gases in seawater to the lower mantle to generate the OIB heavy noble gas signature is problematic. We are not aware of any studies that independently document such a large percentage of the return flux to the mantle to be associated with pore water or fluid inclusions. Therefore, a lower degree of degassing for the OIB source remains a viable explanation for differences in MORB and OIB heavy noble gas compositions.

2.5. CONCLUSIONS

We used a Monte Carlo simulation of global water exchange between the mantle and exosphere to constrain the magnitudes of the flux of water (1) into trenches and (2) beyond depths of magma generation, based on reconstructions of Phanerozoic sea level change. We find that previous estimates of both of the above fluxes are frequently too large to reflect long-term water cycling. We estimate trench input fluxes from $5.7_{-1.2} - 5.9^{+2.2} \times 10^{13}$ moles/yr and $6.5^{+2.8}_{-1.4} \times 10^{13}$ moles/yr (near steady-state and upper limit sea level statistics, respectively), which suggest a limited extent of serpentinization of subducting lithospheric mantle. Our preferred return flux to the mantle, based on 0–100 m of sea level decrease over the Phanerozoic, is between $1.4 - 2.0^{+0.4}_{-0.3} \times 10^{13}$ moles/yr. The associated net flux would also be compatible with sea level change since

the end-Archean based on continental freeboard, and would lead to an increase in bulk mantle water content of up to 60 ppm since 2.5 Gyr. Furthermore, our study indicates that while water in the MORB source may be accounted for by recycling of chemically-bound water in subducted slabs, recycled slab water contents may not be high enough to support all of the OIB source water, such that a juvenile source is required for some fraction of OIB water.

2.6 REFERENCES

Abbott, D., Burgess, L., Longhi, J., Smith, W. H. F., 1994. An empirical thermal history of the Earth's upper-mantle. J. Geophys. Res.-Solid Earth 99, 13835-13850.

Algeo, T. J., Wilkinson, B. H., 1991. Modern and ancient continental hypsometries. Journal Geol. Soc. London 148, 643-653.

Allegre, C. J., 2002. The evolution of mantle mixing. Philos. Trans. Roy. Soc. A 360, 2411-2431, doi: 10.1098/rsta.2002.1075.

Almeev, R., Holtz, F., Koepke, J., Haase, K., Devey, C., 2008. Depths of partial crystallization of H_2O-bearing MORB: Phase equilibria simulations of basalts at the MAR near Ascension Island (7-11 degrees s). J. Petrol. 49, 25-45, doi: 10.1093/petrology/egm068.

Aubaud, C., Hauri, E. H., Hirschmann, M. M., 2004. Hydrogen partition coefficients between nominally anhydrous minerals and basaltic melts. Geophys. Res. Lett. 31, L20611, doi: 10.1029/2004gl021341.

Baker, E. T. , German, C. R., 2004. On the global distribution of hydrothermal vent fields, in: German, C. R., Lin, J., Parson, L. M (Eds.), Mid-ocean ridges: Hydrothermal interactions between the lithosphere and oceans, AGU Geophysical Monograph Series 148, 245-266.

Benjamin, E. R., Plank, T., Wade, J. A., Kelley, K. A., Haun, E. H., Alvarado, G. E., 2007. High water contents in basaltic magmas from Irazu volcano, Costa Rica. J. Volcanol. Geotherm. Res. 168, 68-92, doi: 10.1016/j.jvolgeores.2007.08.008.

Cervantes, P., Wallace, P. J., 2003. Role of H_2O in subduction-zone magmatism: New insights from melt inclusions in high-Mg basalts from Central Mexico. Geology 31, 235-238.

Conrad, C. P., Husson, L., 2009. Influence of dynamic topography on sea level and its rate of change. Lithosphere 1, 110-120, doi: 10.1130/l32.1.

Crisp, J. A., 1984. Rates of magma emplacement and volcanic output. J. Volcanol. Geotherm. Res. 20, 177-211.

Crowley, J. W., Gerault, M., O'Connell, R. J., 2011. On the relative influence of heat and water transport on planetary dynamics. Earth Planet. Sci. Lett. 310, 380-388, doi: 10.1016/j.epsl.2011.08.035.

Dixon, J. E., Leist, L., Langmuir, C., Schilling, J. G., 2002. Recycled dehydrated lithosphere observed in plume-influenced mid-ocean-ridge basalt. Nature 420, 385-389, doi: 10.1038/nature01215.

Fretzdorff, S., Livermore, R. A., Devey, C. W., Leat, P. T., Stoffers, P., 2002. Petrogenesis of the back-arc East Scotia Ridge, South Atlantic Ocean. J. Petrol. 43, 1435-1467.

Galer, S. J. G., 1991. Inter-relationships between continental freeboard, tectonics and mantle temperature. Earth Planet. Sci. Lett. 105, 214-228.

Gonnermann, H. M., Mukhopadhyay, S., 2009. Preserving noble gases in a convecting mantle. Nature 459, 560-U588, doi: 10.1038/Nature08018.

Hacker, B. R., 2008. H_2O subduction beyond arcs. Geochem. Geophys. Geosyst. 9, Q03001, doi: 10.1029/2007gc001707.

Hallam, A., 1984. Pre-Quaternary sea-level changes. Annu. Rev. Earth Pl. Sc. 12, 205-243.

Hallam, A., 1992. Phanerozoic sea level changes, Columbia University Press, New York, 266 pp.

Haq, B. U., Hardenbol, J., Vail, P. R., 1987. Chronology of fluctuating sea levels since the Triassic. Science 235, 1156-1167.

Haq, B. U., Schutter, S. R., 2008. A chronology of Paleozoic sea-level changes. Science 322, 64-68, doi: 10.1126/science.1161648.

Hardenbol, J. R., Vail, P. R., Ferrer, J., 1981. Interpreting paleoenvironments, subsidence history and sea-level changes of passive margins from seismic and biostratigraphy. Oceanologica Acta, Proceedings 26th International Geological Congress, Geology of Continental Margins Symposium, Paris, 7-17 July, 1980 Supplement to Volume 3, 33-44.

Harrison, C. G. A., 1990. Long-term eustasy and epeirogeny in continents, in: N. R. C. Geophysics Study Committee (Ed), Sea-level change. National Academy Press, Washington, D. C., pp. 141-158.

Hauri, E. H., Gaetani, G. A., Green, T. H., 2006. Partitioning of water during melting of the Earth's upper mantle at H_2O-undersaturated conditions. Earth Planet. Sci. Lett. 248, 715-734, doi: 10.1016/j.epsl.2006.06.014.

Hays, J. D., Pitman, W. C., 1973. Lithospheric plate motion, sea-level changes and climatic and ecological consequences. Nature 246, 18-22.

Hirschmann, M. M., 2006. Water, melting, and the deep Earth H_2O cycle. Annu. Rev. Earth Pl. Sc. 34, 629-653, doi: 10.1146/annurev.earth.34.031405.125211.

Hirth, G., Kohlstedt, D. L., 1996. Water in the oceanic upper mantle: Implications for rheology, melt extraction and the evolution of the lithosphere. Earth Planet. Sci. Lett. 144, 93-108.

Holland, G., Ballentine, C. J., 2006. Seawater subduction controls the heavy noble gas composition of the mantle. Nature 441, 186-191, doi: 10.1038/Nature04761.

Inoue, T., 1994. Effect of water on melting phase-relations and melt composition in the system Mg_2SiO_4-$MgSiO_3$- H_2O up to 15 GPa. Phys. Earth Planet. In. 85, 237-263.

Jarrard, R. D., 2003. Subduction fluxes of water, carbon dioxide, chlorine, and potassium. Geochem. Geophys. Geosyst. 4, 8905, doi: 10.1029/2002gc000392.

Johnson, E. R., Wallace, P. J., Granados, H. D., Manea, V. C., Kent, A. J. R., Bindeman, I. N., Donegan, C. S., 2009. Subduction-related volatile recycling and magma generation beneath Central Mexico: Insights from melt inclusions, oxygen isotopes and geodynamic models. J. Petrol. 50, 1729-1764, doi: 10.1093/petrology/egp051.

Karato, S. I., Jung, H., 2003. Effects of pressure on high-temperature dislocation creep in olivine. Philos. Mag. 83, 401-414, doi: 10.1080/0141861021000025829.

Kasting, J. F., Holm, N. G., 1992. What determines the volume of the oceans? Earth Planet. Sci. Lett. 109, 507-515.

Kawabata, H., Hanyu, T., Chang, Q., Kimura, J. I., Nichols, A. R. L., Tatsumi, Y., 2011. The petrology and geochemistry of St. Helena alkali basalts: Evaluation of the oceanic crust-recycling model for HIMU OIB. J. Petrol. 52, 791-838, doi: 10.1093/petrology/egr003.

Kelley, K. A., Plank, T., Grove, T. L., Stolper, E. M., Newman, S., Hauri, E., 2006. Mantle melting as a function of water content beneath back-arc basins. J. Geophys. Res.-Solid Earth 111, B09208, doi: 10.1029/2005jb003732.

Kelley, K. A., Plank, T., Newman, S., Stolper, E. M., Grove, T. L., Parman, S., Hauri, E. H., 2010. Mantle melting as a function of water content beneath the Mariana Arc. J. Petrol. 51, 1711-1738, doi: 10.1093/petrology/egq036.

Labrosse, S., Jaupart, C., 2007. Thermal evolution of the Earth: Secular changes and fluctuations of plate characteristics. Earth Planet. Sci. Lett. 260, 465-481, doi: 10.1016/j.epsl.2007.05.046.

Langmuir, C. H., Bezos, A., Escrig, S., Parman, S. W., 2006. Chemical systematics and hydrous melting of the mantle in back-arc basins, in: Christie, D. M., Fisher, C. R. Lee, S.-M, Givens, S. (Eds.), Back-arc spreading systems: Geological, biological, chemical, and physical interactions, AGU Geophysical Monograph Series 166, 87-146.

Lee, C. T. A., Leeman, W. P., Canil, D., Li, Z. X. A., 2005. Similar V/Sc systematics in MORB and arc basalts: Implications for the oxygen fugacities of their mantle source regions. J. Petrol. 46, 2313-2336, doi: 10.1093/petrology/egi056.

Li, Z. X. A., Lee, C. T. A., 2006. Geochemical investigation of serpentinized oceanic lithospheric mantle in the Feather River Ophiolite, california: Implications for the recycling rate of water by subduction. Chem. Geol. 235, 161-185, doi: 10.1016/j.chemgeo.2006.06.011.

Mei, S., Kohlstedt, D. L., 2000. Influence of water on plastic deformation of olivine aggregates 2. Dislocation creep regime. J. Geophys. Res.-Solid Earth 105, 21471-21481.

Michael, P., 1995. Regionally distinctive sources of depleted MORB - evidence from trace-elements and H_2O. Earth Planet. Sci. Lett. 131, 301-320.

Miller, K. G., Wright, J. D., Fairbanks, R. G., 1991. Unlocking the ice house - Oligocene-Miocene oxygen isotopes, eustasy, and margin erosion. J Geophys Res-Solid 96, 6829-6848.

Miller, K. G., Kominz, M. A., Browning, J. V., Wright, J. D., Mountain, G. S., Katz, M. E., Sugarman, P. J., Cramer, B. S., Christie-Blick, N., Pekar, S. F., 2005. The Phanerozoic record of global sea-level change. Science 310, 1293-1298, doi: 10.1126/science.1116412.

Moucha, R., Forte, A. M., Mitrovica, J. X., Rowley, D. B., Quere, S., Simmons, N. A., Grand, S. P., 2008. Dynamic topography and long-term sea-level variations: There is no such thing as a stable continental platform. Earth Planet. Sci. Lett. 271, 101-108, doi: 10.1016/j.epsl.2008.03.056.

Muller, R. D., Sdrolias, M., Gaina, C., Steinberger, B., Heine, C., 2008. Long-term sea-level fluctuations driven by ocean basin dynamics. Science 319, 1357-1362, doi: 10.1126/science.1151540.

Nedimovic, M. R., Bohnenstiehl, D. R., Carbotte, S. M., Canales, J. P., Dziak, R. P., 2009. Faulting and hydration of the Juan de Fuca plate system. Earth Planet. Sci. Lett. 284, 94-102, doi: 10.1016/j.epsl.2009.04.013.

Newman, S., Stolper, E., Stern, R., 2000. H_2O and CO_2 in magmas from the Mariana arc and back-arc systems Geochem. Geophys. Geosyst. 1, 1013, doi: 10.1029/1999GC000027.

Parsons, B., 1982. Causes and consequences of the relation between area and age of the ocean-floor. J Geophys Res 87, 289-302.

Pineau, F., Shilobreeva, S., Hekinian, R., Bideau, D., Javoy, M., 2004. Deep-sea explosive activity on the Mid-Atlantic Ridge near 34°50'N: A stable isotope (C, H, O) study. Chem. Geol. 211, 159-175, doi: 10.1016/j.chemgeo.2004.06.029.

Plank, T., 2005. Constraints from thorium/lanthanum on sediment recycling at subduction zones and the evolution of the continents. J. Petrol. 46, 921-944, doi: 10.1093/petrology/egi005.

Portnyagin, M., Hoernle, K., Plechov, P., Mironov, N., Khubunaya, S., 2007. Constraints on mantle melting and composition and nature of slab components in volcanic arcs from volatiles (H_2O, S, Cl, F) and trace elements in melt inclusions from the Kamchatka Arc. Earth Planet. Sci. Lett. 255, 53-69.

Ranero, C. R., Morgan, J. P., Mcintosh, K., Reichert, C., 2003. Bending-related faulting and mantle serpentinization at the Middle America trench. Nature 425, 367-373, doi: 10.1038/Nature01961.

Ranero, C. R., Villasenor, A., Phipps-Morgan, J., Weinrebe, W., 2005. Relationship between bend-faulting at trenches and intermediate-depth seismicity. Geochem. Geophys. Geosyst. 6, Q12002, doi: 10.1029/2005gc000997.

Reymer, A., Schubert, G., 1984. Phanerozoic addition rates to the continental-crust and crustal growth. Tectonics 3, 63-77.

Roggensack, K., 2001. Sizing up crystals and their melt inclusions: A new approach to crystallization studies. Earth Planet. Sci. Lett. 187, 221-237.

Rowley, D. B., 2002. Rate of plate creation and destruction: 180 Ma to present. Geol. Soc. Am. Bull. 114, 927-933.

Rüpke, L. H., Morgan, J. P., Hort, M., Connolly, J. A. D., 2004. Serpentine and the subduction zone water cycle. Earth Planet. Sci. Lett. 223, 17-34.

Ruscitto, D. M., Wallace, P. J., Johnson, E. R., Kent, A. J. R., Bindeman, I. N., 2010. Volatile contents of mafic magmas from cinder cones in the Central Oregon High Cascades: Implications for magma formation and mantle conditions in a hot arc. Earth Planet. Sci. Lett. 298, 153-161, doi: 10.1016/j.epsl.2010.07.037.

Ryerson, F. J., Watson, E. B., 1987. Rutile saturation in magmas: Implications for Ti-Nb-Ta depletion in island-arc basalts. Earth Planet. Sci. Lett. 86, 225-239.

Saal, A. E., Hauri, E. H., Langmuir, C. H., Perfit, M. R., 2002. Vapour undersaturation in primitive mid-ocean-ridge basalt and the volatile content of Earth's upper mantle. Nature 419, 451-455.

Sadofsky, S. J., Portnyagin, M., Hoernle, K., Van Den Bogaard, P., 2008. Subduction cycling of volatiles and trace elements through the Central American Volcanic Arc: Evidence from melt inclusions. Contrib. Mineral. Petrol. 155, 433-456, doi: 10.1007/s00410-007-0251-3.

Schmidt, M. W., Poli, S., 1998. Experimentally based water budgets for dehydrating slabs and consequences for arc magma generation. Earth Planet. Sci. Lett. 163, 361-379.

Schmidt, M. W., Poli, S., 2003. 3.17 - Generation of mobile components during subduction of oceanic crust, in: Heinrich, D.H., Turekian, K. K. (Eds-in-Chief), Treatise on Geochemistry, Vol. 3. Pergamon, Oxford, pp. 567-591.

Schubert, G., Reymer, A. P. S., 1985. Continental volume and freeboard through geological time. Nature 316, 336-339.

Shaw, A. M., Hauri, E. H., Fischer, T. P., Hilton, D. R., Kelley, K. A., 2008. Hydrogen isotopes in Mariana Arc melt inclusions: Implications for subduction dehydration and the deep-Earth water cycle. Earth Planet. Sci. Lett. 275, 138-145, doi: 10.1016/j.epsl.2008.08.015.

Simons, K., Dixon, J., Schilling, J. G., Kingsley, R., Poreda, R., 2002. Volatiles in basaltic glasses from the Easter-Salas y Gomez seamount chain and Easter microplate: Implications for geochemical cycling of volatile elements. Geochem. Geophys. Geosyst. 3, 1039, doi: 10.1029/2001gc000173.

Sisson, T. W., Bronto, S., 1998. Evidence for pressure-release melting beneath magmatic arcs from basalt at Galunggung, Indonesia. Nature 391, 883-886.

Standish, J. J., Dick, H. J. B., Michael, P. J., Melson, W. G., O'hearn, T., 2008. MORB generation beneath the ultraslow spreading Southwest Indian ridge (9-25°E): Major element chemistry and the importance of process versus source. Geochem. Geophys. Geosyst. 9, Q05004, doi: 10.1029/2008gc001959.

Stolper, E., Newman, S., 1994. The role of water in the petrogenesis of Mariana trough magmas. Earth Planet. Sci. Lett. 121, 293-325.

Sumino, H., Burgess, R., Mizukami, T., Wallis, S. R., Holland, G., Ballentine, C. J., 2010. Seawater-derived noble gases and halogens preserved in exhumed mantle wedge peridotite. Earth Planet. Sci. Lett. 294, 163-172, doi: 10.1016/j.epsl.2010.03.029.

Syracuse, E. M., Abers, G. A., 2006. Global compilation of variations in slab depth beneath arc volcanoes and implications. Geochem. Geophys. Geosyst. 7, Q05017, doi: 10.1029/2005gc001045.

Vail, P. R., Mitchum, R. M., Thompson, S., 1977. Seismic stratigraphy and global changes of sea level, Part 4: Global cycles of relative changes of sea level, in: Clayton, C. E. (Ed.), Seismic stratigraphy - applications to hydrocarbon exploration. Tulsa, Oklahoma, American Association of Petroleum Geologists Memoir 26, pp.83-98.

van Keken, P. E., Ballentine, C. J., Porcelli, D., 2001. A dynamical investigation of the heat and helium imbalance. Earth Planet. Sci. Lett. 188, 421-434.

van Keken, P. E., Hacker, B. R., Syracuse, E. M., Abers, G. A., 2011. Subduction factory: 4. Depth-dependent flux of H_2O from subducting slabs worldwide. J. Geophys. Res.-Solid Earth 116, B01401, doi: 10.1029/2010jb007922.

Vlaar, N. J., Vankeken, P. E., Vandenberg, A. P., 1994. Cooling of the Earth in the Archean - consequences of pressure-release melting in a hotter mantle. Earth Planet. Sci. Lett. 121, 1-18.

Walker, J. A., Roggensack, K., Patino, L. C., Cameron, B. I., Matias, O., 2003. The water and trace element contents of melt inclusions across an active subduction zone. Contrib. Mineral. Petrol. 146, 62-77, doi: 10.1007/s00410-003-0482-x.

Wallace, P. J., 2005. Volatiles in subduction zone magmas: Concentrations and fluxes based on melt inclusion and volcanic gas data. J. Volcanol. Geotherm. Res. 140, 217-240, doi: 10.1016/j.jvolgeores.2004.07.023.

Windley, B. F., 1977. Timing of continental growth and emergence. Nature 270, 426-428.

Wise, D. U., 1974. Continental margins, freeboard and volumes of continents and oceans through time, in: A. E. M. Nairn and F. G. Stehli (Eds.), The geology of continental margins. Springer, New York, pp. 45-58.

Xu, X. Q., Lithgow-Bertelloni, C., Conrad, C. P., 2006. Global reconstructions of Cenozoic seafloor ages: Implications for bathymetry and sea level. Earth Planet. Sci. Lett. 243, 552-564, doi: 10.1016/j.epsl.2006.01.010.

Zachos, J., Pagani, M., Sloan, L., Thomas, E., Billups, K., 2001. Trends, rhythms, and aberrations in global climate 65 Ma to present. Science 292, 686-693.

Zimmer, M. M., Plank, T., Hauri, E. H., Yogodzinski, G. M., Stelling, P., Larsen, J., Singer, B., Jicha, B., Mandeville, C., Nye, C. J., 2010. The role of water in generating the calc-alkaline trend: New volatile data for Aleutian magmas and a new tholeiitic index. J. Petrol. 51, 2411-2444, doi: 10.1093/petrology/egq062.

Chapter 3: Heterogeneous upper mantle Ne, Ar and Xe isotopic compositions and a possible Dupal noble gas signature recorded in basalts from the Southwest Indian Ridge

[Parai, R., Mukhopadhyay, S., Standish, J. J., 2012. Heterogeneous upper mantle Ne, Ar and Xe isotopic compositions and a possible Dupal noble gas signature recorded in basalts from the Southwest Indian Ridge. *Earth and Planetary Science Letters* **359**, 227-239, doi: 10.1016/j.epsl.2012.10.017.]

ABSTRACT

Variations in heavy noble gas (Ne, Ar, Xe) isotopic compositions provide unique insights into the nature of heterogeneities in the mantle. However, few precise constraints on mantle source heavy noble gas isotopic compositions are available due to ubiquitous shallow-level atmospheric contamination. As a result, the extent of heterogeneity in mid-ocean ridge basalt (MORB) mantle source Ne, Ar and Xe isotopic compositions is unknown. Basalts from the ultra-slow spreading Southwest Indian Ridge (SWIR) between 7 and 25°E exhibit remarkable variability in He isotopic composition: SWIR $^{4}He/^{3}He$ spans half the total range observed in all mantle-derived basalts. Therefore, basalts from the SWIR provide a unique window into upper mantle heterogeneity and present an ideal opportunity to characterize variations in upper mantle heavy noble gas isotopic composition. Here we present new high-precision Ne, Ar and Xe isotopic compositions as well as He, CO_2, Ne, Ar and Xe abundances measured in basalt glasses from the SWIR. After correcting the measured values for shallow-level atmospheric contamination, significant and systematic variations in mantle source Ne, Ar and Xe

compositions are observed. We note that large variations in source $^{40}Ar/^{36}Ar$ and $^{129}Xe/^{130}Xe$ are observed in basalts removed from the influence of known hotspots, indicating a heterogeneous mid-ocean ridge basalt source. Thus, SWIR heavy noble gas data reveal a greater degree of source heterogeneity than is evident in the $^{4}He/^{3}He$ systematics alone. The observed heavy noble gas isotopic heterogeneities imply that the average MORB source $^{40}Ar/^{36}Ar$ and $^{129}Xe/^{130}Xe$ ratios are not yet well-determined.

Variation in MORB source $^{40}Ar/^{36}Ar$ and $^{129}Xe/^{130}Xe$ at a given $^{4}He/^{3}He$ and $^{21}Ne/^{22}Ne$ may reflect heterogeneous recycling of atmospheric Ar and Xe. In particular, we find low mantle source $^{40}Ar/^{36}Ar$ and $^{129}Xe/^{130}Xe$ ratios in the eastern region of the study area, which may reflect the noble gas signature of the Dupal mantle domain. Our observations require that the sampled mantle domain either is very ancient (>4.45 Ga) or has been metasomatized by subduction zone fluids carrying recycled atmospheric Ar and Xe. However, our Xe isotopic measurements indicate that differences between MORB and ocean island basalt (OIB) source noble gas compositions cannot be explained by recycling of atmospheric noble gases alone. Instead, a relatively undegassed mantle reservoir is required to account for OIB noble gases. The SWIR data demonstrate that the reservoir supplying primordial noble gases to mantle plumes differentiated from the MORB source early in Earth history, and the two reservoirs have not been homogenized over 4.45 Gyr of mantle convection.

2.1. INTRODUCTION

Noble gases provide unique constraints on the differentiation history of the Earth. The noble gases are chemically inert and are present in very low abundances in the mantle, such that variations in mantle source noble gas isotopic composition reflect degassing, regassing and nuclear processes such as radioactive decay and spontaneous fission of more abundant parent nuclides. A full complement of noble gas analyses on mantle-derived samples provides information about volatile cycling (Holland and Ballentine, 2006; Kendrick et al., 2011; Sumino et al., 2010), mass fluxes between mantle reservoirs (e.g., Gonnermann and Mukhopadhyay, 2009; O'Nions and Tolstikhin, 1996; Porcelli and Wasserburg, 1995; Tolstikhin and Marty, 1998), budgets of the heat-producing elements (U, Th and K), and constraints on early Earth differentiation based on the decay products of short-lived nuclides (^{244}Pu and ^{129}I; Allègre et al., 1987; Ballentine and Holland, 2008; Caffee et al., 1999; Kunz et al., 1998; Mukhopadhyay, 2012). Therefore, precise determination of mantle source noble gas abundances and isotopes in mid-ocean ridge basalts (MORBs) and ocean island basalts (OIBs) can provide powerful insights into the history, structure and dynamics of the Earth's interior.

Mantle He and Ne isotopic compositions reflect loss due to degassing and subsequent production of select nuclides by nuclear processes, since recycling of He and Ne is thought to be insignificant (Graham, 2002; Holland and Ballentine, 2006; Porcelli and Wasserburg, 1995). ^{4}He is produced by α-decay of U and Th, while ^{3}He is primordial. As a result, high ^{4}He/^{3}He ratios are generated by degassing and subsequent ingrowth of ^{4}He, and are commonly attributed to the presence of degassed recycled material with high (U+Th)/^{3}He in the source region. In contrast, low ^{4}He/^{3}He ratios

reflect a mantle source that has remained relatively undegassed and thus preserved low $(U+Th)/^{3}He$ over time. Among Ne isotopes, ^{20}Ne and ^{22}Ne are primordial, while ^{21}Ne is produced by nuclear reactions associated with U and Th decay ($^{18}O(\alpha,n)^{21}Ne$ and $^{24}Mg(n,\alpha)^{21}Ne$; Yatsevich and Honda, 1997; Wetherill, 1954), such that low source $^{21}Ne/^{22}Ne$ ratios reflect a relatively undegassed mantle reservoir. To first order, radiogenic He should be associated with nucleogenic Ne isotopic composition; however, mixing of mantle sources with different $^{3}He/^{22}Ne$ ratios may generate hyperbolic mixing arrays, complicating the expected relationship between He and Ne isotopes measured in basalts (e.g., Furi et al., 2010; Hanyu and Kaneoka, 1998; Kurz et al., 2005; Madureira et al., 2005; Moreira et al., 1995; Moreira et al., 2011; Parai et al., 2009; Shaw et al., 2001).

Mantle Ar and Xe isotopic compositions are interpreted with respect to nuclear processes, degassing and regassing, since recycling of atmospheric Ar and Xe at subduction zones may be significant (e.g., Holland and Ballentine, 2006; Kendrick et al., 2011; Sumino et al., 2010). ^{36}Ar and ^{38}Ar are primordial, while ^{40}Ar is produced by decay of ^{40}K by electron capture. Among Xe isotopes, ^{128}Xe and ^{130}Xe are primordial, ^{129}Xe was produced by the β-decay of the extinct nuclide ^{129}I ($t_{1/2}$ = 15.7 Ma), and $^{131,132,134,136}Xe$ are produced in characteristic relative proportions by spontaneous fission of both extinct ^{244}Pu ($t_{1/2}$ = 80.0 Ma) and extant ^{238}U ($t_{1/2}$ = 4.468 Gyr). Consequently, Xe isotopic compositions of mantle-derived basalts provide information about the timing and extent of mantle degassing and the differentiation of the early Earth (i.e., up to ~500 Ma after accretion; Allègre et al., 1987; Kunz et al., 1998; Mukhopadhyay, 2012; Pepin and Porcelli, 2002; Staudacher and Allegre, 1982; Yokochi and Marty, 2004).

The majority of noble gas studies of mantle-derived rocks have, however, focused on He and Ne isotopic measurements, as measurements of mantle Ar and Xe are complicated by low abundances and pervasive syn- to post-eruptive atmospheric contamination. Existing He isotopic measurements in mantle-derived rocks indicate distinct degassing histories for the mantle sources of OIBs and MORBs. Basalts erupted at ocean islands exhibit a wide range of $^4He/^3He$ ratios, from ~14,000 to170,000 ($^3He/^4He$ of 50 to 4.1 R_A; Graham et al., 1992; Moreira et al., 1999; Stuart et al., 2003). Basalts erupted at mid-ocean ridges exhibit a more limited range of He isotopic compositions. MORB He isotopes are generally discussed with respect to a narrow "canonical" MORB $^4He/^3He$ range of 80,000 to 100,000 ($^3He/^4He$ of 9 to 7 R_A). However, basalts from the ultra-slow spreading Southwest Indian Ridge (SWIR) from 7 to 25°E exhibit $^4He/^3He$ ratios from 48,300 to 120,000 (14.9 to 6.0 R_A; Georgen et al., 2003; Kurz et al., 1998; Standish, 2006), spanning half the range observed in OIBs. $^4He/^3He$ values above and below the canonical MORB range are found in basalts erupted in close proximity. Additionally, Georgen et al. (2003) observe a smooth spatial gradient in helium isotopic composition in the western half of the study area. The remarkable variability and spatial gradient in helium isotopic compositions suggest that the SWIR between 7 and 25°E affords a unique window into the nature and distribution of heterogeneities in the MORB source.

The extent of heterogeneity in MORB source Ar and Xe isotopic compositions is poorly constrained at present, as determinations of MORB source Ar and Xe isotopic compositions have been limited to a few very gas-rich samples (e.g., N. Atlantic popping rock 2ΠD43, Kunz et al., 1998; Moreira et al., 1998; Harding County well gases, Caffee

et al., 1999; Holland and Ballentine, 2006; Phinney et al., 1978; Staudacher, 1987). However, a number of studies have demonstrated that the heavy noble gases (Ne, Ar and Xe) provide information on the origin of mantle heterogeneities that may not be evident in He or lithophile isotope systematics alone (e.g., Hanyu et al., 2001; Harrison et al., 1999; Holland and Ballentine, 2006; Honda and McDougall, 1998; Honda and Woodhead, 2005; Kunz et al., 1998; Kurz et al., 2005; Moreira et al., 2011; Moreira et al., 1998; Mukhopadhyay, 2012; Parai et al., 2009; Sarda et al., 2000; Tucker et al., 2012; Yokochi and Marty, 2004). For example, Holland and Ballentine (2006) used primordial heavy noble gas isotopes (e.g., ^{36}Ar, ^{130}Xe) measured in continental well gases to demonstrate that the MORB source heavy noble gas abundance pattern is similar to seawater, and suggested that unradiogenic $^{40}Ar/^{36}Ar$ and $^{129}Xe/^{130}Xe$ in OIBs reflect preferential recycling of atmospheric heavy noble gases into the OIB source relative to the MORB source. In contrast, Mukhopadhyay (2012) used Ne, Ar and Xe isotope systematics in Icelandic basalt glass to demonstrate that the Iceland plume and MORB source Ar and Xe cannot be related to each other solely through preferential recycling of atmospheric volatiles. Rather, the MORB and Iceland sources must have differentiated early in Earth history and have not been homogenized by ≥4.45 Gyr of mantle convection Mukhopadhyay (2012). Thus, heavy noble gas systematics in mantle-derived samples can fundamentally improve our understanding of mantle evolution. In order to better constrain the extent and nature of heterogeneity in MORB source Ne, Ar and Xe isotopic compositions, we present new high-precision Ne, Ar and Xe isotopic compositions and abundances along with He and CO_2 abundances in a suite of basalt glasses from the SWIR between 7 and 25°E.

3.2. BACKGROUND AND METHODS

3.2.1 Sample background

Fourteen submarine basalt glass samples erupted along the SWIR between 7 and 25°E (Figure 3.1) were selected for heavy noble gas analysis. The samples were previously characterized for major element, trace element and radiogenic lithophile isotopic compositions (Kurz et al., 1998; Mahoney et al., 1992; Standish, 2006; Standish et al., 2008) as well as helium concentrations and isotopic composition (Georgen et al., 2003; Kurz et al., 1998; Standish, 2006). Samples from a single dredge located at the 7ºE ridge segment, adjacent to Bouvet Island, illustrate the lengthscale of helium isotopic heterogeneity at the SWIR: one sample exhibits $^{4}He/^{3}He$ within the canonical MORB range (96,400; Kurz et al., 1998), while two other samples from the same dredge exhibit low $^{4}He/^{3}He$ ratios (48,300 and 51,000; Kurz et al., 1998). In the center of the study area between the Shaka Fracture Zone (FZ) and 16°E, ridge orientation is highly oblique to the spreading direction, resulting in a low effective spreading rate (Standish et al., 2008). This part of the ridge is known as the Oblique Supersegment and is characterized by amagmatic accretionary ridge segments punctuated by two discrete magmatic segments (Dick et al., 2003) that erupt basalts with the most radiogenic $^{4}He/^{3}He$ ratios measured in the area (up to ~120,000; Standish, 2006; Table A3.1). Ridge orientation changes abruptly at the 16°E discontinuity, and the ridge is nearly orthogonal to the spreading direction between 16°E and the Dutoit FZ. A spatial gradient in helium isotopic composition is evident across the Orthogonal Supersegment, with $^{4}He/^{3}He$ decreasing smoothly from west to east over 630 km of ridge (Georgen et al., 2003).

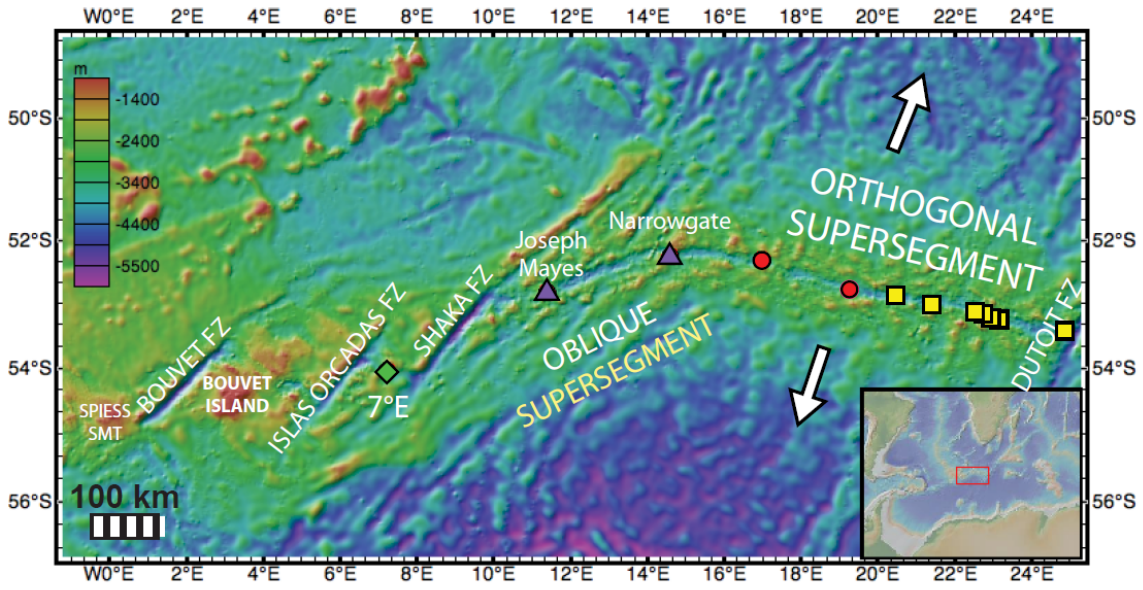

Figure 3.1: Map of the Southwest Indian Ridge study area. The study area is bounded in the west by the Islas Orcadas Fracture Zone (FZ) and by the Dutoit FZ in the east. Bouvet Island is located ~200 km west of the study area. Some samples from 7°E exhibit low $^4He/^3He$ ratios (~48,300; Kurz et al,. 1998). Other samples from 7°E exhibit $^4He/^3He$ ratios within the canonical MORB range (80,000 – 100,000). The Oblique Supersegment runs from 9 to 16°E. Basalts erupted at the Joseph Mayes and Narrowgate Seamounts have very radiogenic $^4He/^3He$ (up to ~120,000; Table A3.1). At the 16°E discontinuity, ridge orientation shifts such that spreading direction is nearly orthogonal to the ridge. The ~630 km long Orthogonal Supersegment exhibits $^4He/^3He$ ratios that vary smoothly from ~110,000 in the west to ~100,000 in the east (Georgen et al., 2003).

3.2.2 Analytical methods

Basalt glass was chipped from pillow lavas. Chips exhibiting light surface alteration were leached in dilute nitric acid for 10-15 minutes and ultrasonically cleaned. Clean glass chips were washed in acetone and dried. 2-5 g of glass were loaded into a stainless steel piston crusher, baked at ~90-100°C for 24 hours, and then pumped for an additional 7-14 days until blanks were low and stable. To release magmatic gases trapped in vesicles, samples were step-crushed under ultra-high vacuum using a hydraulic ram. CO_2 contents were measured by manometers attached directly to the crusher volume. Active gases were removed by sequential exposure to hot and cold SAES getters. The

noble gases were trapped on a cryogenic cold finger and sequentially released to the mass spectrometer volume. He, Ne, Ar and Xe abundances and Ne, Ar and Xe isotopic compositions were measured on a Nu Noblesse noble gas mass spectrometer operating in multicollection mode. Data were obtained over 2 years in 4 sets of measurements. For Ne, an automated liquid nitrogen trap was used to keep Ar and CO_2 blanks low, and corrections for isobaric interference from doubly-charged Ar and CO_2 were made. Ar^{++}/Ar^{+} for the 4 sets of SWIR analyses were 0.031 ± 0.003, 0.077 ± 0.003, 0.078 ± 0.003 and 0.061 ± 0.001; and CO_2^{++}/CO_2^{+} were 0.0045 ± 0.0005, 0.0055 ± 0.0003, 0.0079 ± 0.0006 and 0.0055 ± 0.0003. Procedural blanks were monitored during the step-crushing process. Blanks were stable and typically <1% of the measured sample ^{20}Ne signal, <0.5% of the measured sample ^{40}Ar signal and ~2% of the measured sample ^{130}Xe signal. All measured sample Ne, Ar and Xe isotope ratios reflect some degree of syn- to post-eruptive air contamination. Since blanks were low and statistically indistinguishable from air in isotopic composition, no blank corrections were made to the abundances or isotope ratios reported in Table A3.1. Each sample step-crush was bracketed by multiple air standard runs, which were used to calibrate sensitivity and mass discrimination as a function of signal size. A total of 1,280 heavy noble gas air standard runs were analyzed over the 2 year SWIR analytical campaign, with ~ 10^{-11} to 10^{-9} cc STP ^{20}Ne, ~10^{-9} to 10^{-8} cc STP ^{40}Ar and ~ 10^{-15} to 10^{-13} cc STP ^{130}Xe. Uncertainties in Ne, Ar and Xe isotope ratios for each step-crush are based on the reproducibility of air standards of comparable signal size analyzed within the same time period.

3.3. RESULTS

Fourteen samples were analyzed for He, Ne, Ar, Xe and CO_2 abundances, and Ne, Ar and Xe isotopic compositions. Multiple step-crush analyses were performed for each sample (3-23 steps per sample), giving a total of 169 SWIR analyses. The results are reported in Appendix 2, Table A3.1 and discussed below.

3.3.1 CO_2– Helium systematics

For each sample, individual crushing steps define a linear array in CO_2 - ^{3}He space, which we use to calculate a $CO_2/^3$He ratio using a robust linear least squares fit (Figure A2.1). Following Marty and Tolstikhin (1998), this ratio is corrected for degassing following a Rayleigh fractionation law constrained by ^{4}He/^{40}Ar* ratios (where ^{40}Ar* denotes radiogenic mantle-derived ^{40}Ar):

$$\left(\frac{CO_2}{^3He}\right)_i = \left(\frac{CO_2}{^3He}\right)_{measured} \times \left(\frac{\left(\frac{^4He}{^{40}Ar^*}\right)_{measured}}{\left(\frac{^4He}{^{40}Ar^*}\right)_i} \right)^{\left[\frac{1-\left(K_{He}/K_{CO_2}\right)}{1-\left(K_{He}/K_{Ar}\right)}\right]} \qquad \text{Eq. 3.1}$$

where $(^4\text{He}/^{40}\text{Ar}^*)_i$ is the mantle source ^{4}He/^{40}Ar ratio of 2.5 and K denotes a solubility coefficient ($K_{Ar} = 2.6 \times 10^{-12}$ mol/g, $K_{CO2} = 9.0 \times 10^{-12}$ mol/g, $K_{He} = 2.5 \times 10^{-11}$ mol/g; Marty and Tolstikhin, 1998 and references therein). The magnitude of the degassing correction is uncertain for samples with near-atmospheric ^{40}Ar/^{36}Ar (such as KN162-9 33-49); however, we note that the measured $CO_2/^3$He for KN162-9 33-49 itself is strikingly high (2.2×10^{10}), and correction for magmatic degassing only raises $CO_2/^3$He (since $K_{CO2} < K_{He}$; see Figure A2.1). It is possible that this sample's measured ratio has been affected by assimilation of seawater. However, even if KN162-9 33-49 is ignored, the $CO_2/^3$He ratios in primary SWIR melts vary from 4.8×10^8 to 8.4×10^9 (Table 3.1)

and thus reach values far in excess of the estimated average N-MORB value of ~1-2 $\times 10^9$ (Marty and Tolstikhin, 1998).

3.3.2 Measured Ne, Ar, Xe compositions

We measure $^{20}Ne/^{22}Ne$ values up to 12.41 ± 0.02 (1σ), and $^{21}Ne/^{22}Ne$ ratios up to 0.0653 ± 0.0010 (1σ), among the highest isotopic excesses with respect to atmosphere ($^{20}Ne/^{22}Ne$ = 9.80, $^{21}Ne/^{22}Ne$ = 0.0290) measured in MORBs (Table A3.1). Measured $^{40}Ar/^{36}Ar$ values vary up to 28,500 ± 290 (1σ). The highest measured isotopic ratio in $^{129}Xe/^{130}Xe$ is 7.71 ± 0.11 (1σ), which is comparable to the highest value measured in the popping rock 2ΠD43 ($^{129}Xe/^{130}Xe$ = 7.73 ± 0.23; Moreira et al., 1998) and in Equatorial Atlantic MORBs ($^{129}Xe/^{130}Xe$ = 7.81 ± 0.06; Tucker et al., 2012).

3.4. SOURCE Ne, Ar AND Xe ISOTOPIC COMPOSITIONS CORRECTED FOR SYN- TO POST-ERUPTIVE ATMOSPHERIC CONTAMINATION

Variable syn- to post-eruptive air contamination affects all measurements of Ne, Ar and Xe in mantle-derived rocks (e.g., Ballentine and Barfod, 2000; Sarda et al., 1985), such that measured values represent mixing between the mantle source isotopic composition and the atmospheric composition. Corrections for syn- to post-eruptive air contamination are required to accurately characterize mantle sources and interpret differences between mantle reservoirs. Variations in maximum measured Ar isotopic values have been discussed as indicative of source Ar isotopic heterogeneity (e.g., Sarda et al., 1999); however, maximum measured values may also reflect the degree of atmospheric contamination, which vary randomly or as a function of eruption depth (e.g.,

Burnard, 1999). Therefore, variations in maximum measured values need not accurately reflect heavy noble gas isotope systematics in mantle sources.

Well-defined arrays in $^{20}Ne/^{22}Ne$-$^{21}Ne/^{22}Ne$, $^{40}Ar/^{36}Ar$-$^{20}Ne/^{22}Ne$ and $^{129}Xe/^{130}Xe$-$^{40}Ar/^{36}Ar$ spaces allow us to determine mantle source isotopic compositions by least-squares fitting and extrapolation to a mantle $^{20}Ne/^{22}Ne$ value. We use a $^{20}Ne/^{22}Ne$ value of 12.5 for the MORB source (Holland and Ballentine, 2006; Ballentine and Holland, 2008; Raquin et al., 2008), though correcting to the solar wind composition ($^{20}Ne/^{22}Ne$ of 13.8) would not alter our conclusions. Correction for air contamination is a total least-squares linear extrapolation for mantle $^{21}Ne/^{22}Ne$ (Figure 3.2), and a total least-squares hyperbolic extrapolation for mantle $^{40}Ar/^{36}Ar$ (Figure 3.3). The extrapolated mantle $^{40}Ar/^{36}Ar$ can then be used in a total least-squares hyperbolic extrapolation for mantle $^{129}Xe/^{130}Xe$ (Figure 3.4). Extrapolations are only performed for samples with well-defined mixing arrays. We note that AG22 1-1 and 1-4 overlap in every isotope space; these are likely to sample a single flow and are therefore considered together for extrapolation. Below we discuss SWIR mantle source Ne, Ar and Xe isotopic compositions corrected for the effects of shallow air contamination.

3.4.1 Mantle source neon isotopic compositions

For each SWIR sample, step-crushes define a linear array trending towards the atmospheric composition that reflects variable degrees of atmospheric contamination in $^{20}Ne/^{22}Ne$-$^{21}Ne/^{22}Ne$ space. To correct for air contamination, the data are translated to fix the atmospheric composition at the origin and a total least-squares fit of the form $y = mx$ (to force the fit through air) is determined by minimizing χ^2 given errors in both variables

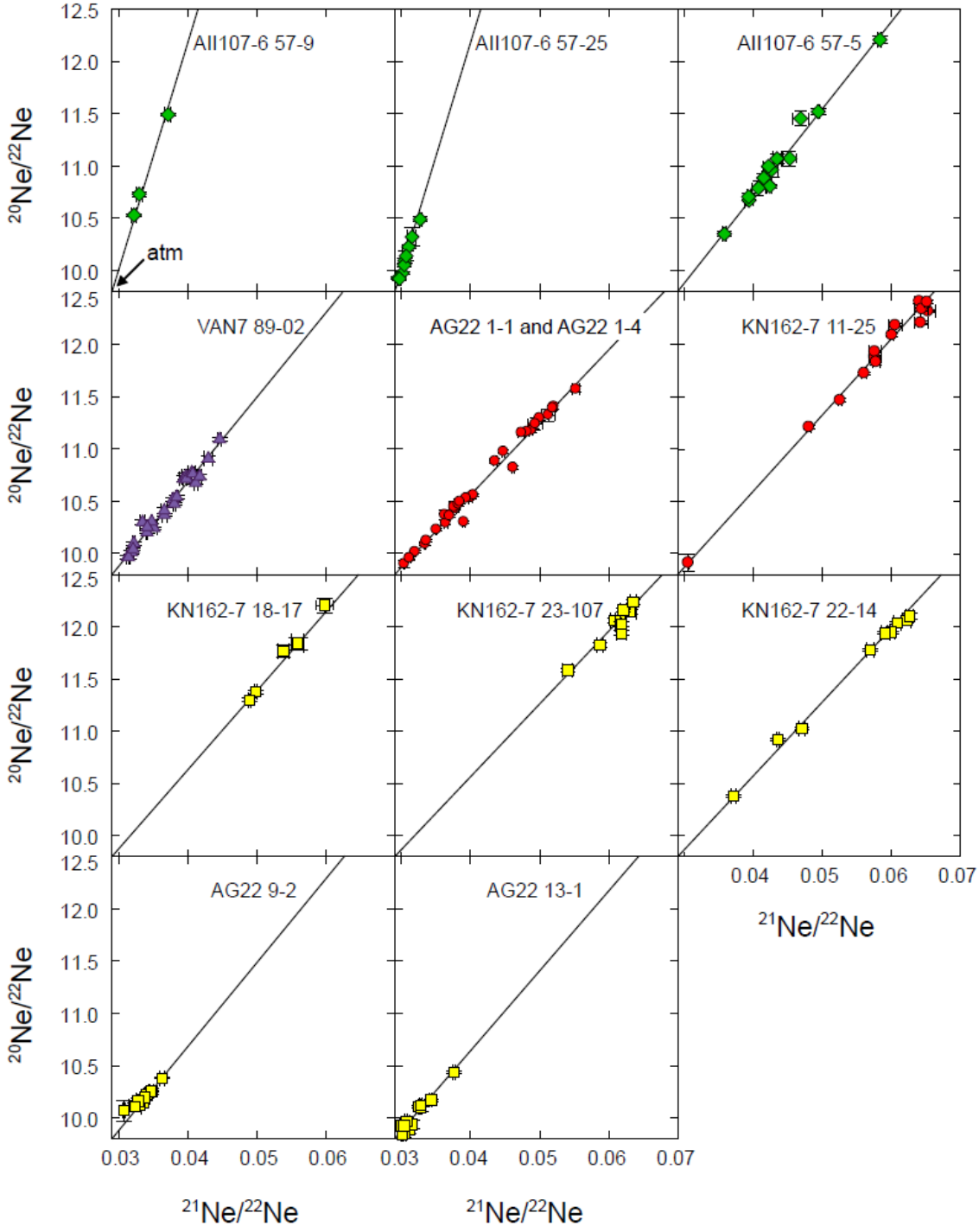

Figure 3.2. Correction for syn- to post-eruptive atmospheric contamination of Ne. For each sample, step-crushing generates a linear array reflecting variable degrees of atmospheric contamination. Each sample is corrected for air contamination by total least squares regression (Section 3.4.1) and extrapolation to determine the source $^{21}Ne/^{22}Ne_{(E)}$ at a mantle $^{20}Ne/^{22}Ne$ of 12.5.

(after York, 1969). Uncertainties in the slopes are determined by Monte Carlo error analysis: for each sample, data are randomly resampled from within the bivariate normal distributions associated with each data point, and the least-squares fit is recomputed using the new values. Well-defined slopes allow us to determine extrapolated mantle source $^{21}Ne/^{22}Ne_{(E)}$ at $^{20}Ne/^{22}Ne = 12.5$ with high precision (Figure 3.2; extrapolations are not performed for samples KN162-7 14-7 and KN162-9 33-49, since all crushing steps are close to atmospheric in composition). The extrapolated mantle source Ne compositions range from $^{21}Ne/^{22}Ne_{(E)} = 0.0414 \pm 0.0020$ (1σ) at 7ºE to $^{21}Ne/^{22}Ne_{(E)} = 0.0680 \pm 0.0004$ (1σ) at the western Orthogonal Supersegment (Table 3.1).

3.4.2 Mantle source argon isotopic compositions

Air contamination generates hyperbolic trends in $^{40}Ar/^{36}Ar$ – $^{20}Ne/^{22}Ne$ space. A best-fit hyperbola reflecting two-component mixing between air and mantle is determined using a total least-squares hyperbolic fit. The curvature of a two-component mixing hyperbolic array is parameterized as $k = (^{36}Ar/^{22}Ne)_{mantle}/(^{36}Ar/^{22}Ne)_{atm}$. We use a grid search to find the combination of k and mantle $^{40}Ar/^{36}Ar$ (corresponding to a mantle $^{20}Ne/^{22}Ne$ of 12.5) that minimizes the χ^2 cost function (Equation 3.2):

$$\chi^2 = \sum_{i=1}^{N} \left[\left(\frac{x_i - m_i}{\sigma_{xi}} \right)^2 + \left(\frac{y_i - n_i}{\sigma_{yi}} \right)^2 \right] \qquad \text{Eq.3.2}$$

where $(x_i \pm \sigma_{xi}, y_i \pm \sigma_{yi})$ are the N observed data points for a given sample and (m_i, n_i) are the σ–normalized closest points to the data along a candidate hyperbola (i.e., the points that minimize χ^2 for the candidate hyperbola). Since there are two free parameters in the

Table 3.1 SWIR mantle source He, CO_2, Ne, Ar, Xe compositions

Sample	Longitude	$^4He/^3He$	$CO_2/^3He$ ($x10^8$)	$^{21}Ne/^{22}Ne_{(E)}$	1σ	$^{40}Ar/^{36}Ar_{(E)}$	1σ		$^{129}Xe/^{130}Xe_{(E)}$	1σ	
AII 107-6 57-5	7.260	96400[a]	29	0.0614	0.0006	23700	+3400	-2400	6.89	+0.39	-0.14
AII 107-6 57-9	7.260	48300[a]	7.2	0.0414	0.0019	12200	+1600	-1100	7.49[e]		-0.68
AII 107-6 57-25	7.260	51000[a]	11	0.0424	0.0017	n.d.			n.d.		
KN162-9 33-49	11.387	120000[b]	370	n.d.		n.d.			n.d.		
VAN7 89-02	14.598	119000[c]	84	0.0624	0.0005	n.d.			n.d.		
AG22 1-1 & 1-4	16.980	108000[c]	16	0.0680	0.0004	49300	+6000	-4600	7.57	+0.18	-0.14
KN162-7 11-25	19.200	104000[b]	9.8	0.0661	0.0004	43400	+1800	-1800	7.80	+0.10	-0.10
KN162-7 14-7	20.398	104000[b]	21	n.d.		n.d.			n.d.		
KN162-7 18-17	21.406	102000[b]	8.3	0.0647	0.0007	23600	+2600	-1700	n.d.		
KN162-7 23-107	22.547	98900[b]	5.7	0.0678	0.0005	27200	+2300	-1700	n.d.		
KN162-7 22-14	22.647	102000[b]	11	0.0672	0.0005	20500[d]			7.10	+0.04	-0.02
AG22 9-2	22.880	99500[b]	4.8	0.0627	0.0013	n.d.			n.d.		
AG22 13-1	24.758	99000[b]	10	0.0643	0.0011	29200	+11900	-5900	7.19	+0.12	-0.09

1σ uncertainties reported for $^{40}Ar/^{36}Ar_{(E)}$ and $^{129}Xe/^{130}Xe_{(E)}$ are 68.3% confidence limits (Section 3.4.2). 'n.d.' = not determined.

[a] Kurz et al. (1998)

[b] Standish (2006)

[c] this study

[d] The $^{40}Ar/^{36}Ar_{(E)}$ confidence interval for KN162-7 22-14 is not well-determined (see Figure A3.2)

[e] The upper bound on the $^{129}Xe/^{130}Xe_{(E)}$ confidence interval for AII107-6 57-9 is not well-determined (see Figure A3.3)

hyperbolic fit (k and mantle $^{40}Ar/^{36}Ar$), the 68.3% confidence interval on the mantle $^{40}Ar/^{36}Ar$ (Table 3.1) is where $\chi^2 \leq \chi^2_{min} + 2.30$ (Press et al., 1992; see Figure A3.2).

For some samples, scatter in the mixing array is much larger than the analytical uncertainties and likely reflects the influence of a second elementally-fractionated air component. Three-component mixing between mantle and two atmospheric components with distinct $^{36}Ar/^{22}Ne$ ratios would generate an array of measured values constrained to lie within a crescent or lens-shaped region. Random sampling of data from within such a region would not necessarily provide a good constraint on the mantle endmember $^{40}Ar/^{36}Ar$. Therefore, we restrict our extrapolations to samples with relatively well-defined hyperbolic mixing arrays (8 extrapolations; Figure 3.3). Such hyperbolic arrays are likely to reflect either a single atmospheric contaminant or two elementally-fractionated atmospheric contaminants present in nearly fixed proportions. Mantle $^{40}Ar/^{36}Ar_{(E)}$ values range from $12{,}200^{+1600}_{-1100}$ at 7ºE to $49{,}300^{+6000}_{-4600}$ in the western Orthogonal Supersegment (Table 3.1).

3.4.3 Mantle source xenon isotopic compositions

Air contamination generates hyperbolic trends in $^{129}Xe/^{130}Xe$ – $^{20}Ne/^{22}Ne$ and $^{129}Xe/^{130}Xe$ – $^{40}Ar/^{36}Ar$ space. Best-fit hyperbolae reflecting two-component mixing between atmosphere and mantle are determined as described in Section 3.4.2. The fits yield extrapolated mantle source $^{129}Xe/^{130}Xe_{(E)}$ values at the mantle $^{40}Ar/^{36}Ar_{(E)}$ values determined above (6 extrapolations; Figure 3.4). Since the best fits have pronounced concave-down curvatures, the extrapolated $^{129}Xe/^{130}Xe_{(E)}$ is only weakly sensitive to uncertainty in the mantle $^{40}Ar/^{36}Ar_{(E)}$; therefore, the 68.3% confidence limits on

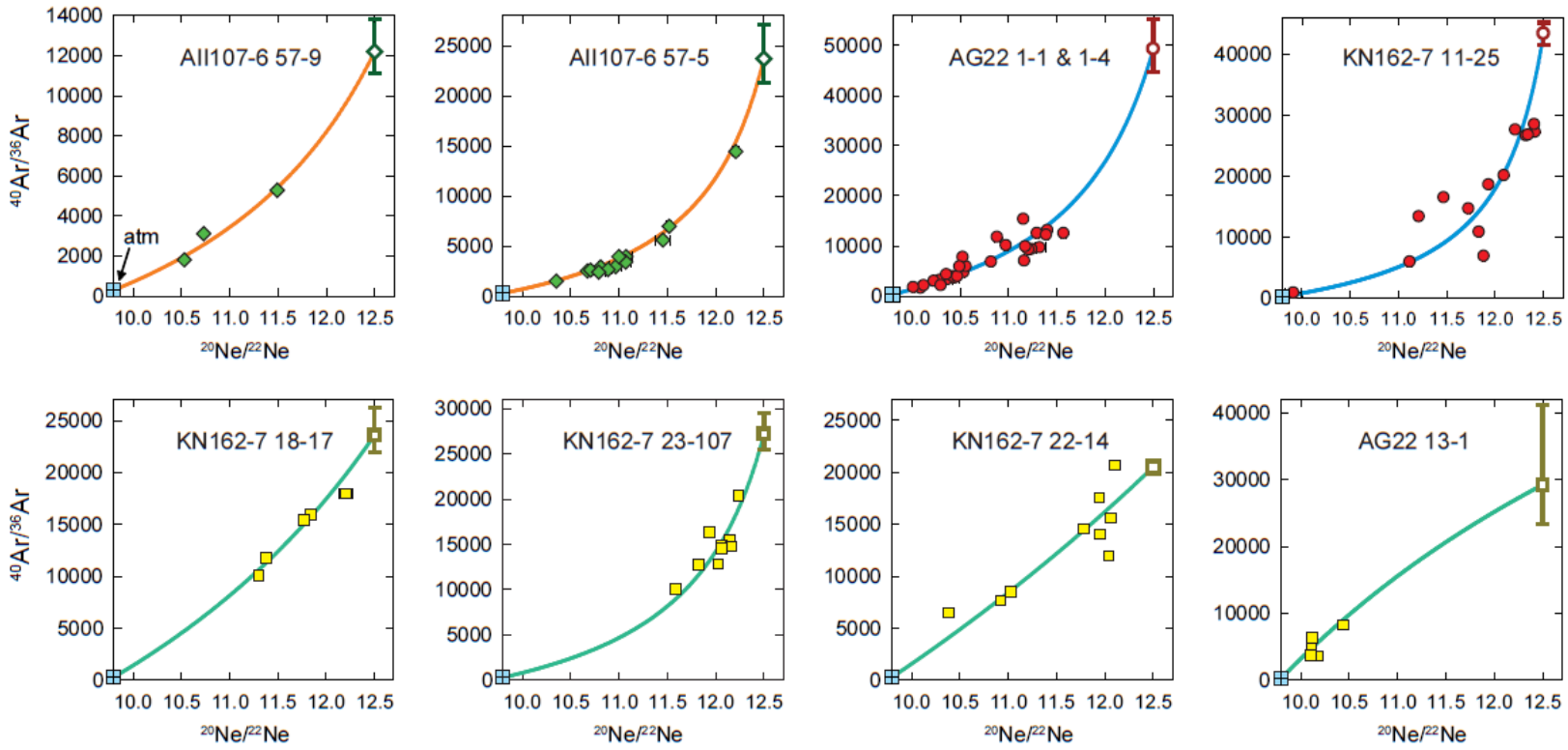

Figure 3.3: Correction for syn- to post-eruptive atmospheric contamination to determine mantle source $^{40}Ar/^{36}Ar$. For each sample, step-crushing generates an array reflecting variable degrees of atmospheric contamination. For samples with well-defined hyperbolic mixing arrays in $^{40}Ar/^{36}Ar$ – $^{20}Ne/^{22}Ne$ space, best fit hyperbolae yield extrapolated mantle $^{40}Ar/^{36}Ar_{(E)}$ at $^{20}Ne/^{22}Ne$ = 12.5. AG22 1-1 and AG22 1-4 were brought up in the same dredge and therefore could sample the same flow. Since major element compositions (Standish, 2006) and isotopic compositions in all heavy noble gas spaces were nearly identical, we considered AG22 1-1 and 1-4 together to better constrain the hyperbolic fits.

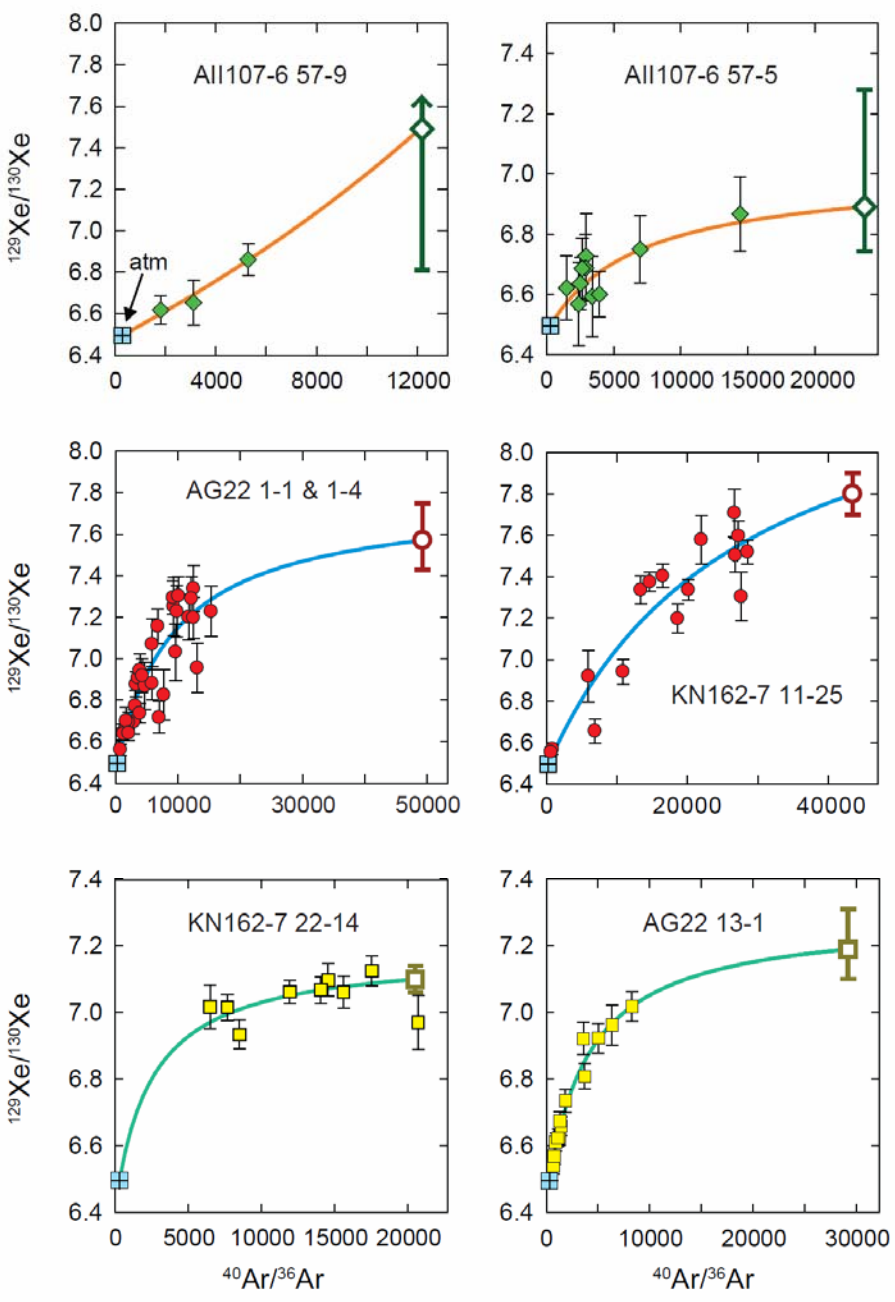

Figure 3.4: Correction for syn- to post-eruptive atmospheric contamination to determine mantle source $^{129}Xe/^{130}Xe$. For each sample, step-crushing generates an array reflecting variable degrees of atmospheric contamination. For samples with well-defined hyperbolic mixing arrays in $^{129}Xe/^{130}Xe$ – $^{40}Ar/^{36}Ar$ space, best fit hyperbolae yield extrapolated mantle $^{129}Xe/^{130}Xe_{(E)}$ at the $^{40}Ar/^{36}Ar_{(E)}$ determined in Figure 3.3. Mixing arrays in $^{20}Ne/^{22}Ne$ – $^{129}Xe/^{130}Xe$ space exhibit more scatter, but are in good agreement with $^{129}Xe/^{130}Xe$ – $^{40}Ar/^{36}Ar$ results. Three data points with sub-atmospheric $^{129}Xe/^{130}Xe$ in AII107-6 57-5 were excluded from the fit. The upper limit of the 68.3% confidence interval for AII107-6 57-9 is poorly constrained and is thus depicted by an upward arrow.

$^{129}Xe/^{130}Xe_{(E)}$ are given assuming the best $^{40}Ar/^{36}Ar_{(E)}$. Mantle $^{129}Xe/^{130}Xe_{(E)}$ values range from $6.89^{+0.39}_{-0.19}$ to 7.80±0.10 (Table 3.1).

3.5. DISCUSSION

The SWIR between 7°E and 25°E is comprised of four compositionally distinct regions: the 7°E ridge segment, the Oblique Supersegment, the western Orthogonal Supersegment and the Eastern Orthogonal Supersegment. Below we discuss the noble gas isotopic systematics observed in the study area and investigate the nature of MORB source noble gas heterogeneity. We then evaluate SWIR Xe isotope systematics and discuss the implications for early mantle differentiation. SWIR Xe fission isotopes and relationships between noble gases and major and trace element ratios will be discussed elsewhere.

3.5.1 Variations in MORB source composition along the SWIR from 7 to 25°E

We observe remarkable and systematic variability in heavy noble gas isotopic composition across the ~1100 km-wide study area (Figures 3.5-3.7). Figure 3.5 illustrates systematic variations in mantle source $CO_2/^3He$ and Ne, Ar and Xe isotopic compositions as a function of longitude. Extremely high $CO_2/^3He$ ratios are observed at the Oblique Supersegment (Figure 3.5a; 3.7×10^{10}), far in excess of the mean values estimated for N-MORB and E-MORB (~1 and ~4×10^9, respectively; Marty and Tolstikhin, 1998). Across the Orthogonal Supersegment, we observe considerable variation in source Ne, Ar and Xe isotopic compositions over a short distance (~600 km). A broad spatial gradient is present in $^{21}Ne/^{22}Ne_{(E)}$, $^{40}Ar/^{36}Ar_{(E)}$ and $^{129}Xe/^{130}Xe_{(E)}$ (Figure 3.5), though sample

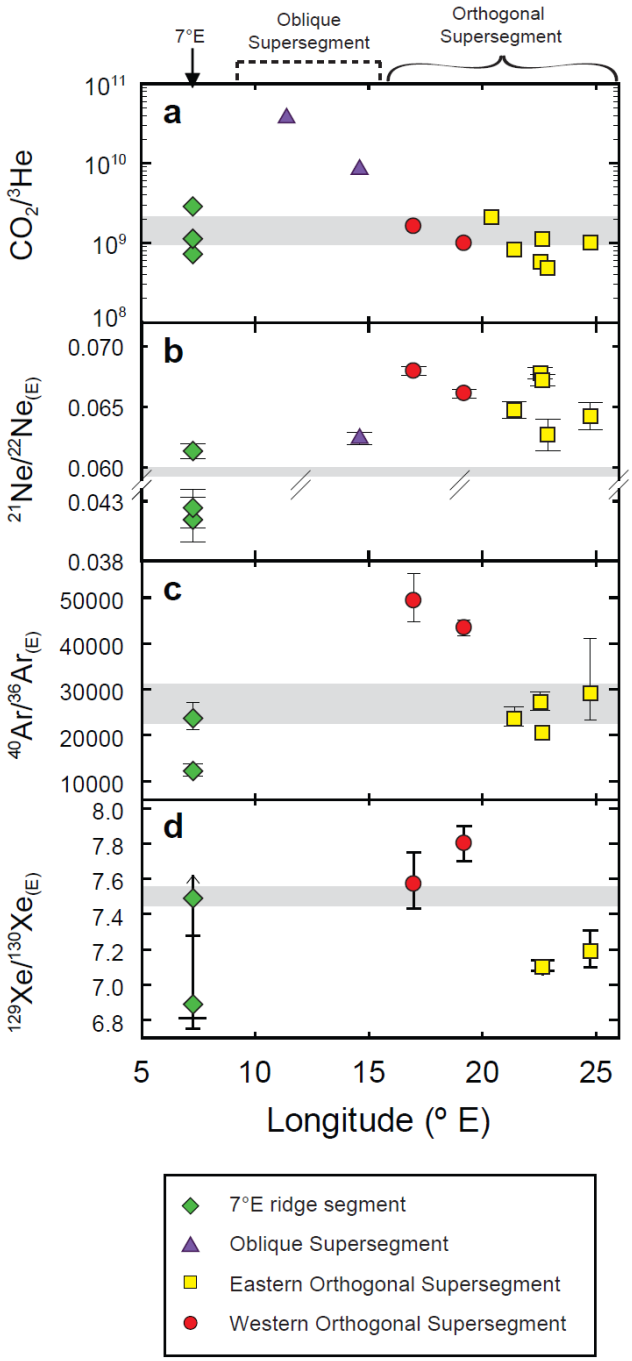

Figure 3.5: Mantle source $CO_2/^3He$, Ne, Ar and Xe isotopic variations with longitude along the SWIR from 7°E to 25°E. Shaded band indicates the source composition of average N-MORB (panel a) and N. Atlantic popping rock 2ΠD43 (panels b-d; Moreira et al., 1998; Raquin et al., 2008). (a) $CO_2/^3He$ corrected for degassing following a Rayleigh fractionation law (see Section 3.3.1) is plotted on a logarithmic scale against longitude. $CO_2/^3He$ in basalts from 7°E and the Orthogonal Supersegment scatter around typical N-MORB values of ~1 × 10^9 (indicated by a dashed line). A large anomaly in $CO_2/^3He$ is observed at the Oblique Supersegment. (b) Mantle source $^{21}Ne/^{22}Ne_{(E)}$ vs. longitude. Along the Orthogonal Supersegment, $^{21}Ne/^{22}Ne_{(E)}$ broadly decreases from west to east.

Figure 3.5 (continued) (c) Mantle source $^{40}Ar/^{36}Ar_{(E)}$ vs. longitude. A broad gradient in $^{40}Ar/^{36}Ar_{(E)}$ is evident across the Orthogonal Supersegment. (d) Mantle source $^{129}Xe/^{130}Xe_{(E)}$ vs. longitude. Fewer samples are plotted here since mixing hyperbolae for some samples were poorly-constrained. Two distinct groupings are also evident in $^{129}Xe/^{130}Xe_{(E)}$ along the Orthogonal Supersegment: a relatively radiogenic group in the west and a less-radiogenic group in the eastern half of the supersegment.

coverage across the Orthogonal Supersegment is not as dense as for $^{4}He/^{3}He$ (Georgen et al., 2003).

Figure 3.6 illustrates He-Ne, He-Ar and Ne-Ar systematics in SWIR mantle sources, with N. Atlantic popping rock 2ΠD43 (Moreira et al., 1998), Equatorial Atlantic depleted MORB (Tucker et al., 2012), Bravo Dome continental well gas source (Holland and Ballentine, 2006) and DICE (Trieloff et al., 2000; Mukhopadhyay, 2012) included for reference. We find a broad positive correlation between SWIR source He, Ne and Ar isotopic compositions, and SWIR source co-variations are consistent with the differences between the relatively undegassed DICE source and the N. Atlantic MORB source. The low $^{4}He/^{3}He$ samples from 7°E are similar to DICE in all panels. We note that Eastern Orthogonal Supersegment source values are more radiogenic in He and more nucleogenic in Ne than the N. Atlantic source, but are low or comparable in $^{40}Ar/^{36}Ar_{(E)}$.

Figure 3.7 shows He-Xe, Ne-Xe and Ar-Xe systematics in the same samples. Relatively low $^{4}He/^{3}He$, $^{21}Ne/^{22}Ne_{(E)}$ and $^{40}Ar/^{36}Ar_{(E)}$ in the Eastern Orthogonal Supersegment are associated with $^{129}Xe/^{130}Xe_{(E)}$ that are low (~7.1) compared to 2ΠD43 and approaching $^{129}Xe/^{130}Xe_{(E)}$ for DICE. On the other hand, western Orthogonal Supersegment source $^{129}Xe/^{130}Xe_{(E)}$ ratios range from ~7.6 – 7.8, slightly higher than the value of ~7.6 in 2ΠD43 (Moreira et al., 1998) and within the range of 7.9±0.14 for the mantle source of continental well gas (Holland and Ballentine, 2006). Significantly, the

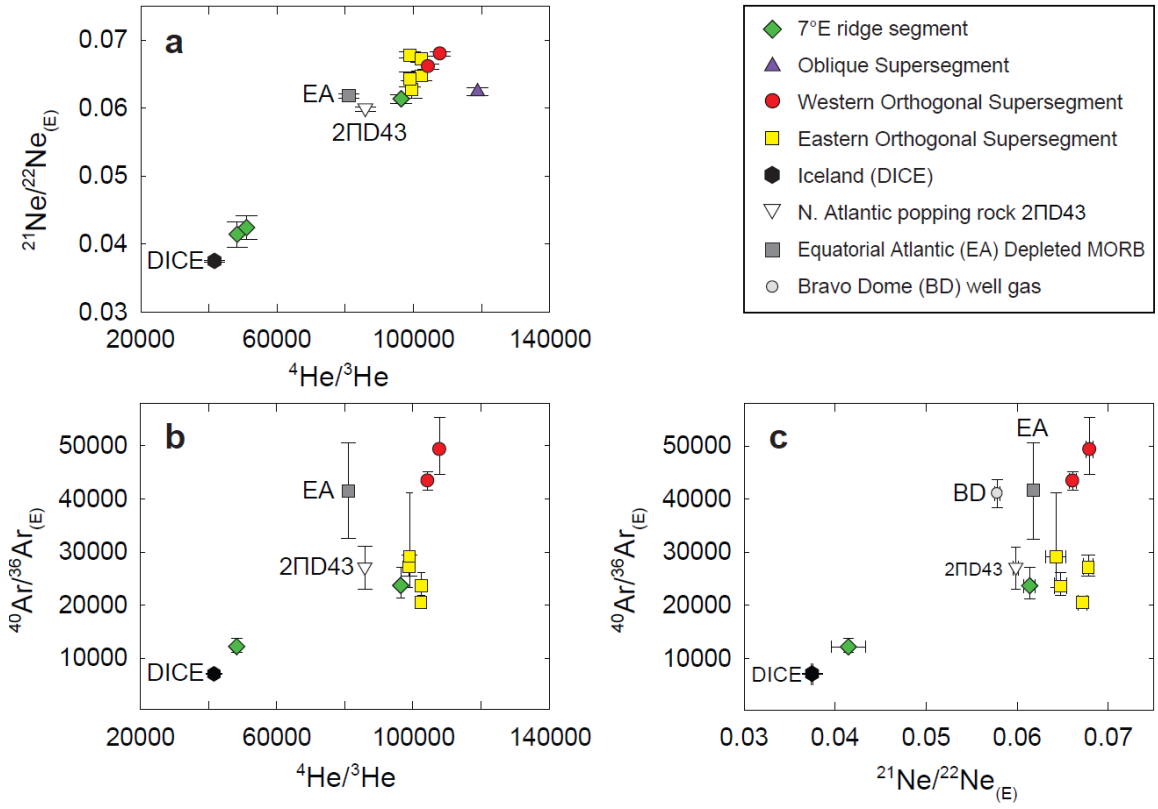

Figure 3.6: (a) He-Ne, (b) He-Ar and (c) Ne-Ar systematics in SWIR mantle sources. SWIR mantle source He, Ne and Ar isotopic compositions behave coherently, such that low $^{4}He/^{3}He$ ratios are associated with low $^{21}Ne/^{22}Ne_{(E)}$ and low $^{40}Ar/^{36}Ar_{(E)}$, and high $^{4}He/^{3}He$ ratios are associated with high $^{21}Ne/^{22}Ne_{(E)}$ and high $^{40}Ar/^{36}Ar_{(E)}$. N. Atlantic popping rock 2ΠD43 (Moreira et al., 1998; Raquin et al., 2008), equatorial Atlantic depleted MORB (Tucker et al., 2012), Bravo Dome continental well gas source (Holland and Ballentine, 2006) and the Icelandic glass DICE (Mukhopadhyay, 2012; Trieloff et al., 2000) are included for comparison. He-Ne-Ar systematics indicate the influence of a reservoir that is relatively undegassed compared to the N. Atlantic popping rock source and similar to the Iceland source, as well as at least two reservoirs that are degassed relative to the popping rock source. Eastern Orthogonal Supersegment source values are more radiogenic in He and more nucleogenic in Ne than the popping rock source, but are low or comparable in $^{40}Ar/^{36}Ar_{(E)}$.

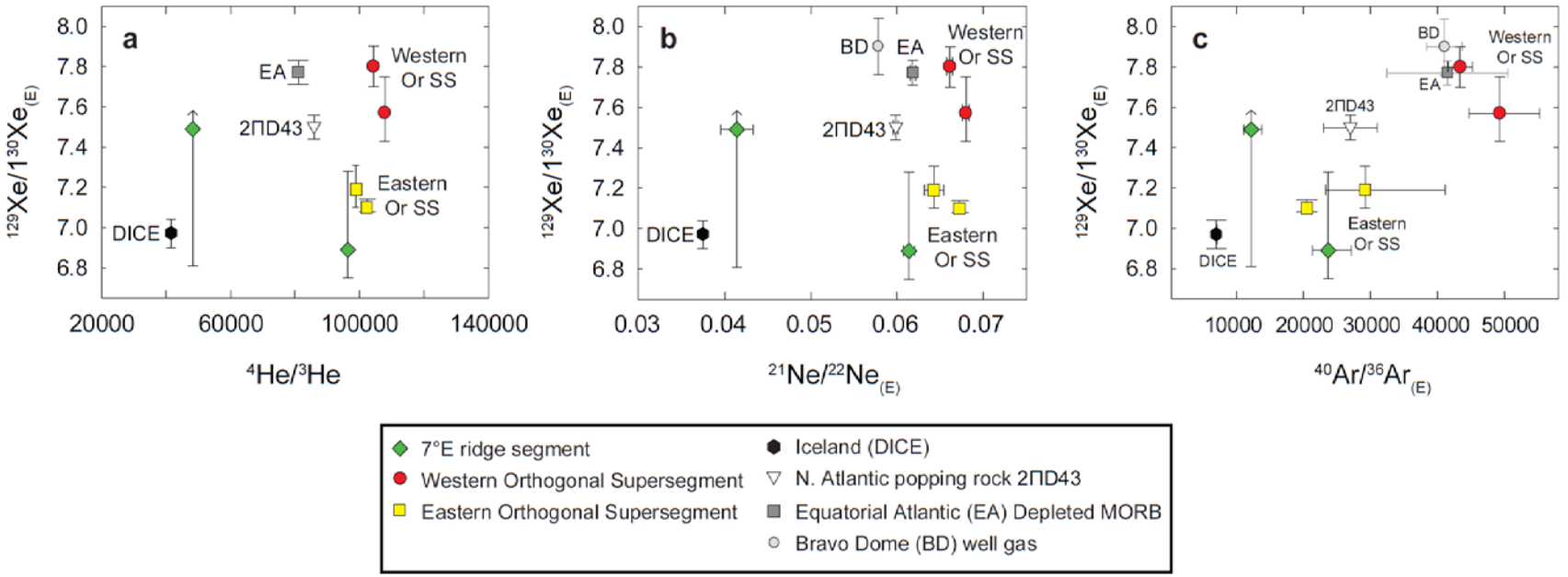

Figure 3.7: (a) He-Xe, (b) Ne-Xe and (c) Ar-Xe systematics in SWIR mantle sources. N. Atlantic popping rock 2ΠD43 (Moreira et al., 1998; Raquin et al., 2008), equatorial Atlantic depleted MORB (Tucker et al., 2012), Bravo Dome continental well gas source (Holland and Ballentine, 2006) and the Icelandic glass DICE (Mukhopadhyay, 2012; Trieloff et al., 2000) are included for comparison. The western and Eastern Orthogonal Supersegments are clearly distinct in $^{129}Xe/^{130}Xe_{(E)}$, and large variations in Orthogonal Supersegment $^{129}Xe/^{130}Xe_{(E)}$ are associated with limited variations in He and Ne isotopic composition. Low $^{129}Xe/^{130}Xe_{(E)}$ in the Eastern Orthogonal Supersegment group is paired with intermediate $^{40}Ar/^{36}Ar_{(E)}$ (panel c). The low $^{4}He/^{3}He$ sample from 7°E is characterized by intermediate $^{129}Xe/^{130}Xe_{(E)}$, although the extrapolation is based on only three data points (Figure 3.4) and the upper limit uncertainty is poorly constrained. We note that the AII 107-6 57-5 sample from 7°E with a $^{4}He/^{3}He$ ratio of 96,400 plots with the Eastern Orthogonal Supersegment samples in all noble gas isotope spaces (also see Figure 3.6).

magnitude of variation in Orthogonal Supersegment $^{40}Ar/^{36}Ar_{(E)}$ and $^{129}Xe/^{130}Xe_{(E)}$ is much larger than the relative variation in $^{4}He/^{3}He$ and $^{21}Ne/^{22}Ne_{(E)}$ (Figures 3.6, 3.7). Low source $^{40}Ar/^{36}Ar_{(E)}$ and $^{129}Xe/^{130}Xe_{(E)}$ at the Eastern Orthogonal Supersegment may be related to recycling of atmospheric Ar and Xe (see Section 3.5.3.3-3.5.3.4). We note that the sample from 7°E with the $^{4}He/^{3}He$ ratio of 96,400 (Table 3.1) groups with the Eastern Orthogonal Supersegment in all isotope spaces (Figures 3.6, 3.7).

3.5.2 A heterogeneous MORB source mantle in heavy noble gas isotopes

Lithophile isotopic variations in mantle sources are often interpreted with respect to a set of theoretical endmember components, such as the depleted MORB mantle (DMM), HIMU, EMI and EMII (enriched mantles I and II). These theoretical endmember compositions are based on compiled lithophile isotopic measurements of mantle-derived rocks (e.g., Hart et al., 1992; Zindler and Hart, 1986; Zindler et al., 1982). Given the scarcity of precise heavy noble gas isotopic data exhibiting clear excesses from air, the magnitude of variation in mantle source heavy noble gas isotopic composition and the specific signatures associated with established mantle endmember components are poorly constrained. However, the variability in source Ne, Ar and Xe isotopic compositions we observe along the SWIR Orthogonal Supersegment (Figures 3.5-3.7) indicates that the MORB source is heterogeneous in heavy noble gas isotopic composition. Significant variation in Orthogonal Supersegment MORB source Ne, Ar and Xe exist independent of any known hotspot influence: $^{21}Ne/^{22}Ne_{(E)}$ varies from 0.0627 ± 0.0013 to 0.0680 ± 0.0004, $^{40}Ar/^{36}Ar_{(E)}$ from 20,500 to $49{,}300^{+6000}_{-4600}$ and $^{129}Xe/^{130}Xe_{(E)}$ from $7.10^{+0.04}_{-0.02}$ to 7.80 ± 0.10 (Figures 3.5-3.7). We note that our argument

for particularly large variation in MORB source $^{129}Xe/^{130}Xe$ is independent of the hyperbolic extrapolations: step-crushing data from KN162-7 22-14 in the Eastern Orthogonal Supersegment indicate that $^{129}Xe/^{130}Xe$ values asymptote with respect to $^{40}Ar/^{36}Ar$ at $^{129}Xe/^{130}Xe$ of ~7.1, significantly lower than measured values of up to 7.71 ± 0.11 in the western Orthogonal Supersegment (Figure 3.4). Therefore, the large variation in Orthogonal Supersegment source $^{129}Xe/^{130}Xe_{(E)}$ is robust.

We observe ~20%, 70% and 80% of the total mantle variation in $^{21}Ne/^{22}Ne_{(E)}$, $^{40}Ar/^{36}Ar_{(E)}$ and $^{129}Xe/^{130}Xe_{(E)}$ ratios, respectively, along the SWIR Orthogonal Supersegment (Figures 3.5-3.7). In light of this source heterogeneity, interpreting any single MORB composition as representative of the average MORB source is problematic. However, geochemical reservoir models have used the composition of the gas-rich N. Atlantic popping rock 2ΠD43 (e.g., Moreira et al., 1998; Staudacher et al., 1989) as representative of the average MORB source (e.g., Davies, 2010; Gonnermann and Mukhopadhyay, 2009; Porcelli and Wasserburg, 1995; Tolstikhin and Marty, 1998) in order to constrain mass exchange between mantle reservoirs. Given the observed large variation in isotopic composition and the small number of mantle source Ar and Xe isotopic constraints, the average Ar and Xe isotopic compositions of the MORB source are probably not yet well-defined.

3.5.3 The nature of the heterogeneities observed at SWIR 7-25°E

3.5.3.1 The 7°E ridge segment

Low $^{4}He/^{3}He$, $^{21}Ne/^{22}Ne_{(E)}$, $^{40}Ar/^{36}Ar_{(E)}$ and $^{129}Xe/^{130}Xe_{(E)}$ at 7°E indicate the influence of a relatively undegassed reservoir in the westernmost SWIR, which may be

related to the Bouvet plume (Figure 3.1). The data are consistent with previous studies of plume-related heavy noble gases (Figures 3.6 and 3.7), indicating that less-nucleogenic $^{21}Ne/^{22}Ne_{(E)}$, less-radiogenic $^{40}Ar/^{36}Ar_{(E)}$ and less-radiogenic $^{129}Xe/^{130}Xe_{(E)}$ are characteristic of plume sources and do not result from syn- to post-eruptive air contamination. The close spatial association between the relatively undegassed and degassed source signatures indicates either that the SWIR source at 7°E is heterogeneous on very fine lengthscales, or that melts from spatially disparate mantle sources are channeled towards common volcanic centers and erupted without being completely homogenized.

3.5.3.2 The Oblique Supersegment

High $^{4}He/^{3}He$ ratios at the Oblique Supersegment reflect a source that is more degassed of primordial ^{3}He than the canonical MORB source. Such sources are commonly attributed to the presence of recycled material in the mantle source (e.g., Graham et al., 1992; Hanyu et al., 1999; Hilton et al., 2000; Kurz et al., 1982; Moreira et al., 1999; Parai et al., 2009). The sample VAN7 89-02 exhibits $^{4}He/^{3}He$ that is amongst the most radiogenic in the study area (119,000; Table A3.1); however, $^{21}Ne/^{22}Ne_{(E)}$ is only slightly nucleogenic compared to N. Atlantic popping rock (e.g., Figures 3.5, 3.6a). Both Oblique Supersegment samples were erupted at shallow depth (1400-2400 m), and hyperbolic arrays for Oblique Supersegment samples in $^{40}Ar/^{36}Ar$ – $^{20}Ne/^{22}Ne$ and $^{129}Xe/^{130}Xe$ – $^{40}Ar/^{36}Ar$ spaces are too poor to determine $^{40}Ar/^{36}Ar_{(E)}$ and $^{129}Xe/^{130}Xe_{(E)}$. Importantly, this sample has a $CO_2/^{3}He$ ratio of 8.4×10^{9}, which is a factor of >3 larger than the averages for both MORBs and OIBs (Marty and Tolstikhin, 1998). While

carbonate may be recycled back to the mantle in significant quantities (e.g., Dasgupta et al., 2004; Huang et al., 2011), ^{3}He is not recycled back to the mantle. Consequently, the high $CO_2/^{3}He$ ratio would be consistent with CO_2 enrichment of the mantle source associated with carbonate-bearing recycled material. Elevated $CO_2/^{3}He$ may also reflect shallow assimilation of altered oceanic crust (e.g., Marty et al., 2001). However, there is no obvious evidence of shallow crustal assimilation in Oblique Supersegment trace element and lithophile isotopic compositions (Standish, 2006), and so the signature of shallow crustal assimilation would have to be limited to $CO_2/^{3}He$.

Based on major element, trace element and lithophile isotopic data, le Roex et al. (1992) argued that the alkali-enriched signature at the Oblique Supersegment reflected melting of a mantle source veined with frozen low-degree melts of Bouvet plume material. Such a process would generate strongly enriched major and trace element compositions at the Oblique Supersegment while preserving Bouvet isotopic compositions (le Roex et al., 1992). However, radiogenic $^{4}He/^{3}He$ and nucleogenic $^{21}Ne/^{22}Ne_{(E)}$ are unlikely to be generated by preferential tapping of frozen low-degree melts of plume material at the Oblique Supersegment. Furthermore, CO_2 and He are both highly incompatible during partial melting and low-degree melts would not be sufficiently enriched in $CO_2/^{3}He$ to account for the 10-fold enhancement in the ratios at the Oblique Supersegment (Figure 3.5a). Therefore, we suggest that at the Oblique Supersegment, a relatively degassed reservoir incorporating recycled material mixes with the ambient depleted mantle source.

3.5.3.3 The Orthogonal Supersegment

The spatial gradient in $^{4}He/^{3}He$ observed along the Orthogonal Supersegment (Georgen et al., 2003) may reflect sampling of a peridotite mantle veined with recycled oceanic crust (pyroxenite), with a gradient either in pyroxenite distribution or in mantle temperature along the SWIR (e.g., Georgen et al., 2003; Graham et al., 2001). More radiogenic $^{4}He/^{3}He$ signatures in the west could reflect a greater proportion of recycled pyroxenite in the source, or preferential melting of pyroxenite at low temperatures. Since recycled oceanic crust is heavily degassed, pyroxenite veins should either have negligible mantle-derived ^{129}Xe and ^{130}Xe or should carry atmospheric $^{129}Xe/^{130}Xe$ ratios. Hence, we would expect either minimal variability of $^{129}Xe/^{130}Xe$ across the Orthogonal Supersegment or lower $^{129}Xe/^{130}Xe$ ratios in the west due to the preferential sampling of recycled pyroxenite veins. However, $^{129}Xe/^{130}Xe_{(E)}$ at the western Orthogonal Supersegment are similar to the Equatiorial Atlantic depleted MORB and Bravo Dome continental well gas sources, and low $^{129}Xe/^{130}Xe_{(E)}$ are found in the Eastern Orthogonal Supersegment (Figure 3.7). Therefore, we suggest that differential sampling of pyroxenite veins embedded in a peridotite matrix does not explain the full suite of noble gas observations from the Orthogonal Supersegment.

A possible explanation for the differences in heavy noble gas composition along the Orthogonal Supersegment is that the eastern region samples a southern Indian Ocean mantle that is inherently characterized by low $^{40}Ar/^{36}Ar_{(E)}$ and $^{129}Xe/^{130}Xe_{(E)}$ (e.g., Sarda et al., 2000) compared to N. Atlantic mantle source. Thus, variation across the Orthogonal Supersegment could reflect sampling of distinct mantle domains in the east and west. In this regard, Mahoney et al. (1992) suggested that the SWIR Orthogonal

Supersegment contained a boundary between the Atlantic MORB mantle and the Indian MORB mantle domain characterized by a Dupal Pb isotopic signature (elevated $^{207}Pb/^{204}Pb$ and $^{208}Pb/^{204}Pb$ at a given $^{206}Pb/^{204}Pb$, compared to the Northern Hemispheric Reference Line; Dupre and Allegre, 1983; Hart, 1984). Compared to the western Orthogonal Supersegment, the Eastern Orthogonal Supersegment is characterized by a stronger Dupal Pb signature. The Dupal signature reflects ancient (>3 Gyr) enrichment of Th/U and is often attributed to the incorporation of subcontinental lithospheric mantle (SCLM) throughout the Indian MORB source in association with the breakup of Gondwanaland (Hart, 1984; Hawkesworth et al., 1986; Mahoney et al., 1992; Mahoney et al., 1989; Storey et al., 1989). Samples from the S. Atlantic from 42 to 50°S also exhibit the Dupal Pb signature (Douglass et al., 1999), and Sarda et al. (2000) argued that Dupal is associated with low source $^{40}Ar/^{36}Ar_{(E)}$ based on noble gas analyses of the same samples (corrected for shallow-level air contamination assuming linear mixing in $^{40}Ar/^{36}Ar$ – $^{20}Ne/^{22}Ne$ space; Sarda et al., 2000). S. Atlantic $^{129}Xe/^{130}Xe$ maximum measured values are also low compared to N. Atlantic popping rock; however, source $^{129}Xe/^{130}Xe_{(E)}$ could not be determined due to large analytical errors and small excesses compared to atmosphere (Sarda et al., 2000). If the Eastern Orthogonal Supersegment samples a Dupal mantle domain, then the observed low $^{40}Ar/^{36}Ar_{(E)}$ and low $^{129}Xe/^{130}Xe_{(E)}$ associated with slightly radiogenic He and nucleogenic Ne (compared to the N. Atlantic popping rock source) is characteristic of Dupal mantle, consistent with Sarda et al. (2000).

3.5.3.4. Constraints on the origin of the Dupal mantle domain

The Dupal Pb signature is commonly attributed to the incorporation of SCLM (>3 Ga) into the southern Indian mantle source (e.g., Hart, 1984; Hawkesworth et al., 1986; Mahoney et al., 1992; Mahoney et al., 1989; Storey et al., 1989). Low $^{40}Ar/^{36}Ar$ ratios in the Dupal mantle domain could reflect evolution of SCLM with low $K/^{36}Ar$, which would effectively freeze the MORB source mantle $^{40}Ar/^{36}Ar$ ratio at the time of SCLM formation (Sarda et al., 2000). However, unmodified SCLM should be characterized by $^{129}Xe/^{130}Xe$ identical to the rest of the MORB source mantle since $^{129}Xe/^{130}Xe$ ratios stopped evolving ~100 Ma after the start of the Solar System, unless the SCLM is ancient (>4.45 Ga). If SCLM is younger than 4.45 Ga, unradiogenic Ar and Xe in the Dupal mantle relative to N. Atlantic or Pacific mantle could reflect incorporation of noble gases from a distinct, relatively undegassed reservoir into SCLM. However, we see no geochemical evidence in He, Ne or any of the lithophile isotopes (Standish, 2006) for the presence a relatively undegassed mantle plume component. Therefore, we do not discuss this option further.

Alternatively, the low $^{40}Ar/^{36}Ar_{(E)}$ and $^{129}Xe/^{130}Xe_{(E)}$ in the Dupal mantle could reflect metasomatism of the SCLM by subduction zone fluids carrying atmospheric Ar and Xe without significant contributions of He and Ne. This conclusion would be consistent with recent studies indicating that atmospheric Ar and Xe are recycled into the mantle (Holland and Ballentine, 2006; Kendrick et al., 2011; Sumino et al., 2010). Furthermore, some previous studies (Matsumoto et al., 2001; Yamamoto et al., 2004) have argued for the introduction of atmospheric heavy noble gases into SCLM based on noble gas measurements in alpine peridotites and lithospheric mantle xenoliths.

Gautheron et al. (2005) also observed low $^{40}Ar/^{36}Ar$ ratios in SCLM xenoliths, but favored shallow-level atmospheric contamination to explain the observed Ar isotopic systematics. If the Dupal Pb signature within our study area is due to delaminated SCLM in the mantle source, then low $^{129}Xe/^{130}Xe_{(E)}$ ratios in the Eastern Orthogonal Supersegment source require either an age of formation >4.45 Ga or more recent metasomatism of the SCLM by fluids carrying atmospheric Ar and Xe.

3.5.4. SWIR Xe evidence for upper mantle heterogeneity, early differentiation and preservation of ancient mantle reservoirs

Xe isotopic compositions of mantle-derived rocks provide information about early degassing and mantle evolution, as the I-Xe and Pu-Xe systems are sensitive to the first ~100 Ma and 500 Ma of Earth history, respectively. In contrast, the U-Xe system evolves throughout Earth history. Given the limited number of Xe isotopic observations from 7°E and the Oblique Supersegment, here we discuss only Xe data from the Orthogonal Supersegment. Depleted MORBs from the equatorial Atlantic (Tucker et al., 2012), N. Atlantic popping rock 2ΠD43 (Moreira et al., 1998; Kunz et al., 1998) and Icelandic basalt DICE (Mukhopadhyay, 2012) are included for comparison.

We present the Xe data in two different Xe isotopic spaces: $^{136}Xe/^{130}Xe$ vs. $^{129}Xe/^{130}Xe$ (Figure 3.8) and error-weighted averages in $^{129}Xe/^{136}Xe$ vs. $^{130}Xe/^{136}Xe$ (Figure 3.9). In $^{136}Xe/^{130}Xe$ vs. $^{129}Xe/^{130}Xe$ space, individual step-crushes define a linear trend (Figure 3.8) that reflects two-component mixing between the mantle source and atmosphere. The slope of the line is inversely proportional to $^{129}Xe/^{136}Xe$ in the mantle source and reflects the mantle source degassing history. For example, a mantle reservoir

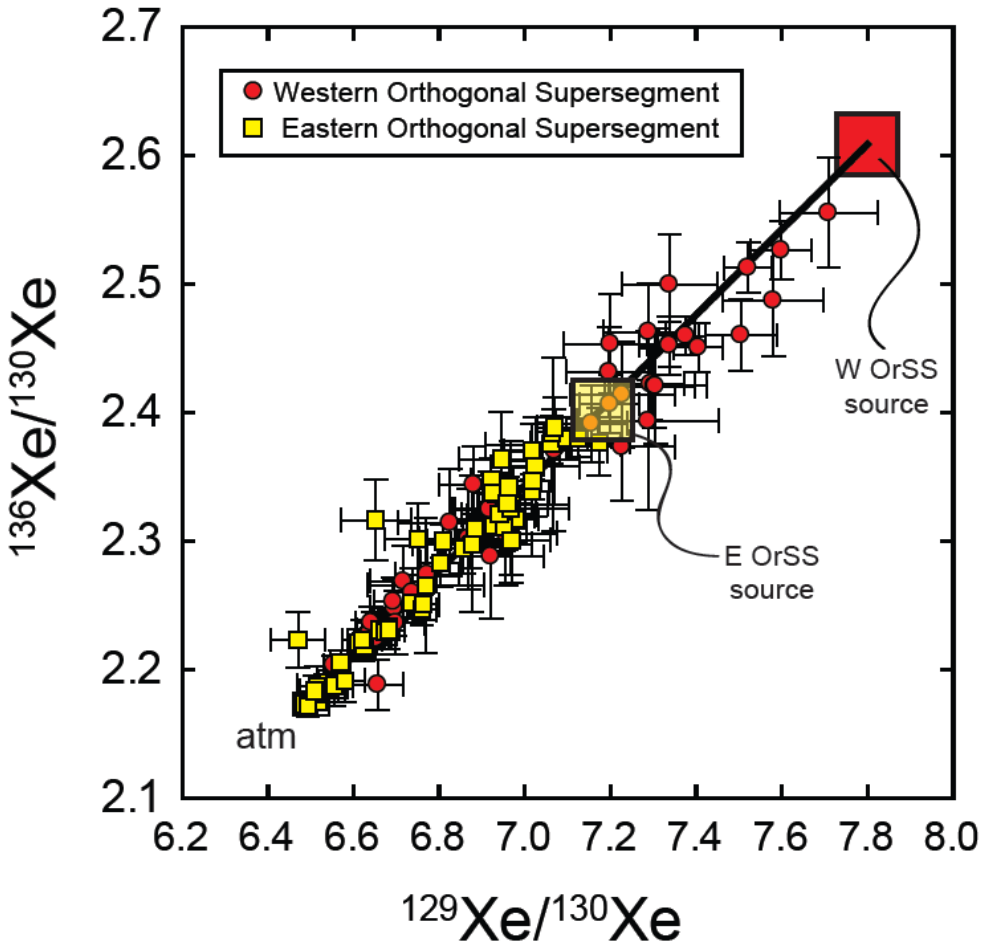

Figure 3.8: SWIR Xe isotope systematics in $^{136}Xe/^{130}Xe$ vs. $^{129}Xe/^{130}Xe$ space for Orthogonal Supersegment samples. Step-crushing generates a well-defined linear mixing array between air and the mantle source (approximate source $^{129}Xe/^{130}Xe$ from Ar-Xe extrapolations; Figure 3.4). The extrapolated source $^{129}Xe/^{130}Xe$ values for Eastern Orthogonal Supersegment samples (yellow box) are significantly lower than the western Orthogonal Supersegment source (red box), and may reflect recycling of atmospheric Xe.

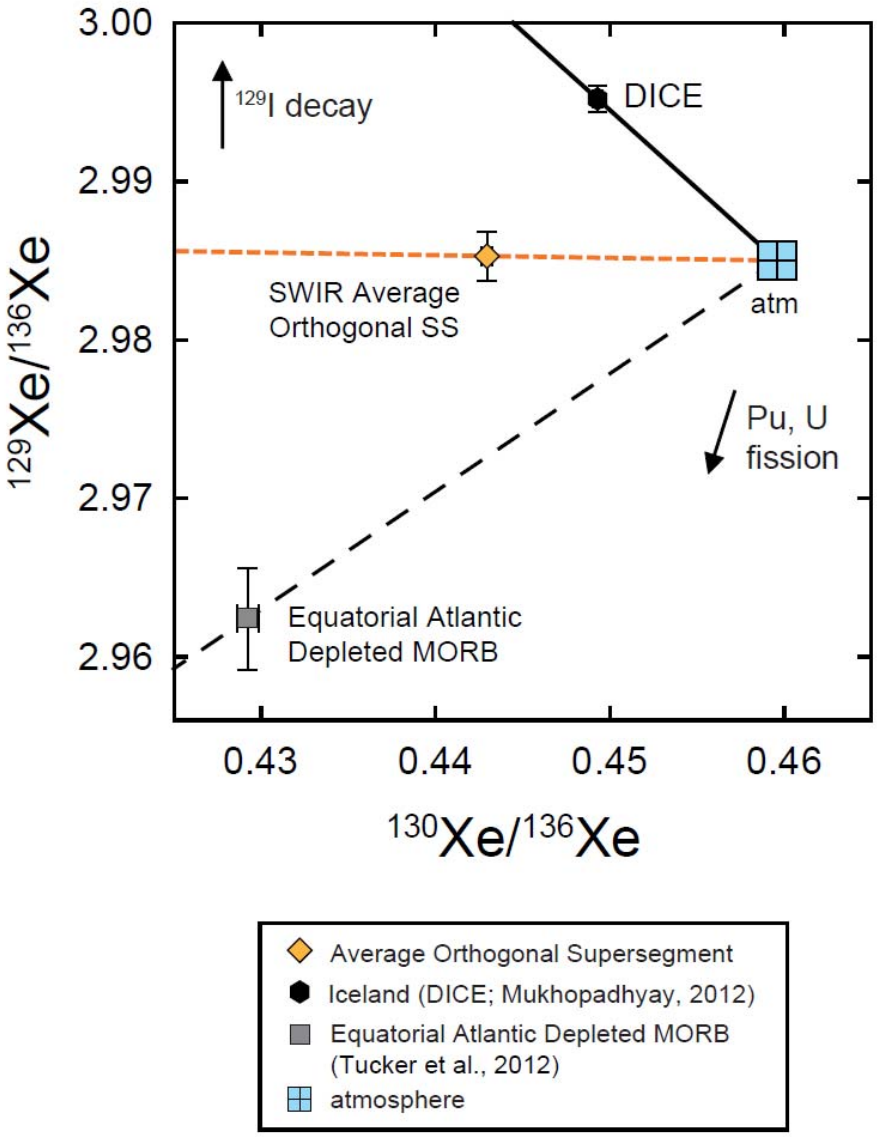

Figure 3.9: Error-weighted averages of measured $^{129}Xe/^{136}Xe$ plotted against error-weighted average of measured $^{130}Xe/^{136}Xe$ for the SWIR Orthogonal Supersegment. Data from Iceland (DICE; Mukhopadhyay, 2012) and depleted equatorial Atlantic MORB (Tucker et al., 2012) are shown for comparison. N. Atlantic popping rock 2ΠD43 is not shown in this figure since $^{129}Xe/^{136}Xe$ ratios are not directly available (Moreira et al., 1998). An advantage of the $^{130}Xe/^{136}Xe$ vs. $^{129}Xe/^{136}Xe$ plot over the $^{129}Xe/^{130}Xe$ vs. $^{136}Xe/^{130}Xe$ representation is that the *x* and *y* errors are not as strongly correlated as in Figure 3.8. The atmospheric composition is indicated along with vectors representing ^{129}I decay and (Pu+U) fission. Mixing in this space is linear and lines representing two-component mixing between the measured composition and atmosphere are indicated. The weighted average of the measured $^{129}Xe/^{136}Xe$ ratio in the SWIR Orthogonal Supersegment is demonstrably distinct from the weighted average of DICE and the depleted equatorial Atlantic MORB samples.

that undergoes degassing after I and Pu are extinct will have low concentrations of primordial ^{130}Xe, radiogenic ^{129}Xe and fissiogenic ^{136}Xe produced by extinct ^{244}Pu. Addition of ^{136}Xe from ^{238}U fission to such a degassed source would not change the $^{129}Xe/^{130}Xe$ ratio of the reservoir, but would increase the $^{136}Xe/^{130}Xe$ ratio. Therefore, a steeper slope in $^{136}Xe/^{130}Xe$ vs. $^{129}Xe/^{130}Xe$ space indicates a relatively degassed source. Likewise, in $^{129}Xe/^{136}Xe$ vs. $^{130}Xe/^{136}Xe$ space (Figure 3.9), a degassed source should have low $^{129}Xe/^{136}Xe$ and $^{130}Xe/^{136}Xe$, since ^{130}Xe is primordial and production of ^{129}Xe stops after the first 100 Ma of Earth history.

Figure 3.8 shows the linear array defined by the SWIR Orthogonal Supersegment data in $^{136}Xe/^{130}Xe$ vs. $^{129}Xe/^{130}Xe$ space. The least-squares best fit slope of 0.331 ± 0.006 is statistically indistinguishable from the 2ΠD43 slope of 0.324 ± 0.006 (Moreira et al., 1998; Kunz et al., 1998). However, the SWIR slope is shallower than the slope of 0.375 ± 0.009 for the depleted equatorial MORBs (Tucker et al., 2012) and steeper than the slope of 0.306 ± 0.01 for Iceland (Mukhopadhyay, 2012). Likewise, the error-weighted average $^{129}Xe/^{136}Xe$ ratio (n = 86; Figure 3.9) from the Orthogonal Supersegment is intermediate to Iceland (DICE; Mukhopadhyay, 2012) and the depleted equatorial Atlantic MORBs (Tucker et al., 2012) and well-resolved from both. Since the SWIR, DICE and equatorial Atlantic samples were all analyzed using the same procedure in the same laboratory, the differences between these three groups of basalts are not related to measurement artifacts. Instead, the differences must reflect different degrees of degassing of the mantle sources: the depleted equatorial MORB source is most degassed; the SWIR Orthogonal Supersegment MORB source is slightly less degassed, and the Iceland source is least degassed. Hence, the depleted MORBs from the equatorial Atlantic and the MORBs from

the SWIR Orthogonal Supersegment indicate that there are small variations in $^{129}Xe/^{136}Xe$ even in regions removed from obvious influence of mantle plumes (Figure 3.9).

Mukhopadhyay (2012) argued that the Iceland and N. Atlantic popping rock mantle sources are distinct in $^{129}Xe/^{136}Xe$-$^{130}Xe/^{136}Xe$ space and that the two sources cannot be related by preferential recycling of atmospheric heavy noble gases (c.f., Holland and Ballentine, 2006) or by addition of fission-produced ^{136}Xe into the Iceland source. The new observations from the SWIR Orthogonal Supersegment provide conclusive evidence for this distinction in Xe isotopic composition between MORBs and Iceland (Figure 3.9). Sources related by recycling of atmospheric Xe would be collinear with the atmospheric composition; the Iceland and SWIR mantle Xe compositions are clearly not collinear. We note that recycling of atmospheric volatiles to the deep Earth may occur, but we emphasize that differential recycling by itself cannot explain the Xe isotopic difference between MORBs and Iceland. Therefore, early separation of the reservoir supplying noble gases to the Iceland plume from the MORB source and a lower degree of degassing for the Iceland source are the only viable explanations for the differences between the Iceland plume and MORB heavy noble gas isotopic compositions (Mukhopadhyay, 2012). However, the persistence of mantle reservoirs created very early in Earth history does not necessarily imply convective isolation; rather, the two reservoirs may have been processed at different rates and have experienced limited direct mixing over Earth history (Gonnermann and Mukhopadhyay, 2009).

3.6. CONCLUSIONS

We present high-precision Ne, Ar and Xe isotopic compositions, and He, CO_2, Ne, Ar and Xe abundances measured in basalt glasses from the SWIR between 7 and 25°E. We find systematic and significant variations in He, Ne, Ar and Xe isotopic compositions across the study area. Basalts with low $^{4}He/^{3}He$ are found to be characterized by low source $^{21}Ne/^{22}Ne_{(E)}$, low $^{40}Ar/^{36}Ar_{(E)}$, and intermediate $^{129}Xe/^{130}Xe_{(E)}$, indicating the influence of a less-degassed reservoir in the mantle source at 7°E. In contrast, basalts with higher $^{4}He/^{3}He$ are characterized by higher $^{21}Ne/^{22}Ne_{(E)}$, $^{40}Ar/^{36}Ar_{(E)}$, and $^{129}Xe/^{130}Xe_{(E)}$, indicating a comparatively degassed mantle source (Figures 3.6, 3.7). However, among MORBs removed from the influence of any known hotspot, we find significant variations in $^{40}Ar/^{36}Ar_{(E)}$ and $^{129}Xe/^{130}Xe_{(E)}$ over a limited range of $^{4}He/^{3}He$ and $^{21}Ne/^{22}Ne_{(E)}$ compositions (Figures 3.6, 3.7), indicating source heterogeneity in Ar and Xe isotopes. The difference in $^{40}Ar/^{36}Ar_{(E)}$ and $^{129}Xe/^{130}Xe_{(E)}$ between the western and Eastern Orthogonal Supersegment reflects sampling of distinct mantle domains, and suggests that the Dupal mantle is characterized by low $^{40}Ar/^{36}Ar_{(E)}$ and $^{129}Xe/^{130}Xe_{(E)}$ relative to N. Atlantic and Pacific MORB mantle sources. Low $^{129}Xe/^{130}Xe_{(E)}$ in the Dupal mantle would indicate that Dupal cannot represent unmodified delaminated SCLM unless the SCLM is very ancient (>4.45 Ga). If SCLM is younger, it must have been metasomatized by subduction zone fluids carrying recycled atmospheric Ar and Xe.

High-precision Xe isotopic measurements allow us to demonstrate that SWIR MORB $^{129}Xe/^{136}Xe$-$^{130}Xe/^{136}Xe$ systematics cannot be related to OIB systematics solely through recycling of atmospheric noble gases (Figures 3.8, 3.9). Therefore, a lower

degree of degassing for the plume source and limited mixing between plume and MORB sources over 4.45 Gyr remain the viable explanation for observed differences in MORB and OIB heavy noble gas compositions.

3.7 REFERENCES

Allègre, C. J., Staudacher, T., Sarda, P., 1987. Rare-gas systematics -formation of the atmosphere, evolution and structure of the earth's mantle. Earth Planet Sc Lett 81, 127-150.

Ballentine, C. J., Barfod, D. N., 2000. The origin of air-like noble gases in MORB and OIB. Earth Planet Sc Lett 180, 39-48, doi: 10.1016/s0012-821x(00)00161-8.

Ballentine, C. J., Holland, G., 2008. What CO_2 well gases tell us about the origin of noble gases in the mantle and their relationship to the atmosphere. Philos T R Soc A 366, 4183-4203, doi: 10.1098/rsta.2008.0150.

Burnard, P., 1999. Origin of argon-lead isotopic correlation in basalts. Science 286, 871.

Caffee, M. W., Hudson, G. U., Velsko, C., Huss, G. R., Alexander, E. C., Chivas, A. R., 1999. Primordial noble gases from Earth's mantle: Identification of a primitive volatile component. Science 285, 2115-2118.

Dasgupta, R., Hirschmann, M. M., Withers, A. C., 2004. Deep global cycling of carbon constrained by the solidus of anhydrous, carbonated eclogite under upper mantle conditions. Earth Planet Sc Lett 227, 73-85, doi: 10.1016/j.epsl.2004.08.004.

Davies, G. F., 2010. Noble gases in the dynamic mantle. Geochem Geophy Geosy 11, doi:10.1029/2009gc002801.

Dick, H. J. B., Lin, J., Schouten, H., 2003. An ultraslow-spreading class of ocean ridge. Nature 426, 405-412, doi: 10.1038/nature02128.

Douglass, J., Schilling, J. G., Fontignie, D., 1999. Plume-ridge interactions of the Discovery and Shona mantle plumes with the southern mid-Atlantic ridge (40 degrees-55 degrees S). J Geophys Res-Sol Ea 104, 2941-2962.

Dupre, B., Allegre, C. J., 1983. Pb-Sr isotope variation in Indian Ocean basalts and mixing phenomena. Nature 303, 142-146.

Furi, E., Hilton, D. R., Halldorsson, S. A., Barry, P. H., Hahm, D., Fischer, T. P., Gronvold, K., 2010. Apparent decoupling of the He and Ne isotope systematics of

the Icelandic mantle: The role of He depletion, melt mixing, degassing fractionation and air interaction. Geochim Cosmochim Ac 74, 3307-3332.

Gautheron, C., Moreira, M., Allegre, C., 2005. He, Ne and Ar composition of the European lithospheric mantle. Chem Geol 217, 97-112, doi: 10.1016/j.chemgeo.2004.12.009.

Georgen, J. E., Kurz, M. D., Dick, H. J. B., Lin, J., 2003. Low $^{3}He/^{4}He$ ratios in basalt glasses from the western Southwest Indian Ridge (10°-24°e). Earth Planet Sc Lett 206, 509-528, doi: 10.1016/s0012-821x(02)01106-8.

Gonnermann, H. M., Mukhopadhyay, S., 2009. Preserving noble gases in a convecting mantle. Nature 459, 560-U588, doi: 10.1038/nature08018.

Graham, D. W., 2002. Noble gas isotope geochemistry of mid-ocean ridge and ocean island basalts: Characterization of mantle source reservoirs. Noble Gases in Geochemistry and Cosmochemistry 47, 247-317.

Graham, D. W., Humphris, S. E., Jenkins, W. J., Kurz, M. D., 1992. Helium isotope geochemistry of some volcanic rocks from Saint-Helena. Earth Planet Sc Lett 110, 121-131.

Graham, D. W., Lupton, J. E., Spera, F. J., Christie, D. M., 2001. Upper-mantle dynamics revealed by helium isotope variations along the Southeast Indian ridge. Nature 409, 701-703.

Hanyu, T., Dunai, T. J., Davies, G. R., Kaneoka, I., Nohda, S., Uto, K., 2001. Noble gas study of the Reunion hotspot: Evidence for distinct less-degassed mantle sources. Earth Planet Sc Lett 193, 83-98.

Hanyu, T., Kaneoka, I., 1998. Open system behavior of helium in case of the HIMU source area. Geophys Res Lett 25, 687-690.

Hanyu, T., Kaneoka, I., Nagao, K., 1999. Noble gas study of HIMU and EM ocean island basalts in the Polynesian region. Geochim Cosmochim Ac 63, 1181-1201.

Harrison, D., Burnard, P., Turner, G., 1999. Noble gas behaviour and composition in the mantle: Constraints from the Iceland plume. Earth Planet Sc Lett 171, 199-207.

Hart, S. R., 1984. A large-scale isotope anomaly in the southern-hemisphere mantle. Nature 309, 753-757.

Hart, S. R., Hauri, E. H., Oschmann, L. A., Whitehead, J. A., 1992. Mantle plumes and entrainment - isotopic evidence. Science 256, 517-520.

Hawkesworth, C. J., Mantovani, M. S. M., Taylor, P. N., Palacz, Z., 1986. Evidence from the Parana of South Brazil for a continental contribution to Dupal basalts. Nature 322, 356-359.

Hilton, D. R., Macpherson, C. G., Elliott, T. R., 2000. Helium isotope ratios in mafic phenocrysts and geothermal fluids from La Palma, the Canary Islands (Spain): Implications for HIMU mantle sources. Geochim Cosmochim Ac 64, 2119-2132.

Holland, G., Ballentine, C. J., 2006. Seawater subduction controls the heavy noble gas composition of the mantle. Nature 441, 186-191, doi: 10.1038/Nature04761.

Honda, M., Mcdougall, I., 1998. Primordial helium and neon in the earth - a speculation on early degassing. Geophys Res Lett 25, 1951-1954.

Honda, M., Woodhead, J. D., 2005. A primordial solar-neon enriched component in the source of EM-I-type ocean island basalts from the Pitcairn seamounts, Polynesia. Earth Planet Sc Lett 236, 597-612, doi: 10.1016/j.epsl.2005.05.038.

Huang, S. C., Farkas, J., Jacobsen, S. B., 2011. Stable calcium isotopic compositions of Hawaiian shield lavas: Evidence for recycling of ancient marine carbonates into the mantle. Geochim Cosmochim Ac 75, 4987-4997, doi: 10.1016/j.gca.2011.06.010.

Kendrick, M. A., Scambelluri, M., Honda, M., Phillips, D., 2011. High abundances of noble gas and chlorine delivered to the mantle by serpentinite subduction. Nat Geosci 4, 807-812, doi: 10.1038/Ngeo1270.

Kunz, J., Staudacher, T., Allegre, C. J., 1998. Plutonium-fission xenon found in Earth's mantle. Science 280, 877-880.

Kurz, M. D., Jenkins, W. J., Schilling, J. G., Hart, S. R., 1982. Helium isotopic variations in the mantle beneath the Central-North Atlantic ocean. Earth Planet Sc Lett 58, 1-14.

Kurz, M. D., Le Roex, A. P., Dick, H. J. B., 1998. Isotope geochemistry of the oceanic mantle near the Bouvet triple junction. Geochim Cosmochim Ac 62, 841-852.

Kurz, M. D., Moreira, M., Curtice, J., Lott, D. E., Mahoney, J. J., Sinton, J. M., 2005. Correlated helium, neon, and melt production on the super-fast spreading East Pacific Rise near 17°S. Earth Planet Sc Lett 232, 125-142, doi: 10.1016/j.epsl.2005.01.005.

Le Roex, A. P., Dick, H. J. B., Watkins, R. T., 1992. Petrogenesis of anomalous K-enriched MORB from the Southwest Indian Ridge - 11°53'E to 14°38'E. Contrib Mineral Petr 110, 253-268.

Madureira, P., Moreira, M., Mata, J., Allegre, C. J., 2005. Primitive neon isotopes in Terceira Island (Azores archipelago). Earth Planet Sc Lett 233, 429-440, doi: 10.1016/j.epsl.2005.02.030.

Mahoney, J., Leroex, A. P., Peng, Z., Fisher, R. L., Natland, J. H., 1992. Southwestern limits of Indian-Ocean ridge mantle and the origin of low $^{206}Pb/^{204}Pb$ mid-ocean ridge basalt - isotope systematics of the central Southwest Indian Ridge (17°E - 50°E). J Geophys Res-Sol Ea 97, 19771-19790.

Mahoney, J. J., Natland, J. H., White, W. M., Poreda, R., Bloomer, S. H., Fisher, R. L., Baxter, A. N., 1989. Isotopic and geochemical provinces of the western Indian-Ocean spreading centers. J Geophys Res-Solid 94, 4033-4052.

Marty, B., Tolstikhin, I. N., 1998. CO_2 fluxes from mid-ocean ridges, arcs and plumes. Chem Geol 145, 233-248.

Marty, B., Sano, Y., France-Lanord, C., 2001. Water-saturated oceanic lavas from the Manus Basin: volatile behaviour during assimilation-fractional crystallisation-degassing (AFCD). J Volcanol Geoth Res 108, 1-10.

Matsumoto, T., Chen, Y. L., Matsuda, J., 2001. Concomitant occurrence of primordial and recycled noble gases in the earth's mantle. Earth Planet Sc Lett 185, 35-47.

Moreira, M., Staudacher, T., Sarda, P., Schilling, J. G., Allegre, C. J., 1995. A primitive plume neon component in MORB - the Shona Ridge anomaly, South-Atlantic (51-52°S). Earth Planet Sc Lett 133, 367-377.

Moreira, M., Kunz, J., Allegre, C., 1998. Rare gas systematics in popping rock: Isotopic and elemental compositions in the upper mantle. Science 279, 1178-1181.

Moreira, M., Doucelance, R., Kurz, M. D., Dupre, B., Allegre, C. J., 1999. Helium and lead isotope geochemistry of the Azores archipelago. Earth Planet Sc Lett 169, 189-205.

Moreira, M., Escartin, J., Gayer, E., Hamelin, C., Bezos, A., Guillon, F., Cannat, M., 2011. Rare gas systematics on Lucky Strike basalts (37°N, North Atlantic): Evidence for efficient homogenization in a long-lived magma chamber system? Geophys Res Lett 38, doi: Artn L08304 10.1029/2011gl046794.

Mukhopadhyay, S., 2012. Early differentiation and volatile accretion recorded in deep-mantle neon and xenon. Nature 486, 101-104, doi: 10.1038/Nature11141.

O'Nions, R. K., Tolstikhin, I. N., 1996. Limits on the mass flux between lower and upper mantle and stability of layering. Earth Planet Sc Lett 139, 213-222.

Parai, R., Mukhopadhyay, S., Lassiter, J. C., 2009. New constraints on the HIMU mantle from neon and helium isotopic compositions of basalts from the Cook-Austral Islands. Earth Planet Sc Lett 277, 253-261, doi: 10.1016/j.epsl.2008.10.014.

Pepin, R. O., Porcelli, D., 2002. Origin of noble gases in the terrestrial planets. Noble Gases in Geochemistry and Cosmochemistry 47, 191-246.

Phinney, D., Tennyson, J., Frick, U., 1978. Xenon in CO_2 well gas revisited. J Geophys Res 83, 2313-2319.

Porcelli, D., Wasserburg, G. J., 1995. Mass-transfer of helium, neon, argon, and xenon through a steady-state upper-mantle. Geochim Cosmochim Ac 59, 4921-4937.

Press, W.H., Teukolsky, S.A., Vetterling, W.T., Flannery, B.P., 1992. Numerical Recipes in C: The Art of Scientific Computing, second edition, Cambridge University Press, New York.

Raquin, A., Moreira, M. A., Guillon, F., 2008. He, Ne and Ar systematics in single vesicles: Mantle isotopic ratios and origin of the air component in basaltic glasses. Earth Planet Sc Lett 274, 142-150, doi: 10.1016/j.epsl.2008.07.007.

Sarda, P., Moreira, M., Staudacher, T., 1999. Argon-lead isotopic correlation in Mid-Atlantic Ridge basalts. Science 283, 666-668.

Sarda, P., Moreira, M., Staudacher, T., Schilling, J. G., Allegre, C. J., 2000. Rare gas systematics on the southernmost Mid-Atlantic Ridge: Constraints on the lower mantle and the Dupal source. J Geophys Res-Sol Ea 105, 5973-5996.

Sarda, P., Staudacher, T., Allegre, C. J., 1985. $^{40}Ar/^{36}Ar$ in MORB glasses - Constraints on atmosphere and mantle evolution. Earth Planet Sc Lett 72, 357-375.

Shaw, A. M., Hilton, D. R., Macpherson, C. G., Sinton, J. M., 2001. Nucleogenic neon in high $^{3}He/^{4}He$ lavas from the Manus back-arc basin: A new perspective on He-Ne decoupling. Earth Planet Sc Lett 194, 53-66.

Standish, J. J., 2006. The influence of ridge geometry at the ultraslow-spreading Southwest Indian Ridge (9 -25°E): Basalt composition sensitivity to variations in source and process. PhD Thesis, MIT WHOI Joint Program in Oceanography / Applied Ocean Science and Engineering.

Standish, J. J., Dick, H. J. B., Michael, P. J., Melson, W. G., O'Hearn, T., 2008. MORB generation beneath the ultraslow spreading Southwest Indian Ridge (9-25°E): Major element chemistry and the importance of process versus source. Geochem Geophy Geosy 9, doi: 10.1029/2008gc001959.

Staudacher, T., 1987. Upper mantle origin for Harding County well gases. Nature 325, 605-607.

Staudacher, T., Allegre, C. J., 1982. Terrestrial xenology. Earth Planet Sc Lett 60, 389-406.

Staudacher, T., Sarda, P., Richardson, S. H., Allegre, C. J., Sagna, I., Dmitriev, L. V., 1989. Noble gases in basalt glasses from a Mid-atlantic Ridge topographic high at 14°N - geodynamic consequences. Earth Planet Sc Lett 96, 119-133.

Storey, M., Saunders, A. D., Tarney, J., Gibson, I. L., Norry, M. J., Thirlwall, M. F., Leat, P., Thompson, R. N., Menzies, M. A., 1989. Contamination of Indian-Ocean asthenosphere by the Kerguelen-Heard mantle plume. Nature 338, 574-576.

Stuart, F. M., Lass-Evans, S., Fitton, J. G., Ellam, R. M., 2003. High $^{3}He/^{4}He$ ratios in picritic basalts from Baffin Island and the role of a mixed reservoir in mantle plumes. Nature 424, 57-59.

Sumino, H., Burgess, R., Mizukami, T., Wallis, S. R., Holland, G., Ballentine, C. J., 2010. Seawater-derived noble gases and halogens preserved in exhumed mantle wedge peridotite. Earth Planet Sc Lett 294, 163-172, doi: 10.1016/j.epsl.2010.03.029.

Tolstikhin, I. N., Marty, B., 1998. The evolution of terrestrial volatiles: A view from helium, neon, argon and nitrogen isotope modeling. Chem Geol 147, 27-52.

Trieloff, M., Kunz, J., Clague, D. A., Harrison, D., Allegre, C. J., 2000. The nature of pristine noble gases in mantle plumes. Science 288, 1036-1038.

Tucker, J. M., Mukhopadhyay, S., Schilling, J. G., 2012. The heavy noble gas composition of the depleted MORB mantle (DMM) and its implications for the origin of heterogeneities in the upper mantle. Earth Planet Sc Lett 355, 244-254, doi: 10.1016/j.epsl.2012.08.025.

Wetherill, G. W., 1954. Variations in the isotopic abundances of neon and argon extracted from radioactive minerals. Phys Rev 96, 679-683.

Yamamoto, J., Kaneoka, I., Nakai, S., Kagi, H., Prikhod'ko, V. S., Arai, S., 2004. Evidence for subduction-related components in the subcontinental mantle from low $^{3}He/^{4}He$ and $^{40}Ar/^{36}Ar$ ratio in mantle xenoliths from Far Eastern Russia. Chem Geol 207, 237-259, doi: 10.1016/j.chemgeo.2004.03.007.

Yatsevich, I., Honda, M., 1997. Production of nucleogenic neon in the Earth from natural radioactive decay. J Geophys Res-Sol Ea 102, 10291-10298.

Yokochi, R., Marty, B., 2004. A determination of the neon isotopic composition of the deep mantle. Earth Planet Sc Lett 225, 77-88, doi: 10.1016/j.espl.2004.06.010.

York, D., 1969. Least squares fitting of a straight line with correlated errors. Earth Planet Sc Lett 5, 320-324.

Zindler, A., Hart, S., 1986. Chemical geodynamics. Annual Review of Earth and Planetary Sciences 14, 493-571.

Zindler, A., Jagoutz, E., Goldstein, S., 1982. Nd, Sr and Pb isotopic systematics in a 3-component mantle - A new perspective. Nature 298, 519-523.

Chapter 4: Constraints from I-Pu-U-Xe systematics in Southwest Indian Ridge basalts on mantle volatile evolution and the timing of the Moon-forming giant impact

ABSTRACT

We present high-precision measurements of the fission isotopes of xenon (Xe) in basalts from the Southwest Indian Ridge (SWIR) between 16 and 25°E. Corrections for syn- to post-eruptive atmospheric contamination yield the Xe isotopic compositions of SWIR mantle sources. We solve for the proportions of mantle Xe derived from the primordial mantle Xe budget, recycling of atmospheric Xe, decay of short-lived ^{129}I, fission of extinct ^{244}Pu and fission of extant ^{238}U. Xe isotope systematics evident in SWIR basalts and other mantle-derived samples provide new insights into the integrated history of mantle source degassing and regassing. We find that recycled atmospheric Xe dominates the Xe inventories of the SWIR Western and Eastern Orthogonal Supersegment mantle sources (~80-90% of ^{132}Xe is recycled in origin), consistent with results from studies of plume-influenced basalts from Iceland (Mukhopadhyay, 2012) and the Rochambeau Rift (Pető et al., 2013). The prevalence of recycled atmospheric Xe in mantle sources indicates incorporation of depleted recycled material into even primitive mantle sources; accordingly, depleted lithophile isotopic compositions in mantle sources with primitive He and Ne do not indicate a non-chondritic bulk silicate Earth. While significant regassing of the mantle is evident, we also find differences in the extent of degassing of the MORB and plume sources. MORB sources are consistently characterized by a lower fraction of fission Xe derived from Pu-fission, indicating a

greater extent of degassing relative to the plume source. To further investigate constraints from fission Xe systematics on early and long-term degassing of the upper mantle, we develop a parameterized two-stage model of MORB source degassing. Using the simplest early degassing scenario and our determinations of $^{129}Xe^*/^{136}Xe_{Pu}$ in MORB sources, we compute an age of the last episode of catastrophic upper mantle outgassing of 44-70 Myr after the start of the Solar System. The Moon-forming giant impact therefore likely occurred prior to ~70 Myr.

4.1. INTRODUCTION

As Earth accreted, the terrestrial volatile inventory was set by a competition between volatile delivery by accreting material and loss by degassing and impact-driven ejection to space. The early Earth environment was likely disrupted by multiple giant impact and atmospheric ejection events (Tucker and Mukhopadhyay, 2014). The Moon-forming giant impact occurred in the end stages of Earth's accretion and initiated the final catastrophic outgassing and bulk volatile ejection event on the early Earth. Subsequent to this event (Harrison, 2009), the planet settled into a regime of long-term, lower-magnitude exchange of volatiles between the mantle and exosphere (atmosphere, oceans and crust) in association with plate tectonics. The chemistry of volatiles in the mantle today may thus provide insight into processes that shaped the volatile inventories of terrestrial reservoirs on a variety of timescales.

The diverse array of radiogenic, fissiogenic and primordial isotopes of Xe serves as a powerful set of tools to explore the history of delivery, degassing and recycling of volatiles into mantle sources. The light, stable non-radiogenic isotopes ^{124}Xe, ^{126}Xe, ^{128}Xe and ^{130}Xe are primordial isotopes; terrestrial inventories for these isotopes were established during accretion. Radiogenic ^{129}Xe was produced by β-decay of the extinct nuclide ^{129}I ($t_{1/2}$ = 15.7 Ma) in the first ~90 Myr of Earth history. Fissiogenic ^{131}Xe, ^{132}Xe, ^{134}Xe, ^{136}Xe are produced in distinct, characteristic proportions by the fission of extinct short-lived ^{244}Pu ($t_{1/2}$ = 80.0 Myr) and extant long-lived ^{238}U ($t_{1/2}$ = 4.468 Gyr). A full set of Xe isotopic compositions measured in mid-ocean ridge basalts (MORBs) and plume-derived basalts thus provide information about the evolution of mantle source volatile budgets on a broad range of timescales.

Previous studies have demonstrated the potential for precise determinations of I-Pu-U-Xe systematics in mantle-derived basalts to shed light on the degassing histories of terrestrial reservoirs. Butler et al. (1963) attributed the first resolved ^{129}Xe excess relative to atmosphere in Harding County CO_2 well gas to ^{129}I decay in the early Earth, and noted that preservation of ^{129}Xe excesses in the mantle indicates that the Earth's interior was never completely outgassed or homogenized with the atmospheric Xe reservoir. Boulos and Manuel (1971) measured Harding County well gases from the Bueyeros field with improved precision and confirmed ^{129}Xe excesses relative to air. The authors also resolved fission Xe isotope excesses relative to air in the well gas, and noted their average compositions were consistent with a ~1:3 mixture of Pu-fission Xe and U-fission Xe. The proportion of well gas fission Xe derived from ^{244}Pu fission sets limits on the degassing history of the well gas mantle source since Pu-fission Xe is only produced for the first ~500 Myr. However, due to the large uncertainties in their measurements, Boulos and Manuel (1971) could not rule out either a pure Pu-fission or pure U-fission origin for the observed Xe excesses.

Wetherill (1975) formulated an expression for the I-Pu-Xe "formation interval" of the Earth, which dates the end of accretion assuming open system quantitative degassing of Xe until accretion is complete, and closed system retention of Xe thereafter. Using existing well gas data (Boulos and Manuel, 1971; Butler et al., 1963), Wetherill (1975) calculated an accretion interval of 127 Myr after the formation of ordinary chondrite Bjurböle. Pepin and Phinney (1976) calculated a more rapid formation interval of 67 ± 20 Myr based on additional measurements. Phinney et al. (1978) found that although no Pu-fission contribution of ^{131,132,134,136}Xe was required to explain their improved

measurements of Harding County well gases, a contribution of up to 20% Pu-fission Xe could be tolerated within their uncertainties. Based on this limit, they calculated an upper limit formation interval of 76 Myr relative to the formation of ordinary chondrites. Staudacher and Allegre (1982) reported measurements of Xe isotope excesses in MORBs, and computed a formation interval of 50-75 Myr after the formation of meteorites, consistent with the results from well gases. Subsequent precise determinations of Xe excesses in the MORB popping rock 2ΠD43 (Kunz et al., 1998) gave a terrestrial formation interval of ~78 Myr after the start of the Solar System and a fraction of fission Xe from Pu-fission of 32 ± 10%. However, the authors noted that the model of quantitative outgassing during accretion and subsequent perfect retention was overly simplistic, and applying a two-stage exponential degassing model, suggested that retention of radiogenic and fissiogenic Xe began 50-70 Myr after the start of the Solar System.

Lastly, based on averages of measured MORB and well gas compositions (Caffee et al., 1999; Kunz et al., 1998), Pepin and Porcelli (2006) calculated formation intervals of ~95-100 Myr for both the MORB mantle source and the atmosphere, and a distinct formation interval from the well gas data of 22-47 Myr. To preserve a distinct Xe isotopic signature indicative of a shorter formation interval (and thus less early degassing), the well gas mantle must have remained distinct and at least partially isolated from the MORB source for most of Earth history. However, well gas mantle Ne and Ar isotopes are indistinguishable from those observed in MORBs (e.g., Ballentine et al., 2005; Holland and Ballentine, 2006; Moreira et al., 1998). Combined Ne-Ar-Xe systematics would require that the well gas mantle source retained its distinct Xe signature from early

degassing but independently evolved K-Ar and U-Th-Ne systematics indistinguishable from the mantle source of MORBs.

In this study, we present high-precision Xe isotopic data for a set of MORB glass samples dredged from the Southwest Indian Ridge between 16°E and 25°E (Figure 4.1). These samples are a subset of the 14 basalt glass samples from the SWIR between 7°E and 25°E previously analyzed for He, Ne, Ar, Xe and CO_2 abundances and Ne, Ar and Xe ($^{129}Xe/^{130}Xe$ and $^{136}Xe/^{130}Xe$) isotopic compositions (Parai et al., 2012). Here we report further analyses of fission isotopes of Xe (^{131}Xe, ^{132}Xe, ^{134}Xe and ^{136}Xe) for samples from the SWIR Orthogonal Supersegment (Figure 4.1), a 630 km region of the SWIR removed from the influence of known mantle plumes. Parai et al (2012) found large magnitude variations in mantle source $^{40}Ar/^{36}Ar$ and $^{129}Xe/^{130}Xe$ ratios between the Western and Eastern Orthogonal Supersegment (where "mantle source" signifies that measured values are corrected for air contamination; see Section 2.1), and argued that these variations reflect heterogeneous incorporation of recycled atmospheric Ar and Xe in the SWIR MORB mantle source.

Here we investigate the integrated history of MORB source degassing and regassing evident in the Xe isotope systematics of SWIR basalts. We discuss our new high precision data and place them in context with an overview of I-Pu-U-Xe systematics in other MORB and plume-derived basalts, as well as CO_2-rich well gases (Holland and Ballentine, 2006; Mukhopadhyay, 2012; Pető et al., 2013; Tucker et al., 2012). To interpret our determinations of the mantle source ratios of radiogenic $^{129}Xe^*$ to Pu-fission $^{136}Xe_{Pu}$ and the fraction of fission Xe derived from Pu-fission, we develop a forward model of upper mantle degassing that takes into account timescales of accretion,

chemical fractionation during delivery of volatiles to the growing Earth, partial volatile retention prior to the last giant impact (≈ end of accretion), and ongoing exponential degassing over Earth history in association with mantle processing and plate tectonics. We thus harness the range of radiogenic, fissiogenic and primordial isotopes of Xe in order to constrain the history of volatile delivery, degassing and exchange between terrestrial reservoirs over Earth history.

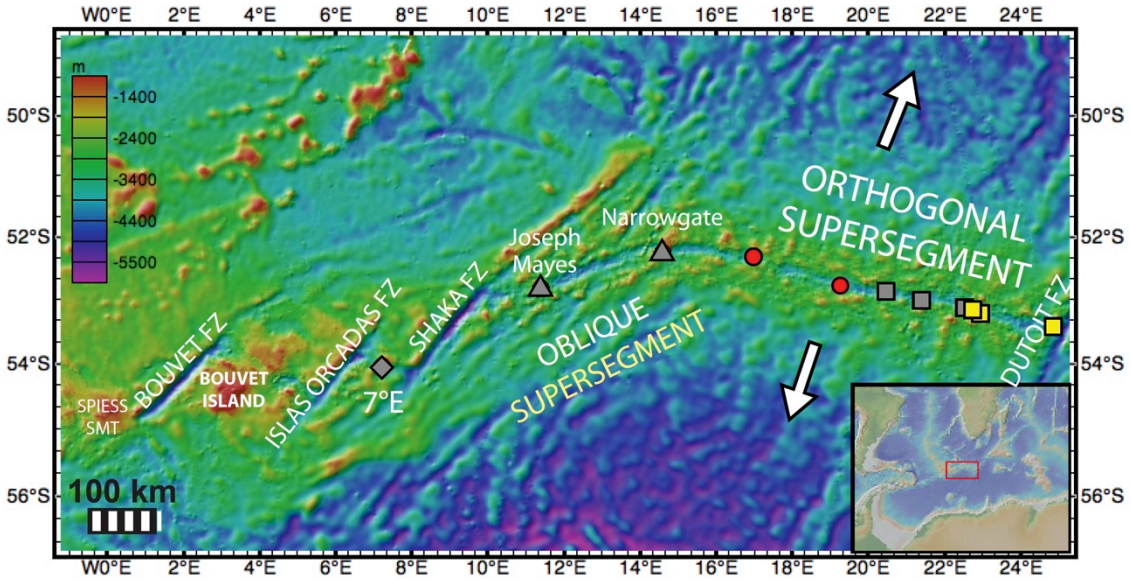

Figure 4.1 Map of the Southwest Indian Ridge study area. Symbols give locations of samples analyzed for He, CO_2, Ne, Ar and Xe compositions (Chapter 3; Parai et al., 2012). Red and yellow symbols represent samples discussed here for Xe fission isotopes.

4.2. SAMPLES AND METHODS

Xenon isotopic compositions were determined for six MORB glass samples dredged from the Southwest Indian Ridge between 16°E and 25°E: three samples from the S.A. Agulhas expedition AG22 (AG22 1-1, AG22 1-4, AG22 9-2 and AG22 13-1)

and two samples from the R/V Knorr expedition KN162-7 (KN162-7 11-25 and KN162-7 22-14). Previous studies have characterized the major element, trace element and radiogenic lithophile isotopic compositions of these samples (Kurz et al., 1998; Mahoney et al., 1992; Standish, 2006; Standish et al., 2008), as well as their He, Ne, Ar, Xe and CO_2 abundances and Ne, Ar and Xe ($^{129}Xe/^{130}Xe$ and $^{136}Xe/^{130}Xe$) isotopic compositions (Georgen et al., 2003; Parai et al., 2012; Standish, 2006). In this study, we focus on the fission isotopes of Xe (^{131}Xe, ^{132}Xe, ^{134}Xe and ^{136}Xe) in samples removed from the influence of known mantle plumes. We divide the study area into two regions based on observed variations in $^{40}Ar/^{36}Ar$ and $^{129}Xe/^{130}Xe$ isotopic composition (Parai et al., 2012): SWIR Western Orthogonal Supersegment (AG22 1-1, AG22 1-4 and KN162-7 11-25) and SWIR Eastern Orthogonal Supersegment (KN162-7 22-14, AG22 9-2 and AG22 13-1). We have noted previously that AG22 1-1 and 1-4 overlap in every isotope space (Chapter 3; Parai et al., 2012). These are rocks from a single dredge and are likely to sample a single flow; therefore, we consider them together as a single sample in all computations.

4.2.1 Sample preparation, gas extraction and mass spectrometry

The largest available glass chips (3-10 mm) were targeted for rare gas analysis, since the largest chips may host large intact vesicles. Chips exhibiting light surface alteration were leached in dilute nitric acid for 10-15 minutes and ultrasonically cleaned. Clean glass chips were washed in acetone and dried at room temperature to limit diffusion and thermal stress on the vesicular glass. One to five grams of glass were

loaded into a stainless steel piston crusher, baked at ~90-100°C for 24 hours, and then pumped for an additional 7-14 days until blanks were low and stable.

Samples were step-crushed under ultra-high vacuum using a hydraulic ram in order to release magmatic gases trapped in vesicles. Active gases were removed by sequential exposure to hot and cold SAES getters. The inert gases were trapped on a cryogenic cold finger and sequentially released to the mass spectrometer volume. He, Ne, Ar and Xe abundances and Ne, Ar and Xe isotopic compositions were measured on a Nu Noblesse noble gas mass spectrometer operating in multicollection mode. Data were obtained over 2 years in 4 sets of measurements. Procedural blanks were monitored during the step-crushing process. Xe blanks were typically ~2% of the measured sample ^{130}Xe signal. Blanks were stable, low and statistically indistinguishable from air in isotopic composition. All measured sample Xe isotope ratios reflect some degree of syn- to post-eruptive atmospheric contamination. Therefore, no blank corrections were made to the abundances or isotope ratios reported in Appendix 3, Table A4.1. Each sample step-crush was bracketed by multiple air standard runs, which were used to calibrate sensitivity and mass discrimination as a function of signal size. A total of 1,280 heavy noble gas air standard runs were analyzed over the 2 year SWIR analytical campaign, with signal sizes ~ 10^{-15} to 10^{-13} cc STP ^{130}Xe. Uncertainties in the Xe isotope ratios for each step-crush are based on the reproducibility of air standards of comparable signal size analyzed within the same time period.

4.2.2 Corrections for syn- to post-eruptive atmospheric contamination

Variable syn- to post-eruptive air contamination affects all measurements of Xe in mantle-derived rocks (e.g., Kunz et al., 1998; Moreira et al., 1998; Mukhopadhyay, 2012; Staudacher and Allegre, 1982; Trieloff and Kunz, 2005; Trieloff et al., 2000). Corrections for syn- to post-eruptive air contamination are required to accurately characterize the mantle source (see Chapter 3, Section 2.4). Measured values can be modeled as two-component mixtures between the unknown mantle source isotopic composition and the known atmospheric composition. Well-defined mixing arrays in $^{129}Xe/^{132}Xe$-$^{40}Ar/^{36}Ar$ space allow us to determine mantle source $^{129}Xe/^{132}Xe$ composition by fitting and extrapolation to mantle source $^{40}Ar/^{36}Ar$ values, which have been determined based on $^{40}Ar/^{36}Ar$-$^{20}Ne/^{22}Ne$ systematics (Chapter 3; Parai et al., 2012). The correction for atmospheric contamination is a total least-squares hyperbolic extrapolation for mantle $^{129}Xe/^{132}Xe$ (Figure 4.2, Figure A4.1). Mantle source $^{130}Xe/^{132}Xe$, $^{131}Xe/^{132}Xe$, $^{134}Xe/^{132}Xe$ and $^{136}Xe/^{132}Xe$ are determined by total least squares linear regression against $^{129}Xe/^{132}Xe$ (Figure A4.2-A4.8) and extrapolation to the mantle source $^{129}Xe/^{132}Xe$ compositions. Correlated errors are taken into account after York (1969; York et al., 2004). Mantle source Xe isotopic compositions are reported in Table 4.1. We use ^{132}Xe as the normalizing isotope as it is the most abundant Xe isotope: a relatively high signal in the normalizing isotope reduces the uncertainty in the measured isotopic ratio and minimizes the error correlation between isotope ratios. Thus, ^{132}Xe-normalized ratios provide the best precision in our determinations of mantle source Xe isotopic compositions.

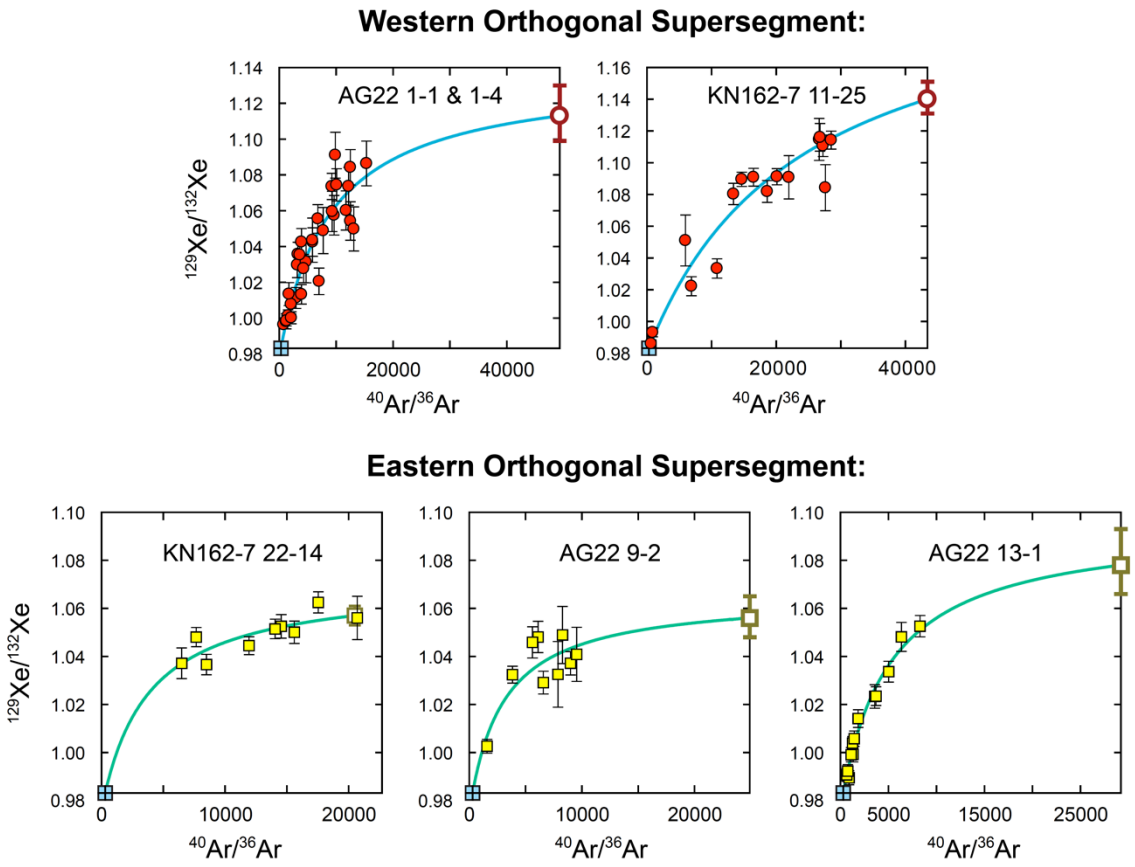

Figure 4.2 Correction for syn- to post-eruptive atmospheric contamination to determine mantle source $^{129}Xe/^{132}Xe$. For each sample, step-crushing generates an array reflecting variable degrees of atmospheric contamination. For samples with well-defined hyperbolic mixing arrays in $^{129}Xe/^{132}Xe$ – $^{40}Ar/^{36}Ar$ space, best fit hyperbolae yield extrapolated mantle source $^{129}Xe/^{132}Xe$ (bold open symbols) at mantle source $^{40}Ar/^{36}Ar$ values determined previously (Chapter 3; Parai et al., 2012). We note that for Eastern Orthogonal Supersegment samples, the extrapolation is not very sensitive to the mantle $^{40}Ar/^{36}Ar$ as best fit hyperbolae asymptote with respect to the x-axis at $^{129}Xe/^{132}Xe$ values of ~1.06 to 1.08. In contrast, measured values in Western Orthogonal Supersegment sample reach $^{129}Xe/^{132}Xe$ of ~1.12.

4.2.3 Linear least squares determination of initial, recycled atmospheric, Pu- and U-fissiogenic Xe components in the SWIR mantle source

The present-day $^{131,132,134,136}Xe$ inventory in mantle sources can be modeled as a mixture of four components: (1) an initial Xe budget that is solar, chondritic or U-Xe

Table 4.1 SWIR mantle source Xe isotopic compositions

Sample	$^{129}Xe/^{132}Xe$	+1σ	–1σ	$^{130}Xe/^{132}Xe$	1σ	$^{131}Xe/^{132}Xe$	1σ	$^{134}Xe/^{132}Xe$	1σ	$^{136}Xe/^{132}Xe$	1σ
AG22 1-1 & 1-4	1.113	+0.017	–0.014	0.1474	0.0009	0.7580	0.0041	0.4225	0.0023	0.3739	0.0021
KN162-7 11-25	1.140	+0.011	–0.009	0.1466	0.0006	0.7671	0.0022	0.4262	0.0014	0.3786	0.0012
KN162-7 22-14	1.057	+0.004	–0.004	0.1486	0.0004	0.7769	0.0016	0.4075	0.0008	0.3553	0.0008
AG22 9-2	1.056	+0.009	–0.008	0.1492	0.0006	0.7818	0.0024	0.4067	0.0012	0.3519	0.0012
AG22 13-1	1.078	+0.015	–0.012	0.1488	0.0007	0.7701	0.0029	0.4143	0.0015	0.3634	0.0015
Avg Western OSS	1.127	+0.014	–0.014	0.1470	0.0005	0.7664	0.0019	0.4237	0.0011	0.3754	0.0010
Avg Eastern OSS	1.064	+0.007	–0.007	0.1487	0.0003	0.7761	0.0012	0.4095	0.0007	0.3572	0.0006

(a theoretical composition derived from meteorite data; Pepin, 2000) in composition; (2) recycled atmospheric Xe; (3) Pu-fission Xe produced within the first ~500 Myr of Earth history and retained in the mantle; and (4) U-fission Xe retained in the mantle. ^{244}Pu and ^{238}U each produce fission ^{131,132,134,136}Xe in characteristic proportions that are distinct from the ^{131,132,134,136}Xe spectra in Earth's atmosphere and in primitive materials such as carbonaceous chondrites. Accordingly, we may describe the Xe isotopic composition of the mantle source today with four equations of the form:

$$x_{init}\left(\frac{^{\zeta}Xe}{^{132}Xe}\right)_{init} + x_{atm}\left(\frac{^{\zeta}Xe}{^{132}Xe}\right)_{atm} + x_{Pu}\left(\frac{^{\zeta}Xe}{^{132}Xe}\right)_{Pu} + x_{U}\left(\frac{^{\zeta}Xe}{^{132}Xe}\right)_{U} = \left(\frac{^{\zeta}Xe}{^{132}Xe}\right)_{mantle} \quad \text{Eq. 4.1}$$

where ζ = ^{130}Xe, ^{131}Xe, ^{134}Xe and ^{136}Xe; x is the molar mixing proportion of ^{132}Xe; *init* designates the initial mantle composition, modeled here using either solar wind, average carbonaceous chondrite (AVCC) or U-Xe; *atm* designates recycled atmospheric Xe; *Pu* designates Pu-fission Xe; and *U* designates U-fission Xe. Component Xe isotopic spectra and references are given in Table 4.2. The ^{132}Xe mixing proportions each fall between 0 and 1 and sum to 1:

$$0 \le x \le 1 \quad \text{Eq. 4.2}$$

$$x_{init} + x_{atm} + x_{Pu} + x_{U} = 1 \quad \text{Eq. 4.3}$$

Therefore, we have four unknowns (the ^{132}Xe mixing proportions, x) and five linear equations relating those unknowns. We find the linear least squares solution to this over-determined system A**x** = **b**, where A is a matrix of mixing endmember isotopic compositions (Table 4.2), **b** is a vector of mantle source Xe isotopic compositions, and **x** is the best fit vector of ^{132}Xe mixing proportions.

Table 4.2 Xenon endmember component compositions

Component	$^{130}Xe/^{132}Xe$	$^{131}Xe/^{132}Xe$	$^{134}Xe/^{132}Xe$	$^{136}Xe/^{132}Xe$
Atmosphere[1]	0.1513	0.7895	0.3880	0.3296
Solar wind[2]	0.1661	0.8272	0.3666	0.2985
AVCC[3]	0.1626	0.8200	0.3836	0.3233
U-Xe[4]	0.1654	0.8262	0.3516	0.2740
Pu-fission[5]	0	0.2777	1.0413	1.1198
U-fission[6]	0	0.1449	1.4370	1.7375

[1]Basford et al. (1973)

[2]Wieler and Baur (1994); Pepin et al. (1995)

[3]Average carbonaceous chondrite; Pepin (1991, 2000)

[4]Pepin (2000); Pepin and Porcelli (2002)

[5]Error-weighted average of data from Alexander et al. (1971), Lewis (1975) and Hudson et al. (1989)

[6]Error-weighted average of data from Wetherill (1953), Hebeda et al. (1987), Eikenberg et al. (1993) and Ragettli et al. (1994)

Based on our solutions for the mixing proportions of initial Xe, recycled atmospheric Xe, Pu-fission Xe and U-fission Xe, we compute the ratios of $^{136}Xe_{Pu}/(^{136}Xe_{Pu}+^{136}Xe_{U})$ and $^{129}Xe^{*}/^{136}Xe_{Pu}$:

$$^{136}Xe_{Pu} = \left[^{132}Xe\right] \cdot x_{Pu} \left(\frac{^{136}Xe}{^{132}Xe}\right)_{Pu} \quad \text{Eq. 4.4}$$

$$^{136}Xe_{U} = \left[^{132}Xe\right] \cdot x_{U} \left(\frac{^{136}Xe}{^{132}Xe}\right)_{U} \quad \text{Eq. 4.5}$$

$$\left[\frac{^{136}Xe_{Pu}}{^{136}Xe_{Pu} + ^{136}Xe_{U}}\right] = \left[\frac{x_{Pu}\left(\frac{^{136}Xe}{^{132}Xe}\right)_{Pu}}{x_{Pu}\left(\frac{^{136}Xe}{^{132}Xe}\right)_{Pu} + x_{U}\left(\frac{^{136}Xe}{^{132}Xe}\right)_{U}}\right] \quad \text{Eq. 4.6}$$

$$^{129}Xe^{*} = \left[^{132}Xe\right] \cdot \left[\left(\frac{^{129}Xe}{^{132}Xe}\right)_{mantle} - x_{init}\left(\frac{^{129}Xe}{^{132}Xe}\right)_{init} - x_{atm}\left(\frac{^{129}Xe}{^{132}Xe}\right)_{atm}\right] \quad \text{Eq. 4.7}$$

$$\left(\frac{^{129}Xe^{*}}{^{136}Xe_{Pu}}\right)=\left[\frac{\left(\frac{^{129}Xe}{^{132}Xe}\right)_{mantle}-\left[x_{init}\left(\frac{^{129}Xe}{^{132}Xe}\right)_{init}+x_{atm}\left(\frac{^{129}Xe}{^{132}Xe}\right)_{atm}\right]}{x_{Pu}\left(\frac{^{136}Xe}{^{132}Xe}\right)_{Pu}}\right] \quad \text{Eq. 4.8}$$

where [^{132}Xe] denotes the concentration of ^{132}Xe; we note that the ratios are not dependent on [^{132}Xe].

The uncertainties in the mixing proportions of ^{132}Xe are determined by Monte Carlo error propagation. Values for the vector of mantle source compositions **b** are randomly drawn from a population distributed normally around the best mantle source values with a dispersion given by the 1 sigma uncertainties reported in Table 4.3. Based on 1x10^6 random drawings of **b**, we collect statistics on the 1x10^6 corresponding solution vectors, **x**, and on the distributions of resulting ratios $^{136}Xe_{Pu}/(^{136}Xe_{Pu}+^{136}Xe_{U})$ and $^{129}Xe^{*}/^{136}Xe_{Pu}$.

4.3. RESULTS

The SWIR mantle source $^{129}Xe/^{132}Xe$ and $^{130,131,134,136}Xe/^{132}Xe$ compositions (corrected for syn- to post-eruptive atmospheric contamination) are shown in Figure 4.2 and Figures A4.2-A4.8, respectively, and reported in Table 4.1. The linear least squares solutions for mixing proportions of ^{132}Xe are reported in Table 4.3 and illustrated in Figure 4.3 and Figures A4.9-A4.10. Mixing proportion results for Equatorial Atlantic depleted MORB (Tucker et al., 2012) and plume-derived samples from Iceland (Mukhopadhyay, 2012) and the Rochambeau Rift (Pető et al., 2013) are also shown in Figure 4.3 for comparison. The median and 68% confidence intervals for the $^{129}Xe^{*}/^{136}Xe_{Pu}$, $^{136}Xe_{Pu}/(^{136}Xe_{Pu}+^{136}Xe_{U})$ and fraction of ^{132}Xe from recycled atmospheric

Table 4.3 Linear least squares solutions for mixing proportions of ^{132}Xe

		initial mantle:								
		Solar wind			*AVCC*			*U-Xe*		
		median	**+1σ**	**–1σ**	**median**	**+1σ**	**–1σ**	**median**	**+1σ**	**–1σ**
SWIR Western	**recycled atmosphere**	0.799	0.066	0.066	0.850	0.069	0.073	0.767	0.065	0.065
Orthogonal Supersegment	**initial mantle**	0.155	0.061	0.061	0.111	0.068	0.064	0.186	0.060	0.060
	Pu-fission	0.022	0.010	0.010	0.014	0.011	0.011	0.016	0.007	0.007
	U-fission	0.024	0.005	0.005	0.025	0.006	0.006	0.031	0.003	0.003
	$^{129}Xe^*/^{136}Xe_{Pu}$	7.3	6.6	2.3	10.8	40.3	4.8	9.8	7.6	2.9
	$^{136}Xe_{Pu}/(^{136}Xe_{Pu}+^{136}Xe_U)$	0.37	0.15	0.17	0.27	0.20	0.21	0.25	0.09	0.10
SWIR Eastern	**recycled atmosphere**	0.877	0.039	0.039	0.891	0.043	0.043	0.865	0.039	0.039
Orthogonal Supersegment	**initial mantle**	0.096	0.036	0.036	0.084	0.040	0.040	0.107	0.036	0.036
	Pu-fission	0.013	0.006	0.006	0.011	0.007	0.007	0.009	0.004	0.004
	U-fission	0.015	0.003	0.003	0.014	0.004	0.004	0.019	0.002	0.002
	$^{129}Xe^*/^{136}Xe_{Pu}$	7.1	6.5	2.3	8.3	14.3	3.2	10.6	10.7	3.5
	$^{136}Xe_{Pu}/(^{136}Xe_{Pu}+^{136}Xe_U)$	0.36	0.15	0.16	0.32	0.19	0.20	0.22	0.09	0.11
MORB average[1]	$^{129}Xe^*/^{136}Xe_{Pu}$	7.8	3.1	1.8	9.4	5.5	2.7	10.5	3.8	2.2
	$^{136}Xe_{Pu}/(^{136}Xe_{Pu}+^{136}Xe_U)$	0.33	0.09	0.09	0.28	0.11	0.10	0.23	0.06	0.06
plume-influenced	$^{129}Xe^*/^{136}Xe_{Pu}$	2.6	2.6	0.2	2.9	0.4	0.1	4.0	1.0	0.7
average[2]	$^{136}Xe_{Pu}/(^{136}Xe_{Pu}+^{136}Xe_U)$	0.97	0.03	0.17	0.96	0.03	0.18	0.59	0.07	0.07

For skewed distributions, +1σ and –1σ give 68% confidence limits.
[1]this study; Tucker et al. (2012)
[2]Mukhopadhyay (2012); Pető et al. (2013)

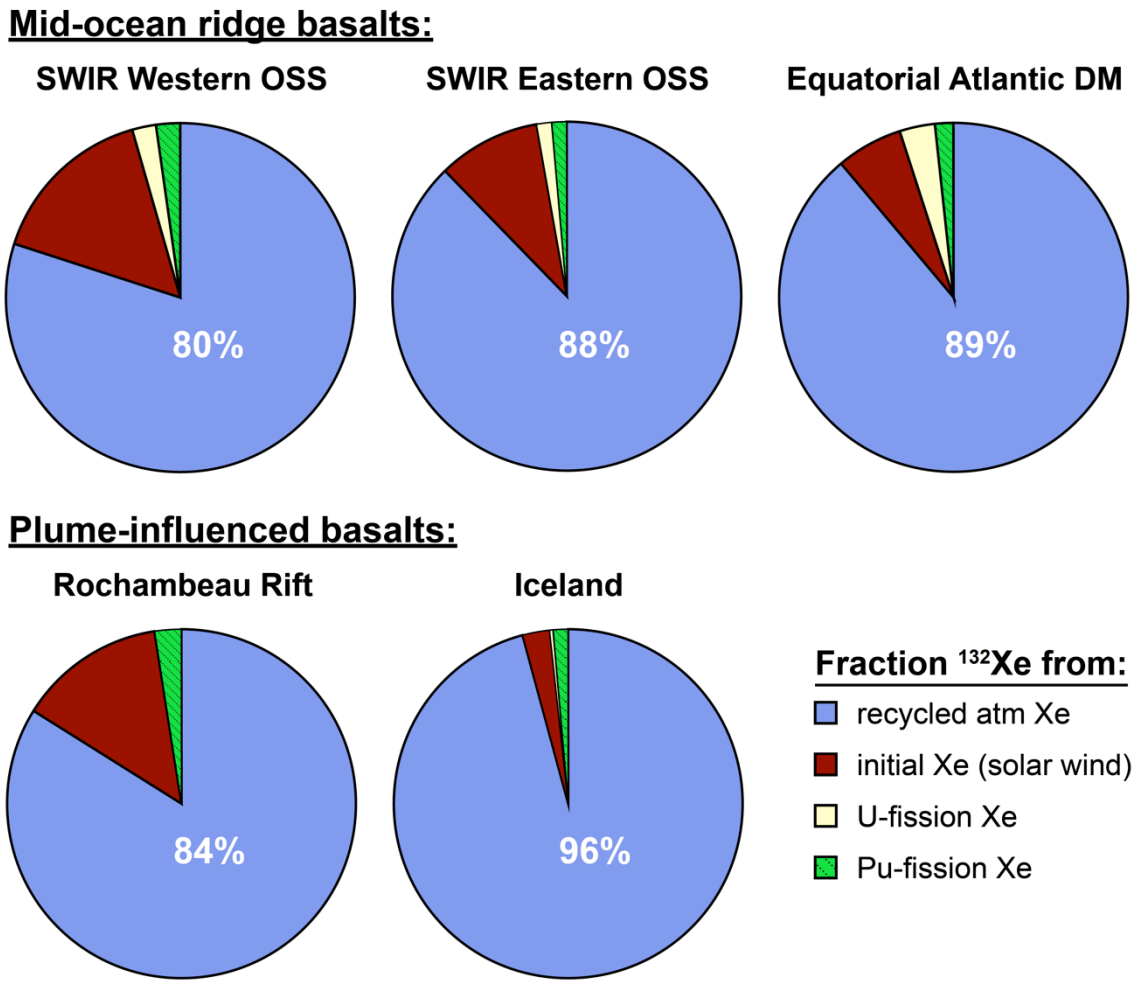

Figure 4.3 Pie charts illustrating the median proportions of present-day mantle ^{132}Xe derived from recycled atmosphere, initial mantle (solar wind shown here; see Figures A4.9 and A4.10 for AVCC and U-Xe results), U-fission and Pu-fission in SWIR Western and Eastern Orthogonal Supersegment mantle sources. Results for Equatorial Atlantic depleted MORB (Tucker et al., 2012), Rochambeau Rift (Pető et al., 2013) and Iceland (Mukhopadhyay, 2012) are shown for comparison. Recycled atmospheric Xe uniformly dominates the mantle Xe budget (percentages given in white). Fission Xe in the mantle sources of plume-influenced basalts is primarily derived from Pu-fission.

Xe for SWIR West and SWIR East are shown in Figures 4.4, 4.5 and 4.6, along with results for Equatorial Atlantic depleted MORBs (Tucker et al., 2012). Results for plume-influenced samples from Iceland (Mukhopadhyay, 2012) and the Rochambeau Rift (Pető et al., 2013) are also shown for comparison in Figures 4.4–4.6.

Our results indicate that mantle source ^{132}Xe budgets are uniformly dominated by the recycled atmospheric component (Figures 4.3, 4.6). 80% of the ^{132}Xe in the SWIR Western Orthogonal Supersegment mantle source and 88% of the ^{132}Xe in the SWIR Eastern Orthogonal Supersegment mantle source is recycled atmospheric Xe (using solar wind as the initial mantle Xe). Similarly, 89% of the ^{132}Xe in the Equatorial Atlantic depleted MORB source is recycled atmospheric Xe (Tucker et al., 2012). Samples from sources influenced by mantle plumes have 84% (Rochambeau Rift; Pető et al., 2013) and 96% (Iceland; Mukhopadhyay, 2012) of ^{132}Xe derived from recycled atmosphere. Thus, even in samples with the most primitive Ne isotopic compositions, more than 80% of the Xe is recycled atmospheric Xe.

$^{129}Xe^*/^{136}Xe_{Pu}$ in the SWIR mantle sources are $7.3\ ^{+6.6}_{-2.3}$ (68% confidence intervals) for SWIR Western Orthogonal Supersegment and $7.1\ ^{+6.5}_{-2.3}$ for SWIR Eastern Orthogonal Supersegment using solar wind for the initial mantle Xe (Table 4.3; Figure 4.4). These ratios are consistent with values of $9.0\ ^{+9.4}_{-3.3}$ computed for Equatorial Atlantic depleted MORBs. We use SWIR Western and Eastern Orthogonal Supersegment $^{129}Xe^*/^{136}Xe_{Pu}$ values together with Equatorial Atlantic depleted MORB (Tucker et al., 2012) $^{129}Xe^*/^{136}Xe_{Pu}$ to compute an error-weighted average value for MORBs of $7.8\ ^{+3.1}_{-1.8}$ with solar wind as the initial mantle Xe (Table 4.3; Figure 4.7) Using average carbonaceous

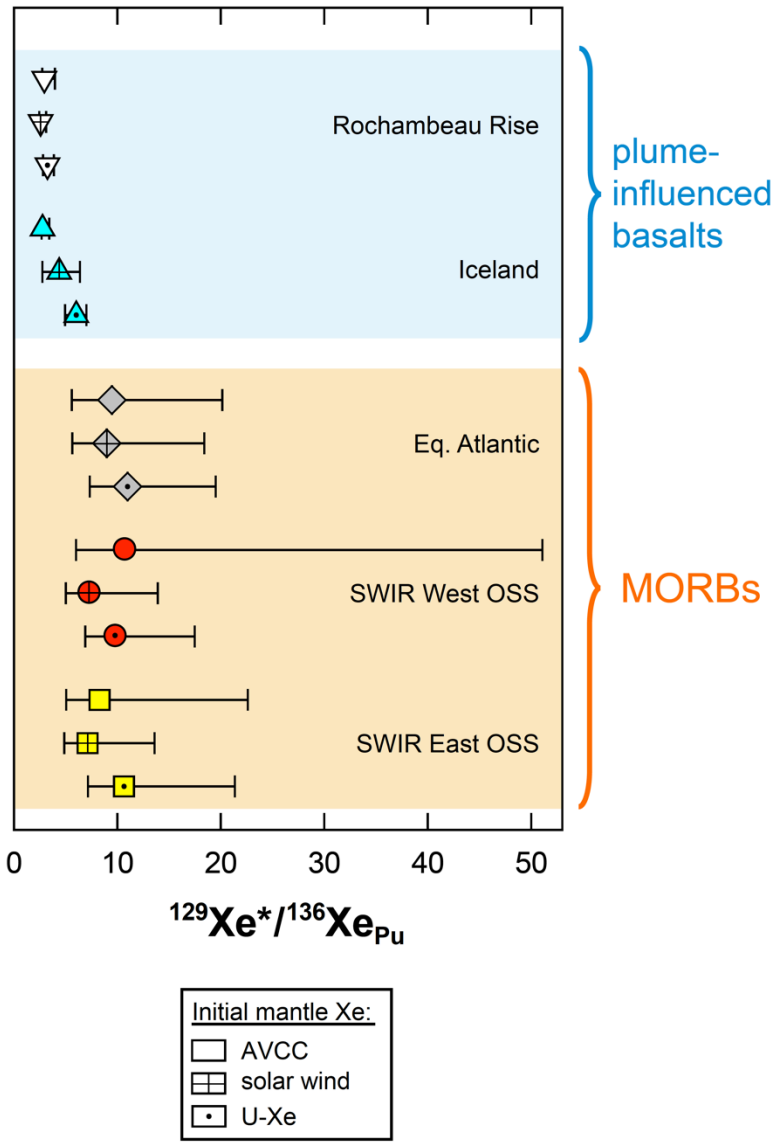

Figure 4.4 Medians and 68% confidence intervals determined by Monte Carlo error propagation for $^{129}Xe^*/^{136}Xe_{Pu}$ are shown for SWIR Western Orthogonal Supersegment, SWIR Eastern Orthogonal Supersegment and Equatorial Atlantic (Tucker et al., 2012) MORB sources. Results for mantle sources of plume-influenced basalts from the Rochambeau Rift (Pető et al., 2013) and Iceland (Mukhopadhyay, 2012) are shown for comparison. Results using AVCC (open symbols; top), solar wind (crossed symbols; middle) and U-Xe (dotted symbols; bottom) for the initial mantle Xe are indicated. Regardless of the choice of initial mantle Xe (AVCC, solar wind or U-Xe), mantle sources of plume-influenced basalts are uniformly characterized by lower $^{129}Xe^*/^{136}Xe_{Pu}$ values (medians range from ~2.5-6) relative to MORB sources (medians range from ~7-11).

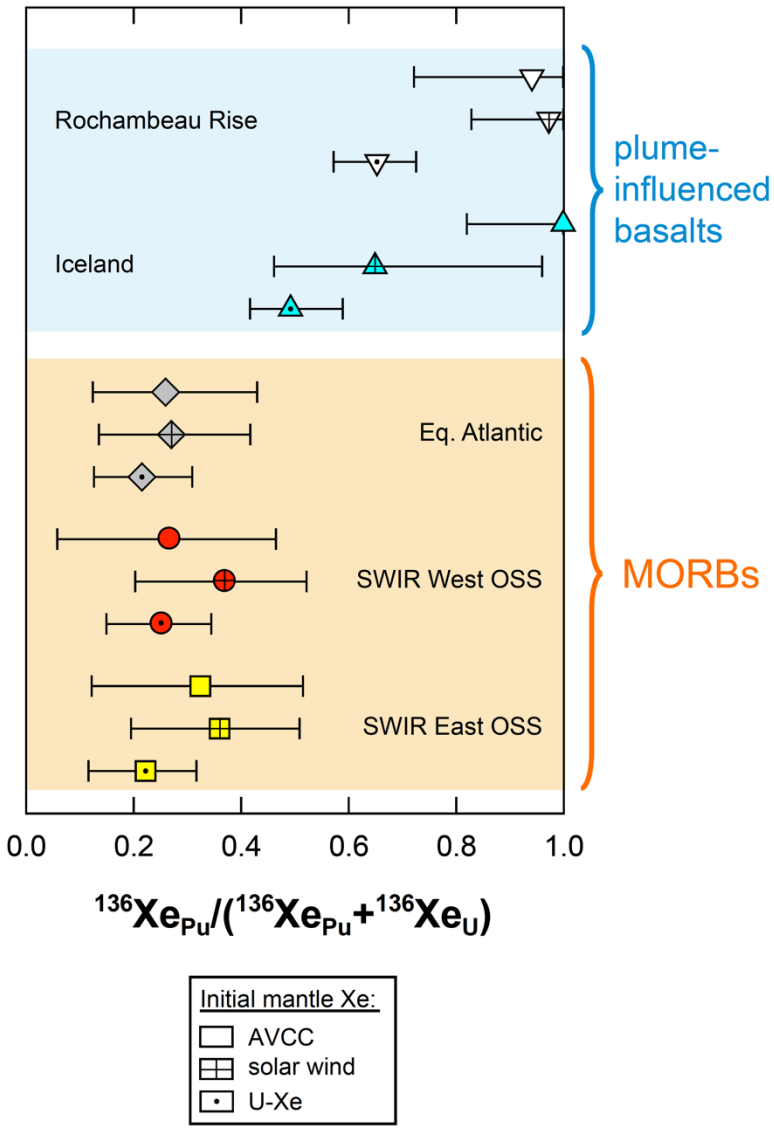

Figure 4.5 Medians and 68% confidence intervals determined by Monte Carlo error propagation for the fraction of fission Xe derived from Pu-fission, $^{136}Xe_{Pu}/(^{136}Xe_{Pu+}{}^{136}Xe_{U})$, are shown for SWIR Western Orthogonal Supersegment, SWIR Eastern Orthogonal Supersegment and Equatorial Atlantic (Tucker et al., 2012) MORB sources. Results for mantle sources of plume-influenced basalts from the Rochambeau Rift (Pető et al., 2013) and Iceland (Mukhopadhyay, 2012) are shown for comparison. Symbols as in Figure 4.4. Regardless of the choice of initial mantle Xe (AVCC, solar wind or U-Xe), mantle sources of plume-influenced basalts are uniformly characterized by higher $^{136}Xe_{Pu}/(^{136}Xe_{Pu+}{}^{136}Xe_{U})$ values (medians range from ~0.49-1.0) relative to MORB sources (medians range from ~0.22-0.37).

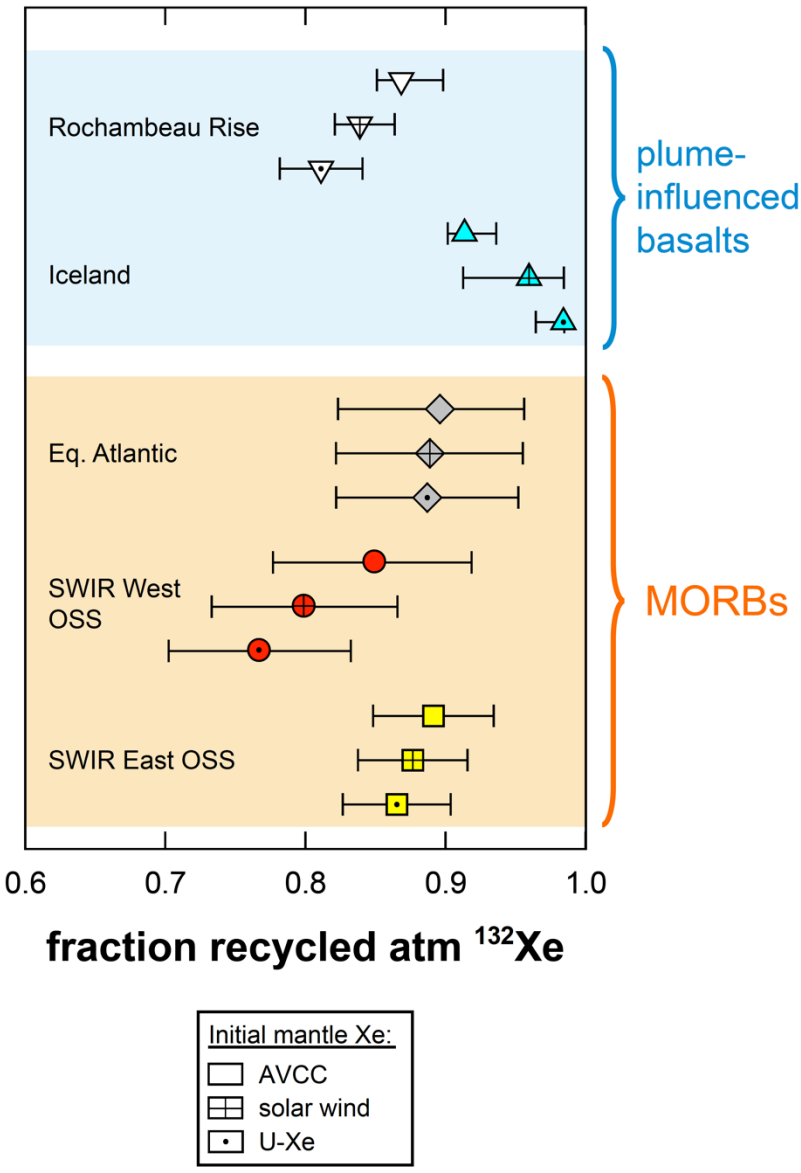

Figure 4.6 Medians and 68% confidence intervals determined by Monte Carlo error propagation for the proportion of mantle ^{132}Xe derived from recycled atmosphere are shown for SWIR Western Orthogonal Supersegment, SWIR Eastern Orthogonal Supersegment and Equatorial Atlantic (Tucker et al., 2012) MORB sources. Results for mantle sources of plume-influenced basalts from the Rochambeau Rift (Pető et al., 2013) and Iceland (Mukhopadhyay, 2012) are shown for comparison. Symbols as in Figure 4.4. Recycled atmospheric Xe dominates the present-day mantle Xe budget. We note that regardless of the choice of initial mantle Xe (AVCC, solar wind or U-Xe), the Eastern Orthogonal Supersegment consistently exhibits a higher proportion of recycled atmospheric Xe relative to the Western Orthogonal Supersegment. This observation supports the interpretation that large variations in SWIR Orthogonal Supersegment ^{40}Ar/^{36}Ar and ^{129}Xe/^{130}Xe reflect heterogeneous incorporation of recycled atmospheric heavy noble gases (Chapter 3; Parai et al., 2012).

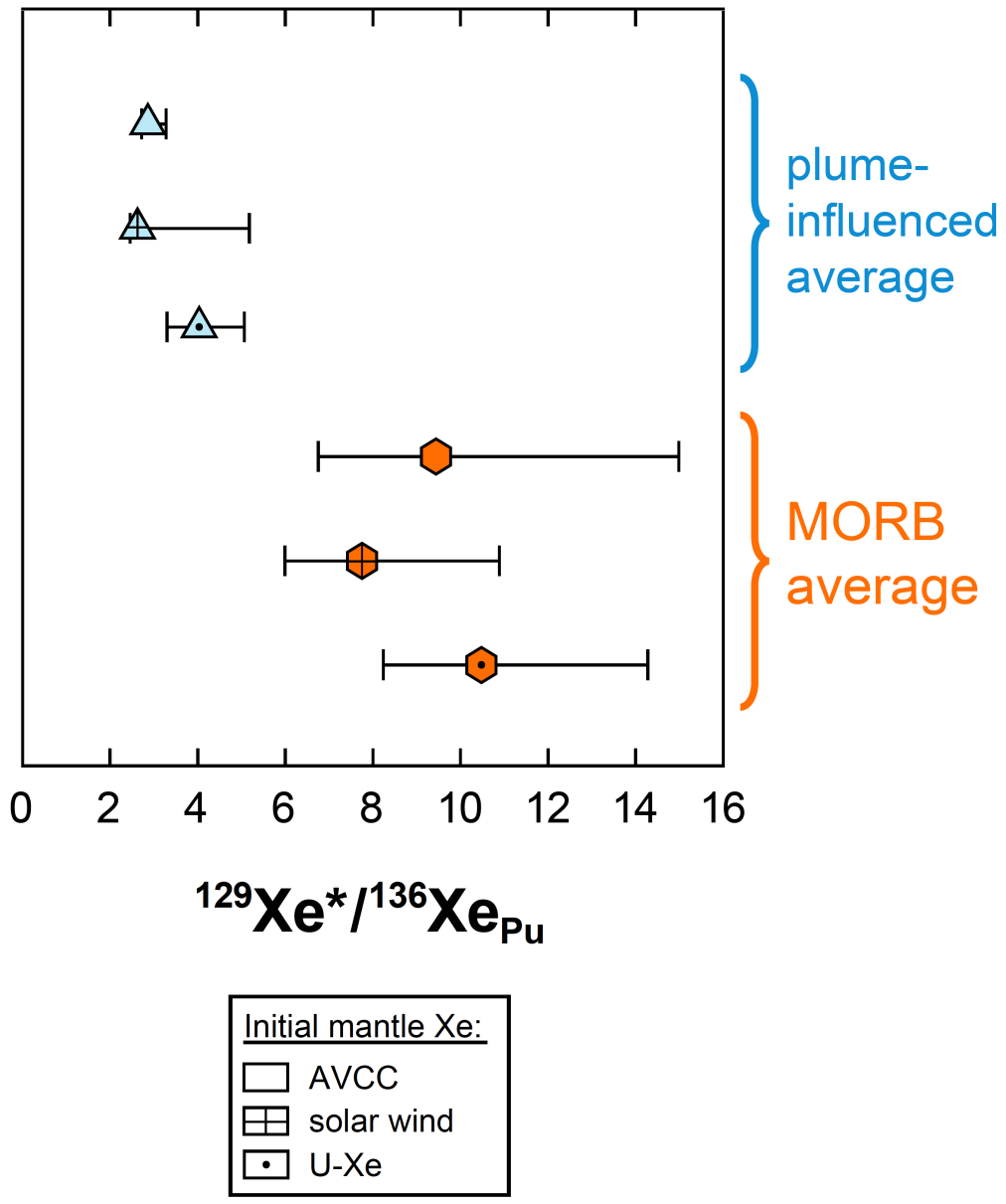

Figure 4.7 Error-weighted averages and 68% confidence intervals for $^{129}Xe^*/^{136}Xe_{Pu}$ in MORB sources (this study; Tucker et al., 2012) and the sources of plume-influenced basalts (Mukhopadhyay, 2012; Pető et al., 2013). Regardless of the choice of initial mantle Xe (AVCC, solar wind or U-Xe), mantle sources of plume-influenced basalts are uniformly characterized by lower $^{129}Xe^*/^{136}Xe_{Pu}$ values relative to MORB sources.

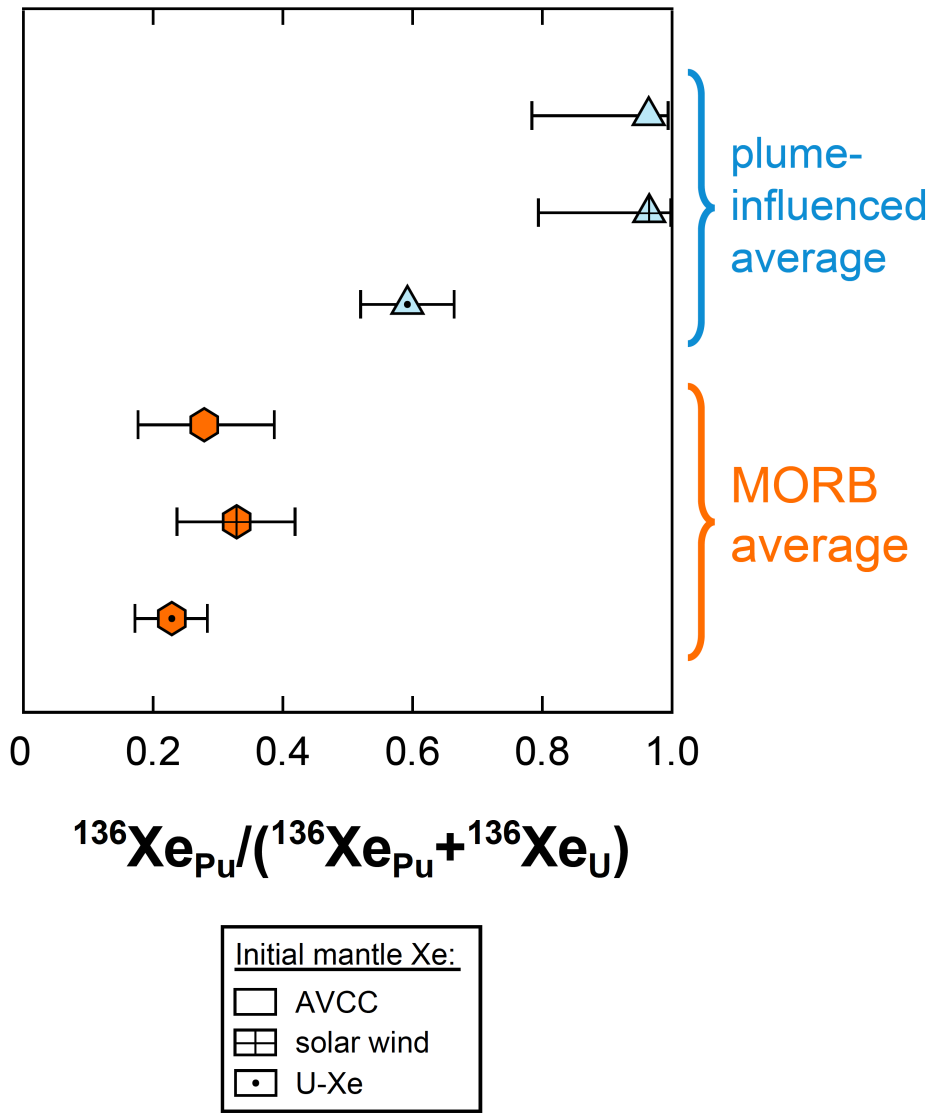

Figure 4.8 Error-weighted averages and 68% confidence intervals for $^{136}Xe_{Pu}/(^{136}Xe_{Pu+}{}^{136}Xe_{U})$ in MORB sources (this study; Tucker et al., 2012) and the sources of plume-influenced basalts (Mukhopadhyay, 2012; Pető et al., 2013). Regardless of the choice of initial mantle Xe (AVCC, solar wind or U-Xe), mantle sources of plume-influenced basalts are uniformly characterized by higher $^{136}Xe_{Pu}/(^{136}Xe_{Pu+}{}^{136}Xe_{U})$ values relative to MORB sources.

chondrite as the initial mantle Xe, $^{129}Xe^*/^{136}Xe_{Pu}$ values of 11 $^{+40}_{-4.8}$, 8.3 $^{+14.3}_{-3.2}$ and 9.5 $^{+11}_{-3.9}$ are computed for the SWIR Western Orthogonal Supersegment, Eastern Orthogonal Supersegment and Equatorial Atlantic depleted MORBs, respectively, giving an error-weighted MORB average $^{129}Xe^*/^{136}Xe_{Pu}$ of 9.4 $^{+5.5}_{-2.7}$ using AVCC as the mantle initial (Table 4.3). These estimates agree within error, indicating computed $^{129}Xe^*/^{136}Xe_{Pu}$ values are not strongly dependent on the choice of the mantle initial Xe component (Figures 4.4 and 4.7).

$^{136}Xe_{Pu}/(^{136}Xe_{Pu}+^{136}Xe_U)$ in the SWIR mantle sources are 0.37 $^{+0.15}_{-0.17}$ for SWIR Western Orthogonal Supersegment and 0.36 $^{+0.15}_{-0.16}$ for SWIR Eastern Orthogonal Supersegment, using solar wind for the initial mantle Xe (Table 4.3; Figure 4.5). These ratios are consistent with values of 0.27 $^{+0.15}_{-0.13}$ computed for Equatorial Atlantic depleted MORBs (Tucker et al., 2012), and give an error-weighted MORB average $^{136}Xe_{Pu}/(^{136}Xe_{Pu}+^{136}Xe_U)$ of 0.33 $^{+0.09}_{-0.09}$ (Figure 4.8). The values for plume-influenced mantle sources are 0.97 $^{+0.03}_{-0.14}$ for Rochambeau Rift (Pető et al., 2013) and 0.65 $^{+0.31}_{-0.19}$ for Iceland (Mukhopadhyay, 2012), giving a plume-influenced mantle error-weighted average of 0.96 $^{+0.03}_{-0.17}$ using solar wind as the initial mantle Xe (Table 4.3). Computed $^{136}Xe_{Pu}/(^{136}Xe_{Pu}+^{136}Xe_U)$ values are relatively insensitive to the choice of mantle initial Xe component (Figures 4.5 and 4.8). We note that MORB source $^{136}Xe_{Pu}/(^{136}Xe_{Pu}+^{136}Xe_U)$ ratios are consistently lower than plume source values.

4.4. A TWO-STAGE MODEL OF MORB SOURCE DEGASSING

In order to interpret the $^{129}Xe^*/^{136}Xe_{Pu}$ and $^{136}Xe_{Pu}/(^{136}Xe_{Pu}+^{136}Xe_U)$ ratios we have determined for MORB mantle sources (Figures 4.4, 4.5, 4.7 and 4.8), we develop a parameterized two-stage MORB source degassing model to explore both the early volatile evolution of the planet during accretion and the long-term history of degassing associated with mantle processing and plate tectonics. Our approach is to forward model upper mantle degassing throughout Earth history to identify regions of parameter space that are able to satisfy our constraints on the present-day $^{129}Xe^*/^{136}Xe_{Pu}$ and $^{136}Xe_{Pu}/(^{136}Xe_{Pu}+^{136}Xe_U)$ ratios simultaneously. Additional constraints from $^{129}Xe/^{130}Xe$ and $^4He/^3He$ may be applied to further test the parameter space under consideration.

Our two-stage degassing model incorporates 14 independent parameters (Table 4.4). We model accretion as a continuous function with 1 free parameter, though we may also use model outputs from N-body simulations of planetary growth for the mass of the growing Earth as a function of time (e.g., O'Brien et al., 2006; Raymond et al., 2009; Walsh et al., 2011). As the Earth accretes, 4 independent parameters describe I and Xe delivery to the mantle before and after the last giant impact (LGI): the delivery parameters *delI_preLGI, delI_postLGI*, *delXe_preLGI* and *delXe_postLGI* vary from 0 to 1 and define the partitioning of accreted I and Xe between the mantle and the surface reservoir, where 0 signifies that all I or Xe is sequestered in the surface reservoir and 1 signifies that all I or Xe is delivered to the mantle. Since some portion of the surface iodine budget may eventually be recycled to the interior over time (we take the MORB mantle and crust together to have bulk 7 ppb I; Deruelle et al., 1992), the *delI* parameters give the effective mantle-surface I partitioning during the lifetime of ^{129}I. Delivered Xe

Table 4.4 Two-stage degassing model parameters

Parameter	Min	Max	Classical Early Degassing	Description
Early degassing stage:				
α (Myr)	3	30	-	accretion time constant
delI_preLGI	0	1	1	delivery of iodine before last giant impact
delI_postLGI	0	1	1	delivery of iodine after last giant impact
retI_preLGI	0	1	1	retention of iodine before last giant impact
retI_LGI	0	1	1	retention of iodine during last giant impact
retI_postLGI	0	1	1	retention of iodine after last giant impact
delXe_preLGI	0	1	-	delivery of xenon before last giant impact
delXe_postLGI	0	1	-	delivery of xenon after last giant impact
retXe_preLGI	0	1	0	retention of xenon before last giant impact
retXe_LGI	0	1	1	retention of xenon during last giant impact
retXe_postLGI	0	1	1	retention of xenon after last giant impact
Long-term degassing stage:				
M_{res} (grams)	2.0×10^{27}	3.6×10^{27}	-	mass of the MORB source reservoir (50-90% of the whole mantle)
N_{res}	2	15	-	number of reservoir masses processed in stage 2
CCmodel	1	3	-	continental crust growth model

The mantle processing rate constant η depends on N_{res} and M_{res}. The scaling factor for ^{238}U extraction Q depends on M_{res} and CCmodel.

is tracked separately from radiogenic ^{129}Xe* produced within the mantle. Six independent parameters describe the retention of I and Xe in the growing mantle before, during and after the last giant impact event (*retI_preLGI, retI_LGI, retI_postLGI, retXe_preLGI, retXe_LGI* and *retXe_postLGI*), where a *retXe* value of 0.99 indicates that 1% of the mantle Xe budget is lost at each time step. The early degassing regime (stage 1) is driven by energetic accretionary impacts; after accretion is complete, the model shifts to a long-term degassing regime (stage 2) driven by mantle processing (described by two parameters: the mass of the MORB mantle reservoir, M_{res}, and the number of reservoir masses processed over 4.567 Gyr, N_{res}) and crustal growth associated with plate tectonics (1 parameter). Table 4.4 gives a brief description and the value range for each of the 14 parameters. Below we describe the two-stage model setup in detail and compare it with previous models of early terrestrial degassing. We then present model results to explore the key parameters that control volatile evolution in the MORB source mantle.

4.4.1 Model details

4.4.1.1 Early degassing stage

During the early degassing stage, volatiles are delivered to the mantle by accreting material but are also lost from the mantle by degassing. For each volatile species, independent parameters describe delivery and retention before and after the LGI, as well as retention during the LGI (Table 4.4). Earth's accretion is modeled as exponential growth parameterized by an accretion time constant α (Equation 4.9). The last giant impact event is constrained to the time period between 99% and 99.9% M_{Earth} accretion, since late accretion of material is limited to 0.1-1% M_{Earth} added after the last

giant impact based on the abundance pattern of highly siderophile elements (e.g., Bottke et al., 2010; Jacobson et al., 2014). Thus, the candidate LGI age range for a given model realization is set by the accretion time constant. The planet remains in the early degassing regime until it has accreted 99.99% M_{Earth}, at which point accretion is considered complete (see illustration in Figure 4.9).

$$M_{Earth}(t) = \left(1 - e^{-t/\alpha}\right) \quad \text{Eq. 4.9}$$

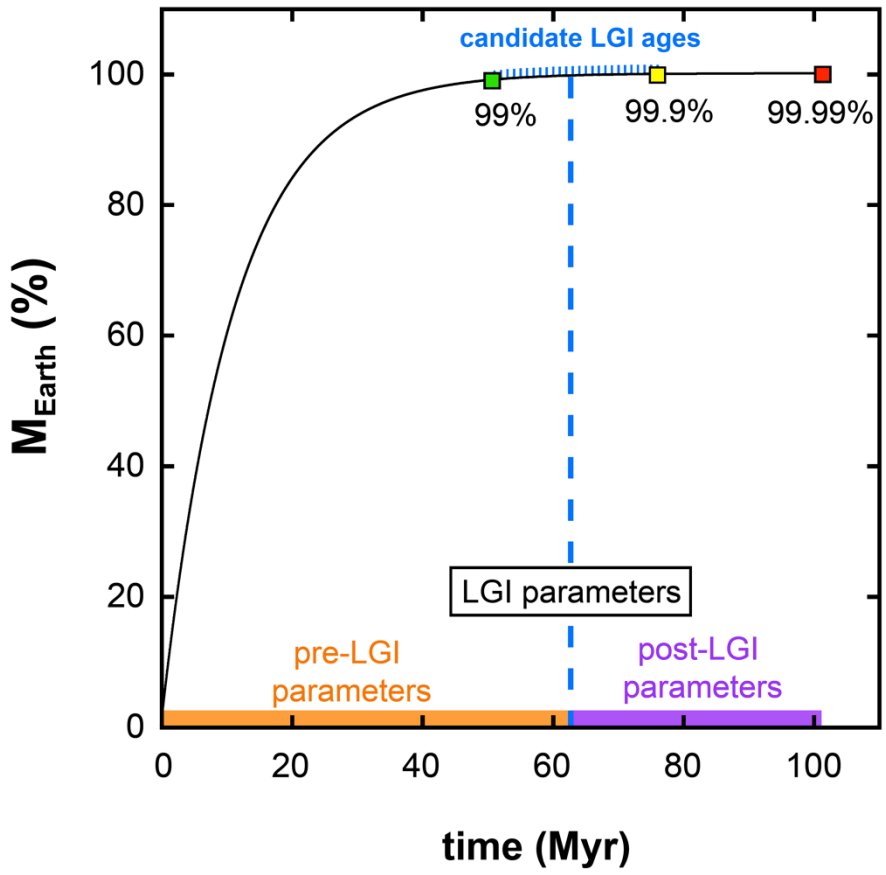

Figure 4.9 Illustration of early degassing stage for an accretion time constant of α = 11 Myr. The last giant impact occurs while the planet is between 99% and 99.9% accreted, such that the mass of material added to the Earth subsequent to the LGI is 0.1-1%. Therefore, in this example, candidate LGI ages range from 51 Myr (green box) to 76 Myr (yellow box) with 1 Myr time steps (blue hatch marks). For the time period prior to the last giant impact, pre-LGI parameters for I, Xe delivery and retention are applied (orange band). During the last giant impact, LGI I and Xe retention parameters are used (blue dashed line). After the last giant impact, post-LGI parameters are used (purple band) until the planet is 99.99% accreted (red box), at which point the early degassing stage ends.

The concentrations of ^{129}I, ^{244}Pu, ^{238}U, radiogenic $^{129}Xe^*$, fissiogenic $^{136}Xe_{Pu}$, fissiogenic $^{136}Xe_U$, delivered $^{129}Xe_{del}$ and delivered $^{130}Xe_{del}$ are tracked throughout the early degassing period (see Equations 4.10-4.19 below). Accreting material is assumed to have 7 ppb ^{127}I (Deruelle et al., 1992; Palme and O'Neill, 2004) and an initial $^{129}I/^{127}I$ ratio of $1.1x10^{-4}$ (Hohenberg et al., 1967). The small amount of material accreted after the last giant impact is modeled as more volatile-rich, with 450 ppb ^{127}I (based on the abundance in carbonaceous chondrites; McDonough and Sun, 1995). Incoming material has a U concentration corresponding to the present-day bulk silicate Earth 21 ppb U (McDonough and Sun, 1995; Palme and O'Neill, 2004), and the ^{244}Pu concentration is computed assuming an initial $^{244}Pu/^{238}U$ of 0.0068 (Hudson et al., 1989). The concentration of radiogenic $^{129}Xe^*$ evolves based solely on radioactive production and degassing (Equation 4.13); delivered $^{129}Xe_{del}$ and $^{130}Xe_{del}$ are tracked separately (Equations 4.18-4.19) to test whether sufficient radiogenic $^{129}Xe^*$ is retained in the mantle to raise the mantle $^{129}Xe/^{130}Xe$ above the delivered $^{129}Xe_{del}/^{130}Xe_{del}$ of 6.436 (Q-Xe component; Pepin and Porcelli, 2006) to $^{129}Xe/^{130}Xe$ values inferred for the ancient MORB mantle (~14; Mukhopadhyay et al., in prep). The concentrations of Pu and U are affected only by radioactive decay; all accreted Pu and U is delivered to the mantle and no outgassing of these refractory species occurs (Equations 4.14 and 4.16). Concentrations of fissiogenic $^{136}Xe_{Pu}$ and $^{136}Xe_U$ evolve based solely on production by spontaneous fission and degassing (Equations 4.15-4.17). The 11 free parameters that describe the early degassing period are summarized in Table 4.4 along with the total range of variation allowed in each parameter.

Equations describing the concentration of each species at a given time based on the previous time step are given below (Equations 4.10-4.19). Radioactive decay constants and fission yields are given in Table 4.5. As the decay of very short-lived species requires relatively fine time resolution, time evolution is modeled numerically with 0.01 Myr time steps in this early period. We assume that for each species, the degassing flux at any time is proportional to the abundance at that time, consistent with degassing based on solubility in a magma ocean environment. Degassing is described by a retention factor, where a retention factor of 0.99 signifies that at each time step, 99% of the gas is retained and 1% of the gas is lost by degassing. Independent variation in the retention of I and Xe allows exploration of the effect of I/Xe fractionation due to degassing, while independent variation in delivery parameters for I and Xe allow us to explore the effect of I/Pu and I/Xe fractionation upon delivery. At each time step, the overall concentration of a species is the mass-weighted average of the concentration in proto-planet (controlled by radioactive decay and retention) and the concentration in the delivered material.

Table 4.5 Radioactive decay constants and fission yields

Species	Decay constant λ	Fission yield of ^{136}Xe[1]
^{129}I	4.4150×10^{-8}	-
^{244}Pu	8.6643×10^{-9}	7.00×10^{-5}
^{238}U	1.5514×10^{-10}	3.43×10^{-8}
^{235}U	9.8486×10^{-10}	-
^{232}Th	4.9334×10^{-11}	-

[1]Fission yields from Ozima and Podosek (1983) and Ragettli et al. (1994)

$$dt = t_{now} - t_{last} \quad \text{Eq. 4.10}$$

$$dM = M_{now} - M_{last} \quad \text{Eq. 4.11}$$

$$^{129}I_{now} = \frac{(^{129}I_{last} * e^{-\lambda_{129}dt} * retI * M_{last} + {}^{129}I_0 * e^{-\lambda_{129}t_{now}} * delI * dM)}{M_{now}} \quad \text{Eq. 4.12}$$

$$^{129}Xe^{rad}_{now} = \frac{((^{129}Xe^{rad}_{last} + {}^{129}I_{last} * (1-e^{-\lambda_{129}dt})) * retXe * M_{last})}{M_{now}} \quad \text{Eq. 4.13}$$

$$^{244}Pu_{now} = \frac{(^{244}Pu_{last} * e^{-\lambda_{244}dt} * M_{last} + {}^{244}Pu_0 * e^{-\lambda_{244}t_{now}} * dM)}{M_{now}} \quad \text{Eq. 4.14}$$

$$^{136}Xe^{Pu}_{now} = \frac{((^{136}Xe^{Pu}_{last} + {}^{244}Pu_{last} * \left(1-e^{-\lambda_{244}dt}\right) * Y^{Pu}_{136}) * retXe * M_{last})}{M_{now}} \quad \text{Eq. 4.15}$$

$$^{238}U_{now} = \frac{(^{238}U_{last} * e^{-\lambda_{238}dt} * M_{last} + {}^{238}U_0 * e^{-\lambda_{238}t_{now}} * dM)}{M_{now}} \quad \text{Eq. 4.16}$$

$$^{136}Xe^{U}_{now} = \frac{((^{136}Xe^{U}_{last} + {}^{238}U_{last} * \left(1-e^{-\lambda_{238}dt}\right) * Y^{U}_{136}) * retXe * M_{last})}{M_{now}} \quad \text{Eq. 4.17}$$

$$^{130}Xe^{del}_{now} = \frac{\left(^{130}Xe^{del}_{last} * retXe * M_{last} + {}^{130}Xe_{del} * delXe * dM\right)}{M_{now}} \quad \text{Eq. 4.18}$$

$$^{129}Xe^{del}_{now} = \frac{\left(^{129}Xe^{del}_{last} * retXe * M_{last} + \left(\frac{^{129}Xe}{^{130}Xe}\right)_{del} * {}^{130}Xe_{del} * delXe * dM\right)}{M_{now}} \quad \text{Eq. 4.19}$$

For species affected by delivery and retention parameters, the time evolution of concentration is computed using the pre-LGI parameter values until the time of the last giant impact. For the time step of the last giant impact, LGI parameter values are used, and subsequent evolution is computed using the post-LGI parameter values until accretion is complete (99.99% M_{Earth}). We determine species evolution curves for each candidate LGI age between the time of 99% accretion and 99.9% accretion, with 1 Myr

resolution on candidate LGI ages (Figure 4.9). Consequently, model output from the early degassing period gives the concentrations of all tracked species at the time of 99.99% accretion as a function of the age of the LGI.

4.4.1.2 Long-term degassing stage

The results from the early degassing stage are input to a long-term degassing and chemical evolution model that tracks mantle processing at mid-ocean ridges and the partial sequestration of Pu and U in the continental crust over time. Long-term mantle evolution of ^{244}Pu, ^{238}U, ^{235}U, ^{232}Th, fissiogenic $^{136}Xe_{Pu}$, fissiogenic $^{136}Xe_{U}$ and radiogenic ^{4}He are computed using Equations 4.20-4.31. Since the early degassing stage may end as early as 27 Myr after the start of the Solar System (the time of 99.99% accretion using an accretion time constant $\alpha = 3$ Myr; Equation 4.9), evolution of ^{129}I and $^{129}Xe^*$ is also tracked throughout the long-term model (Equations 4.32-4.33). Lastly, we keep track of the degassing of primordial ^{3}He, delivered $^{130}Xe_{del}$ and $^{129}Xe_{del}$ to give a sense of the mantle $^{4}He/^{3}He$ and $^{129}Xe_T/^{130}Xe$ ratio ($^{129}Xe_T$ = radiogenic $^{129}Xe^*$ + delivered $^{129}Xe_{del}$) as a function of time given the long-term degassing parameters (Equations 4.34-4.36). Three parameters are used to explore the degassing of noble gases and the extraction of incompatible refractory elements from the MORB source over time: the mantle processing rate is parameterized based on the mass of the MORB source reservoir (M_{res}) and the number of reservoir masses processed over Earth history (N_{res}), while the extraction of incompatible refractory elements is modeled based on a continental crust growth model (CCmodel).

Equations 4.25–4.36 describe the concentration of each species at a given time based on the concentrations at the previous time step. Radioactive decay constants and fission yields are given in Table 4.5. We assume that Xe and He are perfectly incompatible during partial melting, such that degassing due to mantle processing reduces the concentration of Xe or He by the fraction dM/M_{res} at each time step. For instance, if 0.001% of the mass of the MORB source reservoir is processed in a given time step, then the concentration of ^{3}He in the bulk MORB source is reduced by 0.001% in that time step. U and Pu are also highly incompatible; however, the extraction of U, Th and Pu from the mantle at mid–ocean ridges is offset by recycling of U-, Th- and Pu-rich sediment at subduction zones at each time step. In order to model the net extraction of U, Th and Pu from the mantle, U, Th and Pu loss at each time step directly tracks continental crustal growth over time (Equations 4.23-4.28).

4.4.1.2.1 Mantle processing

The mantle processing rate is modeled as an exponential decay anchored to the present-day MORB source processing rate, assuming on average 10% partial melting at mid-ocean ridges (21 km^3/yr MORB production rate corresponds to 6.1×10^{17} g mantle processed per year). Equation 4.20 gives the mantle processing rate, $\dot{M}$, as a function of time, t. The expression for the amount of mass processed over a given time interval is given in Eq. 4.21. For each model realization, T is the duration of the long-term degassing stage (4.567 Gyr minus the time of 99.99% accretion) and η is a unitless parameter that is adjusted to control the total mantle mass processed over T years (a special case of Eq. 4.21 given by Eq. 4.22). We solve for the values of η that correspond

to N_{res} = [2,3,4,5,6,7,8,9,10,15] reservoir masses processed over T years, given a MORB source reservoir mass of $M_{res} = 2\times10^{27}$ g, 3×10^{27} g and 3.6×10^{27} g (50%, 75% and 90% of the mass of the whole mantle).

$$\dot{M}(t) = \dot{M}_{pres} e^{\frac{\eta(T-t)}{T}} \quad \text{Eq. 4.20}$$

mass processed between t_1 and t_2: $$dM_{t1}^{t2} = \dot{M}_{pres} \left(\frac{T}{\eta}\right) \left[e^{\frac{\eta(T-t_1)}{T}} - e^{\frac{\eta(T-t_2)}{T}}\right] \quad \text{Eq. 4.21}$$

total mass processed over T years: $$dM_0^T = \dot{M}_{pres} \left(\frac{T}{\eta}\right) [e^{\eta}-1] \quad \text{Eq. 4.22}$$

4.4.1.2.2 Continental crust growth models

We use three crustal growth models to test a range of growth rates similar to those proposed in the literature (Figure 4.10; e.g., Dhuime et al., 2012; McLennan and Taylor, 1982; Pujol et al., 2013). Two sigmoidal growth curves are adopted: one with relatively rapid growth (CCmodel 1) and one with more protracted crustal growth (CCmodel 2). CCmodel 3 builds the continental crust at a constant rate (linear growth) beginning 300 Myr after the start of the Solar System. We assume that the extraction of U and Pu is directly proportional to the extraction of continental crust from the MORB source reservoir over time. For each combination of M_{res} and CCmodel, we solve for the unique scaling factor Q that yields a present-day U concentration of 1.3 ppm U (Rudnick and Gao, 2003) in the continental crust reservoir (mass 2.2×10^{25} g; McLennan and Taylor, 1982; Rudnick and Gao, 2003) given a total bulk MORB source and continental crust U concentration equal to the bulk silicate Earth value of 21 ppb U (McDonough and Sun, 1995; Palme and O'Neill, 2004). We assume that Pu and U are not fractionated from one another by crustal extraction; thus, Pu extraction tracks U extraction based on the atomic

ratio of the two radioactive species at any given time. The expressions for the extraction of U, Pu and Th from the MORB source are given in Equations 4.25-4.28.

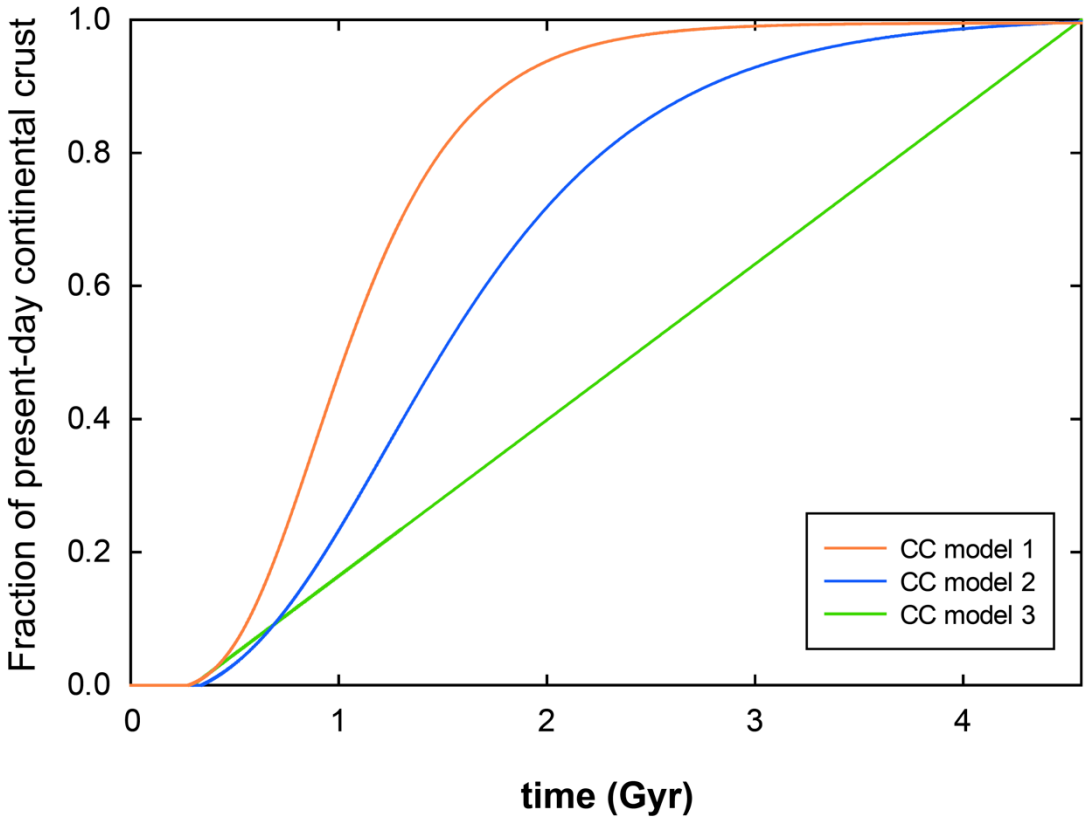

Figure 4.10 Continental crust growth models used for the long-term degassing stage. ^{238}U, ^{235}U and ^{232}Th (and a small amount of ^{244}Pu) extraction from the mantle by partial melting is offset by recycling of sediments at subduction zones at each time step. We model net extraction of U, Th and Pu from the mantle as linearly tracking continental crust growth over time (Equations 4.23-4.28). Three continental crust growth models are adopted: two sigmoidal curves that approximate literature continental crust growth curves (e.g., Dhuime et al., 2012; Pujol et al., 2013) and one linear growth curve.

$$dCC = CC_{now} - CC_{last} \quad \text{Eq. 4.23}$$

$$dU_{CC} = Q * dCC \quad \text{Eq. 4.24}$$

where Q is the scaling factor for ^{238}U extraction for a given M_{res} and CC model

$$^{238}U_{now} = {}^{238}U_{last}e^{-\lambda_{238}dt} - dU_{CC}$$ Eq. 4.25

$$^{244}Pu_{now} = {}^{244}Pu_{last}e^{-\lambda_{244}dt} - \left(\frac{^{244}Pu}{^{238}U}\right)_{now} * dU_{CC}$$ Eq. 4.26

$$^{235}U_{now} = {}^{235}U_{last}e^{-\lambda_{235}dt} - \left(\frac{^{235}U}{^{238}U}\right)_{now} * dU_{CC}$$ Eq. 4.27

$$^{232}Th_{now} = {}^{232}Th_{last}e^{-\lambda_{232}dt} - \left(\frac{^{232}Th}{^{238}U}\right)_{now} * dU_{CC}$$ Eq. 4.28

$$^{136}Xe^{U}_{now} = \left[{}^{136}Xe^{U}_{last} + {}^{238}U_{last} * \left(1 - e^{-\lambda_{238}dt}\right) * Y^{U}_{136}\right] * \left(1 - \frac{dM}{M_{res}}\right)$$ Eq. 4.29

$$^{136}Xe^{Pu}_{now} = \left[{}^{136}Xe^{Pu}_{last} + {}^{244}Pu_{last} * \left(1 - e^{-\lambda_{244}dt}\right) * Y^{Pu}_{136}\right] * \left(1 - \frac{dM}{M_{res}}\right)$$ Eq. 4.30

$$^{4}He_{now} =$$
$$\left[{}^{4}He_{last} + 8 * {}^{238}U_{last}\left(1 - e^{-\lambda_{238}dt}\right) + 7 * {}^{235}U_{last}\left(1 - e^{-\lambda_{235}dt}\right)\right.$$ Eq. 4.31
$$\left. + 6 * {}^{232}Th_{last}\left(1 - e^{-\lambda_{232}dt}\right)\right] * \left(1 - \frac{dM}{M_{res}}\right)$$

$$^{129}I_{now} = {}^{129}I_{last} * e^{-\lambda_{129}dt}$$ Eq. 4.32

$$^{129}Xe^{rad}_{now} = \left[{}^{129}Xe^{rad}_{last} + {}^{129}I_{last}(1 - e^{-\lambda_{129}dt})\right] * \left(1 - \frac{dM}{M_{res}}\right)$$ Eq. 4.33

$$^{3}He_{now} = {}^{3}He_{last} * \left(1 - \frac{dM}{M_{res}}\right)$$ Eq. 4.34

$$^{130}Xe^{del}_{now} = {}^{130}Xe^{del}_{last} * \left(1 - \frac{dM}{M_{res}}\right)$$ Eq. 4.35

$$^{129}Xe^{del}_{now} = {}^{129}Xe^{del}_{last} * \left(1 - \frac{dM}{M_{res}}\right)$$ Eq. 4.36

The range in half-lives of tracked radioactive species necessitates a tailored time step scheme for the long-term chemical evolution model: the time step must be fine enough to accurately capture radioactive decay of short-lived ^{129}I and ^{244}Pu early in Earth

history; however, subsequent to the extinction of ^{129}I and ^{244}Pu, a very fine time step is not required for accuracy and imposes a high computational cost. We carried out convergence tests in order to determine the optimal time resolution scheme that accurately captures decay of I, Pu, U, Th to at least three significant figures. Based on this analysis, the time step is 0.1 Myr from the time accretion has completed until 200 Myr after the start of the Solar System; 1 Myr until 1.3 Gyr after the start of the Solar System; and 5 Myr through the rest of Earth history to 4.567 Gyr.

4.4.2 Comparison with previous early Earth degassing models

In the classical view of early Earth degassing and I-Pu-Xe systematics, outgassing during accretion effectively removes all gaseous species from the silicate Earth until accretion is complete, after which point the mantle retains all radiogenic and fissiogenic Xe (e.g., Pepin and Phinney, 1976; Pepin and Porcelli, 2006; Phinney et al., 1978; Staudacher and Allegre, 1982; Wetherill, 1975). This view is overly simplistic: for example, such a model does not address observations of solar-like primitive He and Ne isotopic compositions in plume-related basalts (e.g., Harrison et al., 1999; Mukhopadhyay, 2012; Stuart et al., 2003; Yokochi and Marty, 2004), which indicate at least partial retention of volatiles acquired by equilibration with an early solar nebular atmosphere (e.g., Harper and Jacobsen, 1996; Tucker and Mukhopadhyay, 2014; Yokochi and Marty, 2004). Likewise, the classical model neglects the onset of low-magnitude outgassing associated with mantle processing within the lifetime of ^{244}Pu (e.g., Pepin and Phinney, 1976; Phinney et al., 1978; Staudacher and Allegre, 1982; Wetherill, 1975). Calculations of an I-Pu-Xe "formation interval" or "closure age" (used

interchangeably to describe the classical model) assume that any radiogenic $^{129}Xe^*$ and fissiogenic $^{136}Xe_{Pu}$ generated prior to the time of closure was lost by degassing; thus, all radiogenic and Pu-fission Xe in the mantle today was generated by radioactive decay in the mantle subsequent to the end of accretion (Equation 4.37). Using our result for the 68% confidence interval on the weighted average MORB source $^{129}Xe^*/^{136}Xe_{Pu}$ with solar wind initial mantle Xe, we compute a classical "closure age" range for the upper mantle of 53–70 Myr. Our results for average carbonaceous chondrite initial mantle Xe yield a classical "closure age" range of 44–66 Myr. These ages are significantly older than the MORB source closure age of ~100 Myr computed by Pepin and Porcelli (2006). Our results are similar to some previous estimates of closure age from both MORBs and well gases (~50-75 Myr; e.g., Kunz et al., 1998; Pepin and Phinney, 1976; Staudacher and Allegre, 1982); however, we note that these authors used atmospheric Xe as the initial mantle Xe budget and are therefore not directly comparable.

$$t_{closure} = \frac{1}{\lambda_{244} - \lambda_{129}} \times ln\left[\frac{\left(\frac{^{129}Xe^*}{^{136}Xe_{Pu}}\right)\left(\frac{^{238}U}{^{127}I}\right)_0\left(\frac{^{244}Pu}{^{238}U}\right)_0 Y_{136}^{Pu}}{\left(\frac{^{129}I}{^{127}I}\right)_0}\right] \qquad \text{Eq. 4.37}$$

We note that we are able to reproduce the classical "closure age" determination by forward modeling with an extremely short accretion time constant ($\alpha = 0.01$ Myr), assuming perfect delivery and retention of I at all times and a Xe retention parameter that switches from 0 to 1 at the candidate time of closure (see Table 4.4; classical degassing parameters). Ignoring degassing associated with mantle processing and any crustal growth prior to the time of ^{244}Pu extinction (i.e., neglecting the long-term degassing

stage), we compute $^{129}Xe^*/^{136}Xe_{Pu}$ for a range of candidate closure ages and find that ages in the range 53-70 Myr generate $^{129}Xe^*/^{136}Xe_{Pu}$ corresponding exactly to our 68% confidence interval on the weighted average MORB source $^{129}Xe^*/^{136}Xe_{Pu}$ (Table 4.3, Figure 4.7; solar wind initial mantle Xe). The relationship between closure age and $^{129}Xe^*/^{136}Xe_{Pu}$ is illustrated in Figure 4.11: early closure yields a higher $^{129}Xe^*/^{136}Xe_{Pu}$ as more ^{129}I is present at the time of closure to produce ^{129}Xe.

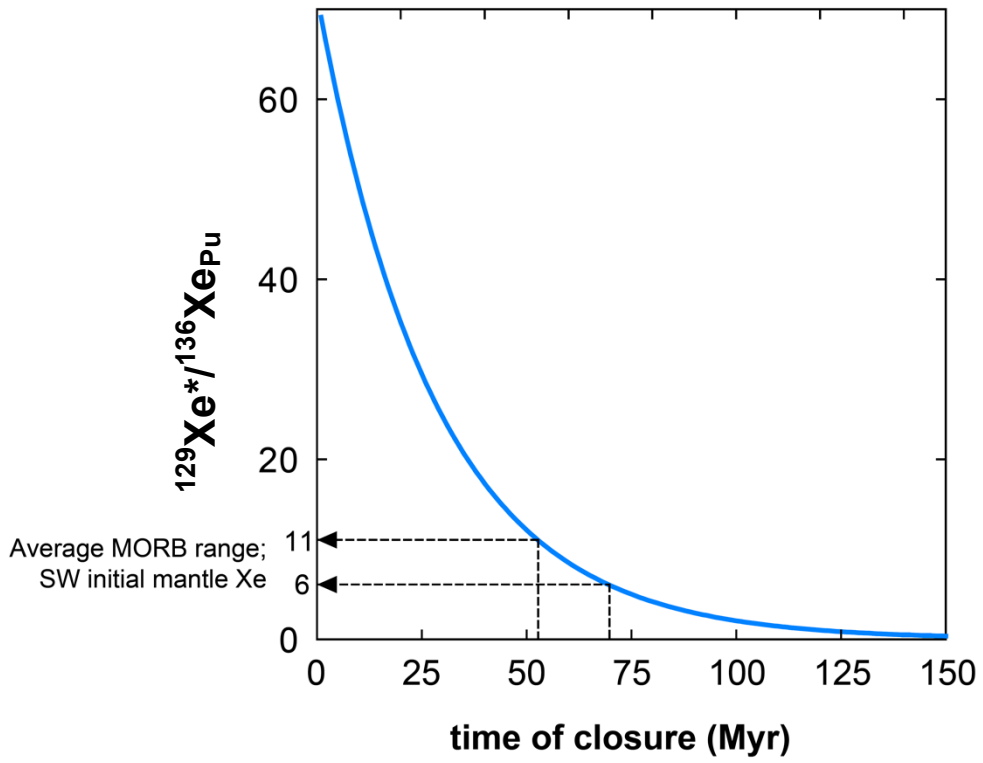

Figure 4.11 Forward modeled $^{129}Xe^*/^{136}Xe_{Pu}$ as a function of time of closure using classical early degassing model parameters (Table 4.4). We are able to reproduce the solutions for $t_{closure}$ attained by using the analytical expression given in Equation 4.37 and the 68% confidence interval limits for average MORBs (Figure 4.7; solar wind initial mantle Xe). $^{129}Xe^*/^{136}Xe_{Pu}$ decreases as a function of the time of closure, because less ^{129}I is live when the mantle begins to retain Xe.

Jacobsen and Harper (1996) developed analytical expressions relating $^{129}Xe^*/^{136}Xe_{Pu}$ and $^{136}Xe_{Pu}/(^{136}Xe_{Pu}+^{136}Xe_U)$ to the mean time of accretion, which

enabled consideration of continuous accretion in their early degassing model. The authors noted that I-Pu-Xe systematics only date the end of accretion if Xe is strongly degassed by the impact process; if radiogenic and fissiogenic Xe are not strongly degassed from impactors, then the system partially reflects the age of gas-dust fractionation in the proto-planetary disk rather than the end of accretion. Our model includes tools for exploration of I/Xe fractionation during delivery through the *delI* and *delXe* parameters. Delivered ^{129}Xe includes some radiogenic ^{129}Xe produced within the impactor and some primordial ^{129}Xe. However, the proportion of delivered ^{129}Xe that is primordial is poorly constrained at present. Therefore, while a treatment of partial (rather than total) I/Xe fractionation during accretion warrants further study, it beyond the scope of the current undertaking, and we use only radiogenic ^{129}Xe* grown within the mantle to calculate $^{129}Xe^*/^{136}Xe_{Pu}$.

Porcelli et al. (2001) noted that the presence of stable, non-radiogenic isotopes of Xe in the mantle with isotopic compositions distinct from air indicated partial retention of Xe in the mantle during accretion. Accordingly, the authors presented a model in which the Earth initially behaves as a closed system that retains all radiogenic and fissiogenic Xe. At some time t_{LGI}, the Moon-forming giant impact drives a discrete instantaneous partial depletion event, in which only some fraction *f* of the mantle Xe budget is retained. Subsequent to the instantaneous depletion event, the mantle again behaves as a closed system. We are able to reproduce the results of Porcelli et al. (2001) with our two-stage degassing model by prescribing a rapid accretion time constant (0.01 Myr), perfect delivery and retention of I (*delI* and *retI* = 1), and perfect Xe retention at all times except for the time of the LGI, at which the Xe retention is set to *f* (i.e., *retXe_preLGI* = 1; *retXe_LGI* = *f*; *retXe_postLGI* = 1). We will refer to similar scenarios in which efficient

retention is punctuated by strong outgassing at the time of the LGI as discrete loss event (DLE) scenarios. We again neglect degassing associated with mantle processing and sequestration of Pu in the growing continental crust prior to the time of ^{244}Pu extinction. Our results are shown as filled contours in Figure 4.12 with the contoured results of Porcelli et al. (2001) overlain as thick dashed lines. The authors estimated a mantle $^{129}Xe^*/^{136}Xe_{Pu}$ of 3.5-10 based on the Bravo Dome well gas data available at the time; we highlight our average MORB source 68% confidence interval in the figure as well. We note that for DLE scenarios, it is possible to preserve high $^{129}Xe^*/^{136}Xe_{Pu}$ ratios (>15) for relative late closures ages (>100 Myr); these systematics will be examined further in Section 4.4.3.3.

Azbel and Tolstikhin (1993) provide a very comprehensive treatment of I-Pu-U-Xe systematics. The authors explore a large number of parameters to account for the timescale of accretion, core formation, mantle differentiation and atmospheric escape, and track chemical fluxes between the atmosphere, crust, upper mantle, lower mantle and core over time. Based on their model, Azbel and Tolstikhin (1993) argue that I-Xe systematics do not provide strong constraints on the timescale of accretion. Instead, the authors argue that Pu-U-Xe systematics indicate a relatively slow timescale of accretion, as a low $^{136}Xe_{Pu}/(^{136}Xe_{Pu}+^{136}Xe_{U})$ value in the mantle may be attributed to low retention of Pu-fission Xe in a slowly-accreting early Earth. However, we note that MORB source $^{136}Xe_{Pu}/(^{136}Xe_{Pu}+^{136}Xe_{U})$ values reflect the integrated history of MORB mantle degassing, and that low $^{136}Xe_{Pu}/(^{136}Xe_{Pu}+^{136}Xe_{U})$ may be explained by long-term outgassing of Xe in association with plate tectonics and ongoing ingrowth of U-fission Xe. Our model shares some common features with the Azbel and Tolstikhin (1993) model: after accretion is

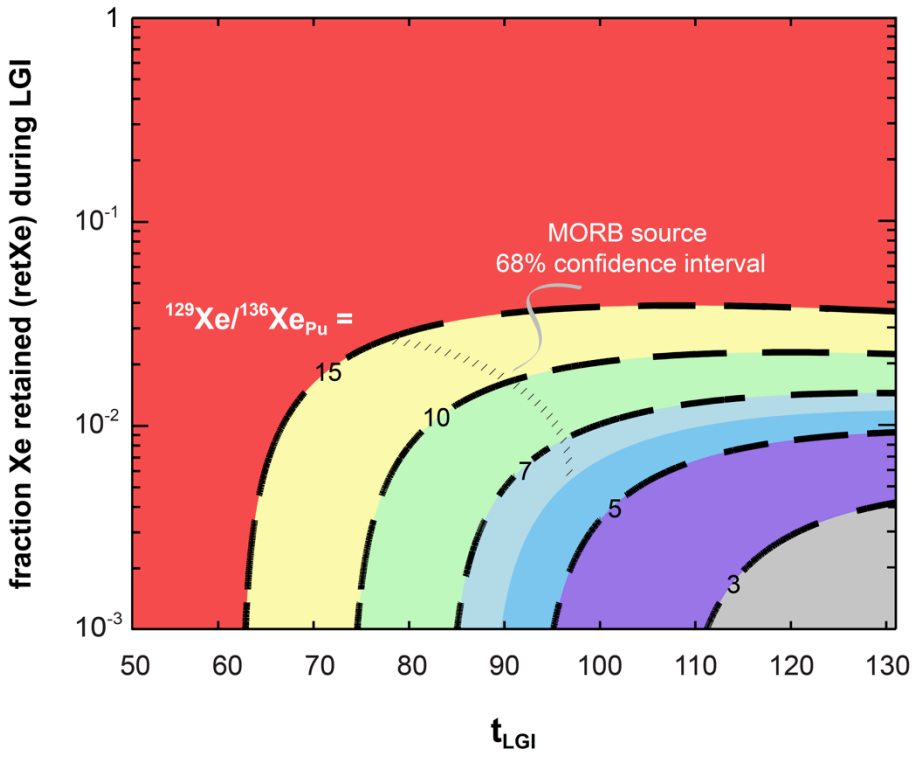

Figure 4.12 Forward modeled $^{129}Xe^*/^{136}Xe_{Pu}$ contoured as a function of the time of the last giant impact (t_{LGI}) and the fraction of Xe retained during a discrete loss event-type LGI (adapted from Porcelli et al., 2001). Xe is quantitatively retained before and after the LGI in this type of model (*retXe_preLGI* = *retXe_postLGI* = 1). Our model results are shown as filled color contours, and agree well with the results obtained by Porcelli et al. (2001; overlain as thick dashed black contours). We use 13 ppb ^{127}I for this computation in order to provide a direct comparison with Porcelli et al. (2001). The limits of the MORB source 68% confidence intervals given in Figure 4.7 (for all initial mantle Xe compositions) are highlighted. For discrete loss events, it is possible to preserve high $^{129}Xe^*/^{136}Xe_{Pu}$ at relatively late $t_{LGI} > 100$ Myr (Section 4.4.3.3).

complete, we transition to a model of long-term degassing associated with mantle processing and account for the concurrent sequestration of Pu and U in the growing continental crust. However, we exclude processes that are unlikely to play a significant role in I-Pu-U-Xe systematics, such as the segregation of Earth's metallic core. We also opt for a more permissive approach to modeling I-Pu-U-Xe systematics with a large number of free parameters: since delivery, degassing and mantle processing are very

poorly constrained, our approach is to allow the parameters to vary freely and to rule out regions of parameter space that are unable in any circumstances to satisfy our observed constraints on I-Pu-U-Xe systematics.

Having ensured that our model agrees with and captures distinct features of previous early degassing models, we may now exploit the flexibility of our two-stage model to explore key parameters controlling MORB source degassing history. We begin by examining I-Pu-U-Xe systematics in a simple degassing scenario, and then develop some intuition for the effect of timescales of accretion, long-term mantle processing, and partial retention of Xe during accretion.

4.4.3 Model results

The diverse radiogenic and fissiogenic isotopes of Xe are sensitive to degassing on different timescales: ^{129}I production of ^{129}Xe* has effectively ceased by ~90 Myr, while ^{244}Pu-fission ^{136}Xe is produced until ~500 Myr and production of ^{136}Xe by fission of extant ^{238}U continues throughout Earth history. Here we examine a simple degassing scenario and systematically assess the effects of select parameters on the degassing history of the MORB source mantle. Retention and delivery parameters for I and Xe are initially set to those used to reproduce the classical early degassing model (Table 4.4; all *delI*, *retI* and *delXe* parameters = 1; *retXe_preLGI* = *retXe_LGI* = 0; *retXe_postLGI* = 1), and unless otherwise specified, we use an accretion time constant α = 11 Myr for illustrative purposes. Figure 4.13 shows time evolution curves for the three radioactive parent species, ^{129}I, ^{244}Pu and ^{238}U, given the classical early degassing parameters. ^{129}I

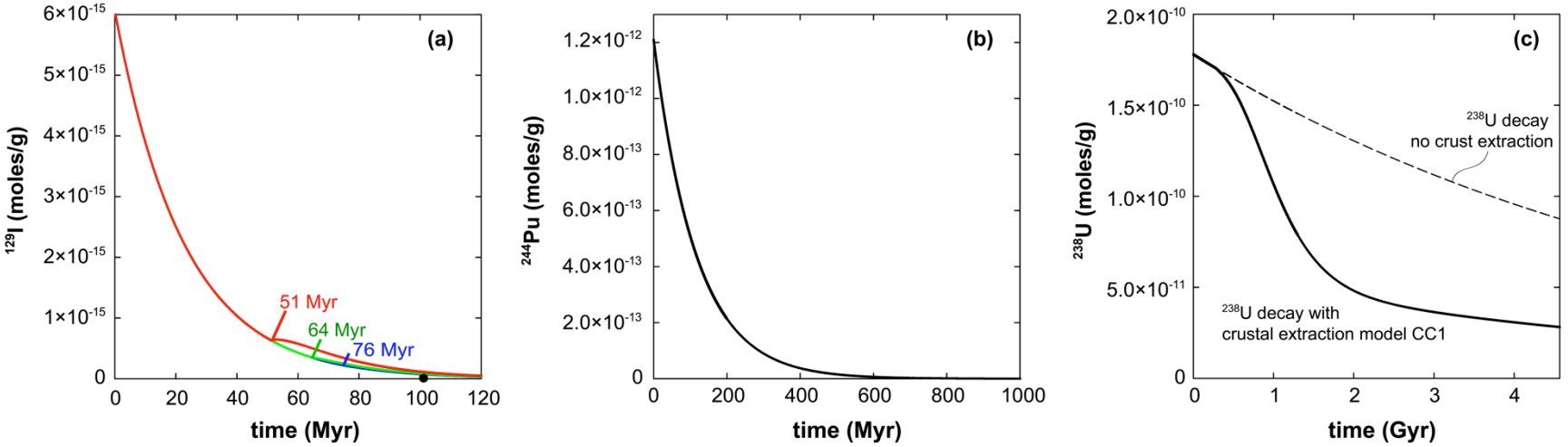

Figure 4.13 Time evolution curves for ^{129}I, ^{244}Pu and ^{238}U given classical early degassing model parameters (Table 4.4). (a) ^{129}I evolution is shown for three t_{LGI} values of 51 Myr, 64 Myr and 76 Myr, corresponding to 99%, 99.5% and 99.9% M_{Earth} accreted with an accretion time constant α = 11 Myr. The small ^{129}I bump initiated at t_{LGI} reflects the influx of a small amount of more volatile-rich material after the last giant impact. (b) ^{244}Pu evolution is not affected by early degassing, and is not significantly affected crustral extraction prior to extinction at ~600 Myr. (c) ^{238}U evolution reflects radioactive decay and sequestration in the continental crust over time (Figure 4.10).

evolution is shown for three t_{LGI} values of 51 Myr, 64 Myr and 76 Myr, corresponding to 99%, 99.5% and 99.9% M_{Earth} accreted, respectively (Figure 4.13a). ^{129}I decays rapidly; a small rise in concentration is initiated at t_{LGI}, as the post-LGI accreted material is assumed to be more volatile-rich (similar to carbonaceous chondrites with 450 ppb I; McDonough and Sun, 1995). ^{244}Pu decay is complete by ~600 Myr; although growth of the continental crust begins before that time, the amount of crust accumulated prior to 600 Myr is small (Figure 4.13b) and so the effect of crustal sequestration on ^{244}Pu evolution is negligible. In contrast, crustal extraction has a marked effect on ^{238}U evolution in the mantle (Figure 4.13c).

Figure 4.14 illustrates the corresponding time evolution curves for $^{129}Xe^*$, $^{136}Xe_{Pu}$ and $^{136}Xe_U$, given t_{LGI} values of 51 Myr, 64 Myr and 76 Myr. Panels b,d and f show the first 400 Myr of Earth history in detail for each Xe species. Retention of Xe begins after t_{LGI}; the radiogenic and fissiogenic species grow in as the planet accretes the last 0.1-1% of mass, and at the end of accretion (marked by a dashed line in panels b,d and f), mantle processing begins. Degassing associated with mantle processing overtakes production of $^{129}Xe^*$ as ^{129}I approaches extinction, and the evolution of ^{129}Xe transitions to an exponential loss due to degassing (Figure 4.13a; Figure 4.14a,b). Similarly, $^{136}Xe_{Pu}$ grows in for ~200 Myr after t_{LGI}, but transitions to exponential loss due to degassing as ^{244}Pu approaches extinction (Figure 4.13b; Figure 4.14c,d). We note that the relative concentrations of Xe species produced by short-lived radioactivity depend strongly on t_{LGI} ($^{129}Xe^*$ and $^{136}Xe_{Pu}$; Figure 4.14a-d), whereas the effect of the t_{LGI} on $^{136}Xe_U$ abundance is non-zero, but negligible (Figure 4.14e-f).

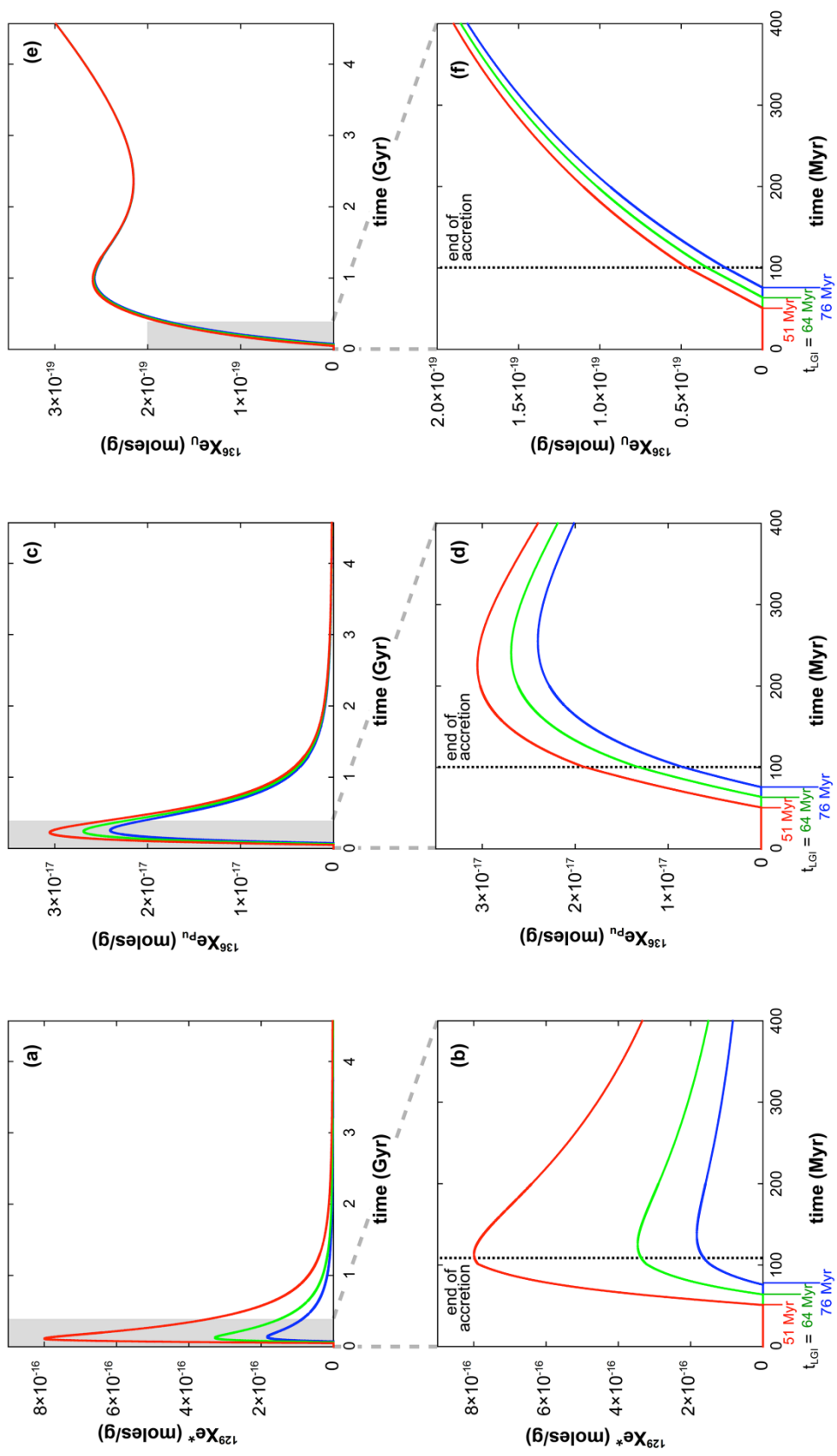

Figure 4.14 Time evolution curves for $^{129}Xe^*$, $^{136}Xe_{Pu}$ and $^{136}Xe_U$ using classical early degassing model parameters and α = 11 Myr (t_{LGI} values of 51 Myr, 64 Myr and 76 Myr correspond to 99%, 99.5% and 99.9% M_{Earth} accreted, respectively). Panels (a), (c) and (e) show the full 4.567 Gyr evolution; panels (b), (d) and (f) show the first 400 Myr of Earth history in detail for each Xe species. Retention of Xe begins after t_{LGI}; radiogenic and fissiogenic species grow in as the planet accretes the last 0.1-1% of mass, and at the end of accretion (marked by a dashed line in panels b,d and f), mantle processing begins. Mantle processing overtakes radiogenic and fissiogenic production as the parent species approach extinction (b,d). Concentrations of Xe species produced by short-lived radioactivity depend strongly on t_{LGI} ($^{129}Xe^*$ and $^{136}Xe_{Pu}$; a-d), whereas the effect of the t_{LGI} on $^{136}Xe_U$ abundance is non-zero, but negligible (e-f).

4.4.3.1 Effect of varying accretion timescales

Figure 4.11 illustrates the relationship between $^{129}Xe^*/^{136}Xe_{Pu}$ and the classical closure age (given near-instantaneous accretion; Section 4.4.2): due to the rapid decay of ^{129}I, mantle $^{129}Xe^*/^{136}Xe_{Pu}$ decreases as the time of closure increases. This relationship holds when we take more realistic timescales of accretion into account using our two-stage model: Figure 4.15 shows the range in $^{129}Xe^*/^{136}Xe_{Pu}$ calculated for the range of candidate t_{LGI} as a function of the accretion time constant, α (model parameters used for the calculation are specified in the figure caption). For each value of α, an earlier t_{LGI} (corresponding to a lower percentage of mass accreted) yields a higher $^{129}Xe^*/^{136}Xe_{Pu}$. However, the highest calculated $^{129}Xe^*/^{136}Xe_{Pu}$ and the magnitude of variation in $^{129}Xe^*/^{136}Xe_{Pu}$ due to t_{LGI} at a given α both decrease as α increases, since ^{129}I has mostly decayed away by the candidate t_{LGI}'s for larger values of α.

Similar systematics are observed in $^{136}Xe_{Pu}/(^{136}Xe_{Pu}+^{136}Xe_U)$, which is plotted as a function of α in Figure 4.16. At a given α, an earlier t_{LGI} yields a higher $^{136}Xe_{Pu}/(^{136}Xe_{Pu}+^{136}Xe_U)$, since more $^{136}Xe_{Pu}$ is retained in the early degassing stage (Figure 4.14d). However, in this case, the magnitude of variation in $^{136}Xe_{Pu}/(^{136}Xe_{Pu}+^{136}Xe_U)$ due to t_{LGI} at a given α increases as α increases. ^{244}Pu is extant at the end of accretion for even the highest α value of 30 Myr (99.9% accreted at ~207 Myr). Therefore, the magnitude of variation in $^{136}Xe_{Pu}/(^{136}Xe_{Pu}+^{136}Xe_U)$ at a given α is controlled by the wider absolute range of t_{LGI} at a high value of α (for α = 3 Myr, 14 Myr < t_{LGI} < 21 Myr; for α = 30 Myr, 138 Myr < t_{LGI} < 207 Myr). In constrast, the broader range in t_{LGI} at high values of α makes little difference for $^{129}Xe^*/^{136}Xe_{Pu}$, since there is almost no ^{129}I remaining in the system (Figure 4.15).

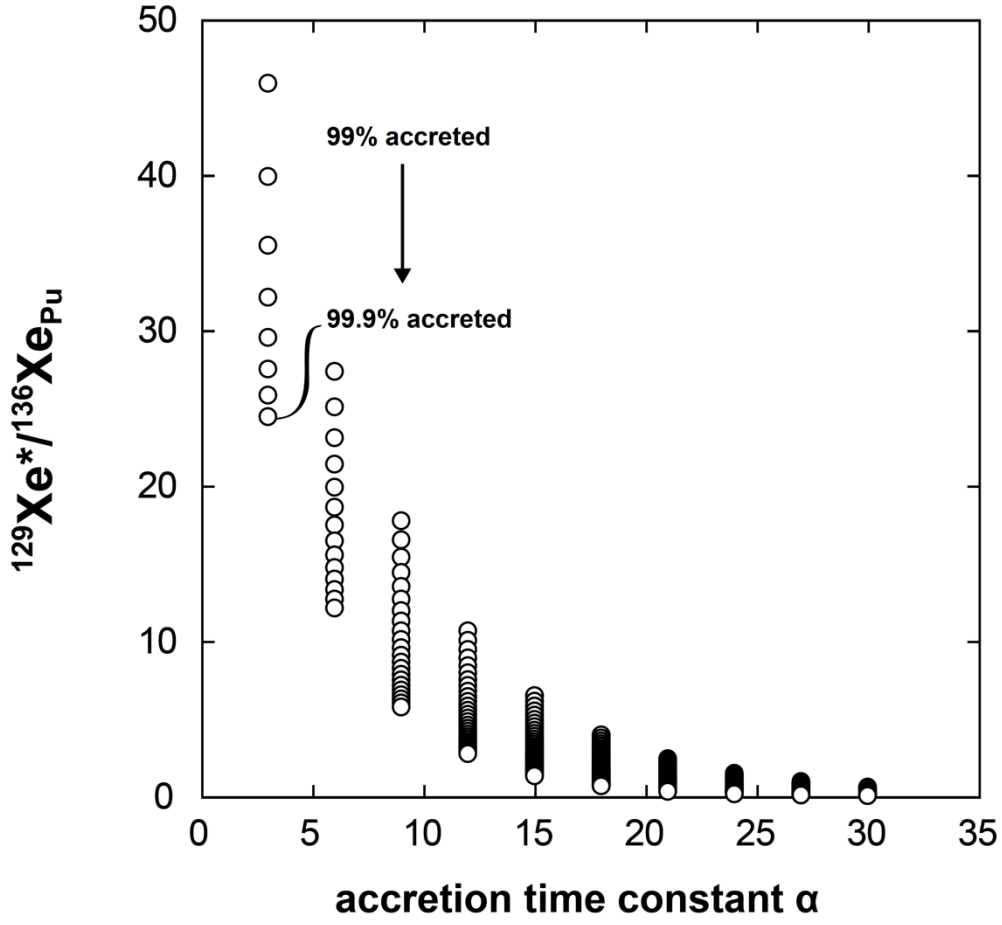

Figure 4.15 Forward modeled $^{129}Xe^*/^{136}Xe_{Pu}$ as a function of the accretion time constant, α, using classical early degassing parameters, $M_{res} = 2\times10^{27}$g, $N_{res} = 6$ and CCmodel = 1. The range in $^{129}Xe^*/^{136}Xe_{Pu}$ at a given α value corresponds to the range in t_{LGI} (99% accretion to 99.9% accretion). $^{129}Xe^*/^{136}Xe_{Pu}$ decreases as α increases, as slower accretion timescales translate to later t_{LGI} and thus less retention of Xe during the lifetime of ^{129}I.

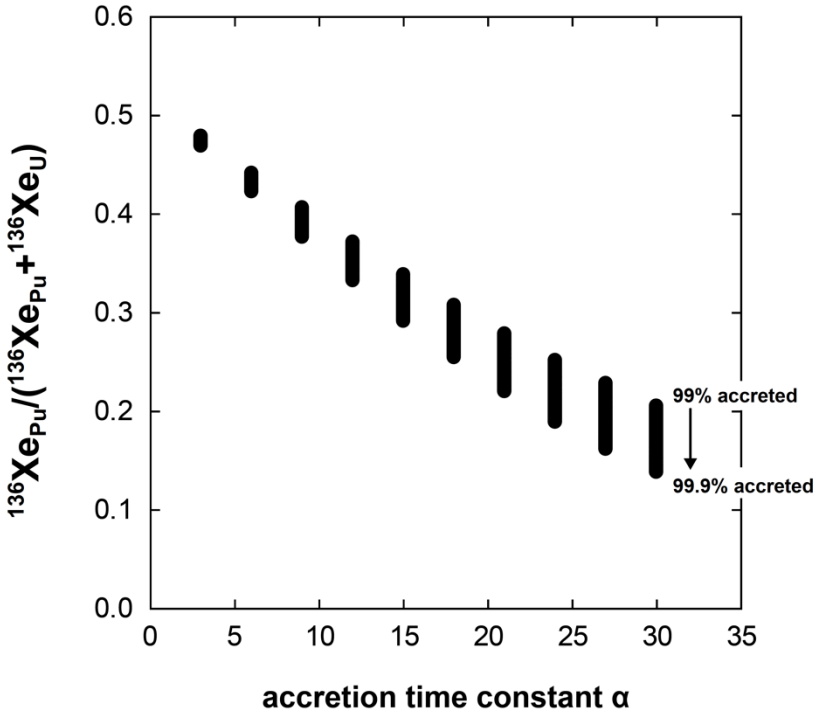

Figure 4.16 Forward modeled $^{136}Xe_{Pu}/ (^{136}Xe_{Pu}+^{136}Xe_U)$ as a function of the accretion time constant, α, using classical early degassing parameters, $M_{res} = 2\times10^{27}$g, $N_{res} = 6$ and CCmodel = 1. The range in $^{136}Xe_{Pu}/(^{136}Xe_{Pu}+^{136}Xe_U)$ at a given α value corresponds to the range in t_{LGI} (99% accretion to 99.9% accretion). $^{136}Xe_{Pu}/(^{136}Xe_{Pu}+^{136}Xe_U)$ decreases as α increases, as slower accretion timescales translate to later t_{LGI} and thus less retention of Xe during the lifetime of ^{244}Pu.

In general, we find that slow accretion timescales (α > ~20 Myr) result in $^{129}Xe^*/^{136}Xe_{Pu}$ and $^{136}Xe_{Pu}/(^{136}Xe_{Pu}+^{136}Xe_U)$ lower than the range determined for the MORB source (Figures 4.4 and 4.7). This reflects the fact that by the time the Earth has accreted 99% of its mass, ^{129}I and ^{244}Pu are severely depleted, and the resulting budgets of Xe isotopes produced by short-lived radioactivitiy are small. We find that for classical early degassing parameters (Table 4.4), accretion time constants of ~8-13 Myr are able to satisfy 68% confidence constraints for both $^{129}Xe^*/^{136}Xe_{Pu}$ and $^{136}Xe_{Pu}/(^{136}Xe_{Pu}+^{136}Xe_U)$ in MORB sources simultaneously.

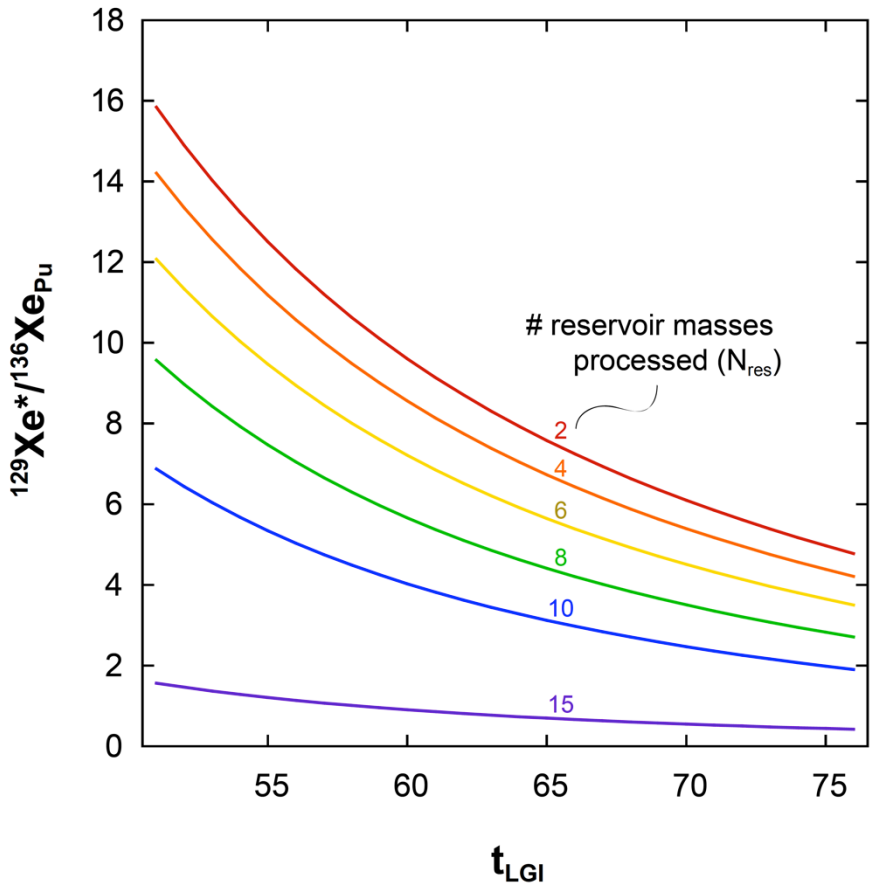

Figure 4.17 Forward modeled $^{129}Xe^*/^{136}Xe_{Pu}$ as a function of t_{LGI} for a range of long-term mantle processing rates (parameterized by N_{res}, the number of reservoir masses processed during the long-term degassing stage). Classical early degassing parameters (Table 4.4) are used; α = 11 Myr, $M_{res} = 2\times10^{27}$ g and CCmodel = 1. Degassing that occurs after ^{129}I is extinct but before ^{244}Pu is extinct drives $^{129}Xe^*/^{136}Xe_{Pu}$ downwards.

4.4.3.2 Effect of long-term mantle processing

The ^{129}Xe budget is highly sensitive to volatile loss that occurs during the early degassing stage (Figure 4.14a,b). However, we note that the $^{129}Xe^*/^{136}Xe_{Pu}$ ratio is also sensitive to degassing in association with mantle processing that occurs after accretion is complete but before ^{244}Pu is extinct: Xe loss at any point after ^{129}I extinction but during the lifetime of ^{244}Pu drives $^{129}Xe^*/^{136}Xe_{Pu}$ to lower values. Figure 4.17 shows $^{129}Xe^*/^{136}Xe_{Pu}$ as a function of t_{LGI} modeled using the classical early degassing

parameters (Table 4.4) for a range of processing rates, parameterized by N_{res} (the number of MORB reservoir masses processed over 4.567 Gyr). As N_{res} increases, $^{129}Xe^*/^{136}Xe_{Pu}$ at a given t_{LGI} decreases due to increased mantle processing (and thus degassing) after the extinction of ^{129}I and before the extinction of ^{244}Pu.

Figure 4.18 illustrates the relationship between $^{136}Xe_{Pu}/(^{136}Xe_{Pu}+^{136}Xe_U)$ and N_{res}. For higher values of N_{res}, the MORB mantle experiences a higher processing rate and thus more degassing. Both $^{136}Xe_{Pu}$ and $^{136}Xe_U$ are lost by degassing, but only $^{136}Xe_U$ grows back after the extinction of ^{244}Pu at ~500 Myr. Therefore, as N_{res} increases, $^{136}Xe_{Pu}/(^{136}Xe_{Pu}+^{136}Xe_U)$ decreases. The upper limit $^{136}Xe_{Pu}/(^{136}Xe_{Pu}+^{136}Xe_U)$ value reflecting closed-system decay of ^{244}Pu and ^{238}U is ~0.96-0.97; $^{136}Xe_{Pu}/(^{136}Xe_{Pu}+^{136}Xe_U)$ approaches this limit for lower values of N_{res}. We note that for a given N_{res} value, varying M_{res} will also affect $^{136}Xe_{Pu}/(^{136}Xe_{Pu}+^{136}Xe_U)$: in order to process a larger reservoir mass N_{res} times over 4.567 Gyr, a higher processing rate is required, and so $^{136}Xe_{Pu}/(^{136}Xe_{Pu}+^{136}Xe_U)$ will decrease with increasing M_{res}. Lastly, the time of the LGI has very limited effect on $^{136}Xe_{Pu}/(^{136}Xe_{Pu}+^{136}Xe_U)$ at a given value of N_{res}, consistent with the observation that the evolution curves for $^{136}Xe_{Pu}$ and $^{136}Xe_U$ at the three t_{LGI}'s specified in Figure 4.14 (panels d and f) converge over 4.567 Gyr of mantle processing.

4.4.3.3 Effect of varying Xe retention in early degassing stage

Having gained a broad sense of how the accretion and mantle processing rates affect $^{129}Xe^*/^{136}Xe_{Pu}$ and $^{136}Xe_{Pu}/(^{136}Xe_{Pu}+^{136}Xe_U)$, we now depart from the early degassing scenario envisioned in the classical model and explore the effect of partial Xe retention in the growing mantle prior to the last giant impact. Figures 4.15 and 4.16

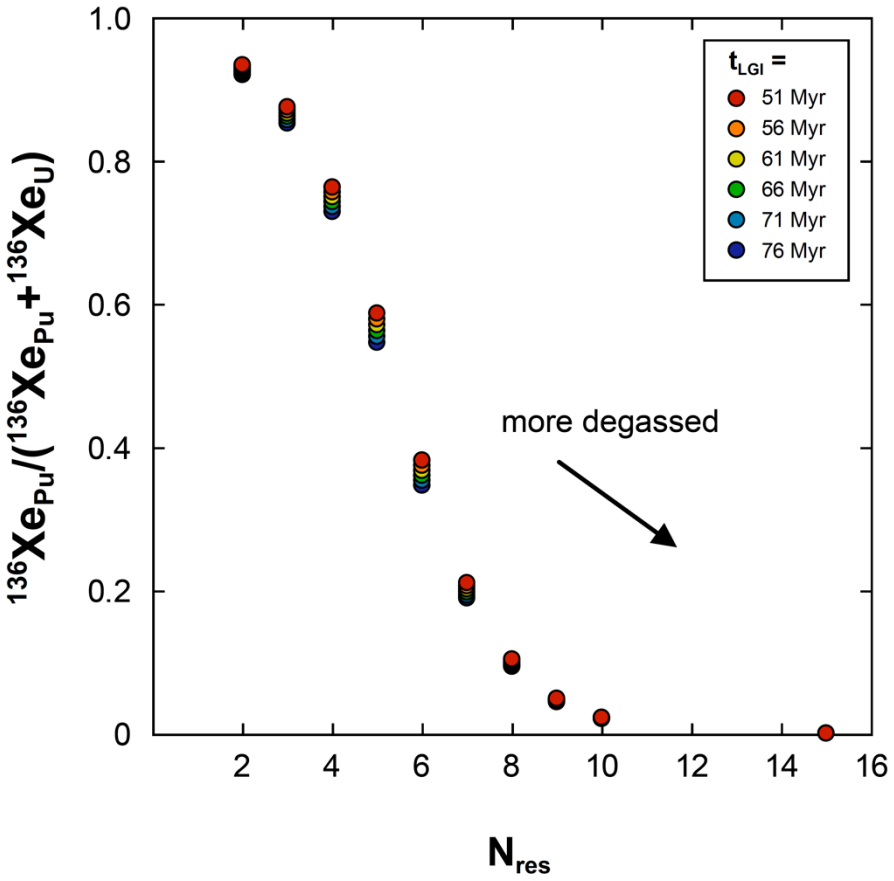

Figure 4.18 Forward modeled $^{136}Xe_{Pu}/(^{136}Xe_{Pu}+^{136}Xe_{U})$ as a function of the number of MORB source reservoir masses processed during the long-term degassing stage. The accretion time constant α = 11 Myr and classical early degassing parameters are used. $M_{res} = 2\times10^{27}$g and CCmodel =1. A reservoir that experiences more degassing develops low $^{136}Xe_{Pu}/(^{136}Xe_{Pu}+^{136}Xe_{U})$, since all isotopes of Xe are degassed, but only $^{136}Xe_{U}$ continues to grow after ~500 Myr. While $^{136}Xe_{Pu}/(^{136}Xe_{Pu}+^{136}Xe_{U})$ is strongly controlled by long-term degassing, the effect of early degassing (variation in t_{LGI}) is minimal.

demonstrate that for slow accretion (α > ~20 Myr), early degassing generates $^{129}Xe^*/^{136}Xe_{Pu}$ and $^{136}Xe_{Pu}/(^{136}Xe_{Pu}+^{136}Xe_{U})$ values lower than the range observed in MORBs (Figures 4.4-4.8). Similarly, high mantle processing rates drive strong degassing and yield $^{129}Xe^*/^{136}Xe_{Pu}$ and $^{136}Xe_{Pu}/(^{136}Xe_{Pu}+^{136}Xe_{U})$ values below the MORB range (Figures 4.17 and 4.18). In contrast, partial retention of Xe in the mantle during accretion

preserves some fraction of the $^{129}Xe^*$ and $^{136}Xe_{Pu}$ generated in the mantle during accretion, and thus generates $^{129}Xe^*/^{136}Xe_{Pu}$ and $^{136}Xe_{Pu}/(^{136}Xe_{Pu}+^{136}Xe_U)$ higher than those obtained with the classical degassing *retXe_preLGI* and *retXe_LGI* values of 0 (Table 4.4). We note that the remaining early degassing parameters either do not affect $^{129}Xe^*/^{136}Xe_{Pu}$ (*delXe*) or would decrease $^{129}Xe^*/^{136}Xe_{Pu}$ if altered from the classical degassing values (*retI* and *delI* = 1; Table 4.4).

Since early partial retention of Xe has the potential to raise $^{129}Xe^*/^{136}Xe_{Pu}$ and $^{136}Xe_{Pu}/(^{136}Xe_{Pu}+^{136}Xe_U)$, we investigate *retXe_preLGI* systematics assuming an accretion time constant $\alpha = 30$ Myr. This relatively large accretion time constant yields a candidate t_{LGI} range of 138-207 Myr and generates low $^{129}Xe^*/^{136}Xe_{Pu}$ and $^{136}Xe_{Pu}/(^{136}Xe_{Pu}+^{136}Xe_U)$ values (Figures 4.15 and 4.16). We seek the minimum *retXe_preLGI* required to bring (if possible) computed ratios for this time constant into agreement with the range determined for MORBs (Figures 4.7 and 4.8). The other Xe retention parameters (*retXe_LGI* and *retXe_postLGI*) are set to 1 to isolate the effect of Xe retention before the last giant impact. Figure 4.19 shows the relationship between *retXe_preLGI* and both $^{129}Xe^*/^{136}Xe_{Pu}$ and $^{136}Xe_{Pu}/(^{136}Xe_{Pu}+^{136}Xe_U)$. The magnitude of variation in $^{129}Xe^*/^{136}Xe_{Pu}$ and $^{136}Xe_{Pu}/(^{136}Xe_{Pu}+^{136}Xe_U)$ at a given *retXe_preLGI* value reflects the range in t_{LGI}. We find that for *retXe_preLGI* values below 0.9995, the *retXe_preLGI* parameter has almost no effect on either $^{129}Xe^*/^{136}Xe_{Pu}$ or $^{136}Xe_{Pu}/(^{136}Xe_{Pu}+^{136}Xe_U)$. Above 0.9995, *retXe_preLGI* drives both $^{129}Xe^*/^{136}Xe_{Pu}$ and $^{136}Xe_{Pu}/(^{136}Xe_{Pu}+^{136}Xe_U)$ up towards a limit corresponding to no early outgassing of Xe (indicated by red stars; Figures 4.19). Accordingly, variation due to the t_{LGI} disappears at a *retXe_preLGI* value of 1, since there can be no dependence on the time of the last giant impact if no degassing

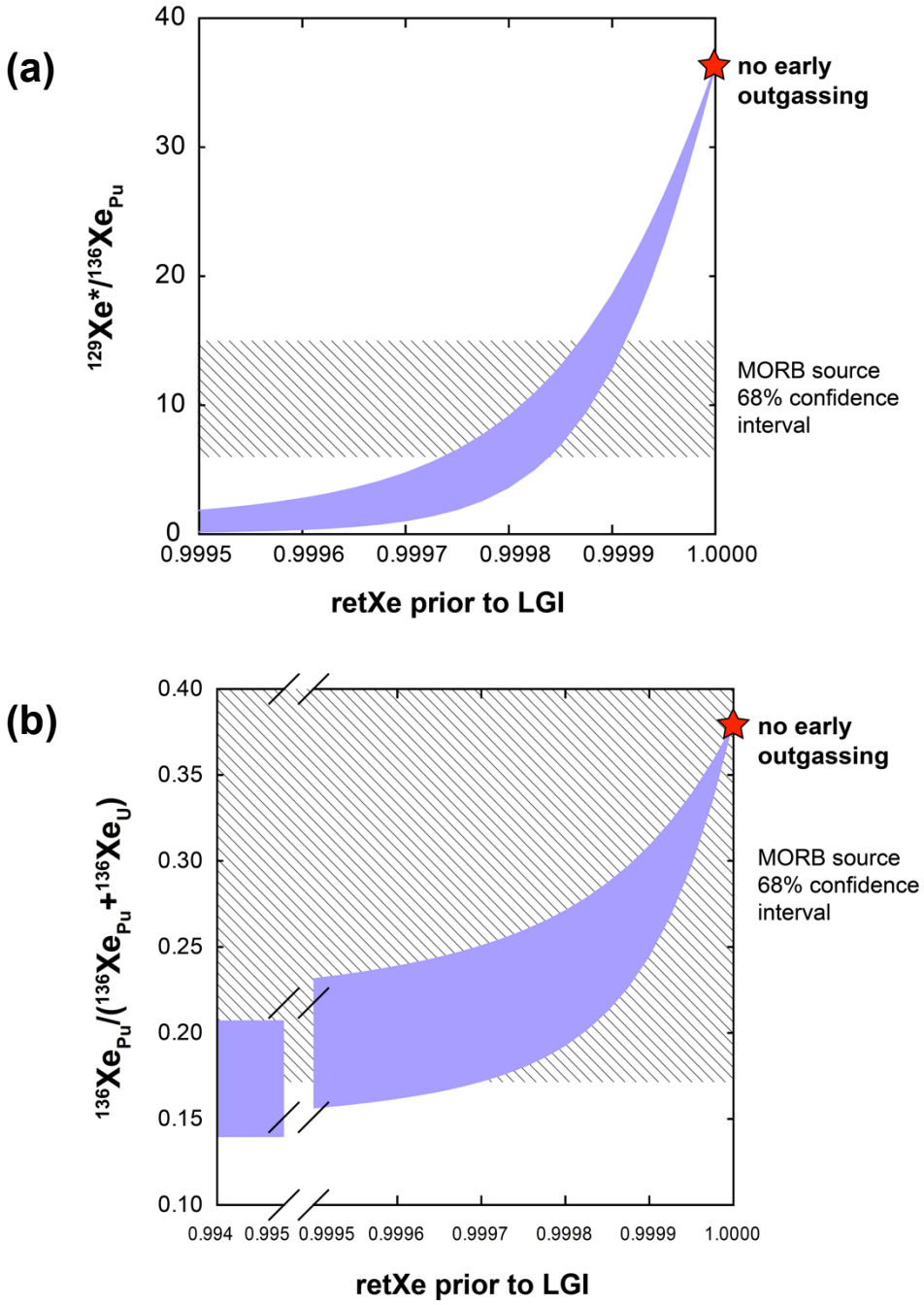

Figure 4.19 Effect of Xe retention prior to the last giant impact (*retXe_preLGI*) on modeled (a) $^{129}Xe^*/^{136}Xe_{Pu}$ and (b) $^{136}Xe_{Pu}/(^{136}Xe_{Pu}+^{136}Xe_U)$. Early degassing stage model parameters are the same as classical early degassing (Table 4.4) except *retXe_LGI* is set to 1 and *retXe_preLGI* is allowed to vary. The accretion time constant α = 30 Myr, $M_{res} = 2\times10^{27}$g, N_{res} = 6 and CCmodel =1. Significant retention of Xe during accretion (~8-25% of $^{130}Xe_{del}$ relative to a no-outgassing scenario; see Section 4.4.3.3) must occur in order to satisfy constraints on MORB source $^{129}Xe^*/^{136}Xe_{Pu}$ and $^{136}Xe_{Pu}/(^{136}Xe_{Pu}+^{136}Xe_U)$ given an accretion time constant of 30 Myr.

occurs before, during or after that impact. Values of *retXe_preLGI* ~0.99985 are required to raise $^{129}Xe^*/^{136}Xe_{Pu}$ above ~6, the lower limit of the 68% confidence interval for average MORBs (Figure 4.7). To gain some intuition for the extent of total early degassing corresponding to *retXe_preLGI* of 0.99985, we compute the percentage of primordial $^{130}Xe_{del}$ retained relative to the $^{130}Xe_{del}$ budget given no outgassing (*retXe_preLGI* of 1): for last giant impacts between 138 and 207 Myr, a *retXe_preLGI* of 0.99985 signifies that ~8-25% of $^{130}Xe_{del}$ must be retained in the early degassing stage relative to the no- early-outgassing budget (range corresponds to variation in t_{LGI}).

We include an independent parameter to describe retention of Xe during the last giant impact (vs. before of after the LGI) in our model to enable investigation of discrete loss events similar to those envisioned by Porcelli et al. (2001). One interesting feature of the Porcelli et al. (2001) model results (reproduced in Figure 4.12) is that at a given fraction of Xe retained in the loss event (*retXe_LGI*), $^{129}Xe^*/^{136}Xe_{Pu}$ initially decreases as expected with increasing t_{LGI}, but ultimately turns over and begins to increase with t_{LGI} (illustrated in Figure 4.20 for *retXe_LGI* = 0.03; instantaneous accretion and no long-term degassing). As a result, at a given *retXe_LGI*, the same $^{129}Xe^*/^{136}Xe_{Pu}$ value can be generated at two t_{LGI} values, with a significant difference in age (e.g, ~75 Myr and 170 Myr in Figure 4.20).

Since our model tracks the evolving concentrations of $^{129}Xe^*$ and $^{136}Xe_{Pu}$, we may determine what drives the observed DLE systematics. Figure 4.21 shows DLE evolution curves for $^{129}Xe^*$ and $^{136}Xe_{Pu}$ for relatively slow accretion with t_{LGI}'s of 140 Myr, 160 Myr, 180 Myr and 200 Myr. $^{129}Xe^*$ and $^{136}Xe_{Pu}$ are quantitatively retained until the LGI, at which point 97% of the gas is instantaneously depleted (*retXe_LGI* = 0.03). For LGI's

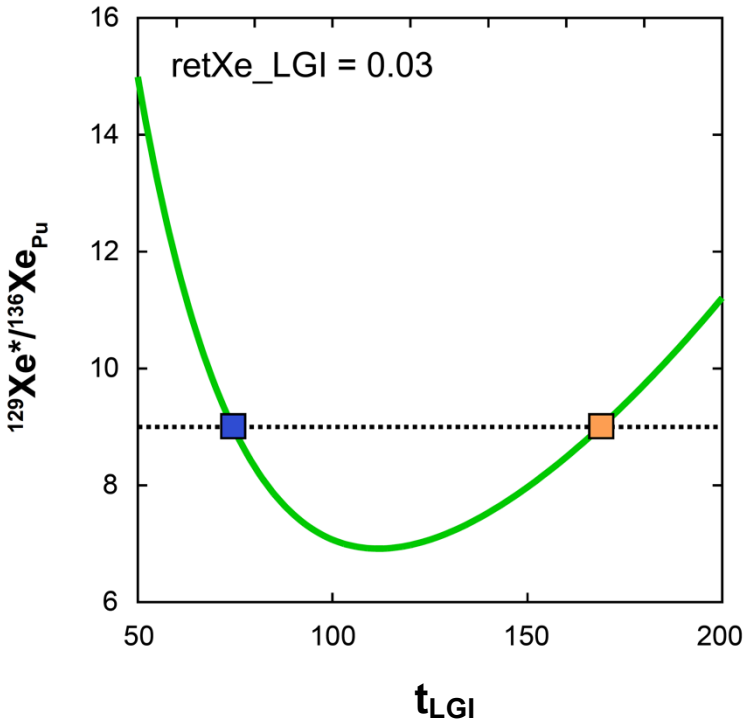

Figure 4.20 Forward modeled $^{129}Xe^*/^{136}Xe_{Pu}$ as a function of t_{LGI} for discrete loss events (after Porcelli et al., 2001) using *retXe_LGI* of 0.03 (see Figure 4.12). Accretion and the long-term degassing stage are both neglected for ease of comparison with Porcelli et al. (2001) and Figure 4.12. The same $^{129}Xe^*/^{136}Xe_{Pu}$ value can be generated at two significantly different t_{LGI} values.

that occur before ^{129}I is extinct (not depicted), the amount of $^{129}Xe^*$ produced after the LGI decreases rapidly for later t_{LGI}'s. The decrease in post-LGI $^{129}Xe^*$ surpasses the associated decrease in post-LGI $^{136}Xe_{Pu}$, such that $^{129}Xe^*/^{136}Xe_{Pu}$ decreases overall with t_{LGI} up to ~100 Myr. However, for LGI's that occur after ^{129}I has mostly decayed (i.e., after ~100 Myr), instantaneous depletion of the $^{129}Xe^*$ budget by a constant factor (e.g., 0.03) yields nearly identical $^{129}Xe^*$ budgets for different t_{LGI}'s: all $^{129}Xe^*$ was retained prior to the LGI, and very little grows after the LGI (Figure 4.21a). ^{244}Pu is still extant, and so the $^{136}Xe_{Pu}$ budget at the end of accretion still depends on t_{LGI}: for late t_{LGI}'s, less $^{136}Xe_{Pu}$ grows in after the LGI and so $^{129}Xe^*/^{136}Xe_{Pu}$ is higher (Figure 4.21b).

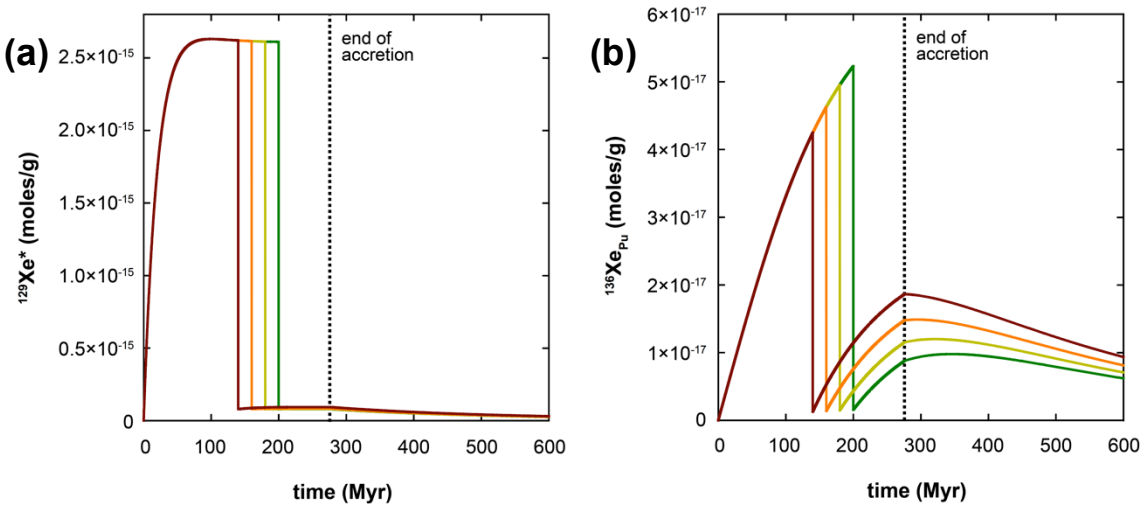

Figure 4.21 Time evolution curves for (a) ^{129}Xe* and (b) ^{136}Xe$_{Pu}$ for 4 modeled discrete loss events at t_{LGI} = 140 Myr, 160 Myr, 180 Myr and 200 Myr (accretion time constant α = 30 Myr; *retXe_LGI* = 0.03). The ^{129}Xe*/^{136}Xe$_{Pu}$ systematics illustrated in Figure 4.20 reflect the fact that for DLE's that occur after the extinction of ^{129}I, the ^{129}Xe* budget is largely insensitive to t_{LGI}, while ^{136}XePu decreases with increasing t_{LGI}. Thus, ^{129}Xe*/^{136}Xe$_{Pu}$ reverses after the extinction of ^{129}I and increases as a function of t_{LGI} (Figure 4.20).

Accordingly, for DLE's that occur after ~100 Myr, ^{129}Xe*/^{136}Xe$_{Pu}$ increases as t_{LGI} increases. It is important to note that Porcelli et al. (2001) neglected the effect of long-term degassing in their model. We find that for discrete loss events, long-term degassing (after the end of accretion; Figure 4.21) largely erases the ^{129}Xe*/^{136}Xe$_{Pu}$ dependence on t_{LGI} and lowers the overall ^{129}Xe*/^{136}Xe$_{Pu}$ by depleting the ^{136}Xe$_{Pu}$ budgets for all t_{LGI}. We also note that the absolute concentration of ^{129}Xe* remaining after a discrete loss event is relatively low. The examples shown in Figure 4.21 would raise the ancient mantle ^{129}Xe/^{130}Xe from the primordial value of 6.436 (Q-Xe component; Pepin and Porcelli, 2006) to ~6.48, far below values of ~14 inferred for the ancient MORB mantle (Mukhopadhyay et al., in prep), and also below the highest measured present-day values of ~7.8 (Chapter 3; Parai et al., 2012; Tucker et al., 2012). Therefore, although late

DLE's generate the same $^{129}Xe^*/^{136}Xe_{Pu}$ ratios as early DLE's for a given *retXe_LGI*, the absolute amount of radiogenic $^{129}Xe^*$ retained in the late DLE is too low to satisfy additional available constraints.

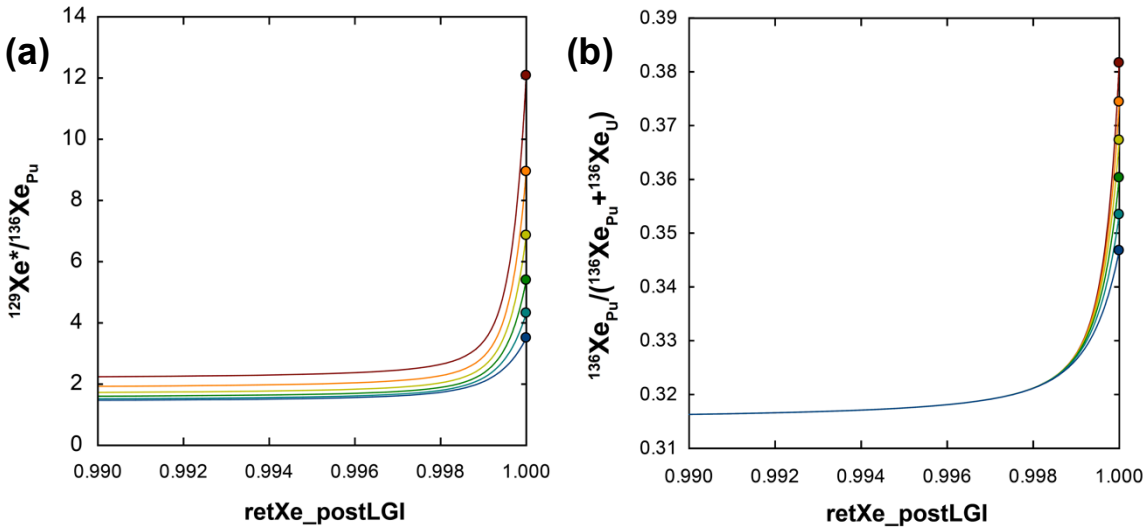

Figure 4.22 Effect of varying Xe retention subsequent to the last giant impact (retXe_postLGI) on forward modeled (a) $^{129}Xe^*/^{136}Xe_{Pu}$ and (b) $^{136}Xe_{Pu}/(^{136}Xe_{Pu}+^{136}Xe_U)$. The accretion time constant α = 11 Myr; all early degassing parameters are set to the classical early degassing model parameters, except *retXe_postLGI* is allowed to vary. M_{res} = 2×10^{27}g, N_{res} = 6 and CCmodel =1. Late degassing at the very end of accretion rapidly decreases both $^{129}Xe^*/^{136}Xe_{Pu}$ and $^{136}Xe_{Pu}/(^{136}Xe_{Pu}+^{136}Xe_U)$.

Finally, we investigate the effect of varying the retention of Xe subsequent to the last giant impact (*retXe_postLGI*). So far we have only considered scenarios with *retXe_postLGI* of 1 (Table 4.4); using values less than 1 should yield lower $^{129}Xe^*/^{136}Xe_{Pu}$ and $^{136}Xe_{Pu}/(^{136}Xe_{Pu}+^{136}Xe_U)$ values. Therefore, we return to an accretion time constant α = 11 Myr and set *retXe_preLGI* and *retXe_LGI* to 0 for ease of comparison with results from previous sections (see Table 4.4). Figure 4.22 shows the effect of reducing the retention of Xe subsequent to the LGI until the end of accretion on

$^{129}Xe^*/^{136}Xe_{Pu}$ and $^{136}Xe_{Pu}/(^{136}Xe_{Pu}+^{136}Xe_U)$. The results for *retXe_postLGI* = 1 are highlighted on the right axis (Figure 4.22; filled circles); these correspond to the classical degassing scenario explored previously (e.g., Figure 4.17, $N_{res} = 6$). Our results illustrate that both $^{129}Xe^*/^{136}Xe_{Pu}$ and $^{136}Xe_{Pu}/(^{136}Xe_{Pu}+^{136}Xe_U)$ drop rapidly as *retXe_postLGI* decreases from 1, but level off towards a limit reflecting the time of the end of accretion.

4.5 DISCUSSION

Xenon fission isotope systematics in the SWIR mantle source contribute to an emerging portrait of a MORB mantle that has experienced heterogeneous degassing and regassing on a variety of lengthscales and timescales. Here we discuss our determinations of SWIR mantle fission Xe in the context of results for other MORB sources and plume-influenced sources, and consider some implications of our two-stage model for MORB mantle degassing.

4.5.1 Recycling of atmospheric Xe into MORB and plume sources: Evidence for incorporation of recycled material into mantle reservoirs

Subduction zones were long thought to be efficient barriers to the recycling of noble gases into the deep mantle (e.g., Staudacher and Allegre, 1988). However, recent work indicates that atmospheric heavy noble gases are carried in subducted materials beyond depths of magma generation to be recycled into the mantle (e.g., Holland and Ballentine, 2006; Kendrick et al., 2011; Mukhopadhyay, 2012; Parai et al., 2012; Pető et al., 2013; Tucker et al., 2012). Having explicitly corrected for syn- to post-eruptive atmospheric contamination, here we evaluate the prevalence of atmospheric Xe

incorporation into mantle sources over time. We find that ~80-95% of the Xe budget of MORB and plume mantle sources is recycled atmospheric Xe (Table 4.3; Figures 4.3, 4.6, A4.9, A4.10). The dominance of recycled atmospheric Xe indicates that recycled material is incorporated into both MORB and plume sources. However, differential incorporation of atmospheric Xe cannot explain observed differences in $^{129}Xe/^{130}Xe$ between MORB and plume sources (Holland and Ballentine, 2006): ^{129}Xe-^{136}Xe-^{130}Xe systematics illustrate that MORB and plume sources (1) are not related by mixing with the atmosphere; (2) separated within 100 Ma of the start of the Solar System; and (3) have not been homogenized by 4.45 Ga of mantle convection (Mukhopadhyay, 2012; Tucker et al., 2012; Parai et al., 2012; Pető et al., 2013).

Among noble gases, Xe isotope systematics are a uniquely able to resolve the injection and incorporation of recycled atmospheric components into the mantle. Mantle source He and Ne isotopic compositions are not sensitive to incorporation of recycled material due to low overall concentrations of He and Ne in recycled material relative to ambient mantle material (e.g., Parai et al., 2009). For example, although Iceland Ne isotopes are primitive and near-solar, ~90% of Iceland Xe is recycled in origin (Mukhopadhyay, 2012), indicating incorporation of recycled material devoid of atmospheric Ne into the Iceland source. Since He and Ne isotopes are not sensitive indicators of recycling, plume-related samples with primitive He and Ne isotopic compositions may not reflect sampling of an undiluted primordial mantle, such that major and trace element compositions of samples with primitive He and Ne (e.g., Jackson et al., 2010; Jackson and Jellinek, 2013) are unlikely to represent the composition of a pristine primordial bulk silicate Earth. We note that the incorporation of recycled material

generates depleted $^{143}Nd/^{144}Nd$ ratios over time in both the upper mantle and the plume source: if continental crust with low Sm/Nd is built via extraction processes at subduction zones, then the average recycled slab package (i.e., crust and mantle lithosphere) over Earth history must have high Sm/Nd relative to the bulk silicate Earth. Therefore, the association of primitive He and Ne with super-chondritic $^{143}Nd/^{144}Nd$ isotopes is not an indication of non-chondritic bulk silicate Earth (e.g., Jackson et al., 2010; Jackson and Jellinek, 2013), but likely arises from incorporation of depleted recycled material into primordial sources (e.g., Gonnermann and Mukhopadhyay, 2009).

4.5.2 MORB and plume sources have experienced different degassing histories

Mantle $^{136}Xe_{Pu}/(^{136}Xe_{Pu}+^{136}Xe_{U})$ ratios provide constraints on the long-term degassing histories of mantle sources. ^{244}Pu decays with a half-life of 80.0 Myr; production of Pu-fission $^{136}Xe_{Pu}$ is effectively complete at ~500 Myr (e.g,. Figure 4.13b). In contrast, ^{238}U decays with a half-life of 4.468 Gyr and production of U-fission $^{136}Xe_{U}$ is ongoing. In order to preserve a high $^{136}Xe_{Pu}/(^{136}Xe_{Pu}+^{136}Xe_{U})$ ratio, a mantle source must retain a high proportion of the Pu-fission $^{136}Xe_{Pu}$ budget developed in the first 500 Myr of Earth history. A mantle source that experiences significant degassing loses both $^{136}Xe_{Pu}$ and $^{136}Xe_{U}$, but only grows $^{136}Xe_{U}$ back over time. Thus, a relatively degassed mantle source develops a low $^{136}Xe_{Pu}/(^{136}Xe_{Pu}+^{136}Xe_{U})$ ratio over time.

We find that MORB mantle sources uniformly exhibit a low $^{136}Xe_{Pu}/(^{136}Xe_{Pu}+^{136}Xe_{U})$ ratio relative to plume-related sources (Figures 4.5 and 4.8; Mukhopadhyay, 2012; Tucker et al., Pető et al., 2013). MORB source $^{136}Xe_{Pu}/(^{136}Xe_{Pu}+^{136}Xe_{U})$ ratios range from 0.27 to 0.37, with an error-weighted average

of 0.33 ±0.09; plume-related source $^{136}Xe_{Pu}/(^{136}Xe_{Pu}+^{136}Xe_{U})$ ratios range from 0.65 to 0.97, with an error-weighted average of $0.97^{+0.03}_{-0.17}$ (all values using solar wind as the mantle initial Xe). The observed difference in $^{136}Xe_{Pu}/(^{136}Xe_{Pu}+^{136}Xe_{U})$ indicates that MORB mantle sources have uniformly experienced a greater extent of integrated degassing associated with long-term mantle processing relative to plume sources. We note that this observation is independent of the interpretation of $^{4}He/^{3}He$ systematics in MORBs and plume-derived basalts.

4.5.3 Constraints on the age of the Moon-forming giant impact from I-Pu-U-Xe systematics

Combined short-lived ^{129}I-^{129}Xe and ^{244}Pu-Xe isotope systematics provide a powerful tool to probe the earliest degassing history of the Earth. ^{129}I decays with a half-life of 15.7 Myr and is effectively extinct at 90 Myr, while ^{244}Pu continues to produce $^{131,132,134,136}Xe$ until ~500 Myr after the start of the Solar System. In the classical view of early Earth degassing (Section 4.4.2), the mantle $^{129}Xe^{*}/^{136}Xe_{Pu}$ ratio depends simply on the $^{129}I/^{244}Pu$ ratio at the time of the last giant impact: all radiogenic and fissiogenic Xe produced prior to the LGI was lost, and all Xe produced subsequent to the LGI was retained. Using this classical model and the limits of the MORB $^{129}Xe^{*}/^{136}Xe_{Pu}$ 68% confidence intervals for solar wind, AVCC and U-Xe mantle initial Xe compositions (Table 4.3; Figure 4.7), we compute a classical closure age range of 44-70 Myr for the last giant impact.

Our determination of the upper mantle closure age is significantly older than the age of ~95-100 Myr computed by Pepin and Porcelli (2006). We note that we have

focused on mantle source Xe isotopic compositions corrected for syn-to-post-eruptive contamination based on multiple step-crushes for each sample (Section 4.2.2). In contrast, Pepin and Porcelli (2006) used abundance-weighted averages of measured values of MORBs (mostly the popping rock 2ΠD43; Kunz et al., 1998) affected by variable degrees of atmospheric contamination. The authors computed a relatively high fraction of fission Xe from Pu-fission for average MORBs, with $^{136}Xe_{Pu}/(^{136}Xe_{Pu}+^{136}Xe_{U})$ = 0.75 using solar wind as the mantle initial (Pepin and Porcelli, 2006). Such a value is approximately twice as high as we have computed for the MORB error-weighted average (0.33 ±0.09 using solar wind as the mantle initial). Accordingly, the $^{129}Xe^{*}/^{136}Xe_{Pu}$ of $3.8^{+2.0}_{-0.4}$ computed by Pepin and Porcelli (2006) is approximately half the value we have computed for average MORBs ($7.8^{+3.1}_{-1.8}$; suggesting good agreement in our estimates of the $^{129}Xe^{*}$ budgets of MORBs). Such a low value of $^{129}Xe^{*}/^{136}Xe_{Pu}$ yields a later time of closure. However, we also note that the authors used a relatively high ^{127}I abundance of 13 ppb in their computations. In order to provide a direct comparison, we compute the closure age range of 71-86 Myr corresponding to their 1σ limits on $^{129}Xe^{*}/^{136}Xe_{Pu}$ assuming 7 ppb ^{127}I in the ancient MORB mantle (Deruelle et al., 1992; Palme and O'Neill, 2004). This range is still younger than our determination of 44-70 Myr, but agrees at the 68% confidence limit.

Our two-stage forward model of I-Pu-U-Xe systematics has the potential to provide additional constraints on the timing of the Moon-forming giant impact. We have explored the effect of accretion timescales, mantle processing rate, and early retention of Xe on I-Pu-U-Xe systematics (Section 4.4.3). Here we briefly discuss implications of our model results, though we note that a Monte Carlo simulation is most appropriate to fully

explore the model parameter space and identify regions of parameter space that satisfy our observational constraints, as well as regions of parameter space that cannot satisfy constraints from I-Pu-U-Xe systematics under any circumstances.

We have demonstrated that long-term degassing directly affects MORB mantle $^{129}Xe^*/^{136}Xe_{Pu}$, since degassing that occurs after ^{129}I extinction but before ^{244}Pu extinction lowers $^{129}Xe^*/^{136}Xe_{Pu}$ (Figure 4.17). In this sense, the time of the last giant impact computed by neglecting long-term degassing (e.g., the classical closure age computed above) is likely an upper limit, since accounting for Xe/Pu fractionation before ~500 Myr would raise the $^{129}Xe^*/^{136}Xe_{Pu}$ and thus push the time of the last giant impact further back in time.

We further note that a modeled $^{136}Xe_{Pu}$ evolution that satisfies constraints on $^{129}Xe^*/^{136}Xe_{Pu}$ after ~500 Myr (degassing after this time will not fractionate $^{129}Xe^*/^{136}Xe_{Pu}$) must also satisfy constraints on $^{136}Xe_{Pu}/(^{136}Xe_{Pu}+^{136}Xe_U)$ after ~4.5 Gyr of mantle processing (Figure 4.18). Thus, the I-Pu-Xe system is tightly linked to the Pu-U-Xe system. The Pu-U-Xe system is also linked to other long-lived noble gas systems primarily sensitive to long-term mantle degassing. We have incorporated U-Th-He systematics into our model in order to investigate whether long-term degassing parameters that are required to generate favorable $^{136}Xe_{Pu}/(^{136}Xe_{Pu}+^{136}Xe_U)$ ratios also generate $^4He/^3He$ ratios close to the observed MORB range. Thus, additional constraints on mantle degassing on a variety of timescales can be leveraged to better constrain the earliest degassing history of the MORB mantle source, and the timing of the Moon-forming giant impact.

Our model results indicate that for late t_{LGI} (>80 Myr; includes all candidate t_{LGI}'s for α > 18 Myr), our forward model cannot simultaneously satisfy the 68% confidence limits for $^{129}Xe^*/^{136}Xe_{Pu}$ and $^{136}Xe_{Pu}/(^{136}Xe_{Pu}+^{136}Xe_U)$ in the MORB mantle without invoking partial retention of Xe prior to the last giant impact (Figure 4.19). Even if the effect of mantle processing after ^{129}I extinction and before the extinction of ^{244}Pu is minimized by setting N_{res} to its lowest value, $^{129}Xe^*/^{136}Xe_{Pu}$ values calculated for t_{LGI}'s later than 80 Myr are too low (maximum value of ~5) to match our range for MORBs ($7.8^{+3.1}_{-1.8}$ using solar wind as the mantle initial). The corresponding $^{136}Xe_{Pu}/(^{136}Xe_{Pu}+^{136}Xe_U)$ ratios generated with minimal mantle processing are far too high (>0.80) to match the average MORB 68% confidence range (0.33 ±0.09 using solar wind as the mantle initial; Figure 4.8). In contrast, for t_{LGI}'s between ~35 and 70 Myr, we are able able to satisfy constraints on both $^{129}Xe^*/^{136}Xe_{Pu}$ and $^{136}Xe_{Pu}/(^{136}Xe_{Pu}+^{136}Xe_U)$ simultaneously without invoking partial retention of Xe prior to the last giant impact.

We note that non-zero early retention of Xe is necessary to explain the budgets of primordial $^{124,126,128,130}Xe$ in the MORB source mantle (Mukhopadhyay et al., in prep). However, a very high degree of Xe retention in the upper mantle throughout accretion is physically unlikely, since degassing through multiple magma ocean events (Tucker and Mukhopadhyay, 2014) will deplete the upper mantle volatile inventory. Therefore, further consideration of partial Xe retention in the accreting Earth is necessary to better understand I-Pu-U-Xe constraints on the timing of the Moon-forming giant impact.

4.5.4 The emerging portrait of distinct ancient, heterogeneous and continuously-evolving mantle sources

Xenon isotopic data from the Southwest Indian Ridge (this study; Chapter 3; Parai et al., 2012) add to a growing pool of high-precision Xe data in mid-ocean ridge basalts (Kunz et al., 1998; Tucker et al., 2012) and plume-influenced basalts (Mukhopadhyay, 2012; Pető et al., 2013). We find that the origin of the reservoir supplying primordial noble gases to plumes is fundamentally distinct from that of the MORB mantle reservoir: the two reservoirs cannot be related simply by differential degassing or incorporation of recycled atmospheric volatiles (Chapter 3; Mukhopadhyay, 2012; Parai et al., 2012; Pető et al., 2013; Tucker et al., 2012). Based on the extinct ^{129}I-^{129}Xe system, the plume source separated from the MORB source within 100 Myr of the start of the Solar System, and the two sources have not been homogenized by 4.45 Gyr of mantle convection (Chapter 3; Mukhopadhyay, 2012; Parai et al., 2012; Pető et al., 2013; Tucker et al., 2012). Xe fission isotope systematics further indicate that the plume source exhibits a distinct $^{129}Xe^*/^{136}Xe_{Pu}$ signature that is low relative to the MORB source (Figures 4.4, 4.7). This feature likely signifies that the plume source is characterized by a lower I/Pu than the MORB source, and may reflect heterogeneous accretion, with early accretion being volatile-poor. Thus, Xe isotopic data in mantle-derived basalts reflect very ancient differences that persist in the MORB and plume mantle reservoirs today.

Although differences between the upper mantle and plume source cannot be explained by recycling of atmospheric volatiles, injection and incorporation of atmospheric heavy noble gases (Ar, Kr, Xe) into the mantle must occur over Earth history. Evaluation of high-precision measurements of fission Xe isotopic compositions

in MORBs and plume-influenced basalts indicate that the mantle Xe budget is dominated by recycled atmospheric Xe (Section 4.3; Section 4.5.1; Figure 4.3; Mukhopadhyay, 2012; Pető et al., 2013; Tucker et al., 2012). In addition, large variations are evident in upper mantle $^{40}Ar/^{36}Ar$ and $^{129}Xe/^{130}Xe$ isotopic composition in regions of the Southwest Indian Ridge removed from the influence of known mantle plumes, indicating heterogeneous incorporation of recycled atmospheric noble gases into the MORB source (Chapter 3; Parai et al., 2012). Our evaluation of SWIR fission Xe isotopes (Section 4.3; Figure 4.4) supports this conclusion, as recycled atmospheric Xe constitutes ~5-10% more of the ^{132}Xe budget in the Eastern Orthogonal Supersegment mantle source relative to the Western Orthogonal Supersegment source (Figure 4.4; see caption). The persistence of large Ar and Xe isotopic variations generated by heterogeneous regassing reflects inefficient homogenization of recycled material in the MORB mantle source.

We note that mantle source He and Ne isotopic compositions may not be sensitive to incorporation of recycled material due to low overall concentrations of He and Ne in recycled material relative to ambient mantle (Section 4.5.1). Thus, the broad homogeneity noted in MORB helium isotopic compositions (Graham, 2002; Graham et al., 1992; Kurz et al., 1982) does not indicate a homogeneous MORB source. Based on Ar and Xe isotopic compositions measured in mantle-derived samples, we propose that MORB and plume source heterogeneities reflect the ongoing incorporation of recycled material into distinct ancient mantle reservoirs.

4.6 CONCLUSIONS

We present new high-precision measurements of the fission isotopes of Xe (^{131}Xe, ^{132}Xe, ^{134}Xe and ^{136}Xe) in basalts from the Southwest Indian Ridge between 16 and 25°E. Based on determinations of the mantle source isotopic compositions corrected for syn- to post-eruptive atmospheric contamination, we solve for the proportions of mantle ^{132}Xe attributed to the primordial mantle Xe budget, recycling of atmospheric Xe, fission of extinct ^{244}Pu and ongoing fission of extant ^{238}U.

We developed a parameterized two-stage model of MORB source degassing to investigate constraints from I-Pu-U-Xe systematics on the timing of the Moon-forming giant impact. Based on our determinations of $^{129}Xe^*/^{136}Xe_{Pu}$ in MORB sources, we compute a classical closure age range of 44-70 Myr for the last giant impact. Our model results indicate that for late t_{LGI} (>80 Myr), our model cannot simultaneously satisfy 68% confidence limits for $^{129}Xe^*/^{136}Xe_{Pu}$ and $^{136}Xe_{Pu}/(^{136}Xe_{Pu}+^{136}Xe_{U})$ in the MORB mantle without invoking partial retention of Xe prior to the last giant impact. Further investigation of early retention of Xe during planet formation is needed to better constrain the timing of the Moon-forming giant impact.

We find that recycled atmospheric Xe dominates the Xe inventories of the SWIR Western and Eastern Orthogonal Supersegment mantle sources (~80-90% of ^{132}Xe is recycled in origin), consistent with results from recent studies of Equatorial Atlantic MORBs (Tucker et al., 2012) and plume-influenced basalts from Iceland (Mukhopadhyay, 2012) and the Rochambeau Rift (Pető et al., 2013). We assert that super-chondritic $^{143}Nd/^{144}Nd$ isotopes in mantle sources with primitive He and Ne do not necessitate a non-chondritic bulk silicate Earth; rather, the prevalence of recycled

atmospheric Xe in these sources indicates the incorporation of depleted recycled material into primitive mantle sources. While significant regassing of the mantle is evident, we also find differences in the extent of degassing of the MORB and plume sources. MORB sources are consistently characterized by a lower fraction of fission Xe derived from Pu-fission, indicating a greater extent of degassing relative to the plume source. Therefore, our Southwest Indian Ridge Xe isotopic data contribute to an emerging portrait of two ancient mantle sources with distinct histories of early outgassing, processing via partial melting and incorporation of recycled material in association with plate tectonics.

4.7 REFERENCES

Alexander, E.C., Lewis, R.S., Reynolds, J.H., Michel, M.C., 1971. Plutonium-244 - Confirmation as an extinct radioactivity. Science, 172(3985): 837-840.

Azbel, I.Y.A., Tolstikhin, I.N., 1993. Accretion and early degassing of the earth – constraints from Pu-U-I-Xe isotopic systematics. Meteoritics, 28(5): 609-621.

Ballentine, C.J., Marty, B., Lollar, B.S., Cassidy, M., 2005. Neon isotopes constrain convection and volatile origin in the Earth's mantle. Nature, 433(7021): 33-38.

Basford, J.R., Dragon, J.C., Pepin, R.O., Coscio, M.R., Jr., Murthy, V.R., 1973. Krypton and xenon in lunar fines. Proceedings of the Lunar Science Conference, Geochimica Et Cosmochimica Acta Supplement 4, 1915-1955.

Bottke, W.F., Walker, R.J., Day, J.M.D., Nesvorny, D., Elkins-Tanton, L., 2010. Stochastic Late Accretion to Earth, the Moon, and Mars. Science, 330(6010): 1527-1530.

Boulos, M.S., Manuel, O.K., 1971. Xenon record of extinct radioactivities in Earth. Science, 174: 1334.

Butler, W.A., Jeffery, P.M., Reynolds, J.H., Wasserburg, G.J., 1963. Isotopic variations in terrestrial xenon. Journal of Geophysical Research, 68(10): 3283.

Caffee, M.W. et al., 1999. Primordial noble gases from Earth's mantle: Identification of a primitive volatile component. Science, 285(5436): 2115-2118.

Deruelle, B., Dreibus, G., Jambon, A., 1992. Iodine Abundances in Oceanic Basalts - Implications for Earth Dynamics. Earth and Planetary Science Letters, 108(4): 217-227.

Dhuime, B., Hawkesworth, C.J., Cawood, P.A., Storey, C.D., 2012. A Change in the Geodynamics of Continental Growth 3 Billion Years Ago. Science, 335(6074): 1334-1336.

Eikenberg, J., Signer, P., Wieler, R., 1993. U-Xe, U-Kr, AND U-Pb systematics for dating uranium minerals and investigations of the production of nucleogenic neon and argon. Geochimica Et Cosmochimica Acta, 57(5): 1053-1069.

Georgen, J.E., Kurz, M.D., Dick, H.J.B., Lin, J., 2003. Low $^{3}He/^{4}He$ ratios in basalt glasses from the western Southwest Indian Ridge (10°-24°E). Earth and Planetary Science Letters, 206(3-4): 509-528.

Gonnermann, H.M., Mukhopadhyay, S., 2009. Preserving noble gases in a convecting mantle. Nature, 459(7246): 560-564.

Graham, D.W., 2002. Noble Gas Isotope Geochemistry of Mid-Ocean Ridge and Ocean Island Basalts: Characterization of Mantle Source Reservoirs. Reviews in Mineralogy and Geochemistry, 47(1): 247-317.

Graham, D.W. et al., 1992. Helium Isotope Geochemistry of Midocean Ridge Basalts from the South-Atlantic. Earth and Planetary Science Letters, 110(1-4): 133-147.

Harper, C.L., Jacobsen, S.B., 1996. Noble gases and Earth's accretion. Science, 273(5283): 1814-1818.

Harrison, D., Burnard, P., Turner, G., 1999. Noble gas behaviour and composition in the mantle: Constraints from the Iceland Plume. Earth and Planetary Science Letters, 171(2): 199-207.

Harrison, T.M., 2009. The Hadean Crust: Evidence from >4 Ga Zircons. Annual Review of Earth and Planetary Sciences, 37(1): 479-505.

Hebeda, E.H., Schultz, L., Freundel, M., 1987. Radiogenic, fissiogenic and nucleogenic noble gases in zircons. Earth and Planetary Science Letters, 85(1-3): 79-90.

Hohenberg, C.M., Podosek, F.A., Reynolds, J.H., 1967. Xenon-Iodine Dating - Sharp Isochronism in Chondrites, Science, 233-236.

Holland, G., Ballentine, C.J., 2006. Seawater subduction controls the heavy noble gas composition of the mantle. Nature, 441(7090): 186-191.

Hudson, G.B., Kennedy, B.M., Podosek, F.A., Hohenberg, C.M., 1989. The early Solar System abundance of Pu-244 as inferred from the St. Severin chondrite, Proceedings of the 19th Lunar and Planetary Science Conference, 547-557.

Jackson, M.G. et al., 2010. Evidence for the survival of the oldest terrestrial mantle reservoir. Nature, 466(7308): 853-856.

Jackson, M.G., Jellinek, A.M., 2013. Major and trace element composition of the high He-3/He-4 mantle: Implications for the composition of a nonchonditic Earth. Geochemistry Geophysics Geosystems, 14(8): 2954-2976.

Jacobsen, S.B., Harper, C.L., 1996. Accretion and Early Differentiation History of the Earth Based on Extinct Radionuclides, Earth Processes: Reading the Isotopic Code. American Geophysical Union, 47-74.

Jacobson, S.A. et al., 2014. Highly siderophile elements in Earth's mantle as a clock for the Moon-forming impact. Nature, 508(7494): 84-87.

Kendrick, M.A., Scambelluri, M., Honda, M., Phillips, D., 2011. High abundances of noble gas and chlorine delivered to the mantle by serpentinite subduction. Nature Geoscience, 4(11): 807-812.

Kunz, J., Staudacher, T., Allegre, C.J., 1998. Plutonium-fission xenon found in Earth's mantle. Science, 280(5365): 877-880.

Kurz, M.D., Jenkins, W.J., Schilling, J.G., Hart, S.R., 1982. Helium Isotopic Variations in the Mantle beneath the Central-North Atlantic-Ocean. Earth and Planetary Science Letters, 58(1): 1-14.

Kurz, M.D., Le Roex, A.P., Dick, H.J.B., 1998. Isotope geochemistry of the oceanic mantle near the Bouvet triple junction. Geochimica Et Cosmochimica Acta, 62(5): 841-852.

Lewis, R.S., 1975. Rare-gases in separated whitlockite from St. Severin chondrite - Xenon and krypton from fission extinct Pu-244. Geochimica Et Cosmochimica Acta, 39(4): 417-432.

Mahoney, J., Leroex, A.P., Peng, Z., Fisher, R.L., Natland, J.H., 1992. Southwestern limits of Indian-Ocean ridge mantle and the origin of low $^{206}Pb/^{204}Pb$ mid-ocean ridge basalt - isotope systematics of the Central Southwest Indian Ridge (17°E - 50°E). Journal of Geophysical Research-Solid Earth, 97(B13): 19771-19790.

McDonough, W.F., Sun, S.S., 1995. The Composition of the Earth, Chemical Geology, 223-253.

McLennan, S.M., Taylor, S.R., 1982. Geochemical constraints on the growth of the continental crust. Journal of Geology, 90(4): 347-361.

Moreira, M., Kunz, J., Allegre, C., 1998. Rare gas systematics in Popping Rock: Isotopic and elemental compositions in the upper mantle. Science, 279(5354): 1178-1181.

Mukhopadhyay, S., 2012. Early differentiation and volatile accretion recorded in deep-mantle neon and xenon. Nature, 486(7401): 101-104.

Mukhopadhyay, S., Parai, R., Pető, M.K., Tucker, J.M., in prep. Formation of the early atmosphere from late-accreting planetesimals. To be submitted to Nature Geoscience.

O'Brien, D.P., Morbidelli, A., Levison, H.F., 2006. Terrestrial planet formation with strong dynamical friction. Icarus, 184(1): 39-58.

Ozima, M., Podosek, F.A., 2002. Noble Gas Geochemistry. Cambridge University Press.

Palme, H., O'Neill, H.S.C., 2004. 2.01 - Cosmochemical Estimates of Mantle Composition. In: Holland, H.D., Turekian, K.K. (Eds.), Treatise on Geochemistry. Pergamon, Oxford, 1-38.

Parai, R., Mukhopadhyay, S., Lassiter, J.C., 2009. New constraints on the HIMU mantle from neon and helium isotopic compositions of basalts from the Cook-Austral Islands. Earth and Planetary Science Letters, 277(1-2): 253-261.

Parai, R., Mukhopadhyay, S., Standish, J.J., 2012. Heterogeneous upper mantle Ne, Ar and Xe isotopic compositions and a possible Dupal noble gas signature recorded in basalts from the Southwest Indian Ridge. Earth and Planetary Science Letters, 359: 227-239.

Pepin, R.O., 1991. On the Origin and Early Evolution of Terrestrial Planet Atmospheres and Meteoritic Volatiles. Icarus, 92(1): 2-79.

Pepin, R.O., 2000. On the isotopic composition of primordial xenon in terrestrial planet atmospheres. Space Science Reviews, 92(1-2): 371-395.

Pepin, R.O., Becker, R.H., Rider, P.E., 1995. Xenon and Krypton Isotopes in Extraterrestrial Regolith Soils and in the Solar-Wind. Geochimica Et Cosmochimica Acta, 59(23): 4997-5022.

Pepin, R.O., Phinney, D., 1976. The Formation Interval of the Earth. Abstracts of the Lunar and Planetary Science Conference, 7: 682-684.

Pepin, R.O., Porcelli, D., 2002. Origin of Noble Gases in the Terrestrial Planets. Reviews in Mineralogy and Geochemistry, 47(1): 191-246.

Pepin, R.O., Porcelli, D., 2006. Xenon isotope systematics, giant impacts, and mantle degassing on the early Earth. Earth and Planetary Science Letters, 250(3-4): 470-485.

Pető, M.K., Mukhopadhyay, S., Kelley, K.A., 2013. Heterogeneities from the first 100 million years recorded in deep mantle noble gases from the Northern Lau Back-arc Basin. Earth and Planetary Science Letters, 369: 13-23.

Phinney, D., Tennyson, J., Frick, U., 1978. Xenon in CO_2 well gas revisited. Journal of Geophysical Research, 83: 2313-2319.

Porcelli, D., Woolum, D., Cassen, P., 2001. Deep Earth rare gases: initial inventories, capture from the solar nebula, and losses during Moon formation. Earth and Planetary Science Letters, 193(1-2): 237-251.

Pujol, M., Marty, B., Burgess, R., Turner, G., Philippot, P., 2013. Argon isotopic composition of Archaean atmosphere probes early Earth geodynamics. Nature, 498(7452): 87-90.

Ragettli, R.A., Hebeda, E.H., Signer, P., Wieler, R., 1994. Uranium Xenon Chronology - Precise Determination of Lambda(SF)* Y136(SF) for Spontaneous Fission of U-238. Earth and Planetary Science Letters, 128(3-4): 653-670.

Raymond, S.N., O'Brien, D.P., Morbidelli, A., Kaib, N.A., 2009. Building the terrestrial planets: Constrained accretion in the inner Solar System. Icarus, 203(2): 644-662.

Rudnick, R.L., Gao, S., 2003. 3.01 - Composition of the Continental Crust. In: Holland, H.D., Turekian, K.K. (Eds.), Treatise on Geochemistry. Pergamon, Oxford, 1-64.

Standish, J.J., 2006. The influence of ridge geometry at the ultraslow-spreading Southwest Indian Ridge (9 -25°E): Basalt composition sensitivity to variations in source and process. PhD Thesis, Joint Program in Oceanography/Applioed Ocean Science and Engineering.

Standish, J.J., Dick, H.J.B., Michael, P.J., Melson, W.G., O'Hearn, T., 2008. MORB generation beneath the ultraslow spreading Southwest Indian Ridge (9-25°E): Major element chemistry and the importance of process versus source. Geochemistry Geophysics Geosystems, 9.

Staudacher, T., Allegre, C.J., 1982. Terrestrial Xenology. Earth and Planetary Science Letters, 60(3): 389-406.

Staudacher, T., Allegre, C.J., 1988. Recycling of Oceanic-Crust and Sediments - the Noble-Gas Subduction Barrier. Earth and Planetary Science Letters, 89(2): 173-183.

Stuart, F.M., Lass-Evans, S., Fitton, J.G., Ellam, R.M., 2003. High $^{3}He/^{4}He$ ratios in picritic basalts from Baffin Island and the role of a mixed reservoir in mantle plumes. Nature, 424(6944): 57-59.

Trieloff, M., Kunz, J., 2005. Isotope systematics of noble gases in the Earth's mantle: possible sources of primordial isotopes and implications for mantle structure. Physics of the Earth and Planetary Interiors, 148(1): 13-38.

Trieloff, M., Kunz, J., Clague, D.A., Harrison, D., Allegre, C.J., 2000. The nature of pristine noble gases in mantle plumes. Science, 288(5468): 1036-1038.

Tucker, J.M., Mukhopadhyay, S., 2014. Evidence for multiple magma ocean outgassing and atmospheric loss episodes from mantle noble gases. Earth and Planetary Science Letters, 393(0): 254-265.

Tucker, J.M., Mukhopadhyay, S., Schilling, J.G., 2012. The heavy noble gas composition of the depleted MORB mantle (DMM) and its implications for the preservation of heterogeneities in the mantle. Earth and Planetary Science Letters, 355: 244-254.

Walsh, K.J., Morbidelli, A., Raymond, S.N., O'Brien, D.P., Mandell, A.M., 2011. A low mass for Mars from Jupiter's early gas-driven migration. Nature, 475(7355): 206-209.

Wetherill, G.W., 1953. Spontaneous fission yields from uranium and thorium. Physical Review, 92(4): 907-912.

Wetherill, G.W., 1975. Radiometric chronology of early Solar System. Annual Review of Nuclear and Particle Science, 25: 283-328.

Wieler, R., Baur, H., 1994. Krypton and Xenon from the Solar-Wind and Solar Energetic Particles in 2 Lunar Ilmenites of Different Antiquity. Meteoritics, 29(5): 570-580.

Yokochi, R., Marty, B., 2004. A determination of the neon isotopic composition of the deep mantle. Earth and Planetary Science Letters, 225(1-2): 77-88.

York, D., 1969. Least squares fitting of a straight line with correlated errors. Earth and Planetary Science Letters, 5(5): 320-324.

York, D., Evensen, N.M., Martinez, M.L., Delgado, J.D., 2004. Unified equations for the slope, intercept, and standard errors of the best straight line. American Journal of Physics, 72(3): 367-375.

Chapter 5: Strontium isotopic constraints on early Solar System chronology and the history of planetary volatile depletion

ABSTRACT

The long-lived radioactive rubidium-strontium (^{87}Rb-^{87}Sr) system provides a powerful chronometer for volatile depletion in the early Solar System. Here we present a suite of high-precision Sr isotopic data in planetary materials and assess constraints on the chronology of lunar formation. We compute initial ^{87}Sr/^{86}Sr ratios for lunar anorthosite 60025, the eucrite Juvinas and Moore County plagioclase. Since we have precisely measured the offset between standard reference materials NIST SRM 987 and Pacific seawater, we are able to properly normalize literature initial ^{87}Sr/^{86}Sr data from a large set of studies that report only one or the other of these standards. Therefore, we are able to place our own determinations of initial ^{87}Sr/^{86}Sr in planetary materials in the context of a normalized compilation of initial ^{87}Sr/^{86}Sr data from the literature. Careful normalization of literature data resolves some discrepancies among different studies; however, in many cases, inter-laboratory differences persist. We estimate the Solar System initial ^{87}Sr/^{86}Sr based on our determination of the Moore County plagioclase initial, and use this estimate to explore different models of Sr isotopic evolution to account for the initial ^{87}Sr/^{86}Sr determined for the lunar anorthosite 60025. If the Moon is derived from proto-Earth material that experienced volatile loss (and thus Rb/Sr fractionation) in the aftermath of the Moon-forming giant impact, then based on Sr isotope systematics in lunar anorthosite 60025, the Moon formed prior to ~62 Myr.

5.1 INTRODUCTION

Planetary bodies in the Solar System are uniformly characterized by a depletion in volatile elements relative to the composition of the Sun (e.g., Ringwood, 1979; Morgan and Anders, 1980). Proto-planetary materials grew within a cooling solar nebula, and volatile depletion within the proto-planetary disk was accomplished by some combination of incomplete condensation from the solar nebula and volatile loss during high-energy impacts. The diverse present-day volatile inventories of planetary bodies in the Solar System are the outcomes of unique histories of volatile accretion and loss. Consequently, chemical constraints on the timing and nature of volatile depletion in Solar System materials potentially inform our understanding of the processes that shaped planetary bodies in the Solar System as they grew and evolved to their present-day state.

The long-lived radioactive rubidium-strontium (^{87}Rb-^{87}Sr) system provides a powerful chronometer for early Solar System events. Due to a high volatility of Rb relative to Sr, ^{87}Sr/^{86}Sr ratios record information about the timing of Rb/Sr fractionation by volatile loss or incomplete condensation. For Rb-poor Solar System materials, corrections for radiogenic ingrowth of ^{87}Sr after the time of formation are small, such that initial ^{87}Sr/^{86}Sr ratios can be determined with far better precision than internal Rb-Sr isochron ages. Systematic variations observed in initial ^{87}Sr/^{86}Sr are interpreted to reflect differences in the timing of volatile depletion (and thus Rb/Sr fractionation) in various planetary bodies growing within in the proto-planetary disk (e.g., Papanastassiou and Wasserburg, 1969; Gray et al., 1973; Wasserburg et al., 1977a; 1977b; Halliday and Porcelli, 2001; Halliday, 2008). Thus, a chronology of early Solar System events may be

constructed based on relative variations in initial $^{87}Sr/^{86}Sr$ in planetary materials (i.e., Sr model ages), rather than absolute ages derived by the internal ^{87}Rb-^{87}Sr isochron method.

Earth's Moon is thought to have formed from a debris disk generated by a giant impact in the end stages of terrestrial accretion (Hartmann and Davis, 1975; Cameron and Ward, 1976) and is broadly characterized by a low abundance of volatile elements and compounds relative to the Earth (Ringwood, 1979). The Rb-Sr system was one of the first radiometric systems applied to constrain the timing of lunar formation. Papanastassiou and Wasserburg determined Sr model ages for lunar soils, basalts, anorthosites and a troctolite (Papanastassiou and Wasserburg, 1971; 1972b; 1972a; 1976a). In particular, Papanastassiou and Wasserburg (1972b) noted a measured $^{87}Sr/^{86}Sr$ for the lunar anorthosite 60025 lower than the basaltic achondritic best fit initial $^{87}Sr/^{86}Sr$ (BABI; Papanastassiou and Wasserburg, 1969). The authors argued for early separation of lunar precursor material with low Rb/Sr from the high Rb/Sr solar nebular environment in order to preserve the very primitive Sr isotopic composition observed in 60025. Based on these results and constraints from U-Pb, Wasserburg et al. (1977a) argued that the Moon formed before ~4.45 Ga.

Additional age determinations for the lunar anorthosite 60025 were made based on U-Pb and ^{147}Sm-^{143}Nd systematics. Hanan and Tilton (1987) reported U-Pb data for the lunar anorthosite 60025 and calculated a ^{207}Pb-^{206}Pb model age of 4.520 ± 0.007 Ga. Carlson and Lugmair (1988) calculated a ^{147}Sm-^{143}Nd isochron age for 60025 of 4.44 ± 0.02 Ga. The authors also reported $^{87}Sr/^{86}Sr$ data, and noted that if 60025 formed at 4.44 Ga as indicated by ^{147}Sm-^{143}Nd systematics, then the initial $^{87}Sr/^{86}Sr$ determined for 60025 required lunar derivation from a reservoir of material with Rb/Sr similar to the

bulk Earth. Halliday (2008) used the 60025 initial $^{87}Sr/^{86}Sr$ ratio of Carlson and Lugmair (1988) to calculate a Sr model age range of 70-110 Myr based on a Solar System initial $^{87}Sr/^{86}Sr$ from the angrite SAH99555 and Efremovka CAI (Nyquist et al., 2003) and assuming an Earth-like Rb/Sr for lunar precursor material. In contrast, Borg et al. (2011) calculated a very late 60025 crystallization age of 4.360 ± 0.003 Ga based on ^{207}Pb-^{206}Pb, ^{147}Sm-^{143}Nd and ^{146}Sm-^{142}Nd using a half-life for ^{146}Sm of 103 Myr (a ^{146}Sm-^{142}Nd age of ~4.40 Ga is calculated using the 68 Myr half-life recently determined by Kinoshita et al., 2012). Borg et al. (2011) argued that either the Moon itself was young (formation up to ~200 Myr after the first Solar System solids) or that the anorthosite crust was not generated in association with a lunar magma ocean. The authors noted that a late formation of the Moon would be consistent with ^{182}Hf-^{182}W studies arguing for lunar formation after the extinction of ^{182}Hf at ~60 Myr (Touboul et al., 2007). However, since the Moon and Earth have indistinguishable Hf/W ratios (e.g., Elkins-Tanton et al., 2011) as well as identical W isotopic compositions (Touboul et al., 2007), no inference can be made regarding the age of the Moon from Hf-W systematics (cf. Yu and Jacobsen, 2011).

Constraints on the timing of Moon formation inform our understanding of Earth's accretion, segregation of the metallic core, silicate differentiation, early mantle outgassing and formation of the atmosphere (e.g., Chapter 3; Pepin and Porcelli, 2006; Touboul et al., 2007; Jacobsen et al., 2008; Yu and Jacobsen, 2011). Furthermore, the timing of the Moon-forming giant impact provides information about the timescales of planetary growth and the era of giant impacts in early Solar System history. Thus, a strict constraint on the age of the Moon is critical to our understanding of both the early Earth and the broader evolution of the Solar System. Here we present a new suite of high-

precision $^{87}Sr/^{86}Sr$ determinations for the lunar anorthosite 60025, a plagioclase separate from the cumulate eucrite Moore County, the eucrite Juvinas and the angrite D'Orbigny. We compute initial $^{87}Sr/^{86}Sr$ ratios for lunar anorthosite 60025 and Moore County plagioclase and place these in context of a normalized compilation of initial $^{87}Sr/^{86}Sr$ data from the literature. Based on Sr isotopic systematics in 60025 and Moore County plagioclase, we examine various models of Rb-Sr evolution and explore implications for the timing and extent of volatile depletion in the early Solar System.

5.2 SAMPLES AND METHODS

Four samples were selected for Sr isotopic analysis: one 25 mg piece of the lunar ferroan anorthosite 60025; strontium separated from Moore County plagioclase generously provided by D. A. Papanastassiou; two separate pieces of the basaltic eucrite Juvinas of 47 mg and 384 mg; and a 232 mg piece of the angrite D'Orbigny provided by B. P. Weiss. Samples were dissolved as small chips with the exception of the D'Orbigny sample, which was gently crushed in a stainless steel mortar prior to dissolution.

5.2.1 Dissolution and chemical separation of Sr

Samples were dissolved in 1:3:4 HF:HCl:HNO_3 at 180°C, dried and re-dissolved in excess concentrated nitric acid 2-3 times, and lastly dried and re-dissolved in 6N hydrochloric acid to ensure total dissolution. Chemical separation of Sr was achieved by column chromatography using the Eichrom Sr Spec ion exchange resin. Clean 6 mL Savillex PFA microcolumns were prepared with polyethelene frits and 200 μL of Sr Spec resin, which was discarded after each use. The resin column was built in Milli-Q purified

water (18.2 MOhm), washed with 2 reservoir volumes of Milli-Q water and then conditioned with 2 mL of 3N nitric acid. Samples were taken up in 200 μL of 3N nitric acid and loaded onto the columns. All elements except Sr were eluted using 2 mL of 3N nitric acid, and an additional 3 mL of 3N nitric acid was used to elute Ba (for a total of 5 mL 3N nitric acid). Sr was eluted with 2 mL of Milli-Q purified water and dried down.

To load sample Sr onto filaments, 300-500 ng of Sr were picked up in 2 μL of 0.3N nitric acid and mixed with 0.5 μL of 8N phosphoric acid. Samples were loaded onto Ta single filaments held at a current of 1 amp and heated to dryness. The current was slowly raised and held at 1.5 amps for 5 minutes, slowly heated to a dark red glow was apparent (typically at 2.8 amps), held for 2-3 seconds and then quickly turned down to zero amps.

5.2.2 Thermal ionization mass spectrometry

Strontium isotope ratios were measured by thermal ionization mass spectrometry (TIMS) using the GV Isoprobe-T at Harvard using a multi-dynamic collection method with two magnet steps using Xact amplifier boards generously provided by Isotopx. In the first step, ^{84}Sr, ^{86}Sr, ^{87}Sr and ^{88}Sr are collected on the L2, H1, H2 and H3 cups, respectively, and a correction for ^{87}Rb interference on the H2 cup is made based on ^{85}Rb monitored on the axial cup. In the second step, ^{84}Sr, ^{86}Sr, ^{87}Sr and ^{88}Sr are collected on the axial, H2, H3 and H4 cups, respectively, and a correction for ^{87}Rb interference on the H3 cup is made based on ^{85}Rb monitored on the H1 cup. In all runs, the rubidium interference correction is negligible (< 3 ppm). Samples ran for 10-50 blocks of 10 cycles each with an integration time of 10 seconds. Measured isotope ratios were corrected for

instrumental mass fractionation to $^{86}Sr/^{88}Sr = 0.1194$ using an exponential fractionation law.

NIST SRM 987 and Pacific seawater standard analyses bracket our sample analyses to monitor instrumental drift and external reproducibility. The two-step multicollection method enables the cancellation of cup factors and affords improved external reproducibility of standards compared to a static multicollection method. We achieve 4 ppm (2 standard error) external reproducibility on both standards (Figure 5.1). The first Juvinas split was analyzed in the summer of 2013, while all other samples were analyzed in the spring of 2014. A slight shift (~12 ppm) in the absolute average values for NIST SRM 987 and Pacific seawater was observed between the two analytical periods; however, the offset measured between the two standards remained constant (Figure 5.2). The shift is likely due to replacement of parts in the Faraday amplifier and control unit during the interval between the two analytical periods.

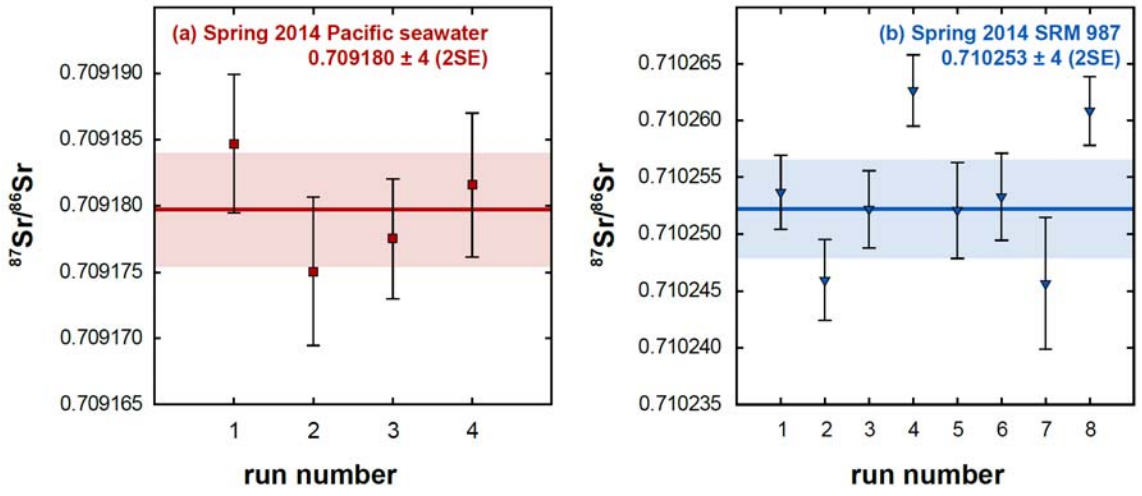

Figure 5.1 Analyses of standard reference materials in Spring 2014. Runs for (a) Pacific seawater and (b) NIST SRM 987 typically lasted 20-50 blocks of 10 cycles each. Block-averaged run data (each run represents a distinct filament) and 2σ errors are shown. The grand mean and 2 standard errors are indicated by the bold line and shaded interval. We are able to achieve 4 ppm (2 standard error) precision in our measurements.

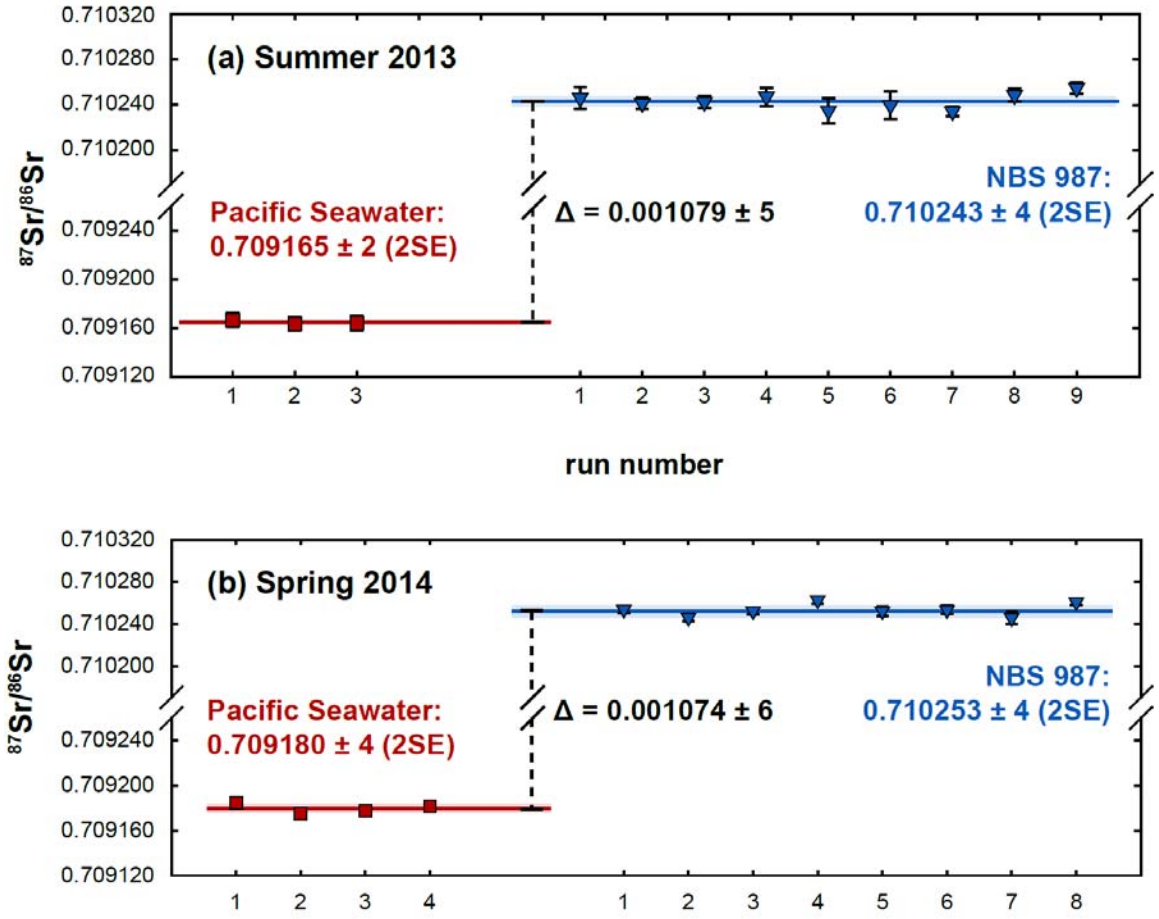

Figure 5.2 Analyses of standard reference materials in (a) Summer 2013 and (b) Spring 2014. A slight shift (~12 ppm) in the absolute means for Pacific seawater and SRM 987 is observed between the two analytical periods, and is likely related to replacement of parts in the Faraday amplified and control unit in the winter of 2013. However, the offset between the two standards is constant within the uncertainties between the two analytical periods.

5.3 RESULTS

We present high-precision Sr isotopic data for the lunar anorthosite 60025, a plagioclase separate from the cumulate eucrite Moore County, two splits of the eucrite Juvinas and the angrite D'Orbigny. NIST SRM 987 and a sample of Pacific seawater were measured repeatedly as standards in order to monitor instrumental performance, and

to provide a common point of reference with literature data. Here we present our measurements of $^{87}Sr/^{86}Sr$ in standard reference materials (Table 5.1) and a suite of planetary materials (Table 5.2), as well as determinations of initial $^{87}Sr/^{86}Sr$ in Juvinas, Moore County plagioclase and the lunar anorthosite 60025. Since we have precisely measured the offset between NIST SRM 987 and Pacific seawater, we are able to properly normalize data from a large set of studies that report only one or the other of these standards (Table 5.3, Table 5.4). Thus, we place our results in context by constructing a new normalized compilation of initial $^{87}Sr/^{86}Sr$ variations in planetary materials.

5.3.1 Measurements of $^{87}Sr/^{86}Sr$ in planetary materials

Strontium isotopic results are presented in Figure 5.3 and Table 5.2. Figure 5.3a shows block-averaged run data for 3 filaments loaded with Sr purified from lunar anorthosite 60025. We measure a grand mean $^{87}Sr/^{86}Sr$ ratio of 0.699103 ± 4 (2 standard errors) for 60025. Using a 60025 $^{87}Rb/^{86}Sr$ ratio of 0.00028 (Papanastassiou and Wasserburg, 1972b), we compute an initial $^{87}Sr/^{86}Sr$ of 0.699085 ± 4 (2 standard errors). Figure 5.3b shows block-averaged run data for 4 filaments loaded with Sr purified from Moore County plagioclase. We measure a grand mean $^{87}Sr/^{86}Sr$ ratio of 0.699085 ± 6 (2 standard errors) for Moore County plagioclase. Using a Moore County plagioclase $^{87}Rb/^{86}Sr$ ratio of 0.0011 (Papanastassiou and Wasserburg, 1972a), we compute an initial $^{87}Sr/^{86}Sr$ of 0.699012 ± 6 (2 standard errors).

Figure 5.3c shows block-averaged run data for 4 filaments loaded with Sr purified from Juvinas split 1. We measure a grand mean $^{87}Sr/^{86}Sr$ ratio of 0.699236 ± 8 (2

Table 5.1 Sr isotopic measurements in standard reference materials

Analytical Period	Sample	$^{87}Sr/^{86}Sr$[1]	±2 SE	Mean $^{87}Sr/^{86}Sr$	±2 SE
Summer 2013	*Pacific SW TP24N*	0.709167	0.000006	0.709165	0.000002
		0.709164	0.000005		
		0.709164	0.000006		
	NIST SRM 987	0.710246	0.000010	0.710243	0.000004
		0.710241	0.000005		
		0.710242	0.000006		
		0.710247	0.000008		
		0.710235	0.000011		
		0.710240	0.000012		
		0.710234	0.000004		
		0.710249	0.000006		
		0.710255	0.000005		
Spring 2014	*Pacific SW TP24N*	0.709185	0.000005	0.709180	0.000004
		0.709175	0.000006		
		0.709178	0.000005		
		0.709182	0.000005		
	NIST SRM 987	0.710254	0.000003	0.710253	0.000004
		0.710246	0.000004		
		0.710252	0.000003		
		0.710263	0.000003		
		0.710252	0.000004		
		0.710253	0.000004		
		0.710246	0.000006		
		0.710261	0.000003		

[1]Block-averaged $^{87}Sr/^{86}Sr$ ratios are corrected using an exponential fractionation law to $^{86}Sr/^{88}Sr = 0.1194$. Grand means and two standard errors of the mean are given. A slight shift in absolute values is observed between the two analytical periods, likely due to replacement of parts in the Faraday amplifier and control until in the interval between analytical periods. The offset between the two standards remains constant between the two analytical periods: for measurements made in Summer 2013, we calculate an offset of 0.001079 ± 5; for measurements made in Spring 2014, the offset is 0.001074 ± 6. Since the majority of measurements were made in Spring 2014, we apply a correction of +0.000010 to the Juvinas split 1 sample reported in Table 5.2 to normalize to the rest of the data.

Table 5.2 Sr isotopic measurements in planetary materials

Sample	$^{87}Sr/^{86}Sr$[1]	±2 SE	Mean $^{87}Sr/^{86}Sr$	±2 SE	$^{87}Rb/^{86}Sr$	Initial $^{87}Sr/^{86}Sr$	±2 SE
Juvinas - split 1[2]	0.699229	0.000014	0.699236	0.000008	0.00256	0.699067	0.000008
	0.699229	0.000008					
	0.699244	0.000015					
	0.699240	0.000007					
Juvinas - split 2	0.699470	0.000006	0.699472	0.000004	--	--	
	0.699470	0.000004					
	0.699470	0.000003					
	0.699478	0.000004					
Moore County plagioclase	0.699083	0.000003	0.699085	0.000006	0.0011[3]	0.699012	0.000006
	0.699092	0.000004					
	0.699083	0.000004					
	0.699080	0.000004					
Lunar anorthosite 60025	0.699104	0.000004	0.699103	0.000004	0.00028[4]	0.699085	0.000004
	0.699099	0.000007					
	0.699106	0.000004					
D'Orbigny	0.699134	0.000007	0.699146	0.000014	--	--	
	0.699158	0.000009					
	0.699146	0.000003					

[1]Block-averaged $^{87}Sr/^{86}Sr$ ratios are corrected using an exponential fractionation law to $^{86}Sr/^{88}Sr = 0.1194$. [2]Juvinas split 1 was analyzed in Summer 2013; a correction of +0.000010 has been applied to the values reported above for consistency with the rest of the samples (see Table 5.1). All other measurements were conducted in Spring 2014. Grand mean $^{87}Sr/^{86}Sr$ ratios are given for each sample split along with 2 standard errors of the mean. Based on the $^{87}Rb/^{86}Sr$ ratio, corrections for radiogenic ingrowth are made based on $^{87}Rb/^{86}Sr$ to determine the initial $^{87}Sr/^{86}Sr$ for Juvinas split 1, lunar anorthosite 60025 and Moore County plagioclase. [3]Papanastassiou and Wasserburg (1972a); [4]Papanastassiou and Wasserburg (1972b).

Table 5.3 Normalized literature Sr isotopic data

Reference	Sample	initial $^{87}Sr/^{86}Sr$[1]	±2σ	standard	standard $^{87}Sr/^{86}Sr$[1]	±2σ	adjust.[2]	norm initial $^{87}Sr/^{86}Sr$	norm ±2σ[3]
Papanastassiou and Wasserburg (1969)	*Juvinas*	0.698962	0.000057	seawater	0.709080	0.000030	+0.000100	0.699062	0.000064
	Pasamonte	0.698985	0.000181	seawater	0.709080	0.000030	+0.000100	0.699085	0.000183
	Sioux County	0.698990	0.000081	seawater	0.709080	0.000030	+0.000100	0.699090	0.000086
	Nuevo Laredo	0.699047	0.000118	seawater	0.709080	0.000030	+0.000100	0.699147	0.000122
	Jonzac	0.698983	0.000138	seawater	0.709080	0.000030	+0.000100	0.699083	0.000141
	Stannern	0.698928	0.000137	seawater	0.709080	0.000030	+0.000100	0.699028	0.000140
	Moore County	0.698989	0.000107	seawater	0.709080	0.000030	+0.000100	0.699089	0.000111
	BABI[4]	0.698990	0.000047	seawater	0.709080	0.000030	+0.000100	0.699090	0.000056
Gray et al. (1973)	*Allende CAI D7*	0.69877	0.00004	seawater	0.70909	0.000065	+0.00009	0.69886	0.00008
Papanastassiou and Wasserburg (1972a)	*Moore Co. plag*	0.69891	0.00003	seawater	0.70910	0.00001	+0.00008	0.69899	0.00003
Papanastassiou and Wasserburg (1976a)[5]	*Moore Co. plag*	0.69891	0.00003	seawater	0.70910	0.00001	+0.00008	0.69899	0.00003
	60015-36	0.69900	0.00003	seawater	0.70910	0.00001	+0.00008	0.69908	0.00003
	60015-95	0.69895	0.00004	seawater	0.70910	0.00001	+0.00008	0.69903	0.00004
	60025-65	0.69894	0.00003	seawater	0.70910	0.00001	+0.00008	0.69902	0.00003
	76535	0.69900	0.00004	seawater	0.70910	0.00001	+0.00008	0.69908	0.00004
Wasserburg et al. (1977)[6]	*ADOR TR-1*	0.69883	0.00007	seawater	0.70910	0.00003	+0.00008	0.69891	0.00008
	ADOR TR-2	0.69884	0.00004	seawater	0.70910	0.00003	+0.00008	0.69892	0.00005
	ADOR TR-3	0.69879	0.00005	seawater	0.70910	0.00003	+0.00008	0.69887	0.00006
	ADOR TR-3r	0.69880	0.00005	seawater	0.70910	0.00003	+0.00008	0.69888	0.00006
	ADOR TR-4	0.69888	0.00006	seawater	0.70910	0.00003	+0.00008	0.69896	0.00007
	ADOR TR-4r	0.69886	0.00004	seawater	0.70910	0.00003	+0.00008	0.69894	0.00005
	ADOR pyx	0.69883	0.00004	seawater	0.70910	0.00003	+0.00008	0.69891	0.00005
	ADOR whit-C	0.69885	0.00008	seawater	0.70910	0.00003	+0.00008	0.69893	0.00009
	ADOR whit-D	0.69883	0.00005	seawater	0.70910	0.00003	+0.00008	0.69891	0.00006
Allegre et al. (1975)	*Juvinas*	0.69898	0.00005	SRM 987	0.71017	0.00002	+0.00008	0.69906	0.00005
Jacobsen and Wasserburg (1984)	*Moama*	0.69890	0.00003	seawater	0.70906	0.00003	+0.00012	0.69902	0.00004

[1]Values reported by the authors. [2]Adjustment applied to reported values to yield normalized initial $^{87}Sr/^{86}Sr$. [3]normalized 2σ include errors related to normalization. [4]Basaltic achondrite best initial. [5]60015 and 60025 are lunar anorthosites; 76535 is a lunar troctolite. [6]ADOR is an abbreviation for Angra dos Reis; TR stands for total rock.

Table 5.3 (continued): Normalized literature Sr isotopic data

Reference	Sample	$^{87}Sr/^{86}Sr$[1]	±2σ	standard	standard $^{87}Sr/^{86}Sr$[1]	±2σ	adjust.[2]	norm initial $^{87}Sr/^{86}Sr$	norm ±2σ[3]
Carlson and Lugmair (1988)	*60025 plag*	0.699084	0.00002	SRM 987	0.71026	0.00002	–0.000007	0.699077	0.000028
	60025 plag	0.699072	0.000022	SRM 987	0.71026	0.00002	–0.000007	0.699065	0.000030
	60025 mafic	0.699089	0.00004	SRM 987	0.71026	0.00002	–0.000007	0.699082	0.000045
	Moore Co. plag	0.698987	0.00002	SRM 987	0.71026	0.00002	–0.000007	0.698980	0.000028
Podosek et al. (1991)	*Allende CAI D7*[7]	0.69887	0.00002	SRM 987	0.71014	0.00002	+0.00011	0.69898	0.000028
	Allende CAI D7[7]	0.69887	0.00002	seawater	0.70907	0.00002	+0.00011	0.69898	0.000028
Lugmair and Galer (1992)	*Angra dos Reis 1*	0.698974	0.000016	SRM 987	0.710263	0.000005	–0.000010	0.698964	0.000017
	Angra dos Reis 2	0.698955	0.000016	SRM 987	0.710263	0.000005	–0.000010	0.698945	0.000017
	Angra dos Reis 3	0.698963	0.000014	SRM 987	0.710263	0.000005	–0.000010	0.698953	0.000015
	LEW86010 ol	0.698957	0.000020	SRM 987	0.710263	0.000005	–0.000010	0.698947	0.000021
	LEW86010 pyx	0.698979	0.000015	SRM 987	0.710263	0.000005	–0.000010	0.698969	0.000016
	Moore Co. plag	0.698986	0.000017	SRM 987	0.710263	0.000005	–0.000010	0.698976	0.000018
Nyquist et al. (1994)	*Angra dos Reis pyx*	0.698970	0.000018	SRM 987	0.71025	0.000014	+0.000003	0.698973	0.000023
	LEW86010	0.698972	0.000008	SRM 987	0.71025	0.000014	+0.000003	0.698975	0.000016
Nyquist et al. (2003)	*Efremovka CAI*	0.698934	0.000020	SRM 987	0.71025	0.000014	+0.000003	0.698937	0.000024
Tonui et al. (2003)	*D'Orbigny pyx*	0.698820	0.000005	SRM 987	0.710150	0.000005	+0.000103	0.698923	0.000007
Hans et al. (2013)	*Juvinas*	0.698929	0.000003	SRM 987	0.710250	0.000003	+0.000003	0.698932	0.000004
	Juvinas plag	0.698974	0.000003	SRM 987	0.710250	0.000003	+0.000003	0.698977	0.000004
	Moama	0.698997	0.000003	SRM 987	0.710250	0.000003	+0.000003	0.699000	0.000004
	Moore Co. plag	0.698967	0.000003	SRM 987	0.710250	0.000003	+0.000003	0.698970	0.000004
	D'Orbigny	0.698979	0.000003	SRM 987	0.710250	0.000003	+0.000003	0.698982	0.000004
	Angra dos Reis	0.698952	0.000003	SRM 987	0.710250	0.000003	+0.000003	0.698955	0.000004
	LEW86010	0.698999	0.000003	SRM 987	0.710250	0.000003	+0.000003	0.699002	0.000004
	ADOR	0.698978	0.000004	SRM 987	0.710250	0.000003	+0.000003	0.698981	0.000005
	BABI	0.698970	0.000028	SRM 987	0.710250	0.000003	+0.000003	0.698973	0.000028
this study	*Juvinas*	0.699057	0.000008	SRM 987	0.710243	0.000004	+0.000010	0.699067	0.000009
	Moore Co. plag	0.699012	0.000006	–	–	–	–	0.699012	0.000006
	60025	0.699085	0.000004	–	–	–	–	0.699085	0.000004

[7]Allende CAI D7 is referred to by the authors as inclusion 3898. Podosek et al. (1991) report SRM 987 and seawater; the two standards give identical normalized results.

Table 5.4 Normalized literature initial $^{87}Sr/^{86}Sr$ by planetary material

Type	Reference	Sample	norm initial $^{87}Sr/^{86}Sr$	norm ±2σ
CAIs	Gray et al. (1973)	*Allende CAI D7*	0.69886	0.00008
	Podosek et al. (1991)	*Allende CAI D7*	0.69898	0.00003
	Nyquist et al. (2003)	*Efremovka CAI*	0.698937	0.000024
Angrites	Wasserburg et al. (1977)	*Angra dos Reis avg*	0.69891	0.00002
	Lugmair and Galer (1992)	*Angra dos Reis avg*	0.698954	0.000011
	Nyquist et al. (1994)	*Angra dos Reis pyx*	0.698973	0.000023
	Hans et al. (2013)	*Angra dos Reis*	0.698955	0.000004
	Lugmair and Galer (1992)	*LEW86010*	0.698958	0.000022
	Nyquist et al. (1994)	*LEW86010*	0.698975	0.000016
	Hans et al. (2013)	*LEW86010*	0.699002	0.000004
	Tonui et al. (2003)	*D'Orbigny pyx*	0.698923	0.000007
	Hans et al. (2013)	*D'Orbigny*	0.698982	0.000004
Eucrites	Papanastassiou and Wasserburg (1972a)	*Moore Co. plag*	0.69899	0.00003
	Carlson and Lugmair (1988)	*Moore Co. plag*	0.698980	0.000028
	Lugmair and Galer (1992)	*Moore Co. plag*	0.698976	0.000018
	Hans et al. (2013)	*Moore Co. plag*	0.698970	0.000004
	this study	*Moore Co. plag*	0.699012	0.000006
	Jacobsen and Wasserburg (1984)	*Moama*	0.69902	0.00004
	Hans et al. (2013)	*Moama*	0.699000	0.000004
	Papanastassiou and Wasserburg (1969)	*Juvinas*	0.699062	0.000064
	Allegre et al. (1975)	*Juvinas*	0.69906	0.00005
	Hans et al. (2013)	*Juvinas*	0.698932	0.000004
	this study	*Juvinas*	0.699067	0.000009
	Papanastassiou and Wasserburg (1969)	*BABI*	0.699090	0.000056
	Hans et al. (2013)	*BABI*	0.698973	0.000028
Lunar rocks	Papanastassiou and Wasserburg (1976a)	*76535*	0.69908	0.00004
	Papanastassiou and Wasserburg (1976a)	*60025-65*	0.69902	0.00003
	Carlson and Lugmair (1988)	*60025*	0.699075	0.000010
	this study	*60025*	0.699085	0.000004

All abbreviations and designations same as in Table 5.3.

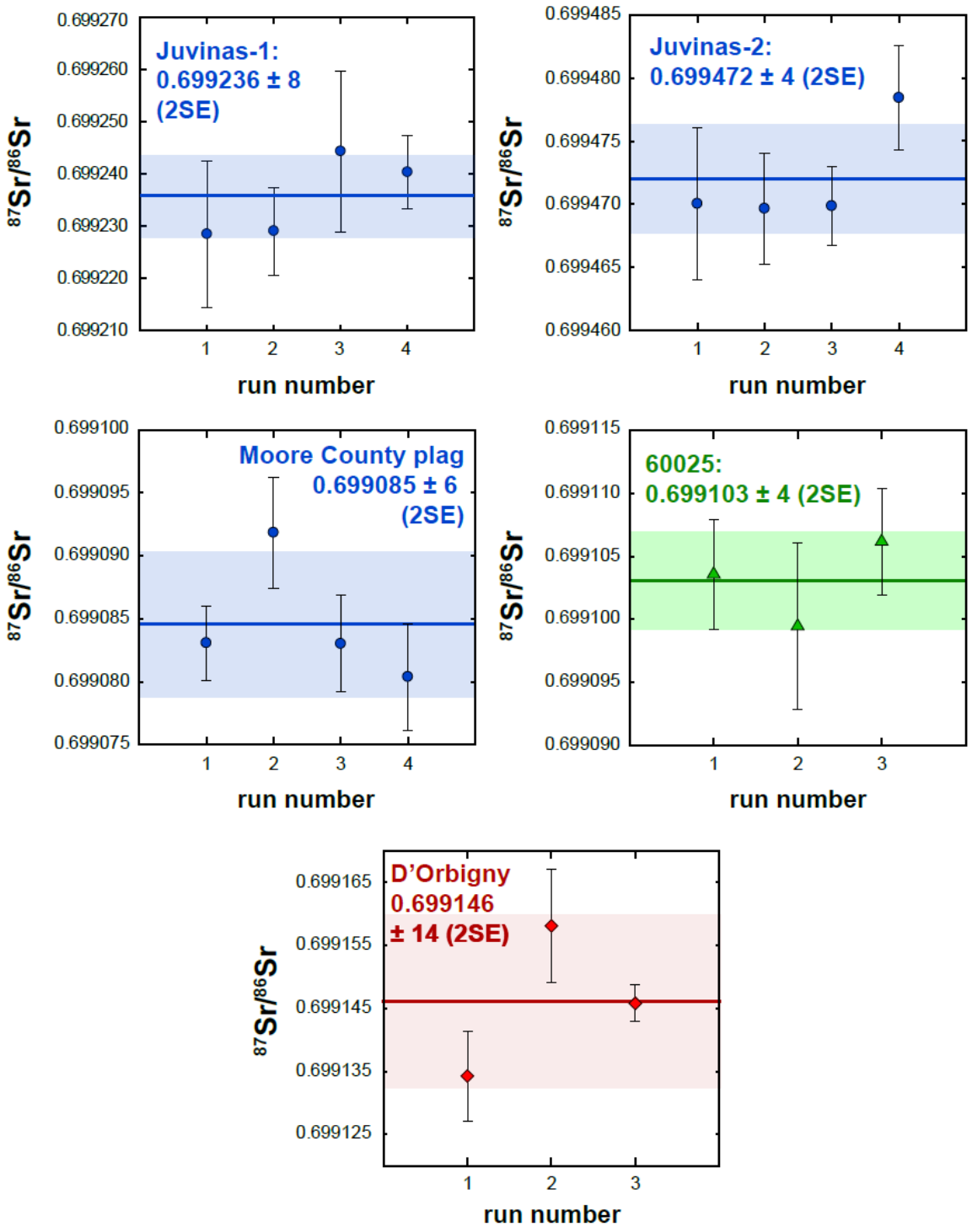

Figure 5.3 Measured $^{87}Sr/^{86}Sr$ in planetary materials. Runs typically lasted 10-50 blocks of 10 cycles each. Block-averaged run data (each run represents a distinct filament) and 2σ errors are shown. The grand mean and 2 standard errors are indicated by bold lines and shaded intervals.

standard errors) for Juvinas split 1. Block-averaged run data for 3 filaments loaded with Sr purified from Juvinas split 2 (Figure 5.3d) yield a grand mean $^{87}Sr/^{86}Sr$ ratio of 0.699472 ± 4 (2 standard errors). Figure 5.3e shows block-averaged run data for 3 filaments loaded with Sr purified from the angrite D'Orbigny. We measure a grand mean $^{87}Sr/^{86}Sr$ ratio of 0.699146± 14 (2 standard errors) for D'Orbigny.

5.3.2 A new normalized compilation of initial $^{87}Sr/^{86}Sr$ in planetary materials

Halliday and Porcelli (2001) compiled Sr isotopic data from the literature on the oldest Solar System materials and lunar rocks, and discussed these as supporting a late Moon formation (70-110 million years). In order to make chronological comparisons across a wide array of literature Sr data obtained on several generations of mass spectrometers in different labs over many decades, Halliday and Porcelli (2001) normalized their compiled data based on reported measurements of the widely-used National Institute of Standards and Technology $SrCO_3$ standard NIST SRM 987. However, the earliest Rb-Sr studies in Solar System materials reported only Pacific seawater as a standard (Papanastassiou and Wasserburg, 1969; 1972b; 1972a; Gray et al., 1973; 1976a; 1976b; Wasserburg et al., 1977b; Jacobsen and Wasserburg, 1984). Since inter-laboratory biases exist on the order of tens of ppm (far greater than the uncertainties in modern data), a precise determination of the offset between the NIST SRM 987 standard and Pacific seawater is required to reliably normalize literature data for comparison with modern data.

Our precise determination of $^{87}Sr/^{86}Sr$ in NIST SRM 987 and Pacific seawater (Figure 5.1, Figure 5.2) allows us to correct for inter-laboratory biases in literature data

that use either material as a standard. We present an internally consistent compilation of literature initial $^{87}Sr/^{86}Sr$ data for early Solar System materials (Tables 5.3, 5.4; Figures 5.4, 5.5). Figure 5.4 shows initial $^{87}Sr/^{86}Sr$ data grouped by study and indicates the reference material reported for each study (Table 5.3). Studies that reported initial $^{87}Sr/^{86}Sr$ along with Pacific seawater as a standard reference material (Papanastassiou and Wasserburg, 1969; 1972b; 1972a; Gray et al., 1973; 1976a; 1976b; Wasserburg et al., 1977b; Jacobsen and Wasserburg, 1984) are normalized to our value for Pacific seawater of 0.709180, while studies that reported initial $^{87}Sr/^{86}Sr$ along with NIST SRM 987 (Allegre et al., 1975; Podosek et al., 1991; Lugmair and Galer, 1992; Nyquist et al., 1994; Nyquist et al., 2003; Tonui et al., 2003; Hans et al., 2013) are normalized to our value for NIST SRM 987 of 0.710253. Figure 5.5 shows initial $^{87}Sr/^{86}Sr$ determined by different studies grouped by material (Table 5.4).

5.4 DISCUSSION

We have determined initial $^{87}Sr/^{86}Sr$ ratios for Moore County plagioclase and the lunar anorthosite 60025 and placed them in context of a new compilation of normalized literature data. Here we discuss implications of our results for volatile depletion in the proto-planetary disk and the chronology of the early Solar System.

5.4.1 Issues resolved by our new normalization

Using a new normalization based on our measurements of NIST SRM 987 and Pacific seawater (Figure 5.4, Figure 5.5), we find that some samples with discrepant reported initial $^{87}Sr/^{86}Sr$ values agree within error when properly normalized: for

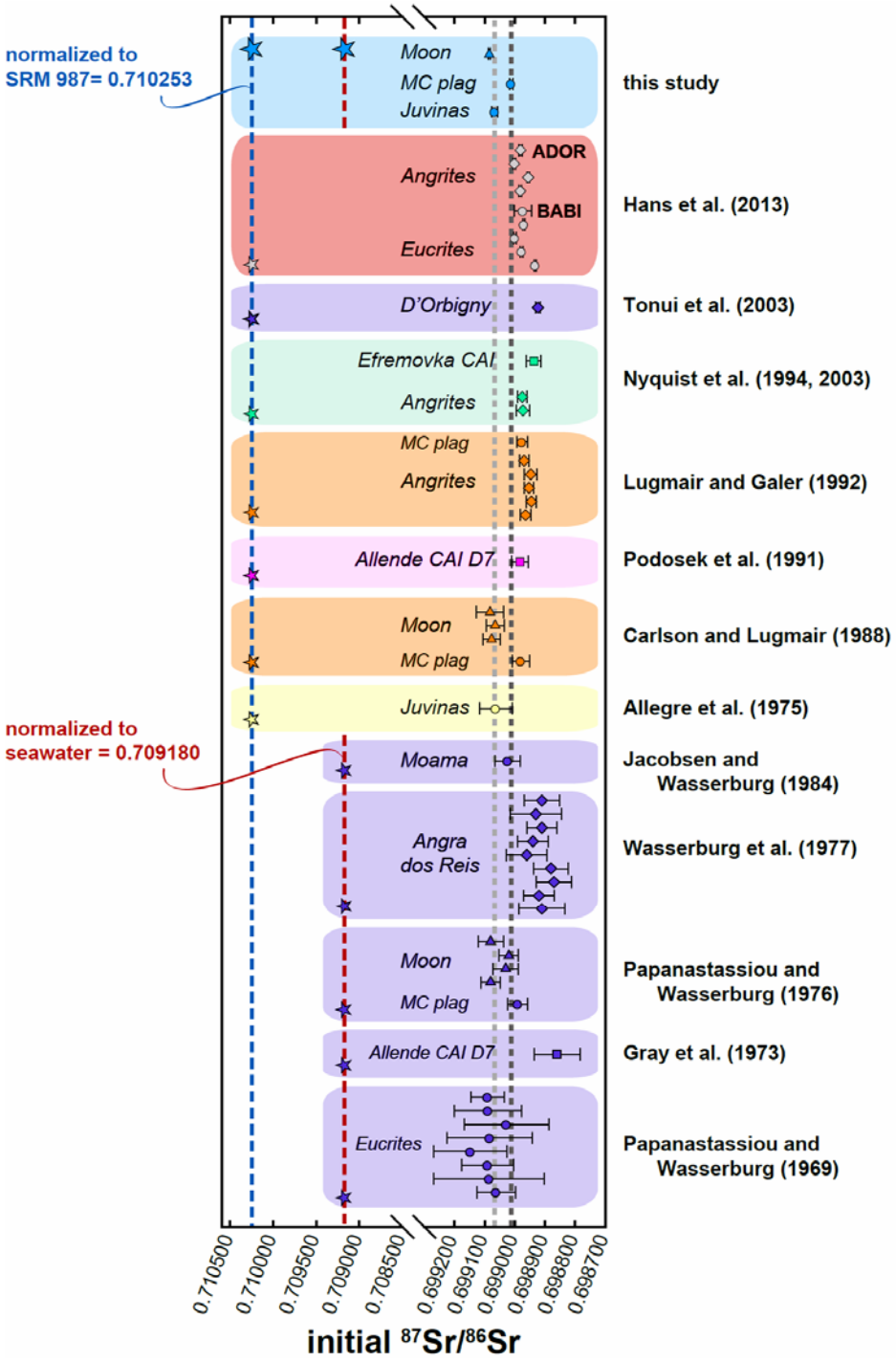

Figure 5.4 Normalized compilation of literature initial $^{87}Sr/^{86}Sr$ in planetary materials. Data are grouped by study, with the most recent studies at the top. For studies that report NIST SRM 897 as a standard, data are normalized based on SRM 987 $^{87}Sr/^{86}Sr$ = 0.710253 (dashed blue line) while data from studies that report seawater as a standard are normalized using seawater $^{87}Sr/^{86}Sr$ = 0.709180 (dashed red line; Table 5.1). Gray dotted reference lines for our determinations of Juvinas and Moore County plagioclase initials are given.

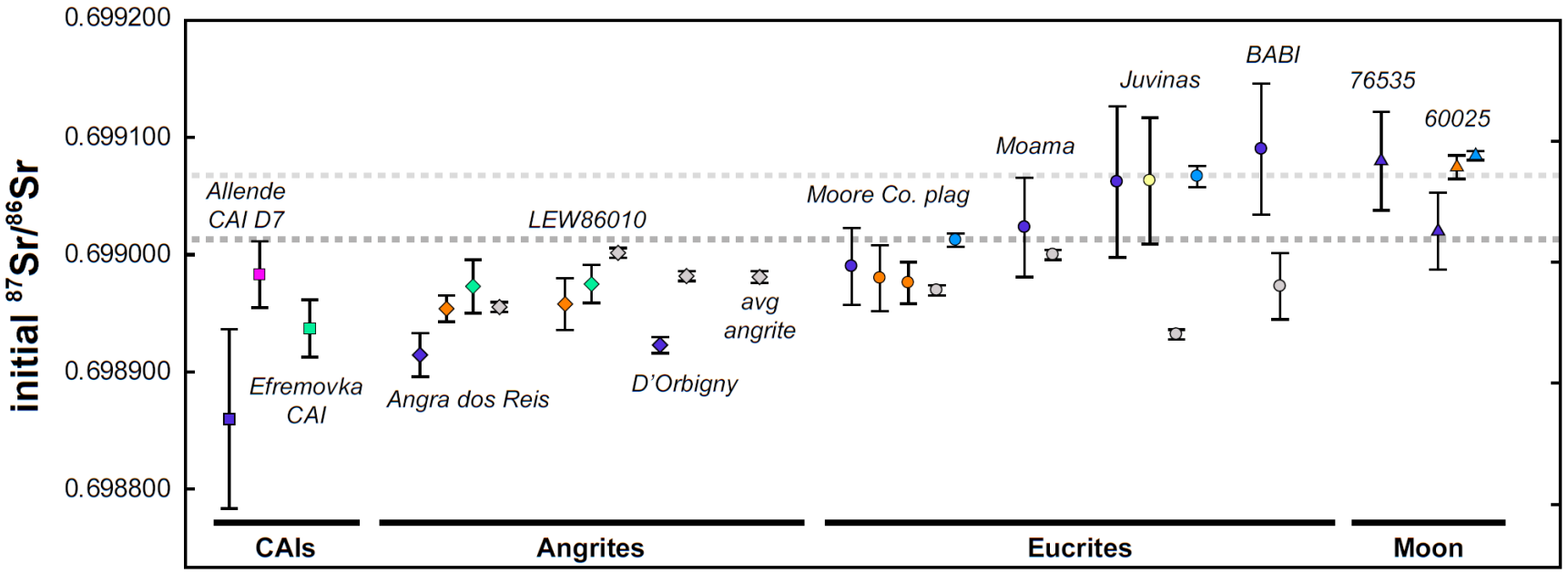

Figure 5.4 Normalized compilation of literature initial $^{87}Sr/^{86}Sr$ in planetary materials, grouped by type of material. Normalization resolves some discrepancies between determinations of initial $^{87}Sr/^{86}Sr$, but some differences persist. Reference lines for our determinations of the Moore County plagioclase initial (dark gray dotted line) and Juvinas (light gray dotted line) are given.

example, Moore County plagioclase from Papanastassiou and Wasserburg (1972a), Carlson and Lugmair (1988), Lugmair and Galer (1992) and Hans et al. (2013) all agree. Our determination of initial $^{87}Sr/^{86}Sr$ in the eucrite Juvinas reproduces the determinations of Papanastassiou and Wasserburg (1969) and Allegre et al. (1975) an order of magnitude improvement in the uncertainty.

However, some differences in initial $^{87}Sr/^{86}Sr$ data persist after normalization. For example, normalized determinations of initial $^{87}Sr/^{86}Sr$ in angrites Angra dos Reis and LEW86010 do not agree within their uncertainties (Figure 5.5; Wasserburg et al., 1977b; Lugmair and Galer, 1992; Nyquist et al., 1994; Hans et al., 2013). Our determination of Moore County plagioclase initial $^{87}Sr/^{86}Sr$ initial agrees within error of the determination by Papanastassiou and Wasserburg (1976a), but does not agree with other determinations within the uncertainties (Figure 5.5; Carlson and Lugmair, 1988; Lugmair and Galer, 1992; Hans et al., 2013). We note that early data was corrected for mass fractionation during analysis using a linear or power law, neither of which is accurate to the level we achieve in our measurements. More recent studies generally apply an exponential law to correct for mass fractionation during analysis as this provides a better fit for thermal ionization data (e.g., Russell et al., 1978). Thus, variations in the mass fractionation law applied to correct measured data may introduce bias between studies. It is also possible that discrepancies are related to mixing of distinct mass fractionation trends during analysis, reflecting concurrent ionization of distinct sample spots on a single filament. Depending on the extent of differential mass fractionation, such a process could result in an offset in measured $^{87}Sr/^{86}Sr$ greater than the uncertainties in modern measurements. Lastly, we note that differences in the initial $^{87}Sr/^{86}Sr$ for lunar anorthosite 60025 persist

after correcting for inter-laboratory bias (Figure 5.5; this study; Papanastassiou and Wasserburg, 1976a; Carlson and Lugmair, 1988), though our own determination agrees well with that of Carlson and Lugmair (1988). This may reflect the fact that 60025 is a shocked monomict breccia: the lunar crust experienced significant bombardment, such that individual plagioclase grains may have been reset at different points during early lunar history. Accordingly, the true 60025 initial $^{87}Sr/^{86}Sr$ may be lower than the value we have determined here.

5.4.2 Early Solar System Rb-Sr chronology

Here we construct a chronology of early Solar System volatile depletion based on relative variations in initial $^{87}Sr/^{86}Sr$. We note that CAIs exhibit large variations in $^{84}Sr/^{86}Sr$ that likely reflect Sr nucleosynthetic anomalies (Moynier et al., 2012). Furthermore, initial $^{87}Sr/^{86}Sr$ values determined for CAIs from Allende and Efremovka differ significantly (Figure 5.5; Gray et al., 1973; Podosek et al., 1991; Nyquist et al., 2003). Consequently, $^{87}Sr/^{86}Sr$ in CAIs may not represent the bulk initial Solar System $^{87}Sr/^{86}Sr$. Instead, we use the Moore County plagioclase to estimate the Solar System initial $^{87}Sr/^{86}Sr$. Magmatism on the eucrite parent body was likely driven by heat produced by short-lived radioactivities (26Al, 53Mn, 60Fe; e.g., Urey, 1955; Lee et al., 1976; Shukolyukov and Lugmair, 1993; Lugmair and Shukolyukov, 1998; Srinivasan et al., 1999; Bizzarro et al., 2005; Schiller et al., 2010). Formation of the eucrite Juvinas was dated by short-lived ^{26}Al-^{26}Mg systematics to 3 Myr after CAIs (Schiller et al., 2010). Given that the Moore County plagioclase initial $^{87}Sr/^{86}Sr$ is either similar to (Hans et al., 2013) or lower than the initial $^{87}Sr/^{86}Sr$ determined for Juvinas (Papanastassiou and

Wasserburg, 1969; Allegre et al., 1975), Moore County likely also crystallized by ~3 Myr. We note that the ~80 ppm difference in initial $^{87}Sr/^{86}Sr$ between Juvinas and Moore County may reflect the fact that Juvinas is brecciated and may have been reset subsequent to crystallization. Therefore we estimate the Solar System initial $^{87}Sr/^{86}Sr$ by anchoring eucrite parent body evolution to the Moore County plagioclase initial $^{87}Sr/^{86}Sr$ at 3 Myr and tracking back to time zero using a bulk eucrite parent body $^{87}Rb/^{86}Sr$ ratio of 0.003294 (Table 5.5).

Table 5.5 Bulk Rb and Sr abundances in planetary bodies

Planetary object	Rb (ppm)	Sr (ppm)	Rb/Sr	$^{87}Rb/^{86}Sr$
Angrite parent body	0.008	26	0.00032	0.00089
Eucrite parent body	0.056	17	0.00338	0.00953
Moon	0.2465	25.5	0.00991	0.02798
Earth	0.58	20	0.02973	0.08393

Ringwood, 1979; Wasserburg et al., 1977; Halliday and Porcelli, 2001.

Having established an estimate of the Solar System initial $^{87}Sr/^{86}Sr$, we may explore models of Sr isotopic evolution that generated the initial $^{87}Sr/^{86}Sr$ determined for the lunar anorthosite 60025. If Rb/Sr fractionation was predominantly driven by volatile loss driven by impacts, then proto-planetary material initially spent some amount of time in an environment with very high Rb/Sr (close to the solar ratio of ~0.6; Gray et al., 1973). This first stage of very rapid Sr isotopic evolution may have been followed by any number of stages of evolution with successively lower Rb/Sr. Example three-stage evolution models of 60025 Sr isotopic evolution are illustrated in Figure 5.6. The Moore County plagioclase initial $^{87}Sr/^{86}Sr$ at 3 Myr is shown as a blue circle with the Solar System initial indicated at the y-axis intercept. In such progressive Rb/Sr depletion

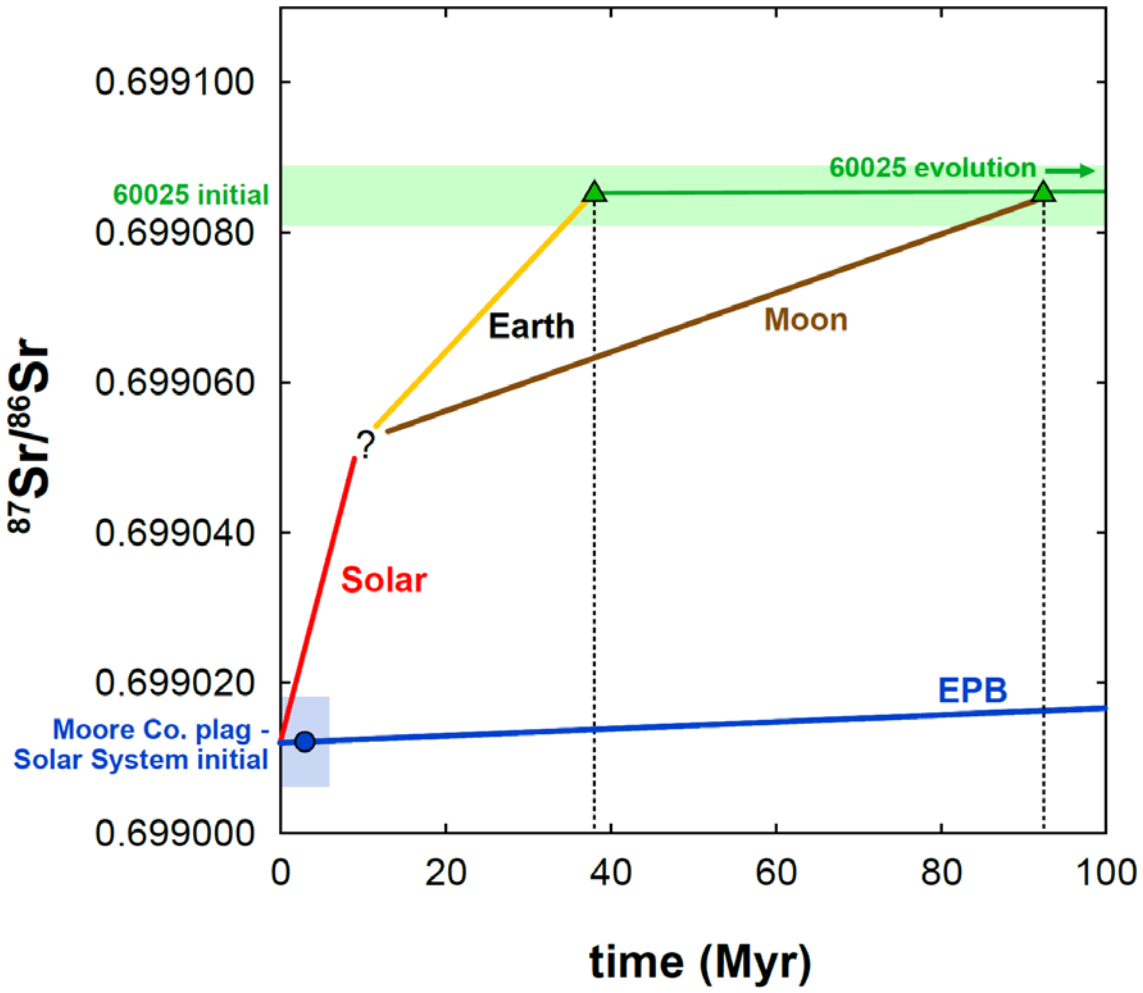

Figure 5.6 Three stage evolution models of Sr isotopic evolution. The Solar System initial $^{87}Sr/^{86}Sr$ is estimated using the Moore County plagioclase initial $^{87}Sr/^{86}Sr$ anchored at 3 Myr and the eucrite parent body (EPB) $^{87}Rb/^{86}Sr$ (Table 5.5). If Rb/Sr fractionation occurs dominantly by progressive volatile depletion associated with impacts during accretion, then lunar precursor material spent some unconstrained amount of time in an environment with high Rb/Sr (the solar value of ~0.6 is indicated in red), and then evolved with lower $^{87}Rb/^{86}Sr$ – either Earth-like (shown in gold) or Moon-like $^{87}Rb/^{86}Sr$ (shown in brown) – such that the time of lunar formation is unconstrained.

models, the timing of lunar formation is unconstrained by Rb-Sr systematics, as the amount of time spent in an environment with high Rb/Sr is unknown (Figure 5.6).

Although progressive depletion models yield no Rb-Sr age constraints, we may apply independent age constraints for 60025 in order to estimate the time-averaged or "effective" $^{87}Rb/^{86}Sr$ of 60025 precursor material (e.g., Halliday and Porcelli, 2001).

Based on our estimate of the Solar System initial and our determination of the 60025 initial $^{87}Sr/^{86}Sr$, we compute the effective $^{87}Rb/^{86}Sr$ ratio of the precursor material for 60025 as a function of the age of 60025 (Figure 5.7). For a later time of 60025 formation, a lower effective $^{87}Rb/^{86}Sr$ ratio is required in the precursor material. A time of formation of ~50-70 Myr after the start of the Solar System indicates an Earth-like effective $^{87}Rb/^{86}Sr$ of ~0.08. We note that for 60025 formation ages greater than 200 Myr after the start of the Solar System, the precursor material for 60025 must have evolved with effective $^{87}Rb/^{86}Sr$ lower than the bulk Moon value of ~0.03. Such sluggish Sr isotopic evolution would require that the precursor material for 60025 never mixed or equilibrated with either bulk Earth material or bulk Moon material; i.e., that the source of the lunar anorthosite crust was never in equilibrium with the rest of the Moon. However, lunar mare basalts exhibit Eu anomalies consistent with a mantle source that was genetically related to the anorthosite crust (Taylor and Jakes, 1974); accordingly, an isolated source for lunar anorthosites with $^{87}Rb/^{86}Sr$ lower than the bulk Moon is improbable, and 60025 ages greater than ~200 Myr are ruled out.

An alternative model of volatile depletion holds that Rb/Sr fractionation in the early Solar System was driven primarily by incomplete condensation from the solar nebula rather than progressive volatile loss. Thus, differences in Rb/Sr were established very early in Solar System history, such that planetary bodies evolved with Rb/Sr ratios similar to their bulk Rb/Sr throughout early Solar System history. We note that the lunar Rb/Sr is about a factor of 3 lower than bulk Earth Rb/Sr (Table 5.5), consistent with overall lunar volatile depletion relative to the (Ringwood, 1979). The Moon likely formed

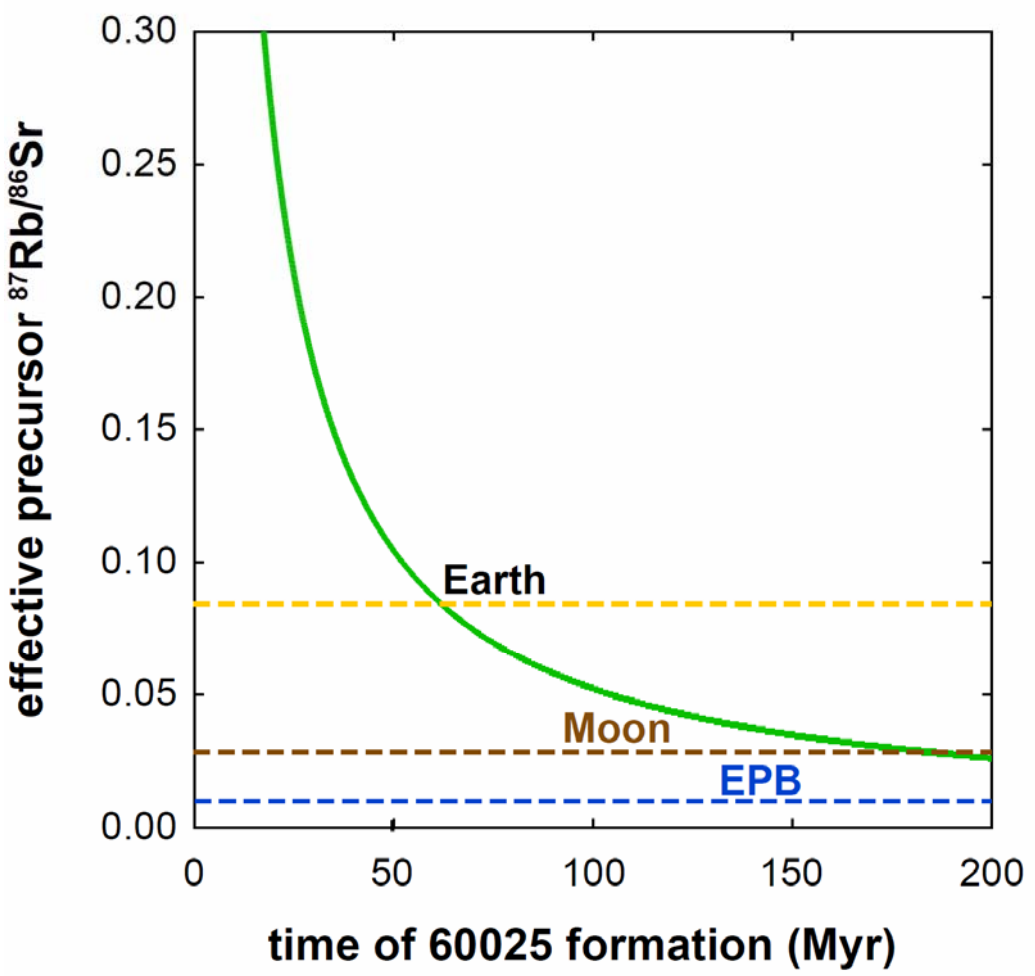

Figure 5.7 Effective 87Rb/86Sr in the lunar precursor as a function of the crystallization age of 60025. For a later time of 60025 formation, a lower effective $^{87}Rb/^{86}Sr$ ratio is required in the precursor material. For 60025 formation ages greater than ~186 Myr after the start of the Solar System, the precursor material for 60025 must have evolved with effective $^{87}Rb/^{86}Sr$ lower than the bulk Moon value of ~0.03; i.e., a very late crystallization age of 60025 requires that the source of the lunar anorthosite crust was never in equilibrium with the rest of the Moon. In contrast, a crystallization age of ~50-70 Myr after the start of the Solar System indicates an Earth-like effective $^{87}Rb/^{86}Sr$ of ~0.08 in the lunar precursor.

from a debris disk generated by a giant impact in the end stages of terrestrial accretion (Hartmann and Davis, 1975; Cameron and Ward, 1976). Impact parameters such as the relative size of the impactor and the spin state of the target are debated; depending on the giant impact model, the Moon is either derived primarily from impactor material (Canup,

2004) or from the proto-Earth (Cuk and Stewart, 2012). If the Moon formed mostly from the impactor (Canup, 2004), then the impactor was either always characterized by bulk lunar Rb/Sr, or was more volatile-rich (with no constraints on Rb/Sr beyond an upper limit solar Rb/Sr) and achieved the bulk lunar Rb/Sr through some volatile depletion process related to lunar formation. Alternatively, if the Moon is derived primarily from the Earth (Cuk and Stewart, 2012), then the precursor material for 60025 evolved with an Earth-like Rb/Sr and some process associated with lunar formation drove Rb depletion to generate a lower bulk Moon Rb/Sr.

Figure 5.8 illustrates two endmember two-stage models of Sr evolution. In the first endmember model, proto-Earth material evolves from the Solar System initial $^{87}Sr/^{86}Sr$ (0.699012 ± 6; determined based on Moore County plagioclase) with Earth-like Rb/Sr and reaches the 60025 initial $^{87}Sr/^{86}Sr$ value of 0.699085 ± 4 at ~62 Myr. We note that this Sr model age is similar to the ^{207}Pb-^{206}Pb age determined for 60025 by Hanan and Tilton (1987), indicated within the figure. If the Moon is derived largely from the proto-Earth and the age of 60025 is relatively old (~50-60 Myr), then 60025 must have formed rapidly after lunar formation, as the amount of time spent in a reservoir with low (e.g., bulk lunar) $^{87}Rb/^{86}Sr$ is necessarily limited. If instead the Moon is derived dominantly from impactor material with lunar $^{87}Rb/^{86}Sr$, proto-lunar material evolves from the Solar System initial $^{87}Sr/^{86}Sr$ with lunar $^{87}Rb/^{86}Sr$ and reaches the 60025 initial $^{87}Sr/^{86}Sr$ value of 0.699085 ± 4 at ~186 Myr. We note that for late crystallization ages of ~200 Myr (Borg et al., 2011), a bulk lunar effective $^{87}Rb/^{86}Sr$ is required (Figure 5.7, Figure 5.8). In this case, no fractionation of $^{87}Rb/^{86}Sr$ occurs upon lunar formation.

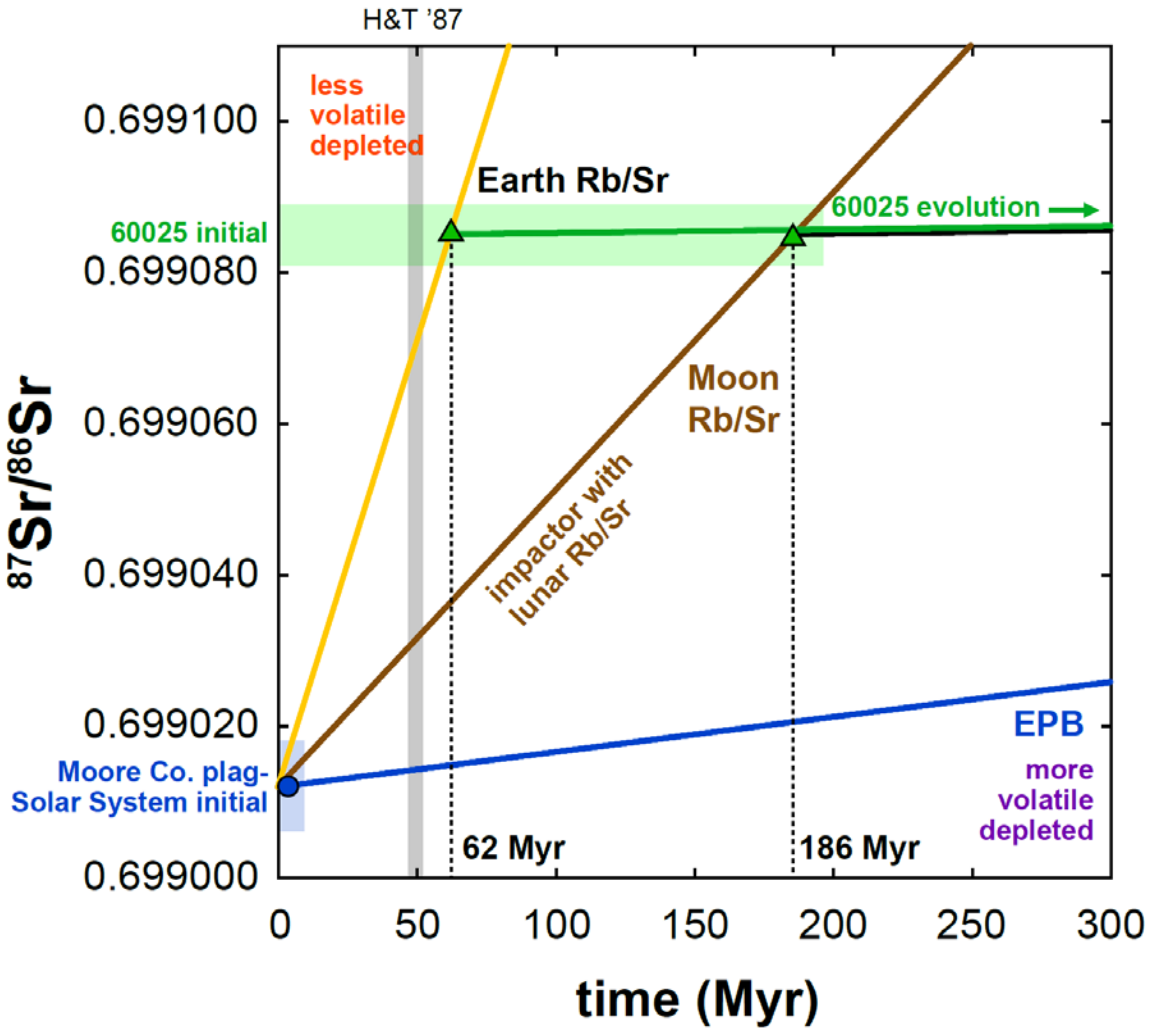

Figure 5.8 Two-stage Sr isotopic evolution models. The Solar System initial $^{87}Rb/^{86}Sr$ is estimated based on Moore County plagioclase (see Figure 5.6 caption). The first stage of Sr isotopic evolution occurs in the lunar precursor body; the second stage is evolution after the crystallization of 60025 (green curves). Planetary bodies that are more volatile-depleted have low Rb/Sr and evolve slowly (shallow slopes; e.g., the eucrite parent body, EPB, shown in blue) while less volatile-depleted bodies evolve with steeper slopes. If the precursor material for 60025 evolved with an Earth-like Rb/Sr (gold curve), then the Sr model age for 60025 is 62 Myr, similar to the 60025 ^{207}Pb-^{206}Pb age determination by Hanan and Tilton (1987; shaded grey band). If the precursor material for 60025 evolved with a bulk lunar Rb/Sr (brown curve), then the Sr model age for 60025 is 186 Myr. In this case, 60025 precursor material was never part of the proto-Earth, and the Moon is derived mostly from an impactor that evolved with distinct Rb/Sr for the first 186 Myr of Solar System history.

Consequently, the amount of Sr isotopic evolution along this bulk lunar trajectory that occurred prior to the Moon-formation giant impact is unconstrained. Accordingly, the Sr model age for 60025 is young (186 Myr), but the Moon may have formed at any point between time zero and 186 Myr.

The Earth and Moon are isotopically indistinguishable in O, Ti, Cr and W isotopes (Lugmair and Shukolyukov, 1998; Wiechert et al., 2001; Touboul et al., 2007; Zhang et al., 2012). This observation is most consistent with a Moon-forming giant impact in which the Moon is derived from the proto-Earth (Cuk and Stewart, 2012). Such a model requires $^{87}Rb/^{86}Sr$ fractionation upon lunar formation to generate the bulk lunar $^{87}Rb/^{86}Sr$ ratio. Paniello et al. (2012) argue that mass-dependent fractionation of moderately-volatile Zn occurred by evaporative loss from a lunar magma ocean. However, evaporation of Zn or Rb from a lunar magma ocean does not necessarily drive bulk lunar volatile depletion, as both species are relatively heavy and are thus likely to remain gravitationally bound to the Moon. Humayun and Clayton (1995) found that lunar K isotopes are not fractionated and argued for lunar volatile depletion by incomplete condensation. Accordingly, Stewart et al. (2013) argued that lunar accretion after the Moon-forming giant impact ended before the proto-lunar disk had cooled below the condensation temperatures for moderately volatile elements. Regardless of the mechanism of volatile depletion, if the Moon is derived from proto-Earth material, Sr isotopes evolve from the Solar System initial $^{87}Sr/^{86}Sr$ with Earth-like $^{87}Rb/^{86}Sr$ until lunar formation, after which point the lunar material evolves with bulk lunar $^{87}Rb/^{86}Sr$ until 60025 crystallizes. Figure 5.9 illustrates example three-stage Sr evolution models:

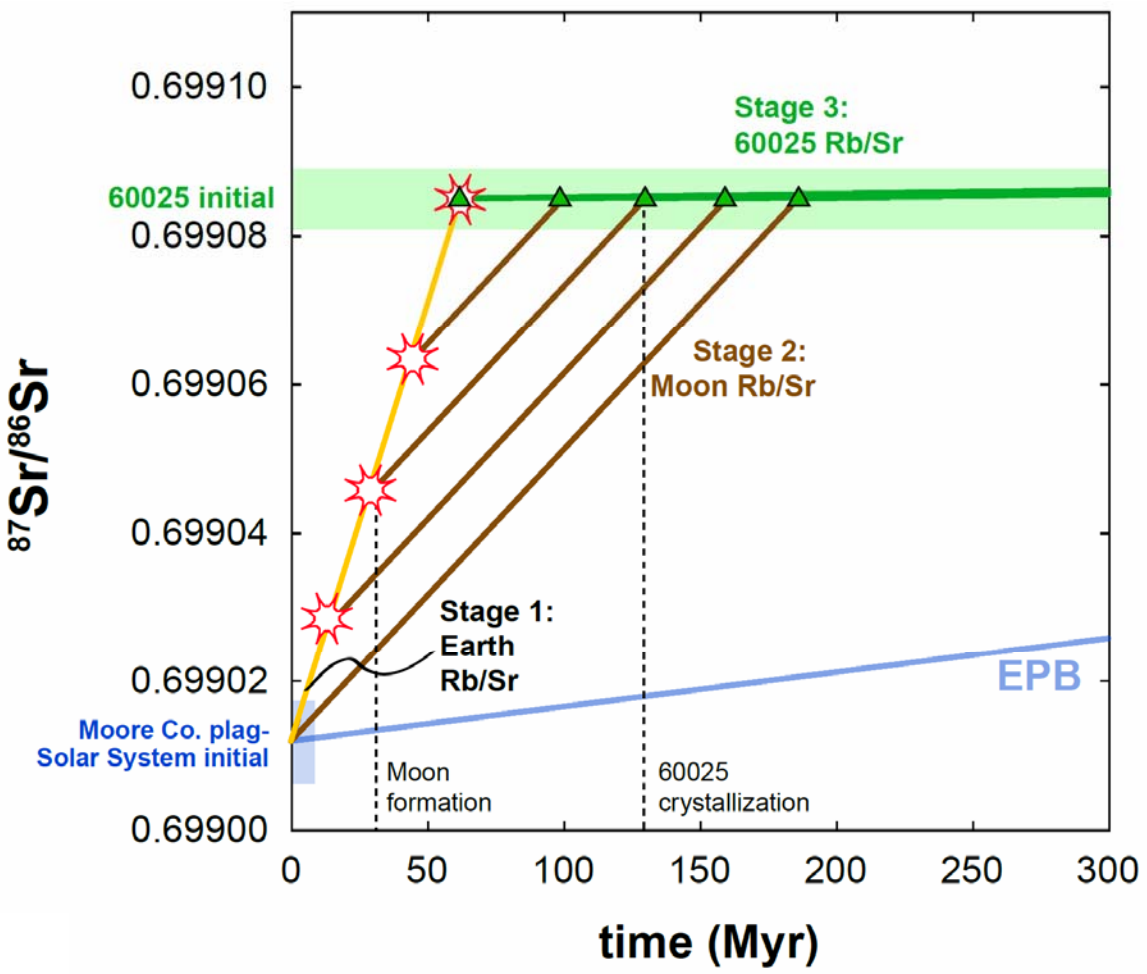

Figure 5.9 Three-stage models illustrating Sr isotopic evolution if the Moon is derived from the proto-Earth. In the first stage, 60025 precursor material evolves from the Solar System initial with Earth Rb/Sr (gold curve) until the time of the Moon-forming giant impact (examples are illustrated as red starbursts). Rb/Sr is fractionated in the aftermath of the giant impact. Thus, 60025 precursor material evolves in the second stage with lunar Rb/Sr (see Table 5.5) until the time of 60025 crystallization (indicated by green triangles). After crystallization, 60025 Sr isotopes evolve according to the 60025 Rb/Sr ratio (green curves; Table 5.2). Later crystallization ages for 60025 require earlier times of Moon formation. For crystallization ages > 180 Myr, the Moon forms near the start of the Solar System and 60025 precursor material spends its whole history evolving with lunar Rb/Sr. In this case, the giant impact model is not applicable. If the Moon is derived from the proto-Earth, the latest time of Moon formation is given by the limit where 60025 crystallizes very rapidly from the lunar magma ocean (~62 Myr) and thus spends no time evolving with lunar Rb/Sr.

the first stage is evolution in the proto-Earth until the formation of the Moon; the second stage is evolution in the lunar magma ocean; and the third stage is isotopic evolution within the anorthosite 60025 after crystallization. Figure 5.9 illustrates that if the Moon is derived from proto-Earth material, then there is an inverse relationship between the crystallization age of 60025 and the time of Moon formation, and the Moon formed at the latest ~62 Myr after the start of the Solar System. For the earliest 60025 crystallization age, the Moon formed at 62 Myr and 60025 crystalized very shortly thereafter. For later crystallization age of 60025, a larger portion of Sr evolution was accomplished with low Rb/Sr, such that the Moon formed earlier. Very late formation of 60025 (~200 Myr, Borg et al., 2011) requires that the Moon formed very rapidly after the start of the Solar System, at which point the giant impact model of lunar formation is not applicable, and an alternate explanation for the isotopic similarity between the Earth and Moon is required.

We conclude our discussion by noting that determination of the Solar System initial $^{87}Sr/^{86}Sr$ is critically important to Sr model age determinations. For example, our computed Sr model age for 60025 using an Earth-like $^{87}Rb/^{86}Sr$ is significantly older (~62 Myr) than that computed by Halliday (~90 Myr; 2008), although our normalized initial $^{87}Sr/^{86}Sr$ values for 60025 agree within error (0.699085 ± 4 from this study; 0.699071 ± 10 from Carlson and Lugmair, 1988). This difference reflects the fact that we use a Solar System initial calculated based on initial $^{87}Sr/^{86}Sr$ in Moore County plagioclase (Solar System initial of 0.699012 ± 6), while Halliday (2008) utilizes the Efremovka CAI initial from Nyquist et al. (2003) of 0.69894 ± 2, > 70 ppm lower than our Solar System initial. We have noted that CAIs may not accurately reflect the

composition of the bulk Solar System; $^{84}Sr/^{86}Sr$ indicating r-process excesses in CAIs (Hans et al., 2013) would necessitate upward correction of measured $^{87}Sr/^{86}Sr$ in CAIs. Hans et al. (2013) recently determined initial $^{87}Sr/^{86}Sr$ ratios determined for eucrites and angrites and corrected initial $^{87}Sr/^{86}Sr$ ratios in Allende CAIs that are indistinguishable within errors. Based on relatively uniform observed initial $^{87}Sr/^{86}Sr$ in planetary materials, the authors argued for early volatile depletion due to incomplete condensation and rapid subsequent accretion of planetary bodies. In light of persistent offsets in normalized initial $^{87}Sr/^{86}Sr$ between studies (Figure 5.4, Figure 5.5), determination of initial $^{87}Sr/^{86}Sr$ in lunar samples, angrites and eucrites within a single laboratory are necessary to better constrain the initial Solar System $^{87}Sr/^{86}Sr$ and the resulting Sr model ages of lunar rocks.

5.5 CONCLUSIONS

We present a new suite of high-precision $^{87}Sr/^{86}Sr$ determinations for lunar anorthosite 60025, Moore County plagioclase, the eucrite Juvinas and the angrite D'Orbigny. We compute initial $^{87}Sr/^{86}Sr$ ratios for the lunar anorthosite 60025, Juvinas and Moore County plagioclase and place these in context of a normalized compilation of initial $^{87}Sr/^{86}Sr$ data from the literature. Careful normalization of literature data resolves some discrepancies among different studies; however, in many cases, inter-laboratory differences persist. Based on Sr isotopic systematics in 60025 and Moore County plagioclase, we find that if the Moon is derived from proto-Earth material, then lunar formation occurred prior to ~62 Myr.

5.6 REFERENCES

Allegre, C.J., Birck, J.L., Fourcade, S., Semet, M.P., 1975. Rubidium-87/strontium-87 age of juvinas basaltic achondrite and early igneous activity in solar-system. Science, 187(4175): 436-438.

Bizzarro, M., Baker, J.A., Haack, H., Lundgaard, K.L., 2005. Rapid timescales for accretion and melting of differentiated planetesimals inferred from al-26-mg-26 chronometry. Astrophysical Journal, 632(1): L41-L44.

Borg, L.E., Connelly, J.N., Boyet, M., Carlson, R.W., 2011. Chronological evidence that the moon is either young or did not have a global magma ocean. Nature, 477(7362): 70-72.

Cameron, A.G.W., Ward, W.R., 1976. The origin of the moon. Abstracts of the Lunar and Planetary Science Conference, 7: 120-122.

Canup, R.M., 2004. Simulations of a late lunar-forming impact. Icarus, 168(2): 433-456.

Carlson, R.W., Lugmair, G.W., 1988. The age of ferroan anorthosite 60025: Oldest crust on a young moon? Earth and Planetary Science Letters, 90(2): 119-130.

Cuk, M., Stewart, S.T., 2012. Making the moon from a fast-spinning earth: A giant impact followed by resonant despinning. Science, 338(6110): 1047-1052.

Elkins-Tanton, L.T., Burgess, S., Yin, Q.Z., 2011. The lunar magma ocean: Reconciling the solidification process with lunar petrology and geochronology. Earth and Planetary Science Letters, 304(3-4): 326-336.

Gray, C.M., Papanastassiou, D.A., Wasserburg, G.J., 1973. The identification of early condensates from the solar nebula. Icarus, 20(2): 213-239.

Halliday, A.N., 2008. A young moon-forming giant impact at 70-110 million years accompanied by late-stage mixing, core formation and degassing of the earth. Philosophical Transactions of the Royal Society a-Mathematical Physical and Engineering Sciences, 366(1883): 4163-4181.

Halliday, A.N., Porcelli, D., 2001. In search of lost planets - the paleocosmochemistry of the inner solar system. Earth and Planetary Science Letters, 192(4): 545-559.

Hanan, B.B., Tilton, G.R., 1987. 60025: Relict of primitive lunar crust? Earth and Planetary Science Letters, 84(1): 15-21.

Hans, U., Kleine, T., Bourdon, B., 2013. Rb-sr chronology of volatile depletion in differentiated protoplanets: Babi, ador and all revisited. Earth and Planetary Science Letters, 374: 204-214.

Hartmann, W.K., Davis, D.R., 1975. Satellite-sized planetesimals and lunar origin. Icarus, 24(4): 504-515.

Humayun, M., Clayton, R.N., 1995. Potassium isotope cosmochemistry: Genetic implications of volatile element depletion. Geochimica et Cosmochimica Acta, 59(10): 2131-2148.

Jacobsen, S.B. et al., 2008. Isotopes as clues to the origin and earliest differentiation history of the earth. Philosophical Transactions of the Royal Society A-Mathematical Physical and Engineering Sciences, 366(1883): 4129-4162.

Jacobsen, S.B., Wasserburg, G.J., 1984. Sm-Nd isotopic evolution of chondrites and achondrites .2. Earth and Planetary Science Letters, 67(2): 137-150.

Kinoshita, N. et al., 2012. A shorter sm-146 half-life measured and implications for sm-146-nd-142 chronology in the solar system. Science, 335(6076): 1614-1617.

Lee, T., Papanastassiou, D.A., Wasserburg, G.J., 1976. Demonstration of Mg-26 excess in allende and evidence for Al-26. Geophysical Research Letters, 3(2): 109-112.

Lugmair, G.W., Galer, S.J.G., 1992. Age and isotopic relationships among the angrites Lewis Cliff 86010 and Angra dos reis. Geochimica et Cosmochimica Acta, 56(4): 1673-1694.

Lugmair, G.W., Shukolyukov, A., 1998. Early solar system timescales according to Mn-53-Cr-53 systematics. Geochimica et Cosmochimica Acta, 62(16): 2863-2886.

Morgan, J.W., Anders, E., 1980. Chemical-composition of Earth, Venus, and Mercury. Proceedings of the National Academy of Sciences of the United States of America-Physical Sciences, 77(12): 6973-6977.

Moynier, F. et al., 2012. Planetary scale Sr isotopic heterogeneity. Meteoritics & Planetary Science, 47: A283-A283.

Nyquist, L.E., Bansal, B., Wiesmann, H., Shih, C.Y., 1994. Neodymium, strontium and chromium isotopic studies of the lew86010 and Angra-dos-reis meteorites and the chronology of the angrite parent body. Meteoritics, 29(6): 872-885.

Nyquist, L.E., Shih, C.Y., Wiesmann, H., Mikouchi, T., 2003. Fossil ^{26}Al and ^{53}Mn in D'orbigny and Sahara 99555 and the timescale for angrite magmatism. Abstracts of the Lunar Planetary Science Conference, 34: 1388.

Paniello, R.C., Day, J.M.D., Moynier, F., 2012. Zinc isotopic evidence for the origin of the moon. Nature, 490(7420): 376-379.

Papanastassiou, D.A., Wasserburg, G.J., 1969. Initial strontium isotopic abundances and resolution of small time differences in formation of planetary objects. Earth and Planetary Science Letters, 5(6): 361-376.

Papanastassiou, D.A., Wasserburg, G.J., 1971. Lunar chronology and evolution from rb-sr studies of apollo-11 and 12 samples. Earth and Planetary Science Letters, 11(1): 37-62.

Papanastassiou, D.A., Wasserburg, G.J., 1972a. Rb-Sr age of a Luna-16 basalt and model age of lunar soils. Earth and Planetary Science Letters, 13(2): 368-374.

Papanastassiou, D.A., Wasserburg, G.J., 1972b. Rb-Sr systematics of Luna-20 and Apollo-16 samples. Earth and Planetary Science Letters, 17(1): 52-63.

Papanastassiou, D.A., Wasserburg, G.J., 1976a. Early lunar differentiates and lunar initial $^{87}Sr/^{86}Sr$. Abstracts of the Lunar and Planetary Science Conference, 7: 665-667.

Papanastassiou, D.A., Wasserburg, G.J., 1976b. Rb-Sr age of troctolite 76535. Proceedings of the Lunar Science Conference, 7: 2035-2054.

Pepin, R.O., Porcelli, D., 2006. Xenon isotope systematics, giant impacts, and mantle degassing on the early Earth. Earth and Planetary Science Letters, 250(3-4): 470-485.

Podosek, F.A. et al., 1991. Correlated study of initial Sr-87/Sr-86 and Al-Mg isotopic systematics and petrologic properties in a suite of refractory inclusions from the allende meteorite. Geochimica et Cosmochimica Acta, 55(4): 1083-1110.

Ringwood, A.E., 1979. Origin of the earth and moon. Springer-Verlag, 295 pp.

Russell, W.A., Papanastassiou, D.A., Tombrello, T.A., 1978. Ca isotope fractionation on Earth and other Solar-system materials. Geochimica et Cosmochimica Acta, 42(8): 1075-1090.

Schiller, M., Baker, J.A., Bizzarro, M., 2010. Al-26-Mg-26 dating of asteroidal magmatism in the young Solar System. Geochimica et Cosmochimica Acta, 74(16): 4844-4864.

Shukolyukov, A., Lugmair, G.W., 1993. Live iron-60 in the early solar-system. Science, 259(5098): 1138-1142.

Srinivasan, G., Goswami, J.N., Bhandari, N., 1999. Al-26 in eucrite Piplia Kalan: Plausible heat source and formation chronology. Science, 284(5418): 1348-1350.

Stewart, S.T., Leinhardt, Z.M., Humayun, M., 2013. Giant impacts, volatile loss, and the K/Th ratios on the Moon, Earth, and Mercury. Abstracts of the Lunar and Planetary Science Conference, 44: 2306.

Taylor, S.R., Jakes, P., 1974. Geochemical zoning in the Moon. Abstracts of the Lunar and Planetary Science Conference, 5: 786-788.

Tonui, E.K., Ngo, H.H., Papanastassiou, D.A., 2003. Rb-Sr and Sm-Nd study of the D'orbigny angrite. Abstracts of the Lunar and Planetary Science Conference, 34: 1812.

Touboul, M., Kleine, T., Bourdon, B., Palme, H., Wieler, R., 2007. Late formation and prolonged differentiation of the Moon inferred from W isotopes in lunar metals. Nature, 450(7173): 1206-1209.

Urey, H.C., 1955. The cosmic abundances of potassium, uranium, and thorium and the heat balances of the Earth, the Moon, and Mars. Proceedings of the National Academy of Sciences of the United States of America, 41(3): 127-144.

Wasserburg, G.J., Papanastassiou, D.A., Tera, F., Huneke, J.C., 1977a. Outline of a lunar chronology. Philosophical Transactions of the Royal Society A-Mathematical Physical and Engineering Sciences, 285(1327): 7-22.

Wasserburg, G.J., Tera, F., Papanastassiou, D.A., Huneke, J.C., 1977b. Isotopic and chemical investigations on Angra dos reis. Earth and Planetary Science Letters, 35(2): 294-316.

Wiechert, U. et al., 2001. Oxygen isotopes and the moon-forming giant impact. Science, 294(5541): 345-348.

Yu, G., Jacobsen, S.B., 2011. Fast accretion of the earth with a late moon-forming giant impact. Proceedings of the National Academy of Sciences of the United States of America, 108(43): 17604-17609.

Zhang, J., Dauphas, N., Davis, A.M., Leya, I., Fedkin, A., 2012. The proto-earth as a significant source of lunar material. Nature Geosci, 5(4): 251-255.

APPENDICES

APPENDIX 1: HYPERBOLIC FITTING

Mixing between two components in nonlinear isotope spaces (i.e., isotope ratio spaces where the normalizing isotopes in the x- and y-coordinate isotope ratios differ) can be described as a hyperbola of the form:

$$Ax + Bxy + Cy + D = 0 \qquad \text{Eq. A1.1}$$

(e.g., Langmuir et al., 1978). In this thesis, we consider mixing in a number of nonlinear isotope spaces. Syn-to post-eruptive atmospheric contamination of mantle-derived basalts generates hyperbolic trends in $^{40}Ar/^{36}Ar$ – $^{20}Ne/^{22}Ne$, $^{129}Xe/^{130}Xe$ – $^{40}Ar/^{36}Ar$ and $^{129}Xe/^{132}Xe$ – $^{40}Ar/^{36}Ar$ isotopic spaces. A best-fit hyperbola reflecting two-component mixing between air and mantle is determined based on total least squares regression to find the best-fit hyperbola for a given set of step-crush data. Here we describe our hyperbolic regression algorithm in more detail.

A1.1 Mixing endmembers and the hyperbolic mixing equation

For samples with well-defined mixing arrays, we model mixing between an atmospheric component and a mantle component. One mixing endmember is taken to have the Ne, Ar and Xe isotopic composition of modern atmosphere ($^{20}Ne/^{22}Ne = 9.8$; $^{40}Ar/^{36}Ar = 296$; $^{129}Xe/^{130}Xe = 6.496$; $^{129}Xe/^{132}Xe = 0.9832$; Porcelli et al., 2002). The mantle endmember $^{20}Ne/^{22}Ne$ is taken to be 12.5 for mid-ocean ridge basalts (Ballentine et al., 2005). The coefficients of the mixing hyperbola (A, B, C and D; Equation A1.1) reflect the x- and y- coordinate isotopic ratios of the endmembers (designated by rAx and rAy for the atmospheric endmember; rMx and rMy for the mantle endmember) as well as the concentrations of the normalizing isotopes in each of the endmembers (designated by

cAx, cAy, cMx and cMy for the concentrations of the x- and y-coordinate normalizing isotopes for atmospheric and mantle components, respectively):

A = cMy*cAx*rMy - cMx*cAy*rAy Eq. A1.2

B = cMx*cAy - cAx*cMy Eq. A1.3

C = cMy*cAx.*rAx - cAy.*cMx.*rMx Eq. A1.4

D = cMx*cAy* rAy*rMx - cAx*cMy*rMy*rAx Eq. A1.5

However, for the purposes of finding the best fit hyperbola (rather than placing constraints on the mixing proportions of the two components), it is not necessary to specify cAx, cAy, cMx and cMy individually. The curvature of the hyperbola depends only on the relative abundances ratios in the two endmembers, k:

$$k = \frac{\text{cMy/cMx}}{\text{cAy/cAx}}$$ Eq. A1.6

In our algorithm, we set cAx, cAy and cMx to 1 and let cMy vary. In this case, k = cMy. The expressions for A, B, C and D can be simplified to:

A = cMy*rMy - rAy Eq. A1.7

B = 1 - cMy Eq. A1.8

C = cMy.*rAx - rMx Eq. A1.9

D = rAy*rMx - cMy*rMy*rAx Eq. A1.10

We note that rAx and rAy are the known atmospheric x- and y- coordinate isotopic ratios, and rMx is the known mantle endmember composition (all hyperbolic fits start with an extrapolation to mantle $^{20}Ne/^{22}Ne$ of 12.5; Chapter 3, Chapter 4). Therefore, the shape of

the hyperbola depends on two parameters: the curvature k = cMy, and the mantle endmember y-coordinate isotope ratio (rMy, which is the extrapolated mantle source composition) at the known mantle x-coordinate composition. Our approach is to perform a grid search of the two unknown parameters (curvature of the hyperbola and the extrapolated mantle source y-coordinate isotope ratio) to find the combination that minimizes the sum of squared residuals (defined below) for each step-crushed sample.

A1.2 Total least squares regression

For each individual sample with multiple step-crushes, we define a wide grid search parameter space and iterate the fitting process to refine our search windows. Once the search windows are set, for each combination of curvature (cMy) and mantle source endmember composition (rMy), we compute the coefficients of the mixing hyperbola using Equations A1.7-A1.10 and the known isotope ratios rAx, rAy and rMx. For a given candidate hyperbola, we identify the closest point along the hyperbola to each data point ($x_i \pm \sigma_{xi}$, $y_i \pm \sigma_{yi}$) by finding the root (using a hybrid Newton-Raphson / bisection method) of the first derivative of the sigma-normalized distance function:

$$D^2 = \left(\frac{x_i - m}{\sigma_{xi}}\right)^2 + \left(\frac{y_i - n}{\sigma_{yi}}\right)^2 \qquad \text{Eq. A1.11}$$

Where (m,n) are points along the hyperbola:

$$n = \frac{-Am - D}{Bm + C} \qquad \text{Eq. A1.12}$$

We monitor the sign of the first derivative of D^2 around the root (m_i, n_i) for each data point (x_i, y_i) to ensure that we have found the minimum. The line connecting (m_i, n_i) and (x_i, y_i) is orthogonal to the hyperbola. Thus, the minimal orthogonal distance from the candidate hyperbola for each data point is identified.

We are then able to compute the χ^2 cost function for the candidate hyperbola:

$$\chi^2 = \sum_{i=1}^{N} \left[\left(\frac{x_i - m_i}{\sigma_{xi}} \right)^2 + \left(\frac{y_i - n_i}{\sigma_{yi}} \right)^2 \right] \qquad \text{Eq. A1.13}$$

where ($x_i \pm \sigma_{xi}$, $y_i \pm \sigma_{yi}$) are the N observed data points for a given sample and (m_i, n_i) are the σ–normalized closest points to the data along the candidate hyperbola.

We repeat this computation for each combination of curvature and mantle endmember y-coordinate isotope ratio. The combination of curvature and mantle endmember that minimizes the cost function gives the best fit hyperbola. The 68.3% confidence contour for the parameter space is defined where the fit degrades by a fixed amount $\chi^2 \leq \chi^2_{min} + 2.30$ (for a 2 parameter fit; e.g., Press et al., 1992). The 68.3% confidence interval on the mantle endmember y-coordinate isotope ratio is determined using the lowest χ^2 at each mantle endmember y-coordinate isotope ratio (given free variation in the curvature) to define the interval where $\chi^2 \leq \chi^2_{min} + 2.30$ (chi-square wells for each of our fits are given in the subsequent appendices).

A1.3 References

Ballentine, C.J., Marty, B., Lollar, B.S., Cassidy, M., 2005. Neon isotopes constrain convection and volatile origin in the Earth's mantle. Nature, 433(7021): 33-38.

Langmuir, C.H., Vocke, R.D., Hanson, G.N., Hart, S.R., 1978. General Mixing Equation with Applications to Icelandic Basalts. Earth and Planetary Science Letters, 37(3): 380-392.

Porcelli, D., Ballentine, C.J., Wieler, R., 2002. An Overview of Noble Gas Geochemistry and Cosmochemistry. Reviews in Mineralogy and Geochemistry, 47(1): 1-19.

Press, W.H., Teukolsky, S.A., Vetterling, W.T., Flannery, B.P., 1992. Numerical Recipes in C: The Art of Scientific Computing, second edition, Cambridge University Press, New York.

APPENDIX 2: SUPPLEMENT TO CHAPTER 2

Table A2.1 Compilation of measured magmatic H_2O contents by tectonic setting

Location	H_2O (wt %)		Material	Reference
Ocean islands				
Hawaii	-----	0.84	MI	Hauri (2002)
Hawaii (Loihi Seamount)	0.38	1.0	SG	Dixon and Clague (2001)
Lakigigar, Iceland	-----	0.47	MI	Metrich et al. (1991)
Iceland	-----	1.0	SG	Nichols et al. (2002)
Hekla, Iceland	0.56	0.71	MI	Moune et al. (2007)
Fernandina Island, Galapagos	0.64	1.0	MI	Koleszar et al. (2009)
Piton de la Fournaise, Reunion	0.50	1.1	MI	Bureau et al. (1998)
Easter-Salas y Gomez Seamount Chain	0.40	1.5	SG	Kinglsey et al. (2002)
Easter-Salas y Gomez Seamount Chain	0.30	1.6	SG	Simons et al. (2002)
Society Islands	0.40	1.2	SG	Aubaud et al. (2005)
Mid-ocean ridges				
N-MORB				
34° N Mid-Atlantic Ridge (MAR)	0.10	0.26	SG	Hekinian et al. (2000)
34° N MAR	0.11	0.26	SG	Pineau et al. (2004)
7-11° S MAR	0.04	0.09	MI	Almeev et al. (2008)
12° N MAR; Siqueros (East Pacific Rise)	0.10	0.12	MI	Sobolev and Chaussidon (1996)
9-10° N East Pacific Rise (EPR)	0.13	0.21	SG	Danyushevsky (2000)
9-10° N EPR	0.18	0.22	SG	Le Roux et al. (2006)
23° S EPR	0.16	0.18	SG	Kingsley et al. (2002)
Siqueros (EPR)	0.04	0.12	MI	Saal et al. (2002)
E-MORB				
14-15° N MAR	0.58	0.6	MI	Sobolev and Chaussidon (1996)
35° N MAR	0.34	0.48	SG	Hekinian et al. (2000)
34° N MAR	0.27	0.37	SG	Pineau et al. (2004)
12-14° N EPR	0.19	0.42	SG	Le Roux et al. (2006)
7-11° S MAR	0.32	0.55	MI	Almeev et al. (2008)
14° N MAR	0.29	0.69	SG	Cartigny et al. (2008)
N-MORB and E-MORB mixed data sets				
Pacific-Nazca Ridge, Juan de Fuca Ridge	0.08	0.73	SG	Michael (1988)
Global compilation	0.056	0.92	SG	Michael (1995)
Global compilation	0.16	0.47	SG	Eiler et al. (2000)
Central Indian Ridge	0.11	0.56	SG	Murton et al. (2005)
Global compilation	-----	0.28	SG, MI	Kovalenko et al. (2006)
Southwest Indian Ridge	0.15	0.92	SG	Standish et al. (2008)

'MI' = melt inclusions, 'SG' = submarine glass (or subglacial, for some Iceland samples).

Table A2.1 (continued) Compilation of measured magmatic H_2O contents by tectonic setting

Location	H_2O (wt %)		Material	Reference
Arcs				
Guatemala and California	1.0	6.2	MI	Sisson and Layne (1993)
Central Oregon, Cascades	1.5	3.0	MI	Ruscitto et al. (2010)
Aleutian Volcanic Arc	2.0	6.4	MI	Zimmer et al. (2010)
Eastern Volcanic Belt, Kamchatka Arc	2.5	2.8	MI	Portnyagin et al. (2007)
Klyuchevskoy, Kamchatka Arc	0.4	7.1	MI	Auer et al. (2009)
Mariana Arc	1.0	5.1	MI	Shaw et al. (2008)
Mariana Arc	2.3	6.1	MI	Kelley et al. (2010)
Galunggung, Indonesia	0.3	0.4	MI	Sisson and Bronto (1998)
Barren Island, Andaman Sea	0.4	3.4	MI	Luhr and Haldar (2006)
Irazu Volcano, Costa Rica	1.0	3.2	MI	Benjamin et al. (2007)
Arenal Volcano, Costa Rica	1.1	3.9	MI	Wade et al. (2006)
Cerro Negro, Nicaragua	1.2	6.1	MI	Roggensack et al. (1997)
Cerro Negro, Nicaragua	2.6	6.2	MI	Roggensack (2001)
Pacaya Volcano, Guatemala	1.7	2.4	MI	Walker et al. (2003)
Central American Volcanic Arc	1.0	5.2	MI	Sadofsky et al. (2008)
Chichinautzin Volc. Fld, Central Mexico	1.3	5.2	MI	Cervantes and Wallace (2003)
Michoacan-Guanajuato, Central Mexico	0.5	5.7	MI	Johnson et al. (2009)
Paricutin Volcano, Mexico	1.8	4.0	MI	Luhr (2001)
Back-arc basins				**Reference**
S Pacific	0.20	1.9	SG	Danyushevsky et al. (1993)
Woodlark Basin	0.09	0.64	SG	Muenow et al. (1991)
Sumisu Rift	1.0	1.4	SG	Hochstaedter et al. (1990)
Mariana Trough	0.5	2.1	SG	Stolper and Newman (1994)
Mariana Trough	0.2	2.8	SG	Gribble et al. (1996)
Mariana Trough	0.6	2.2	SG	Gribble et al. (1998)
Mariana Trough	0.2	2.8	SG, MI	Newman et al. (2000)
Lau Basin / Fiji	0.14	1.5	SG	Aggrey et al. (1988)
Lau Basin	1.4	2.4	MI	Kamenetsky et al. (1997)
Lau Basin	1.2	1.6	SG	Peate et al. (2001)
Lau Basin	0.4	1.7	SG	Kent et al. (2002)
Scotia Basin	0.7	2.0	SG	Muenow et al. (1980)
Scotia Basin	0.1	1.6	SG	Fretzdorff et al. (2002)
Manus Basin	1.0	1.3	SG	Kamenetsky et al. (2001)
Manus Basin	0.1	1.8	SG	Sinton et al. (2003)
Manus Basin	0.6	1.9	SG	Shaw et al. (2004)

'MI' = melt inclusions, 'SG' = submarine glass (or subglacial, for some Iceland samples).

APPENDIX 3: SUPPLEMENT TO CHAPTER 3

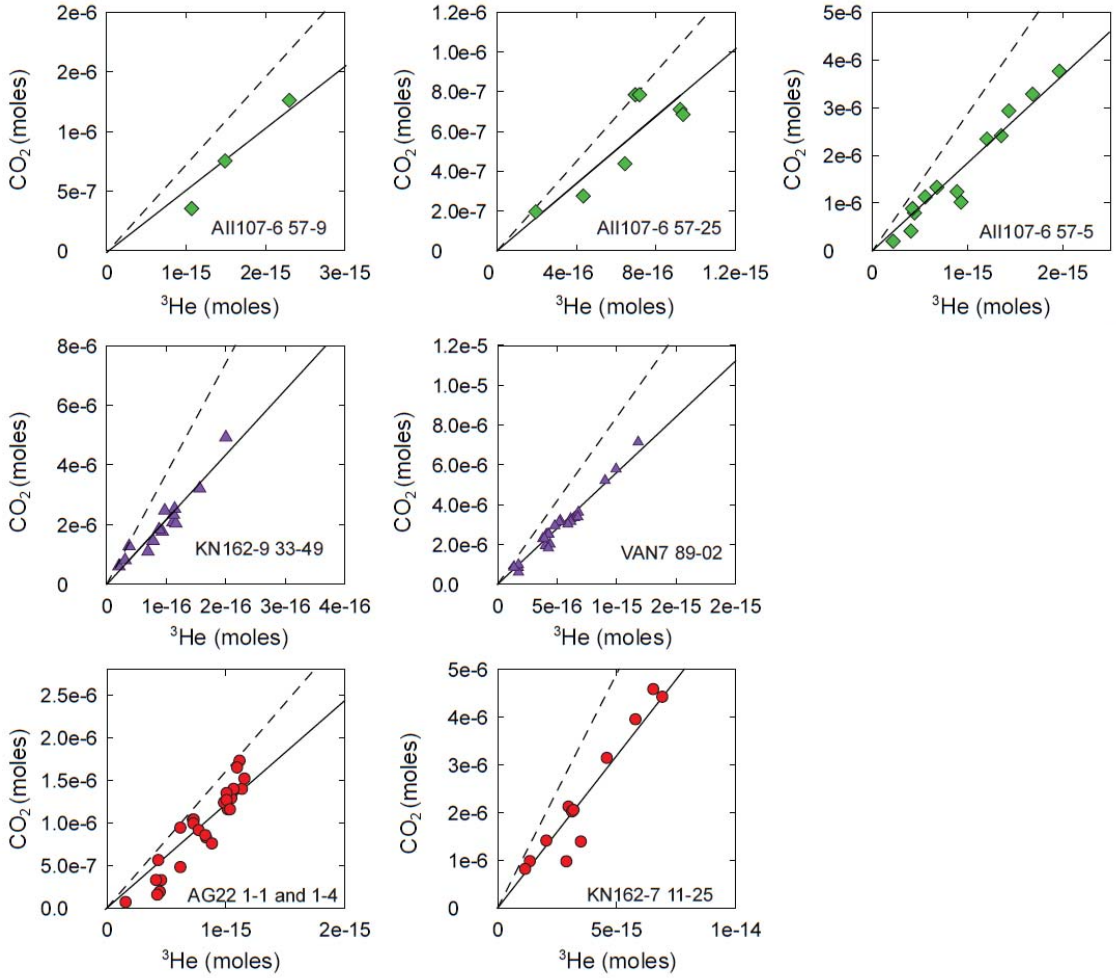

Figure A3.1 CO_2-^{3}He systematics in SWIR basalts. For each sample, individual step-crushes exhibit well-correlated ^{3}He and CO_2 pressures that are used to define a measured $CO_2/^3$He ratio by least squares regression forced through the origin (solid lines). We correct for degassing following a Rayleigh fractionation law constrained by ^{4}He/^{40}Ar* to determine the source $CO_2/^3$He ratio (dashed lines).

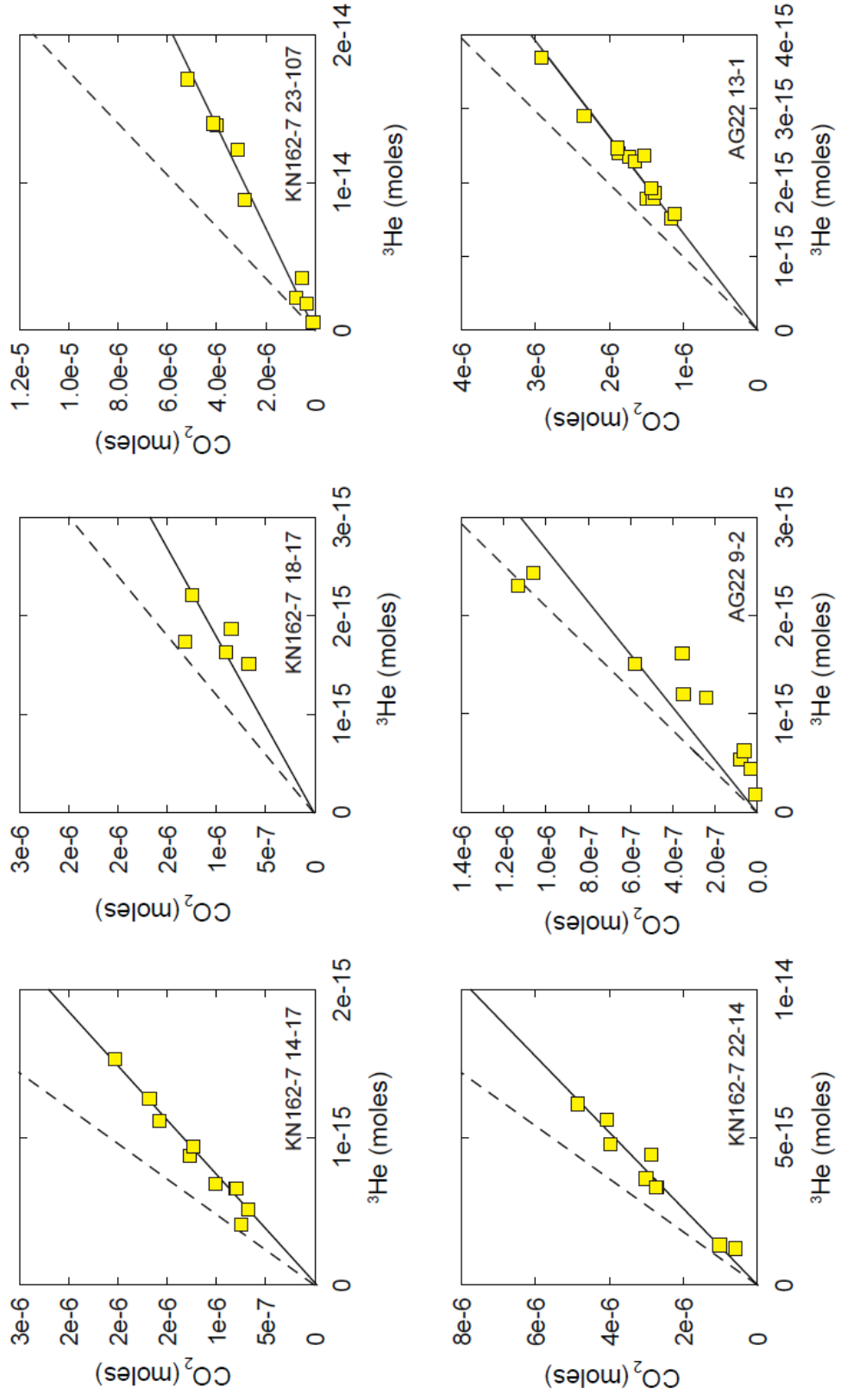

(Figure A3.1 continued) CO_2-^{3}He systematics in SWIR basalts.

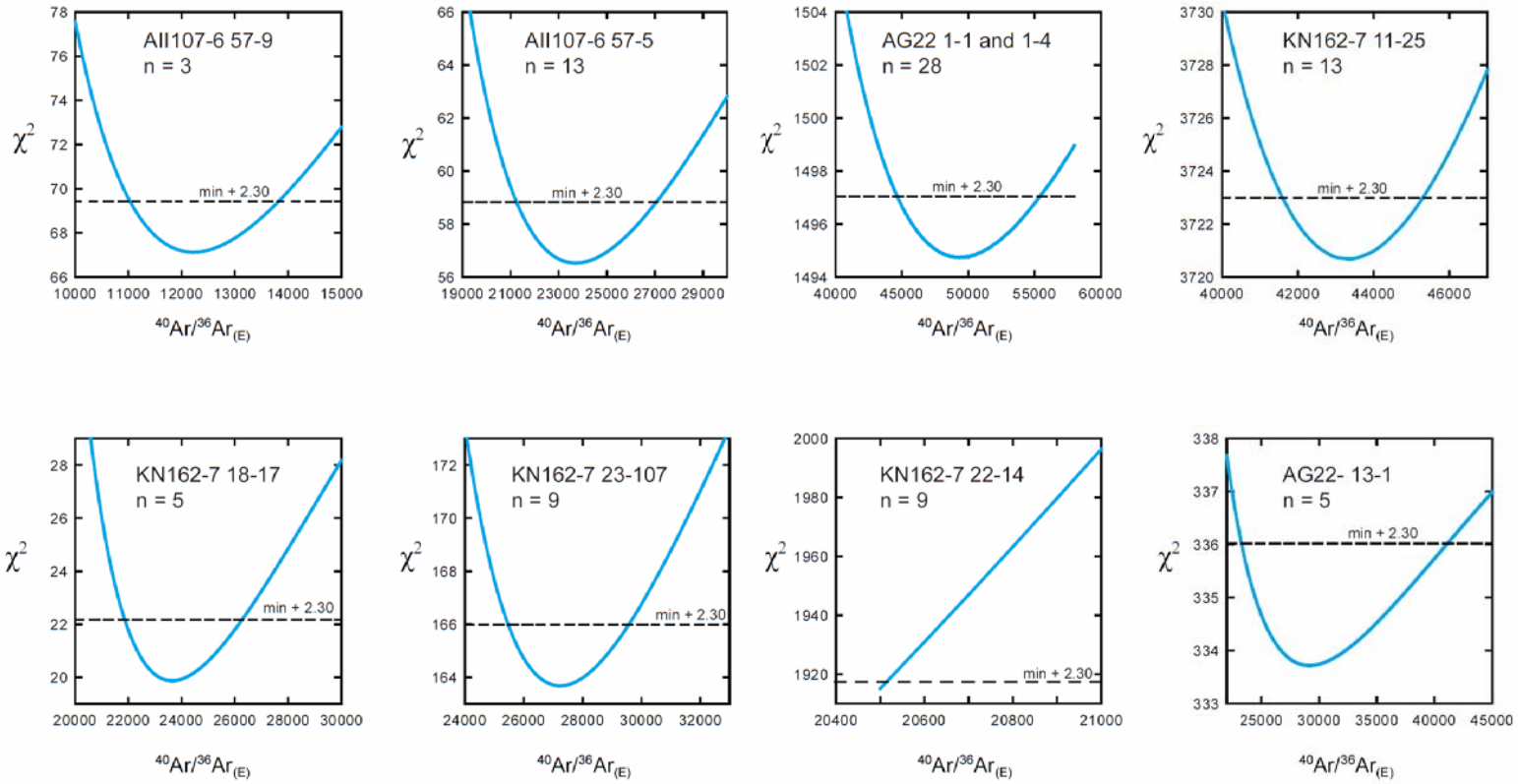

Figure A3.2 Chi-square as a function of mantle endmember $^{40}Ar/^{36}Ar$. The best fit mantle $^{40}Ar/^{36}Ar_{(E)}$ was determined by minimizing the chi-square cost function:

$$\chi^2 = \sum_{i=1}^{N}\left[\left(\frac{x_i - m_i}{\sigma_{xi}}\right)^2 + \left(\frac{y_i - n_i}{\sigma_{yi}}\right)^2\right]$$

where $(x_i \pm \sigma_{xi}, y_i \pm \sigma_{yi})$ are the N observed data points for a given sample and (m_i, n_i) are the σ–normalized closest points to the data along a candidate hyperbola (i.e., the points that minimize χ^2 for the candidate hyperbola). Here χ^2 is given as a function of mantle $^{40}Ar/^{36}Ar_{(E)}$ given free variation in the curvature parameter, k. The 68.3% confidence interval around the best $^{40}Ar/^{36}Ar_{(E)}$ is defined as where the fit degrades by less than 2.30 chi-square units; i.e. $\chi^2 \leq \chi^2_{min} + 2.30$ (dashed line).

The best fit for KN162-7 22-14 occurs below the 1σ uncertainty on the highest measured data point. Therefore, the fit is restricted to $^{40}Ar/^{36}Ar_{(E)}$ > (highest point - 1σ). The fit degrades quickly at higher $^{40}Ar/^{36}Ar_{(E)}$, resulting in a very small confidence interval.

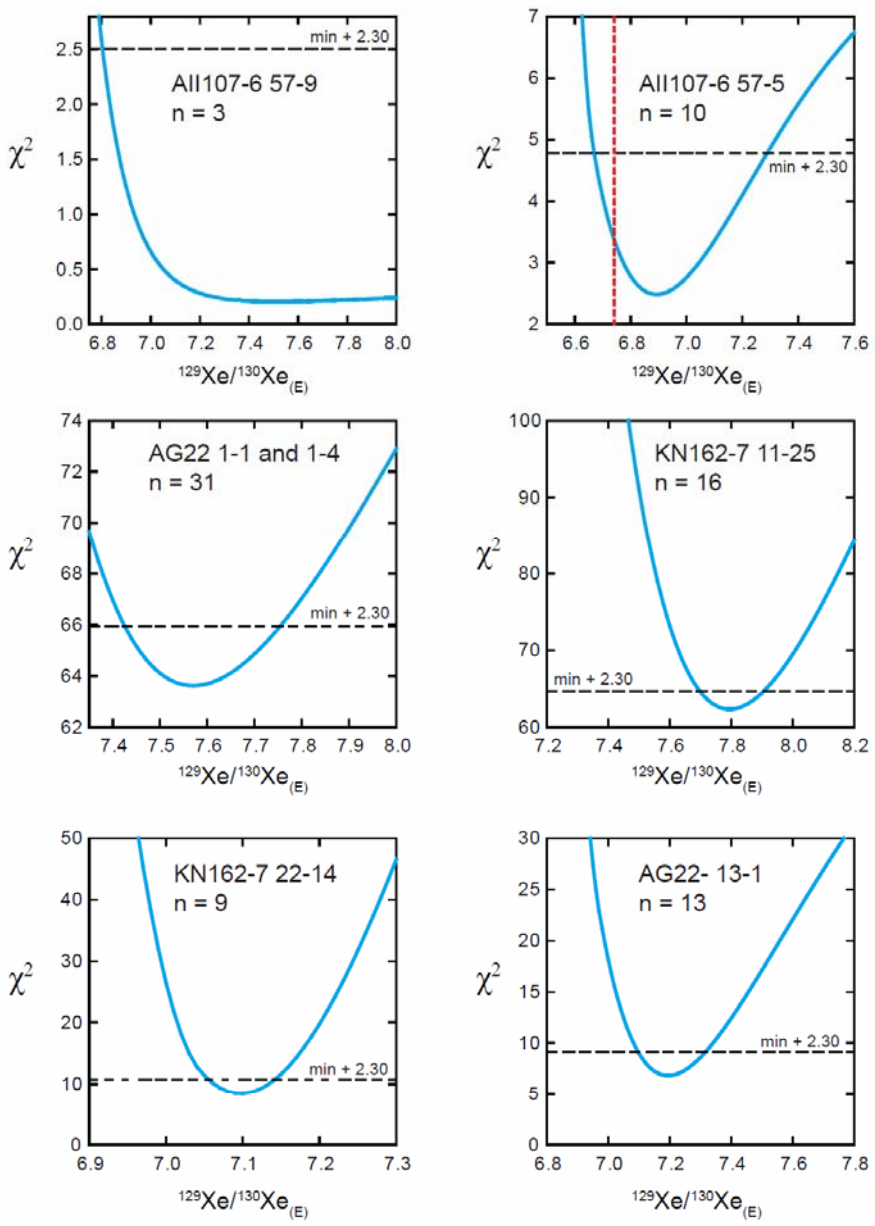

Figure A3.3 Chi-square as a function of mantle endmember $^{129}Xe/^{130}Xe$. The best fit mantle $^{129}Xe/^{130}Xe_{(E)}$ was determined by minimizing the chi-square cost function as described in the Figure A3.2 caption. Here χ^2 is given as a function of mantle $^{129}Xe/^{130}Xe_{(E)}$ given free variation in the curvature parameter, k. The 68.3% confidence interval around the best $^{129}Xe/^{130}Xe_{(E)}$ is defined as where the fit degrades by less than 2.30 chi-square units; i.e. $\chi^2 \leq \chi^2_{min} + 2.30$ (black dashed line).

For All107-6 57-9, N = 3 and a very broad range of Xe endmember isotopic compositions is able to simultaneously fit the three data points within a 1σ range, especially as the curvature k is allowed to vary freely. In reality, the parameter k ($=^{130}Xe/^{36}Ar_{(mantle)}/^{130}Xe/^{36}Ar_{(atm)}$) is probably limited and the solutions with high endmember $^{129}Xe/^{130}Xe_{(E)}$ and very strong curvature are not realistic. However, we are able to place a lower 68.3% confidence bound on the extrapolated value, and depict the upper limit with an arrow in all figures.

For All107-6 57-5, the lower 68.3% confidence bound falls below the (highest measured point - 1σ), and so the lower bound is given as (highest point - 1σ; red dashed line).

Supplementary Table A3.1 Southwest Indian Ridge 7-25°E He, CO_2, Ne, Ar and Xe abundances and He, Ne, Ar and Xe isotopic compositions.

Sample	Lat.	Long.	Depth	$^4He/^3He$	grams	step	x10^{-3} cc CO_2	x10^{-7} cc ^4He	x10^{-12} cc ^{22}Ne	x10^{-11} cc ^{36}Ar	x10^{-14} cc ^{130}Xe
AII 107-6 57-9	54.03	7.26	3767	48300	2.732	1	28.1	24.9	4.7	3.9	1.3
						2	16.9	16.1	7.4	7.6	1.5
						3	7.9	11.6	3.6	2.4	0.7
AII 107-6 57-25	54.03	7.26	3767	51000	3.377	1	17.6	8.0	28.4	13.0	1.9
						2	17.6	8.2	41.3	15.1	2.3
						3	15.9	10.5	46.6	10.6	1.7
					2.264	1	n.d.	15.7	11.0	9.7	1.9
						2	n.d.	12.3	17.6	29.9	2.5
						3	n.d.	7.5	6.5	1.6	0.5
						4	n.d.	12.9	20.5	13.2	2.4
						5	n.d.	6.6	6.8	2.3	0.6
						6	n.d.	2.0	1.7	0.4	0.2
AII 107-6 57-5	54.03	7.26	3767	96400	3.963	1	17.8	9.5	1.0	1.4	0.2
						2	19.8	9.1	1.0	1.2	0.2
						3	65.6	30.9	2.8	3.0	0.5
						4	29.9	14.6	1.7	2.1	0.3
						5	73.5	36.2	2.2	1.3	0.4
						6	25.2	11.9	3.4	5.3	0.5
						7	52.4	25.9	3.6	4.9	0.5
						8	84.1	42.3	5.6	5.7	1.0
						9	53.9	29.2	4.8	6.5	0.7
						10	22.9	20.1	2.3	2.1	0.5
						11	27.7	19.2	2.2	3.0	0.6
						12	9.3	8.7	0.6	0.5	0.2
						13	4.5	4.7	0.5	0.6	0.1
KN162-9 33-49	52.817	11.387	1436	120000	3.68	1	28.7	1.0	--	43.0	--
						2	46.5	3.0	--	11.7	--
						3	13.6	0.5	--	5.8	--
						4	110.3	5.3	--	15.9	--
						5	45.7	3.1	--	24.4	--
						6	71.9	4.2	--	70.4	--
						7	39.6	2.5	--	24.6	--
					3.21	1	18.2	0.8	--	53.7	--
						2	41.3	2.4	--	6.3	--
						3	52.5	3.0	--	17.8	--
						4	56.6	3.0	--	19.9	--
						5	55.3	2.6	--	36.0	--
						6	24.7	1.9	--	21.2	--
						7	32.7	2.1	--	127.3	--
						8	5.4	0.4	--	106.0	--

Supplementary Table A3.1 (continued) Southwest Indian Ridge 7-25°E He, CO_2, Ne, Ar and Xe abundances and He, Ne, Ar and Xe isotopic compositions.

Sample	Lat.	Long.	Depth	$^4He/^3He$	grams	step	$x10^{-3}$ cc CO_2	$x10^{-7}$ cc ^4He	$x10^{-12}$ cc ^{22}Ne	$x10^{-11}$ cc ^{36}Ar	$x10^{-14}$ cc ^{130}Xe
VAN7 89-02	52.25	14.6	2439	119000	4.013	1	19.0	4.7	3.4	5.6	0.5
						2	75.0	17.4	15.9	23.1	3.7
						3	56.4	11.6	9.9	14.9	2.4
						4	116.8	24.2	6.7	8.4	2.3
						5	129.8	26.7	18.1	14.6	4.5
						6	81.4	18.2	5.5	7.4	2.6
						7	73.9	16.5	0.0	5.3	1.7
						8	70.7	16.5	2.7	4.5	0.9
						9	67.9	15.9	2.4	3.4	0.7
						10	75.8	18.1	2.8	3.4	0.7
						11	43.4	10.8	2.3	2.3	0.6
						12	45.3	11.8	1.4	2.3	0.4
						13	40.9	11.4	1.6	3.3	0.7
						14	13.8	4.7	1.4	2.3	0.3
					3.3128	1	56.3	11.0	8.6	16.4	1.9
						2	160.2	31.6	8.1	12.7	2.4
						3	56.5	11.2	4.8	8.4	1.1
						4	56.4	11.5	4.1	6.8	0.8
						5	71.9	14.1	5.6	9.2	1.0
						6	70.4	13.9	2.6	5.1	0.6
						7	66.0	12.9	3.5	4.5	0.7
						8	51.5	10.2	2.0	3.0	0.5
						9	52.0	10.6	1.5	1.5	0.3
						10	22.1	4.7	0.9	0.6	0.1
						11	19.3	3.7	1.0	1.6	0.3
AG22 1-1	52.300	16.980	4000	108000	2.9325	1	20.9	16.2	3.3	6.8	1.1
						2	38.6	29.1	2.3	4.0	1.0
						3	36.6	28.7	38.7	67.5	8.4
						4	23.0	18.9	5.1	7.6	1.7
						5	23.0	19.1	13.6	23.7	3.1
						6	12.4	11.4	0.8	1.2	0.3
						7	22.1	19.0	3.3	5.8	1.0
						8	20.3	20.2	1.4	1.6	0.5
						9	18.3	21.8	1.7	2.9	1.0
						10	7.2	12.0	0.7	0.8	0.3
						11	4.1	11.6	1.4	1.8	0.4
					1.9257	1	29.2	27.3	9.1	21.3	3.4
						2	31.1	29.6	9.3	14.8	2.2
						3	28.6	27.2	2.3	2.6	0.7
						4	25.7	26.6	3.0	4.3	0.9
						5	19.0	21.6	1.9	1.7	0.5

Supplementary Table A3.1 (continued) Southwest Indian Ridge 7-25°E He, CO_2, Ne, Ar and Xe abundances and He, Ne, Ar and Xe isotopic compositions.

Sample	Lat.	Long.	Depth	$^4He/^3He$	grams	step	x10^{-3} cc CO_2	x10^{-7} cc ^4He	x10^{-12} cc ^{22}Ne	x10^{-11} cc ^{36}Ar	x10^{-14} cc ^{130}Xe
						6	7.2	10.8	4.8	8.3	1.2
						7	3.3	11.1	1.3	1.0	0.3
					1.31	1	n.d.	23.4	5.3	17.0	1.5
						2	n.d.	43.1	8.6	18.7	2.4
						3	n.d.	14.4	1.1	1.6	0.4
						4	n.d.	11.1	0.8	1.3	0.4
AG22 1-4	52.300	16.980	4000		2.9982	1	33.7	27.7	18.8	33.3	4.6
						2	31.1	25.5	4.3	7.5	2.4
						3	29.9	24.1	3.9	16.6	3.3
						4	27.5	23.5	1.4	2.1	0.6
						5	28.2	24.2	2.2	4.0	0.9
						6	25.8	24.7	1.6	2.1	0.5
						7	16.8	21.1	4.0	5.2	0.9
						8	10.6	14.8	1.1	1.0	0.4
						9	6.0	10.8	1.5	1.7	0.3
KN162-7 11-25	52.799	19.200	3913	104000	4.064	1	21.7	32.2	1.1	3.7	1.6
						2	47.3	70.2	47.5	86.1	11.1
						3	31.4	48.3	1.3	1.2	0.5
						4	70.0	107.8	3.1	2.7	1.2
						5	18.0	27.7	0.8	0.7	0.4
						6	102.3	153.3	5.1	2.3	2.4
						7	88.3	135.9	6.0	5.6	2.0
						8	45.0	73.6	2.4	2.5	1.1
						9	45.7	75.0	2.1	1.8	0.8
						10	98.8	162.2	4.5	3.7	1.9
						11	31.0	82.2	4.1	3.5	1.2
						12	14.5	35.4	1.0	1.0	0.4
					2.488	1	124.5	197.3	206.5	96.8	43.9
						2	121.9	206.3	7.8	4.0	3.0
						3	21.6	68.0	2.3	4.3	1.6
						4	n.d.	n.d.	n.d.	0.5	0.1
KN162-7 14-7	52.873	20.398	3403	104000	3.838	1	n.d.	8.9	33.4	64.0	8.6
						2	18.2	15.2	33.4	62.7	7.1
						3	18.0	15.2	8.1	14.1	2.7
						4	45.5	35.5	55.7	110.4	18.4
						5	28.4	20.3	52.7	95.4	11.8
						6	37.6	29.3	60.1	107.3	14.1
						7	22.6	15.8	11.9	17.2	2.7
						8	16.8	9.5	9.5	12.5	2.7
						9	15.1	11.9	7.6	12.6	2.4
						10	27.6	21.8	15.8	28.1	1.2
						11	35.4	25.7	20.0	49.7	4.7

Supplementary Table A3.1 (continued) Southwest Indian Ridge 7-25°E He, CO_2, Ne, Ar and Xe abundances and He, Ne, Ar and Xe isotopic compositions.

Sample	Lat.	Long.	Depth	$^4He/^3He$	grams	step	$x10^{-3}$ cc CO_2	$x10^{-7}$ cc ^4He	$x10^{-12}$ cc ^{22}Ne	$x10^{-11}$ cc ^{36}Ar	$x10^{-14}$ cc ^{130}Xe
KN162-7 18-17	52.990	21.406	4525	102000	2.393	1	29.7	40.0	1.4	1.8	3.8
						2	28.0	50.9	1.6	1.9	1.9
						3	19.0	43.1	1.1	1.4	3.4
					2.339	1	20.2	37.4	1.3	1.7	2.4
						2	15.0	34.8	1.3	1.8	1.1
KN162-7 23-107	53.173	22.547	3609	98900	4.3	1	16.9	47.9	0.8	0.6	0.2
						2	64.5	195.9	3.1	2.4	0.9
						3	116.3	376.0	5.5	4.1	1.6
						4	89.1	307.8	4.8	3.5	1.0
						5	92.3	310.8	4.5	2.3	0.7
						6	70.6	270.8	4.0	2.7	3.9
						7	12.2	78.9	1.2	0.7	0.2
						8	7.5	39.4	0.6	0.5	n.d.
						9	1.8	11.1	0.2	0.2	n.d.
KN162-7 22-14	53.109	22.647	3852	102000	3.024	1	22.8	31.0	5.0	4.9	1.4
						2	67.3	82.4	6.5	10.1	3.2
						3	60.8	75.4	3.1	4.7	2.7
						4	61.6	75.3	3.6	5.2	2.5
						5	88.9	109.6	10.9	14.3	3.8
						6	109.2	140.5	5.8	4.6	4.5
						7	90.8	128.2	5.4	3.5	3.6
						8	64.3	100.9	4.3	2.3	2.9
						9	13.1	28.1	1.1	1.1	0.8
AG22 9-2	53.130	22.880	3800	99500	3.921	1	25.3	51.3	27.5	47.2	8.8
						2	23.8	54.1	13.4	18.4	4.7
						3	13.0	33.7	5.3	4.7	2.8
						4	7.8	26.8	6.0	5.6	1.9
						5	7.9	36.2	7.6	7.1	2.7
						6	5.4	26.2	8.0	6.0	1.9
						7	1.8	12.0	2.4	1.8	0.7
						8	1.4	14.0	3.1	1.8	0.8
						9	0.7	10.0	2.7	1.6	0.6
						10	0.2	4.1	1.3	0.6	0.2
AG22 13-1	53.408	24.758	3850	99000	4.6	1	33.7	39.5	10.5	14.1	2.5
						2	52.4	64.5	10.9	9.5	3.0
						3	65.4	81.7	54.1	40.7	12.4
						4	31.6	39.5	31.7	73.1	9.3
						5	26.2	33.5	54.3	102.0	12.5
						6	42.2	53.3	40.9	52.1	6.3
						7	31.0	41.3	57.6	95.0	12.0
						8	32.2	42.5	23.7	30.2	4.5
						9	38.9	52.1	19.4	11.8	3.0
						10	42.2	54.7	21.4	18.5	3.9
						11	37.0	50.8	42.0	55.4	6.9
						12	25.2	34.8	12.8	6.4	1.6
						13	34.3	52.3	51.1	66.4	8.8

Supplementary Table A3.1 (continued) Southwest Indian Ridge 7-25°E He, CO_2, Ne, Ar and Xe abundances and He, Ne, Ar and Xe isotopic compositions.

Sample	Lat.	Long.	Depth	$^4He/^3He$	grams	step	$^{20}Ne/^{22}Ne$	1σ	$^{21}Ne/^{22}Ne$	1σ	$^{40}Ar/^{36}Ar$	1σ
AII 107-6 57-9	54.03	7.26	3767	48300	2.732	1	11.49	0.02	0.0371	0.0004	5282	53
						2	10.53	0.01	0.0322	0.0003	1807	18
						3	10.73	0.02	0.0330	0.0004	3114	31
AII 107-6 57-25	54.03	7.26	3767	51000	3.377	1	9.98	0.02	0.0301	0.0002	1160	12
						2	9.93	0.02	0.0295	0.0002	1061	11
						3	9.92	0.02	0.0297	0.0002	1299	13
					2.264	1	10.49	0.02	0.0327	0.0002	2361	24
						2	10.10	0.02	0.0304	0.0002	1141	11
						3	10.23	0.02	0.0310	0.0002	4801	48
						4	10.06	0.02	0.0304	0.0002	1381	14
						5	10.14	0.05	0.0307	0.0027	2734	27
						6	10.32	0.09	0.0315	0.0006	2691	27
AII 107-6 57-5	54.03	7.26	3767	96400	3.963	1	10.96	0.07	0.0426	0.0010	2937	54
						2	11.07	0.07	0.0453	0.0010	3941	39
						3	11.52	0.03	0.0494	0.0002	6974	70
						4	11.07	0.05	0.0434	0.0006	3406	34
						5	12.21	0.04	0.0583	0.0003	14430	140
						6	10.35	0.02	0.0358	0.0002	1494	15
						7	10.81	0.02	0.0423	0.0004	2919	29
						8	11.00	0.01	0.0422	0.0008	3942	39
						9	10.67	0.01	0.0393	0.0007	2519	25
						10	10.71	0.04	0.0393	0.0003	2601	26
						11	10.89	0.04	0.0415	0.0003	2659	27
						12	11.46	0.07	0.0469	0.0011	5591	103
						13	10.79	0.07	0.0407	0.0010	2391	44
KN162-9 33-49	52.817	11.387	1436	120000	3.68	1	--	--	--	--	317	3
						2	--	--	--	--	339	3
						3	--	--	--	--	319	3
						4	--	--	--	--	357	4
						5	--	--	--	--	337	3
						6	--	--	--	--	322	3
						7	--	--	--	--	332	3
					3.21	1	--	--	--	--	316	3
						2	--	--	--	--	369	4
						3	--	--	--	--	359	4
						4	--	--	--	--	348	3
						5	--	--	--	--	322	3
						6	--	--	--	--	333	3
						7	--	--	--	--	307	3
						8	--	--	--	--	286	3

Supplementary Table A3.1 (continued) Southwest Indian Ridge 7-25°E He, CO_2, Ne, Ar and Xe abundances and He, Ne, Ar and Xe isotopic compositions.

Sample	Lat.	Long.	Depth	$^4He/^3He$	grams	step	$^{20}Ne/^{22}Ne$	1σ	$^{21}Ne/^{22}Ne$	1σ	$^{40}Ar/^{36}Ar$	1σ
VAN7 89-02	52.25	14.598	2439	119000	4.013	1	10.01	0.02	0.0318	0.0004	737	7
						2	9.97	0.02	0.0313	0.0002	669	7
						3	9.97	0.01	0.0314	0.0003	744	7
						4	10.37	0.01	0.0366	0.0004	1451	15
						5	10.10	0.02	0.0322	0.0002	829	8
						6	10.24	0.01	0.0351	0.0004	1239	12
						7	n.d.	---	n.d.	---	1853	19
						8	10.72	0.03	0.0394	0.0005	2297	23
						9	10.74	0.03	0.0397	0.0005	2687	29
						10	10.72	0.03	0.0398	0.0005	3254	33
						11	10.41	0.03	0.0366	0.0005	2725	27
						12	10.91	0.03	0.0430	0.0005	3245	32
						13	10.77	0.03	0.0406	0.0005	2487	25
						14	10.30	0.03	0.0334	0.0004	1464	15
					3.3128	1	10.04	0.02	0.0321	0.0002	888	9
						2	10.52	0.02	0.0378	0.0002	2358	24
						3	10.20	0.01	0.0341	0.0001	1395	14
						4	10.31	0.01	0.0347	0.0002	1694	17
						5	10.25	0.01	0.0341	0.0001	1545	15
						6	10.68	0.02	0.0411	0.0003	2499	25
						7	10.48	0.02	0.0380	0.0002	2764	28
						8	10.76	0.02	0.0407	0.0002	3166	32
						9	11.09	0.02	0.0446	0.0002	6340	63
						10	10.74	0.02	0.0417	0.0002	6469	65
						11	10.54	0.02	0.0384	0.0002	2542	25
AG22 1-1	52.300	16.980	4000	108000	2.9325	1	10.29	0.02	0.0364	0.0002	3169	32
						2	11.21	0.02	0.0491	0.0003	9243	92
						3	9.90	0.03	0.0304	0.0001	766	8
						4	10.23	0.01	0.0350	0.0001	2955	30
						5	9.96	0.02	0.0312	0.0002	1205	12
						6	11.18	0.02	0.0487	0.0003	9847	98
						7	10.43	0.02	0.0376	0.0002	3896	39
						8	11.30	0.02	0.0500	0.0002	12520	130
						9	11.17	0.02	0.0482	0.0003	7000	70
						10	11.41	0.03	0.0521	0.0004	13100	130
						11	10.54	0.02	0.0400	0.0002	4714	47
					1.9257	1	10.09	0.02	0.0334	0.0002	1559	16
						2	10.12	0.02	0.0336	0.0002	2086	21
						3	10.98	0.02	0.0448	0.0002	10090	100
						4	10.56	0.01	0.0404	0.0001	5857	59
						5	10.88	0.02	0.0435	0.0003	11740	120

Supplementary Table A3.1 (continued) Southwest Indian Ridge 7-25°E He, CO_2, Ne, Ar and Xe abundances and He, Ne, Ar and Xe isotopic compositions.

Sample	Lat.	Long.	Depth	$^4He/^3He$	grams	step	$^{20}Ne/^{22}Ne$	1σ	$^{21}Ne/^{22}Ne$	1σ	$^{40}Ar/^{36}Ar$	1σ
						6	10.02	0.02	0.0319	0.0002	1703	17
						7	10.53	0.03	0.0393	0.0004	7729	77
					1.31	1	10.37	0.05	0.0363	0.0003	3275	33
						2	10.45	0.05	0.0376	0.0008	3612	36
						3	11.33	0.06	0.0513	0.0010	9643	96
						4	11.24	0.06	0.0494	0.0010	9317	93
AG22 1-4	52.300	16.980	4000		2.9982	1	9.96	0.01	0.0311	0.0002	1269	13
						2	10.47	0.02	0.0383	0.0002	3906	39
						3	10.30	0.02	0.0390	0.0002	2105	21
						4	11.57	0.03	0.0552	0.0005	12490	120
						5	10.82	0.02	0.0461	0.0002	6786	68
						6	11.39	0.02	0.0519	0.0004	12180	120
						7	10.36	0.02	0.0369	0.0002	4285	43
						8	11.16	0.03	0.0474	0.0005	15340	150
						9	10.50	0.02	0.0384	0.0003	5848	58
KN162-7 11-25	52.799	19.200	3913	104000	4.064	1	11.88	0.01	0.0576	0.0009	6886	69
						2	9.91	0.08	0.0305	0.0001	877	9
						3	12.32	0.01	0.0653	0.0010	26650	270
						4	12.41	0.02	0.0640	0.0007	27240	270
						5	12.21	0.01	0.0642	0.0010	27610	280
						6	12.09	0.02	0.0600	0.0003	20120	200
						7	11.47	0.02	0.0525	0.0003	16490	160
						8	11.93	0.01	0.0576	0.0009	18610	190
						9	12.34	0.01	0.0644	0.0010	26780	270
						10	12.41	0.02	0.0652	0.0004	28500	290
						11	11.21	0.02	0.0480	0.0004	13390	130
						12	12.18	0.01	0.0605	0.0009	21960	220
					2.488	1	9.71	0.03	0.0299	0.0002	647	6
						2	11.72	0.02	0.0560	0.0004	14660	150
						3	11.83	0.03	0.0578	0.0005	10840	110
						4	11.12	0.03	0.0434	0.0003	5955	60
KN162-7 14-7	52.873	20.398	3403	104000	3.838	1	9.84	0.06	0.0294	0.0002	363	4
						2	9.79	0.06	0.0297	0.0002	412	4
						3	10.01	0.01	0.0315	0.0002	770	8
						4	9.83	0.06	0.0301	0.0002	452	5
						5	9.79	0.06	0.0296	0.0002	412	4
						6	9.81	0.06	0.0298	0.0002	422	4
						7	9.96	0.01	0.0309	0.0002	734	7
						8	10.01	0.01	0.0308	0.0002	761	8
						9	9.97	0.01	0.0313	0.0002	749	7
						10	9.97	0.01	0.0309	0.0001	648	6
						11	9.84	0.01	0.0307	0.0001	584	6

Supplementary Table A3.1 (continued) Southwest Indian Ridge 7-25°E He, CO_2, Ne, Ar and Xe abundances and He, Ne, Ar and Xe isotopic compositions.

Sample	Lat.	Long.	Depth	$^4He/^3He$	grams	step	$^{20}Ne/^{22}Ne$	1σ	$^{21}Ne/^{22}Ne$	1σ	$^{40}Ar/^{36}Ar$	1σ
KN162-7 18-17	52.990	21.406	4525	102000	2.393	1	11.84	0.06	0.0559	0.0009	15930	160
						2	11.77	0.06	0.0538	0.0008	15470	150
						3	12.20	0.07	0.0598	0.0012	17990	180
					2.339	1	11.37	0.02	0.0499	0.0002	11810	120
						2	11.30	0.02	0.0490	0.0002	10120	100
KN162-7 23-107	53.173	22.547	3609	98900	4.3	1	12.14	0.02	0.0631	0.0008	15520	160
						2	12.06	0.02	0.0615	0.0006	14810	150
						3	12.16	0.02	0.0621	0.0005	14780	150
						4	11.82	0.02	0.0587	0.0005	12790	130
						5	12.24	0.02	0.0635	0.0005	20330	200
						6	12.06	0.02	0.0608	0.0005	14590	150
						7	11.94	0.02	0.0619	0.0008	16350	160
						8	12.02	0.02	0.0618	0.0008	12830	130
						9	11.58	0.02	0.0541	0.0007	10060	230
KN162-7 22-14	53.109	22.647	3852	102000	3.024	1	10.38	0.01	0.0371	0.0004	6488	65
						2	11.03	0.01	0.0470	0.0004	8492	85
						3	12.06	0.02	0.0622	0.0006	15610	160
						4	11.78	0.02	0.0569	0.0006	14550	150
						5	10.92	0.01	0.0435	0.0003	7665	77
						6	12.04	0.01	0.0608	0.0006	11940	120
						7	11.95	0.01	0.0600	0.0006	14050	140
						8	11.94	0.01	0.0591	0.0006	17540	180
						9	12.10	0.03	0.0626	0.0005	20700	210
AG22 9-2	53.130	22.880	3800	99500	3.921	1	10.07	0.10	0.0308	0.0002	1584	16
						2	10.14	0.01	0.0335	0.0001	3840	38
						3	10.38	0.01	0.0363	0.0004	8991	90
						4	10.22	0.01	0.0340	0.0003	6109	61
						5	10.25	0.01	0.0347	0.0002	6579	66
						6	10.13	0.01	0.0330	0.0002	5614	56
						7	10.25	0.03	0.0347	0.0004	8279	83
						8	10.20	0.03	0.0338	0.0003	9537	95
						9	10.16	0.03	0.0328	0.0003	7883	79
						10	10.11	0.04	0.0324	0.0009	8648	115
AG22 13-1	53.408	24.758	3850	99000	4.6	1	10.17	0.01	0.0343	0.0002	3579	36
						2	10.44	0.01	0.0376	0.0002	8286	83
						3	9.89	0.04	0.0311	0.0002	1259	13
						4	9.85	0.04	0.0304	0.0002	904	9
						5	9.84	0.04	0.0301	0.0002	670	7
						6	9.95	0.04	0.0310	0.0002	1434	14
						7	9.93	0.04	0.0300	0.0002	760	8
						8	9.94	0.04	0.0316	0.0002	1844	18
						9	10.11	0.01	0.0325	0.0002	5028	50
						10	10.10	0.04	0.0327	0.0002	3707	37
						11	9.97	0.04	0.0307	0.0002	1317	13
						12	10.12	0.01	0.0328	0.0001	6347	63
						13	9.93	0.04	0.0304	0.0002	1116	11

Supplementary Table A3.1 (continued) Southwest Indian Ridge 7-25°E He, CO_2, Ne, Ar and Xe abundances and He, Ne, Ar and Xe isotopic compositions.

Sample	Lat.	Long.	Depth	$^4He/^3He$	grams	step	$^{129}Xe/^{130}Xe$	1σ	$^{136}Xe/^{130}Xe$	1σ	$^{129}Xe/^{136}Xe$	1σ
AII 107-6 57-9	54.03	7.26	3767	48300	2.732	1	6.860	0.075	2.303	0.022	2.975	0.024
						2	6.617	0.070	2.244	0.021	2.949	0.024
						3	6.65	0.11	2.245	0.040	2.961	0.037
AII 107-6 57-25	54.03	7.26	3767	51000	3.377	1	6.672	0.062	2.216	0.020	3.012	0.023
						2	6.595	0.055	2.207	0.020	2.989	0.021
						3	6.615	0.066	2.246	0.021	2.947	0.023
					2.264	1	6.700	0.048	2.283	0.017	2.936	0.018
						2	6.586	0.033	2.216	0.013	2.972	0.015
						3	6.80	0.15	2.310	0.063	2.939	0.061
						4	6.644	0.035	2.219	0.014	2.996	0.016
						5	6.57	0.13	2.220	0.056	2.967	0.057
						6	6.76	0.18	2.197	0.076	3.081	0.081
AII 107-6 57-5	54.03	7.26	3767	96400	3.963	1	6.73	0.14	2.225	0.057	3.032	0.050
						2	6.45	0.14	2.146	0.055	2.997	0.050
						3	6.75	0.11	2.267	0.042	2.986	0.038
						4	6.59	0.13	2.193	0.054	2.996	0.048
						5	6.87	0.12	2.319	0.048	2.963	0.041
						6	6.62	0.11	2.201	0.038	3.013	0.037
						7	6.69	0.11	2.251	0.042	2.973	0.038
						8	6.600	0.076	2.207	0.022	2.988	0.025
						9	6.636	0.087	2.254	0.028	2.945	0.029
						10	6.40	0.11	2.156	0.043	2.969	0.041
						11	6.69	0.10	2.330	0.037	2.873	0.033
						12	6.37	0.13	2.125	0.054	2.994	0.050
						13	6.57	0.14	2.153	0.055	3.043	0.051
KN162-9 33-49	52.817	11.387	1436	120000	3.68	1	--	--	--	--	--	--
						2	--	--	--	--	--	--
						3	--	--	--	--	--	--
						4	--	--	--	--	--	--
						5	--	--	--	--	--	--
						6	--	--	--	--	--	--
						7	--	--	--	--	--	--
					3.21	1	--	--	--	--	--	--
						2	--	--	--	--	--	--
						3	--	--	--	--	--	--
						4	--	--	--	--	--	--
						5	--	--	--	--	--	--
						6	--	--	--	--	--	--
						7	--	--	--	--	--	--
						8	--	--	--	--	--	--

Supplementary Table A3.1 (continued) Southwest Indian Ridge 7-25°E He, CO_2, Ne, Ar and Xe abundances and He, Ne, Ar and Xe isotopic compositions.

Sample	Lat.	Long.	Depth	$^4He/^3He$	grams	step	$^{129}Xe/^{130}Xe$	1σ	$^{136}Xe/^{130}Xe$	1σ	$^{129}Xe/^{136}Xe$	1σ
VAN7 89-02	52.25	14.59766	2439	119000	4.013	1	6.52	0.11	2.209	0.043	2.967	0.040
						2	6.605	0.035	2.187	0.012	3.021	0.014
						3	6.528	0.050	2.186	0.019	2.988	0.021
						4	6.552	0.051	2.176	0.019	3.011	0.021
						5	6.608	0.033	2.191	0.011	3.016	0.012
						6	6.523	0.044	2.174	0.017	3.004	0.019
						7	6.518	0.060	2.165	0.020	3.012	0.023
						8	6.542	0.083	2.181	0.026	3.004	0.029
						9	6.780	0.099	2.246	0.034	3.022	0.033
						10	6.805	0.099	2.230	0.033	3.049	0.034
						11	6.80	0.11	2.243	0.041	3.037	0.039
						12	6.65	0.12	2.202	0.046	3.029	0.043
						13	6.69	0.11	2.225	0.038	3.001	0.037
						14	6.59	0.13	2.234	0.052	2.959	0.046
					3.3128	1	6.570	0.054	2.200	0.021	2.989	0.029
						2	6.610	0.045	2.214	0.018	2.986	0.027
						3	6.549	0.072	2.195	0.026	2.988	0.033
						4	6.509	0.086	2.195	0.030	2.975	0.036
						5	6.737	0.075	2.272	0.027	2.968	0.033
						6	6.82	0.10	2.243	0.035	3.047	0.040
						7	6.602	0.091	2.236	0.032	2.962	0.037
						8	6.93	0.11	2.291	0.037	3.026	0.041
						9	6.88	0.12	2.314	0.041	2.969	0.044
						10	7.10	0.13	2.365	0.043	2.993	0.045
						11	6.62	0.12	2.209	0.039	2.986	0.044
AG22 1-1	52.300	16.980	4000	108000	2.9325	1	6.772	0.074	2.274	0.027	2.982	0.032
						2	7.294	0.079	2.422	0.028	3.012	0.033
						3	6.561	0.026	2.187	0.009	3.000	0.010
						4	6.695	0.058	2.248	0.022	2.980	0.029
						5	6.646	0.037	2.231	0.014	2.984	0.019
						6	7.23	0.12	2.373	0.042	3.046	0.044
						7	6.944	0.079	2.319	0.028	2.993	0.033
						8	7.340	0.110	2.500	0.039	2.940	0.039
						9	6.716	0.076	2.268	0.028	2.965	0.033
						10	6.96	0.12	2.306	0.040	2.997	0.044
						11	6.87	0.11	2.302	0.039	2.987	0.043
					1.9257	1	6.653	0.035	2.224	0.012	2.991	0.013
						2	6.693	0.046	2.253	0.019	2.972	0.027
						3	7.302	0.094	2.420	0.033	3.008	0.036
						4	6.881	0.081	2.344	0.029	2.939	0.034
						5	7.20	0.11	2.453	0.039	2.937	0.040

Supplementary Table A3.1 (continued) Southwest Indian Ridge 7-25°E He, CO_2, Ne, Ar and Xe abundances and He, Ne, Ar and Xe isotopic compositions.

Sample	Lat.	Long.	Depth	$^4He/^3He$	grams	step	$^{129}Xe/^{130}Xe$	1σ	$^{136}Xe/^{130}Xe$	1σ	$^{129}Xe/^{136}Xe$	1σ
						6	6.699	0.068	2.236	0.025	2.996	0.031
						7	6.830	0.120	2.314	0.042	2.955	0.044
					1.31	1	6.871	0.057	2.298	0.019	2.992	0.020
						2	6.909	0.032	2.310	0.013	2.992	0.015
						3	7.07	0.16	2.375	0.068	2.973	0.065
						4	7.29	0.17	2.393	0.070	3.047	0.068
AG22 1-4	52.300	16.980	4000		2.998	1	6.637	0.032	2.228	0.011	2.980	0.012
						2	6.737	0.046	2.260	0.019	2.980	0.027
						3	6.641	0.036	2.236	0.012	2.971	0.013
						4	7.197	0.099	2.431	0.035	2.969	0.037
						5	7.156	0.084	2.391	0.030	2.994	0.034
						6	7.29	0.11	2.463	0.037	2.960	0.039
						7	6.918	0.082	2.324	0.029	2.978	0.034
						8	7.23	0.12	2.414	0.042	2.996	0.043
						9	7.07	0.12	2.370	0.042	2.981	0.044
KN162-7 11-25	52.799	19.200	3913	104000	4.064	1	6.656	0.059	2.188	0.019	3.046	0.020
						2	6.569	0.025	2.201	0.009	2.983	0.009
						3	7.71	0.11	2.555	0.043	3.016	0.045
						4	7.598	0.070	2.526	0.023	3.009	0.021
						5	7.31	0.12	2.421	0.045	3.018	0.051
						6	7.338	0.051	2.453	0.017	2.991	0.016
						7	7.405	0.057	2.451	0.019	3.018	0.018
						8	7.199	0.069	2.407	0.023	2.993	0.021
						9	7.505	0.083	2.460	0.028	3.045	0.027
						10	7.521	0.057	2.513	0.019	2.993	0.017
						11	7.337	0.069	2.452	0.023	2.990	0.021
						12	7.58	0.12	2.487	0.044	3.040	0.048
					2.488	1	6.554	0.023	2.203	0.008	2.973	0.007
						2	7.376	0.046	2.460	0.015	2.995	0.016
						3	6.943	0.061	2.310	0.020	3.007	0.020
						4	6.92	0.12	2.288	0.048	3.024	0.059
KN162-7 14-7	52.873	20.398	3403	104000	3.838	1	6.537	0.026	2.185	0.010	2.990	0.010
						2	6.516	0.026	2.174	0.010	2.998	0.011
						3	6.514	0.045	2.187	0.015	2.977	0.016
						4	6.515	0.022	2.181	0.007	2.986	0.007
						5	6.485	0.024	2.173	0.009	2.984	0.009
						6	6.493	0.023	2.172	0.008	2.989	0.008
						7	6.620	0.046	2.223	0.016	2.977	0.016
						8	6.554	0.045	2.187	0.015	2.997	0.016
						9	6.580	0.048	2.191	0.016	3.000	0.017
						10	6.470	0.064	2.223	0.021	2.910	0.021
						11	6.509	0.034	2.183	0.012	2.981	0.013

Supplementary Table A3.1 (continued) Southwest Indian Ridge 7-25°E He, CO_2, Ne, Ar and Xe abundances and He, Ne, Ar and Xe isotopic compositions.

Sample	Lat.	Long.	Depth	$^4He/^3He$	grams	step	$^{129}Xe/^{130}Xe$	1σ	$^{136}Xe/^{130}Xe$	1σ	$^{129}Xe/^{136}Xe$	1σ
KN162-7 18-17	52.990	21.406	4525	102000	2.393	1	6.759	0.035	2.246	0.012	3.007	0.014
						2	6.959	0.058	2.330	0.021	2.993	0.021
						3	6.763	0.036	2.251	0.012	3.004	0.014
					2.339	1	6.803	0.046	2.283	0.019	2.981	0.027
						2	7.173	0.073	2.377	0.026	3.018	0.032
KN162-7 23-107	53.173	22.547	3609	98900	4.3	1	6.77	0.14	2.265	0.053	2.973	0.051
						2	6.652	0.082	2.316	0.031	2.877	0.032
						3	6.855	0.056	2.294	0.020	2.990	0.023
						4	6.750	0.075	2.301	0.028	2.938	0.029
						5	6.944	0.097	2.364	0.037	2.938	0.036
						6	6.682	0.037	2.231	0.015	2.992	0.013
						7	6.88	0.14	2.298	0.053	2.979	0.052
						8	n.d.	---	n.d.	---	n.d.	---
						9	n.d.	---	n.d.	---	n.d.	---
KN162-7 22-14	53.109	22.647	3852	102000	3.024	1	7.017	0.065	2.370	0.022	2.957	0.020
						2	6.934	0.043	2.336	0.015	2.968	0.015
						3	7.061	0.047	2.376	0.016	2.969	0.016
						4	7.098	0.049	2.380	0.017	2.981	0.016
						5	7.016	0.039	2.339	0.014	3.000	0.014
						6	7.062	0.035	2.385	0.013	2.957	0.013
						7	7.068	0.040	2.389	0.014	2.959	0.014
						8	7.125	0.045	2.380	0.015	2.996	0.016
						9	6.971	0.082	2.329	0.029	2.987	0.030
AG22 9-2	53.130	22.880	3800	99500	3.921	1	6.680	0.028	2.233	0.010	2.991	0.010
						2	6.912	0.033	2.311	0.013	2.996	0.012
						3	6.882	0.041	2.309	0.016	2.982	0.016
						4	6.979	0.052	2.317	0.019	3.014	0.021
						5	6.927	0.041	2.312	0.016	2.997	0.016
						6	6.951	0.052	2.310	0.019	3.009	0.021
						7	6.968	0.092	2.301	0.033	3.031	0.035
						8	6.941	0.088	2.321	0.032	2.991	0.034
						9	7.02	0.10	2.358	0.039	2.977	0.039
						10	6.97	0.14	2.325	0.052	2.998	0.050
AG22 13-1	53.408	24.758	3850	99000	4.6	1	6.922	0.049	2.347	0.017	2.947	0.016
						2	7.018	0.045	2.347	0.015	2.988	0.016
						3	6.626	0.024	2.218	0.009	2.987	0.008
						4	6.612	0.026	2.221	0.010	2.976	0.009
						5	6.541	0.024	2.190	0.008	2.986	0.008
						6	6.660	0.027	2.231	0.011	2.987	0.011
						7	6.569	0.024	2.205	0.009	2.977	0.009
						8	6.735	0.035	2.252	0.012	2.989	0.013
						9	6.923	0.044	2.338	0.015	2.956	0.016
						10	6.808	0.038	2.300	0.013	2.961	0.014
						11	6.675	0.027	2.229	0.011	2.995	0.011
						12	6.963	0.060	2.342	0.020	2.968	0.019
						13	6.624	0.026	2.218	0.010	2.990	0.010

APPENDIX 4: SUPPLEMENT TO CHAPTER 4

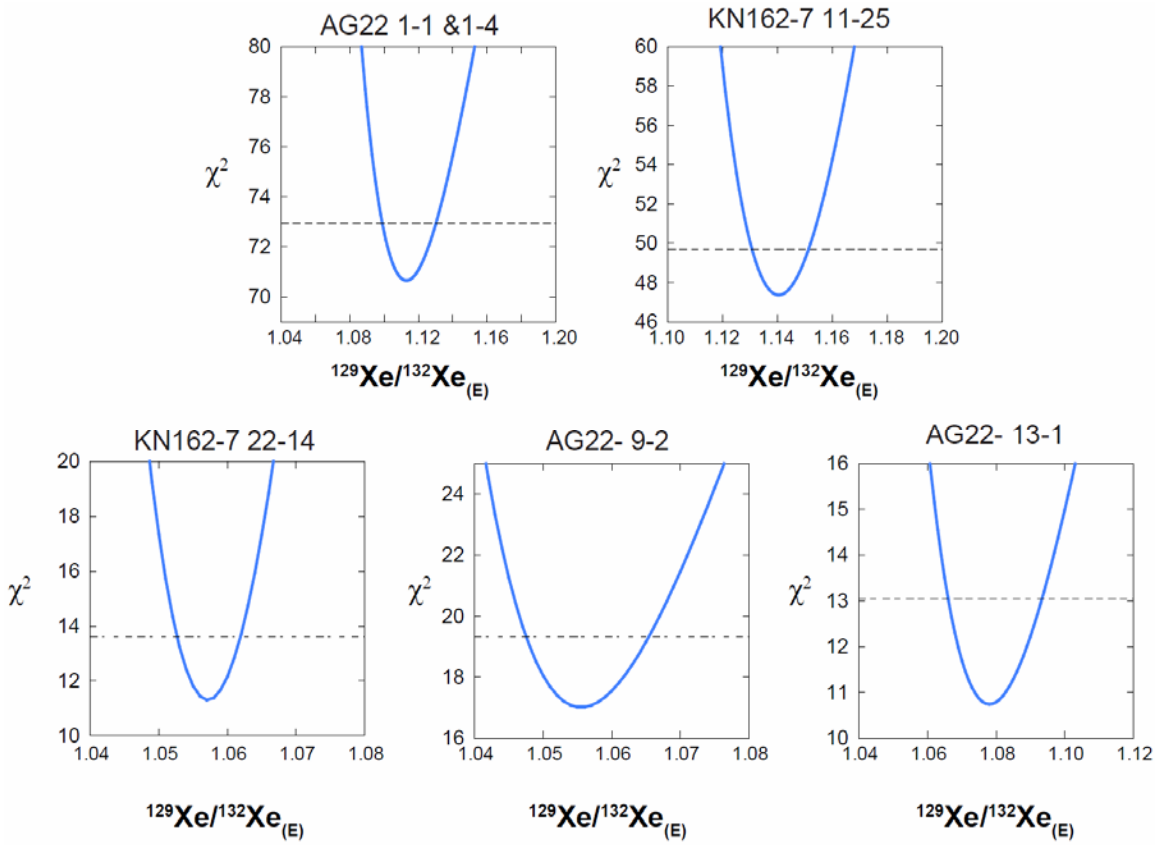

Figure A4.1 Chi-square as a function of mantle endmember $^{129}Xe/^{132}Xe$ for SWIR Orthogonal Supersegment samples. All terms same as in Figure A3.3 and caption.

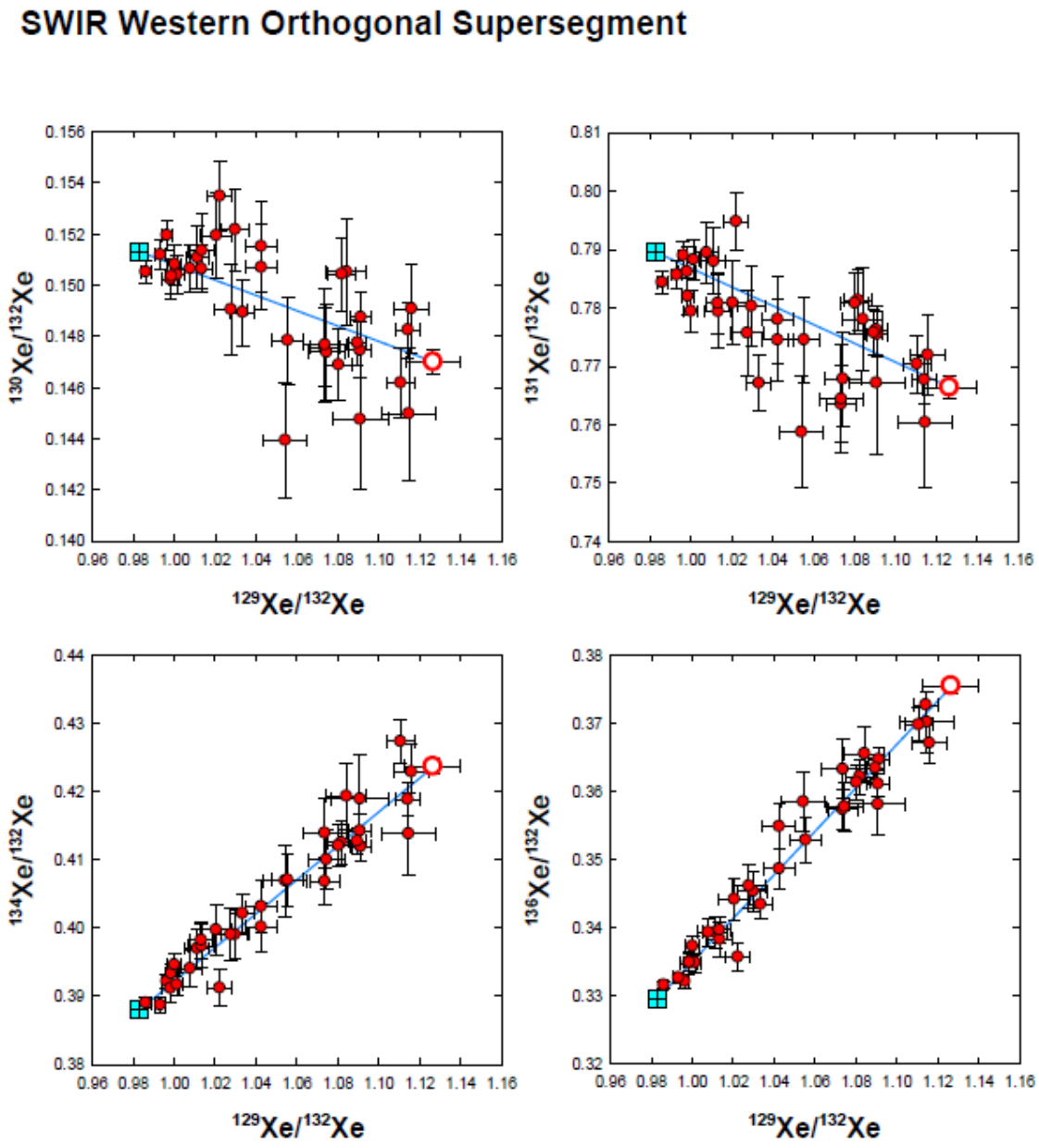

Figure A4.2 Linear least squares determinations of mantle source $^{130,131,134,136}Xe/^{132}Xe$ (bold open symbols) for Western Orthogonal Supersegment.

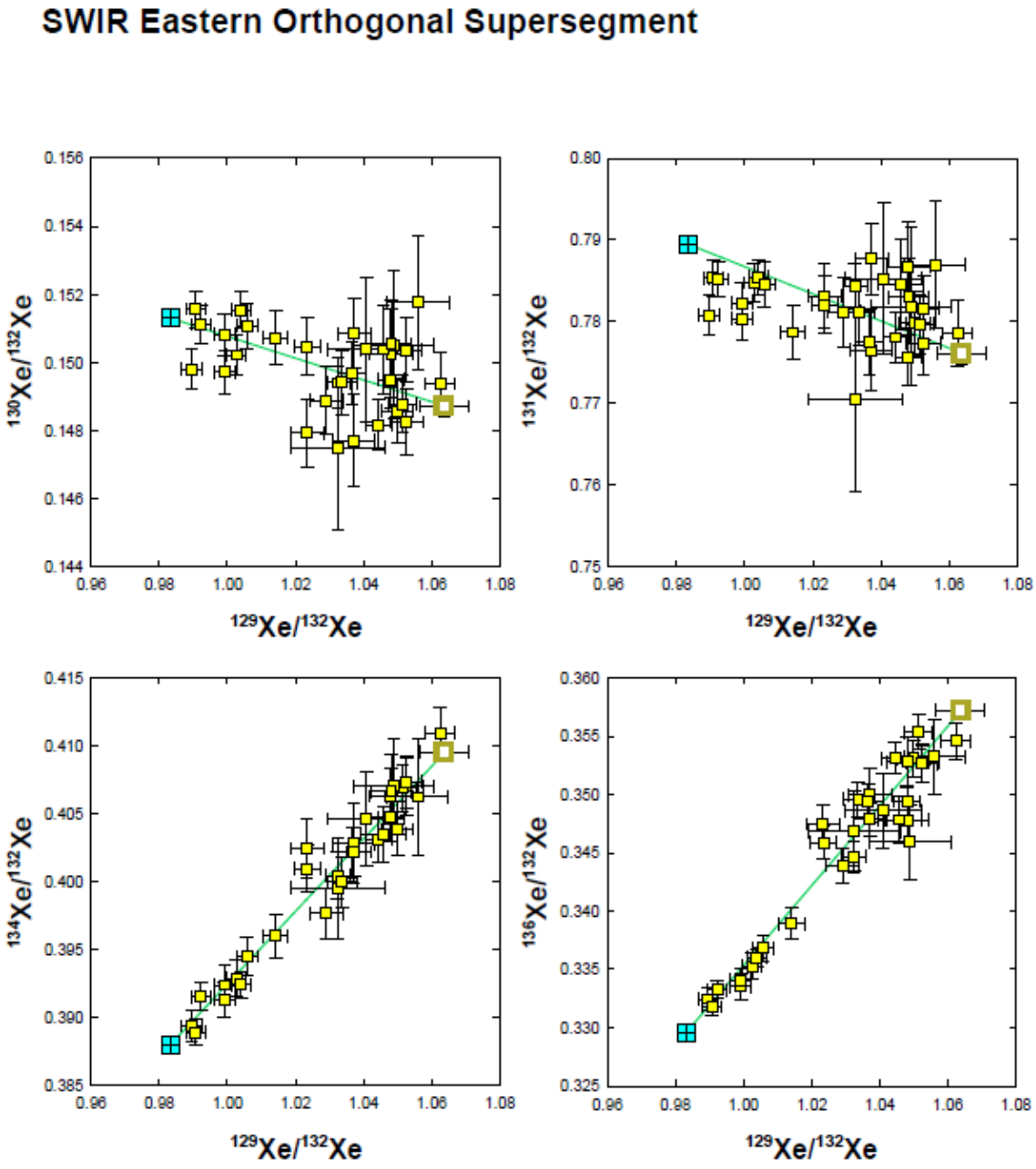

Figure A4.3 Linear least squares determinations of mantle source $^{130,131,134,136}Xe/^{132}Xe$ (bold open symbols) for Eastern Orthogonal Supersegment.

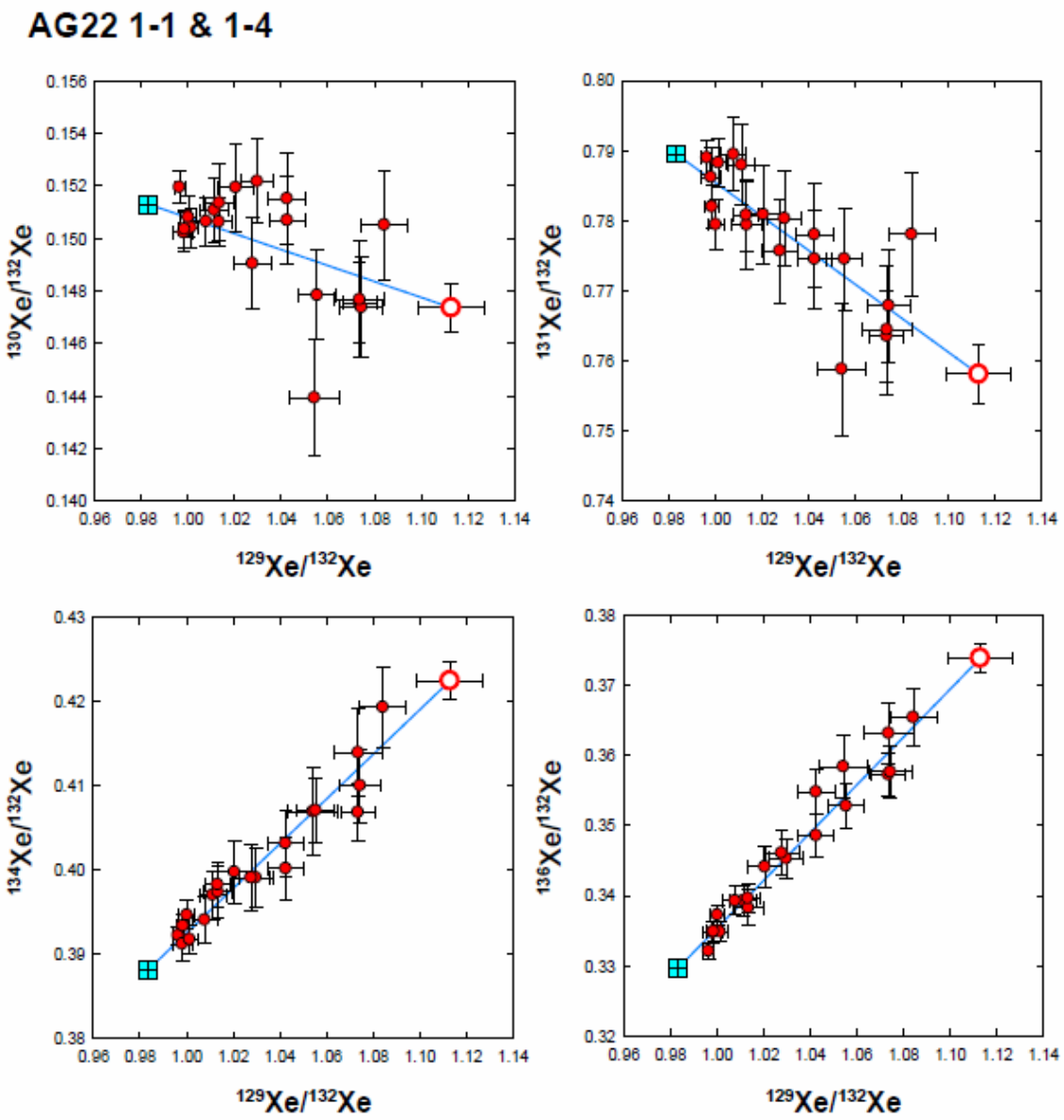

Figure A4.4 Linear least squares determinations of mantle source $^{130,131,134,136}Xe/^{132}Xe$ (bold open symbols) for AG22 1-1 & 1-4.

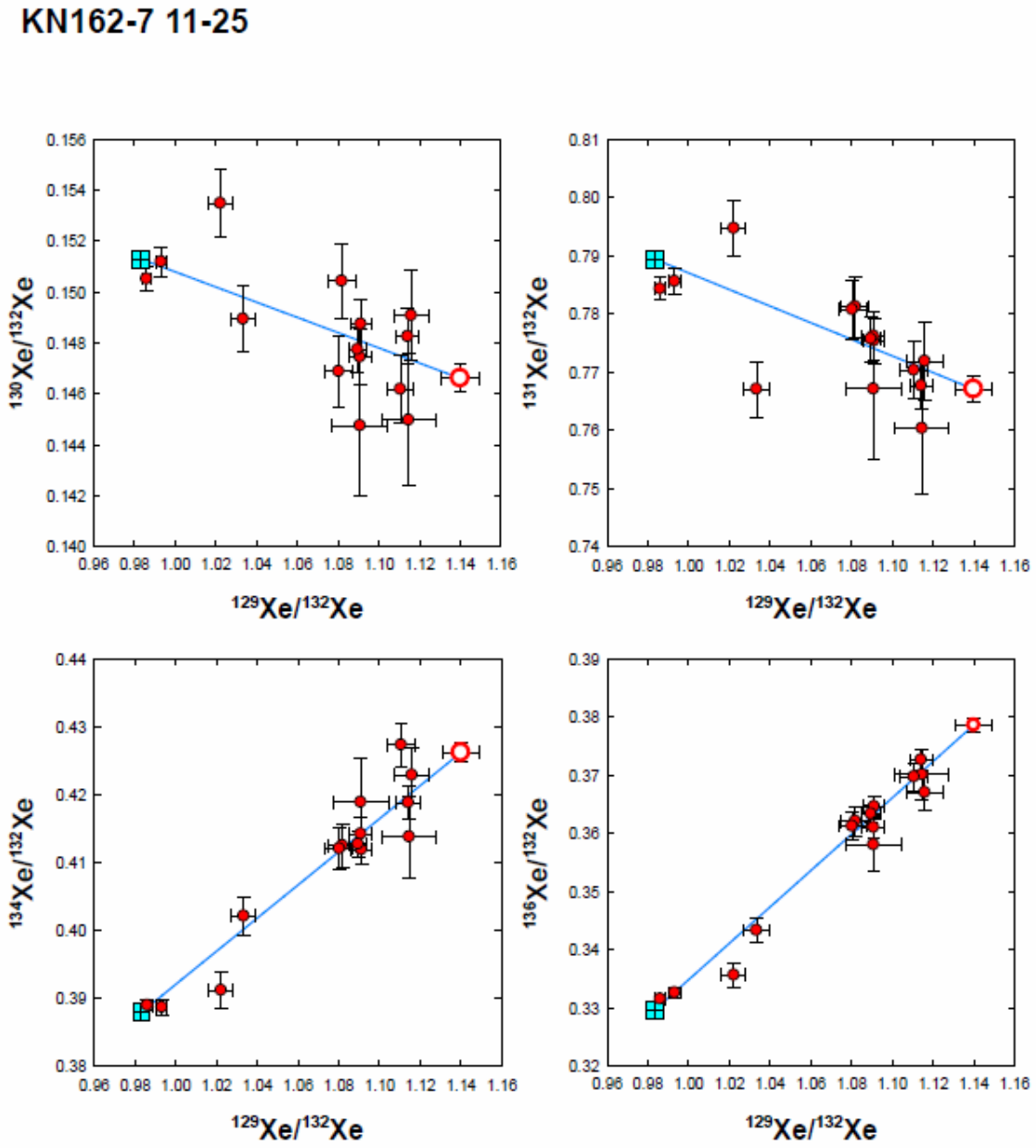

Figure A4.5 Linear least squares determinations of mantle source $^{130,131,134,136}Xe/^{132}Xe$ (bold open symbols) for KN162-7 11-25.

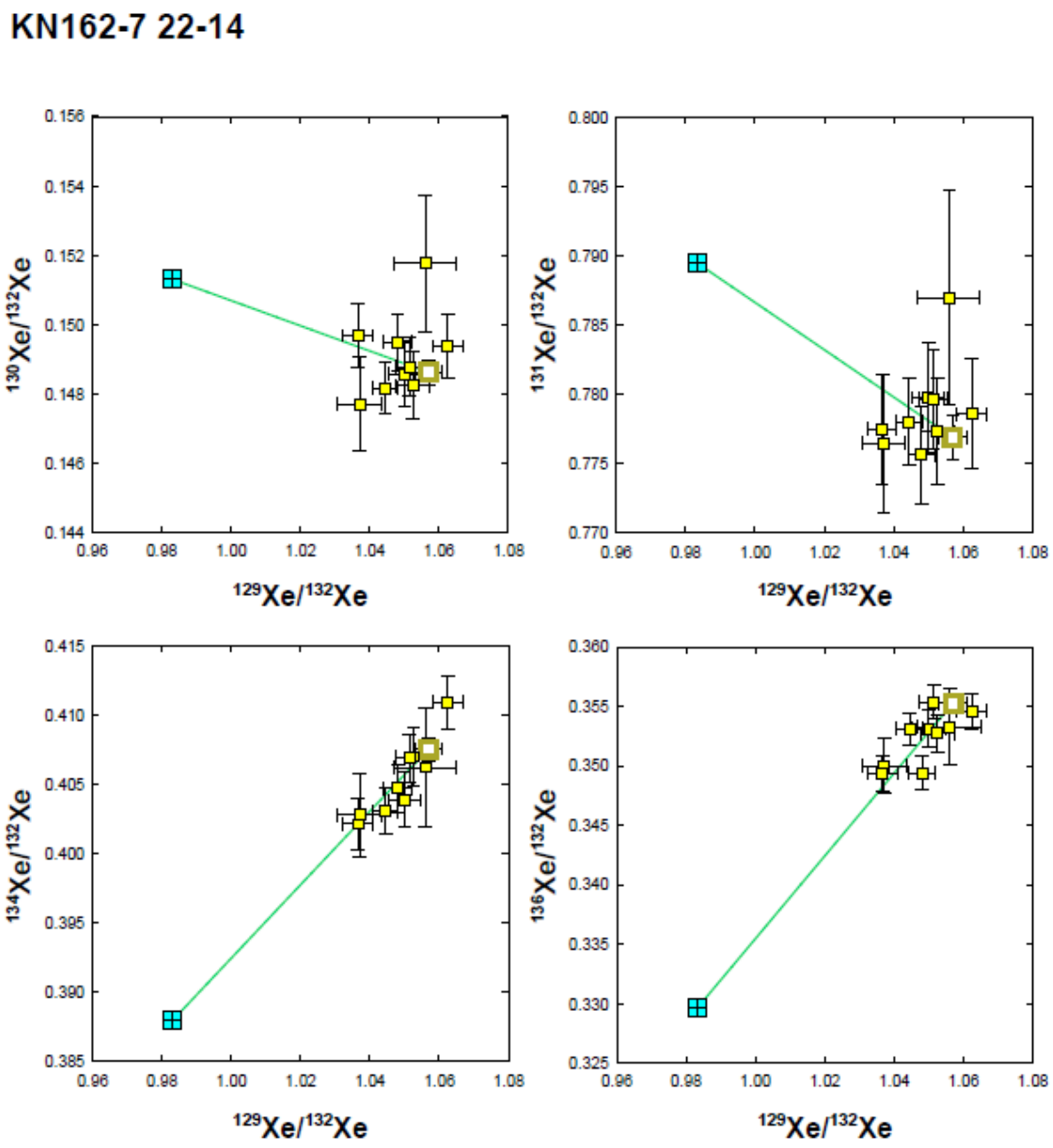

Figure A4.6 Linear least squares determinations of mantle source $^{130,131,134,136}Xe/^{132}Xe$ (bold open symbols) for KN162-7 22-14.

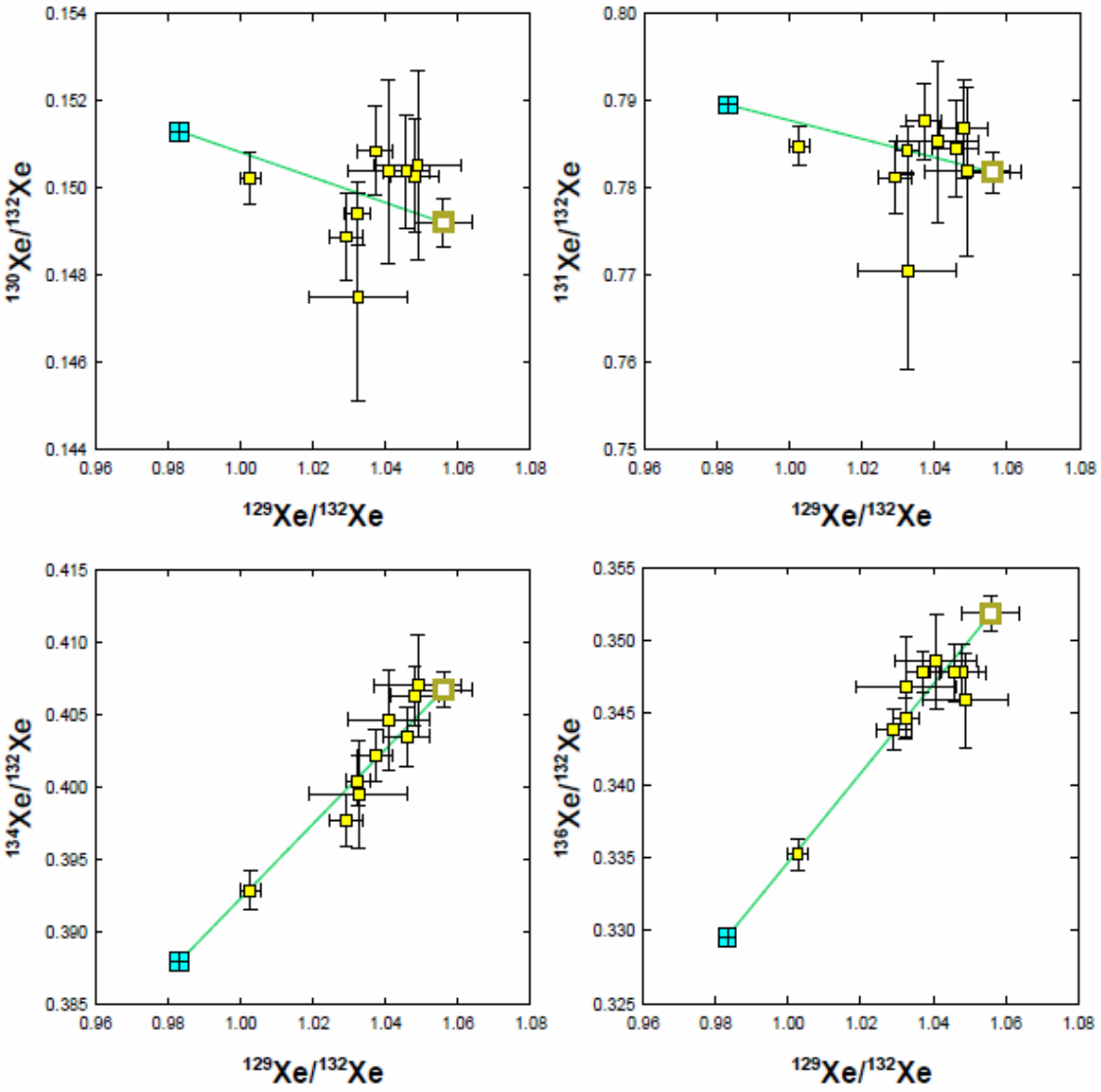

Figure A4.7 Linear least squares determinations of mantle source $^{130,131,134,136}Xe/^{132}Xe$ (bold open symbols) for AG22 9-2.

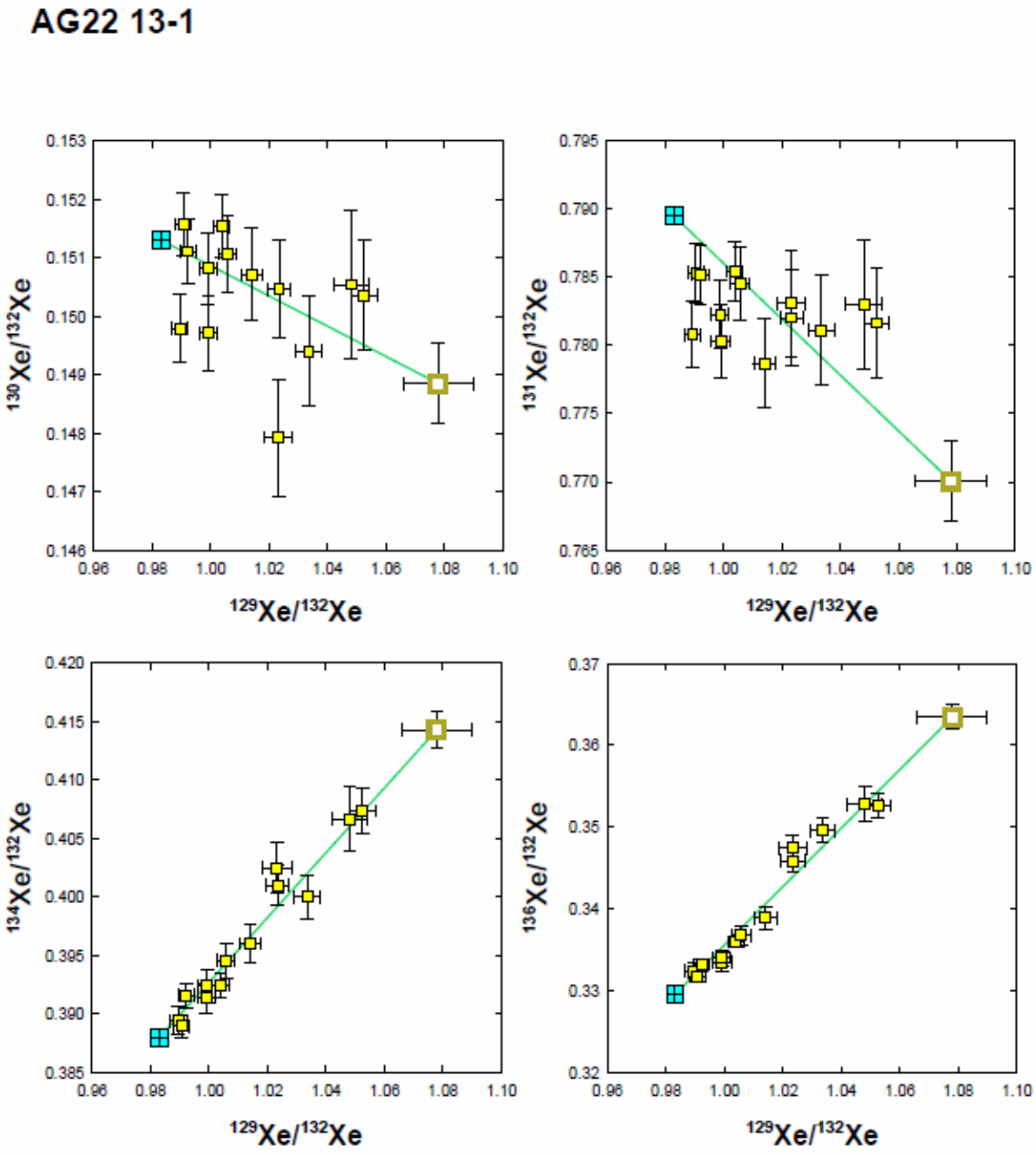

Figure A4.8 Linear least squares determinations of mantle source $^{130,131,134,136}Xe/^{132}Xe$ (bold open symbols) for AG22 13-1.

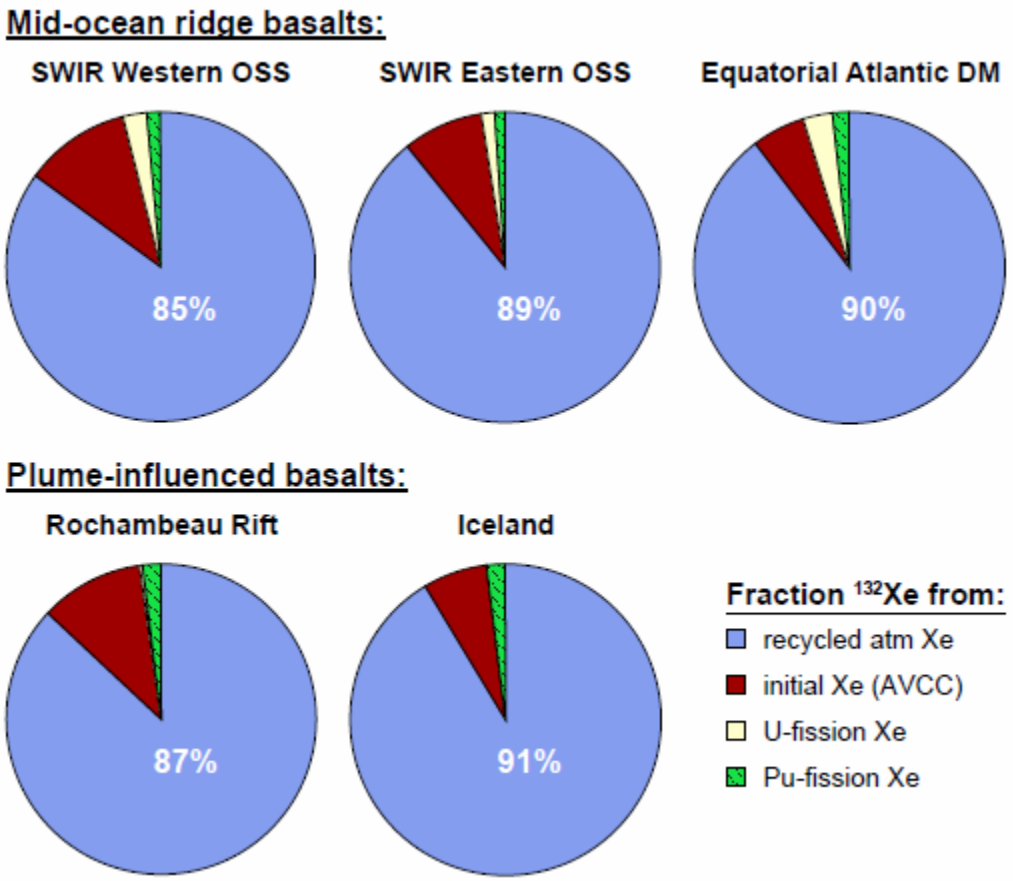

Figure A4.9 Pie charts illustrating the median proportions of present-day mantle ^{132}Xe derived from recycled atmosphere, AVCC initial mantle, U-fission and Pu-fission in SWIR Western and Eastern Orthogonal Supersegment mantle sources. Results for Equatorial Atlantic depleted MORB (Tucker et al., 2012), Rochambeau Rift (Pető et al., 2013) and Iceland (Mukhopadhyay, 2012) are shown for comparison. Recycled atmospheric Xe uniformly dominates the mantle Xe budget (percentages given in white). Fission Xe in the mantle sources of plume-influenced basalts is primarily derived from Pu-fission.

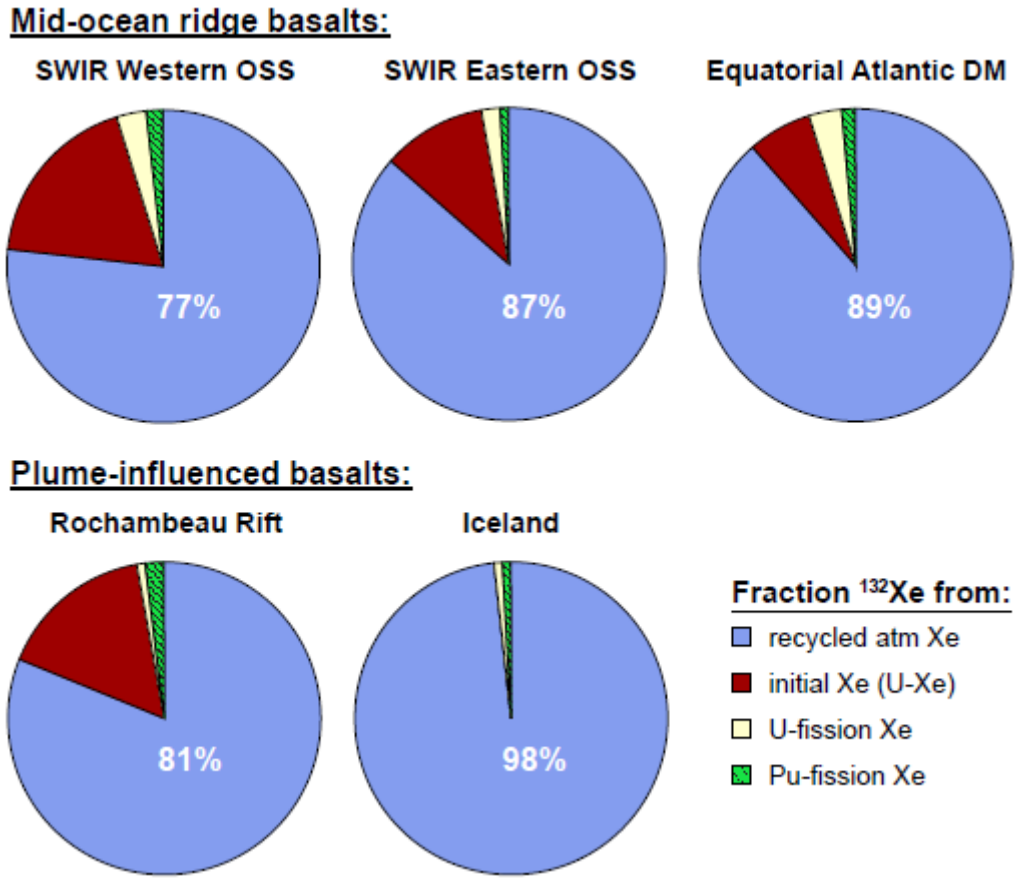

Figure A4.10 Pie charts illustrating the median proportions of present-day mantle ^{132}Xe derived from recycled atmosphere, U-Xe initial mantle, U-fission and Pu-fission in SWIR Western and Eastern Orthogonal Supersegment mantle sources. Results for Equatorial Atlantic depleted MORB (Tucker et al., 2012), Rochambeau Rift (Pető et al., 2013) and Iceland (Mukhopadhyay, 2012) are shown for comparison. Recycled atmospheric Xe uniformly dominates the mantle Xe budget (percentages given in white). Fission Xe in the mantle sources of plume-influenced basalts is primarily derived from Pu-fission.

Table A4.1 Southwest Indian Ridge 16-25°E fission Xe isotopic compositions

Sample	Lat.	Long.	Depth	$^{4}He/^{3}He$	grams	step	$x10^{-11}cc$ ^{36}Ar	$x10^{-14}cc$ ^{130}Xe
AG22 1-1	52.300	16.980	4000	108000	2.9325	1	6.8	1.1
						2	4.0	1.0
						3	67.5	8.4
						4	7.6	1.7
						5	23.7	3.1
						6	1.2	0.3
						7	5.8	1.0
						8	1.6	0.5
						9	2.9	1.0
						10	0.8	0.3
						11	1.8	0.4
					1.9257	1	21.3	3.4
						2	14.8	2.2
						3	2.6	0.7
						4	4.3	0.9
						5	1.7	0.5
						6	8.3	1.2
						7	1.0	0.3
					1.31	1	17.0	1.5
						2	18.7	2.4
						3	1.6	0.4
						4	1.3	0.4
AG22 1-4	52.300	16.980	4000		2.9982	1	33.3	4.6
						2	7.5	2.4
						3	16.6	3.3
						4	2.1	0.6
						5	4.0	0.9
						6	2.1	0.5
						7	5.2	0.9
						8	1.0	0.4
						9	1.7	0.3
KN162-7 11-25	52.799	19.200	3913	104000	4.064	1	3.7	1.6
						2	86.1	11.1
						3	1.2	0.5
						4	2.7	1.2
						5	0.7	0.4
						6	2.3	2.4
						7	5.6	2.0
						8	2.5	1.1
						9	1.8	0.8

Table A4.1 (continued) Southwest Indian Ridge 16-25°E fission Xe isotopic compositions

Sample	Lat.	Long.	Depth	$^{4}He/^{3}He$	grams	step	$x10^{-11}cc$ ^{36}Ar	$x10^{-14}cc$ ^{130}Xe
KN162-7 11-25						10	3.7	1.9
						11	3.5	1.2
						12	1.0	0.4
					2.488	1	96.8	43.9
						2	4.0	3.0
						3	4.3	1.6
						4	0.5	0.1
KN162-7 22-14	53.109	22.647	3852	102000	3.024	1	4.9	1.4
						2	10.1	3.2
						3	4.7	2.7
						4	5.2	2.5
						5	14.3	3.8
						6	4.6	4.5
						7	3.5	3.6
						8	2.3	2.9
						9	1.1	0.8
AG22 9-2	53.130	22.880	3800	99500	3.921	1	47.2	8.8
						2	18.4	4.7
						3	4.7	2.8
						4	5.6	1.9
						5	7.1	2.7
						6	6.0	1.9
						7	1.8	0.7
						8	1.8	0.8
						9	1.6	0.6
						10	0.6	0.2
AG22 13-1	53.408	24.758	3850	99000	4.6	1	14.1	2.5
						2	9.5	3.0
						3	40.7	12.4
						4	73.1	9.3
						5	102.0	12.5
						6	52.1	6.3
						7	95.0	12.0
						8	30.2	4.5
						9	11.8	3.0
						10	18.5	3.9
						11	55.4	6.9
						12	6.4	1.6
						13	66.4	8.8

Table A4.1 (continued) Southwest Indian Ridge 16-25°E fission Xe isotopic compositions

Sample	step	$^{40}Ar/^{36}Ar$	1σ	$^{129}Xe/^{132}Xe$	1σ	$^{130}Xe/^{132}Xe$	1σ
AG22 1-1	1	3169	32	1.030	0.007	0.152	0.002
	2	9243	92	1.074	0.007	0.148	0.002
	3	766	8	0.996	0.002	0.152	0.001
	4	2955	30	1.011	0.006	0.151	0.001
	5	1205	12	0.998	0.004	0.150	0.001
	6	9847	98	1.091	0.013	0.152	0.003
	7	3896	39	1.043	0.008	0.151	0.002
	8	12520	130	1.054	0.011	0.144	0.002
	9	7000	70	1.021	0.007	0.152	0.002
	10	13100	130	1.050	0.012	0.152	0.003
	11	4714	47	1.031	0.012	0.151	0.003
	1	1559	16	1.001	0.003	0.150	0.001
	2	2086	21	1.008	0.005	0.151	0.001
	3	10090	100	1.074	0.009	0.147	0.002
	4	5857	59	1.043	0.008	0.152	0.002
	5	11740	120	1.060	0.011	0.147	0.002
	6	1703	17	1.013	0.006	0.151	0.001
	7	7729	77	1.049	0.013	0.153	0.003
	1	3275	33	1.036	0.007	0.151	0.001
	2	3612	36	1.035	0.007	0.150	0.001
	3	9643	96	1.057	0.011	0.150	0.004
	4	9317	93	1.060	0.011	0.146	0.004
AG22 1-4	1	1269	13	0.999	0.003	0.150	0.001
	2	3906	39	1.013	0.005	0.151	0.001
	3	2105	21	1.000	0.003	0.151	0.001
	4	12490	120	1.084	0.010	0.151	0.002
	5	6786	68	1.055	0.008	0.148	0.002
	6	12180	120	1.074	0.011	0.148	0.002
	7	4285	43	1.028	0.008	0.149	0.002
	8	15340	150	1.086	0.012	0.151	0.003
	9	5848	58	1.044	0.012	0.147	0.003
KN162-7 11-25	1	6886	69	1.022	0.006	0.153	0.001
	2	877	9	0.993	0.003	0.151	0.001
	3	26650	270	1.115	0.013	0.145	0.003
	4	27240	270	1.111	0.007	0.146	0.001
	5	27610	280	1.084	0.014	0.149	0.003
	6	20120	200	1.091	0.005	0.149	0.001
	7	16490	160	1.091	0.006	0.147	0.001
	8	18610	190	1.082	0.007	0.150	0.001
	9	26780	270	1.116	0.009	0.149	0.002

Table A4.1 (continued) Southwest Indian Ridge 16-25°E fission Xe isotopic compositions

Sample	step	$^{40}Ar/^{36}Ar$	1σ	$^{129}Xe/^{132}Xe$	1σ	$^{130}Xe/^{132}Xe$	1σ
KN162-7 11-25	10	28500	290	1.114	0.006	0.148	0.001
	11	13390	130	1.080	0.007	0.147	0.001
	12	21960	220	1.091	0.014	0.145	0.003
	1	647	6	0.986	0.002	0.151	0.000
	2	14660	150	1.090	0.004	0.148	0.001
	3	10840	110	1.033	0.006	0.149	0.001
	4	5955	60	1.051	0.016	0.151	0.003
KN162-7 22-14	1	6488	65	1.037	0.006	0.148	0.001
	2	8492	85	1.037	0.004	0.150	0.001
	3	15610	160	1.050	0.005	0.149	0.001
	4	14550	150	1.053	0.005	0.148	0.001
	5	7665	77	1.048	0.004	0.149	0.001
	6	11940	120	1.044	0.004	0.148	0.001
	7	14050	140	1.051	0.004	0.149	0.001
	8	17540	180	1.063	0.004	0.149	0.001
	9	20700	210	1.056	0.009	0.152	0.002
AG22 9-2	1	1584	16	1.003	0.003	0.150	0.001
	2	3840	38	1.032	0.004	0.149	0.001
	3	8991	90	1.037	0.005	0.151	0.001
	4	6109	61	1.048	0.007	0.150	0.001
	5	6579	66	1.029	0.005	0.149	0.001
	6	5614	56	1.046	0.006	0.150	0.001
	7	8279	83	1.049	0.012	0.151	0.002
	8	9537	95	1.041	0.011	0.150	0.002
	9	7883	79	1.033	0.014	0.147	0.002
	10	8648	115	1.021	0.019	0.147	0.003
AG22 13-1	1	3579	36	1.023	0.005	0.148	0.001
	2	8286	83	1.053	0.004	0.150	0.001
	3	1259	13	1.004	0.003	0.152	0.001
	4	904	9	0.990	0.003	0.150	0.001
	5	670	7	0.991	0.003	0.152	0.001
	6	1434	14	1.006	0.003	0.151	0.001
	7	760	8	0.992	0.003	0.151	0.001
	8	1844	18	1.014	0.004	0.151	0.001
	9	5028	50	1.034	0.004	0.149	0.001
	10	3707	37	1.023	0.004	0.150	0.001
	11	1317	13	0.999	0.003	0.150	0.001
	12	6347	63	1.048	0.006	0.151	0.001
	13	1116	11	0.999	0.003	0.151	0.001

Table A4.1 (continued) Southwest Indian Ridge 16-25°E fission Xe isotopic compositions

Sample	step	$^{131}Xe/^{132}Xe$	1σ	$^{134}Xe/^{132}Xe$	1σ	$^{136}Xe/^{132}Xe$	1σ
AG22 1-1	1	0.780	0.007	0.399	0.003	0.345	0.003
	2	0.763	0.007	0.407	0.004	0.357	0.003
	3	0.789	0.002	0.392	0.001	0.332	0.001
	4	0.788	0.006	0.397	0.003	0.339	0.002
	5	0.786	0.004	0.391	0.002	0.335	0.002
	6	0.784	0.011	0.411	0.006	0.359	0.005
	7	0.774	0.007	0.400	0.004	0.349	0.003
	8	0.759	0.009	0.407	0.005	0.358	0.004
	9	0.781	0.007	0.400	0.004	0.344	0.003
	10	0.791	0.011	0.409	0.006	0.351	0.005
	11	0.781	0.011	0.401	0.006	0.345	0.005
	1	0.788	0.004	0.392	0.002	0.335	0.001
	2	0.789	0.005	0.394	0.003	0.339	0.002
	3	0.768	0.008	0.410	0.004	0.358	0.004
	4	0.778	0.007	0.403	0.004	0.355	0.003
	5	0.778	0.010	0.411	0.005	0.361	0.005
	6	0.779	0.006	0.397	0.003	0.338	0.003
	7	0.779	0.012	0.415	0.007	0.355	0.005
	1	0.787	0.004	0.399	0.002	0.347	0.002
	2	0.781	0.003	0.404	0.002	0.346	0.002
	3	0.778	0.011	0.408	0.008	0.355	0.005
	4	0.792	0.011	0.399	0.008	0.348	0.005
AG22 1-4	1	0.782	0.003	0.393	0.001	0.335	0.001
	2	0.781	0.005	0.398	0.003	0.340	0.002
	3	0.779	0.004	0.395	0.002	0.337	0.001
	4	0.778	0.009	0.419	0.005	0.365	0.004
	5	0.775	0.007	0.407	0.004	0.353	0.003
	6	0.764	0.009	0.414	0.005	0.363	0.004
	7	0.776	0.007	0.399	0.004	0.346	0.003
	8	0.771	0.011	0.411	0.006	0.363	0.005
	9	0.787	0.011	0.403	0.006	0.350	0.005
KN162-7 11-25	1	0.795	0.005	0.391	0.003	0.336	0.002
	2	0.786	0.002	0.389	0.001	0.333	0.001
	3	0.760	0.011	0.414	0.006	0.370	0.004
	4	0.770	0.005	0.427	0.003	0.370	0.002
	5	0.765	0.013	0.403	0.007	0.360	0.005
	6	0.775	0.004	0.412	0.002	0.365	0.002
	7	0.776	0.004	0.414	0.002	0.361	0.002
	8	0.781	0.005	0.413	0.003	0.362	0.003
	9	0.772	0.007	0.423	0.004	0.367	0.003

Table A4.1 (continued) Southwest Indian Ridge 16-25°E fission Xe isotopic compositions

Sample	step	$^{131}Xe/^{132}Xe$	1σ	$^{134}Xe/^{132}Xe$	1σ	$^{136}Xe/^{132}Xe$	1σ
KN162-7 11-25	10	0.768	0.004	0.419	0.002	0.373	0.002
	11	0.781	0.005	0.412	0.003	0.361	0.002
	12	0.767	0.012	0.419	0.006	0.358	0.004
	1	0.784	0.002	0.389	0.001	0.332	0.000
	2	0.776	0.004	0.413	0.002	0.363	0.002
	3	0.767	0.005	0.402	0.003	0.343	0.002
	4	0.816	0.016	0.423	0.008	0.349	0.005
KN162-7 22-14	1	0.776	0.005	0.403	0.003	0.350	0.002
	2	0.777	0.004	0.402	0.002	0.349	0.002
	3	0.780	0.004	0.404	0.002	0.353	0.002
	4	0.777	0.004	0.407	0.002	0.353	0.002
	5	0.776	0.004	0.405	0.002	0.349	0.001
	6	0.778	0.003	0.403	0.002	0.353	0.001
	7	0.780	0.004	0.407	0.002	0.355	0.001
	8	0.779	0.004	0.411	0.002	0.355	0.002
	9	0.787	0.008	0.406	0.004	0.353	0.003
AG22 9-2	1	0.785	0.002	0.393	0.001	0.335	0.001
	2	0.784	0.003	0.400	0.002	0.345	0.001
	3	0.788	0.004	0.402	0.002	0.348	0.001
	4	0.787	0.006	0.406	0.002	0.348	0.002
	5	0.781	0.004	0.398	0.002	0.344	0.001
	6	0.785	0.006	0.403	0.002	0.348	0.002
	7	0.782	0.010	0.407	0.004	0.346	0.003
	8	0.785	0.009	0.405	0.003	0.349	0.003
	9	0.770	0.011	0.400	0.004	0.347	0.003
	10	0.764	0.016	0.394	0.004	0.341	0.004
AG22 13-1	1	0.783	0.004	0.402	0.002	0.347	0.002
	2	0.782	0.004	0.407	0.002	0.353	0.002
	3	0.785	0.002	0.392	0.001	0.336	0.001
	4	0.781	0.002	0.389	0.001	0.332	0.001
	5	0.785	0.002	0.389	0.001	0.332	0.001
	6	0.785	0.003	0.395	0.001	0.337	0.001
	7	0.785	0.002	0.392	0.001	0.333	0.001
	8	0.779	0.003	0.396	0.002	0.339	0.001
	9	0.781	0.004	0.400	0.002	0.350	0.002
	10	0.782	0.004	0.401	0.002	0.346	0.001
	11	0.780	0.003	0.392	0.001	0.334	0.001
	12	0.783	0.005	0.407	0.003	0.353	0.002
	13	0.782	0.002	0.391	0.001	0.334	0.001